Scanning Probe Spectroscopy of Graphene Nanostructures

Von der Fakultät Mathematik und Physik
der Universität Stuttgart zur Erlangung der Würde eines
Doktors der Naturwissenschaften (Dr. rer. nat.)
genehmigte Abhandlung

vorgelegt von
Benjamin Krauß
aus Böblingen

Hauptberichter:	Prof. Dr. Klaus von Klitzing
Mitberichter:	Prof. Dr. Jörg Wrachtrup
Tag der mündlichen Prüfung:	25. Juni 2012

Max-Planck-Institut für Festkörperforschung
Stuttgart, 2012

Contents

Symbols and Abbreviations

2DEG:	two-dimensional electron gas
2DES:	two-dimensional electron system
a:	lattice constant, $a = 2.46$ Å
$\mathbf{a}_{1,2}$:	real space unit vector
AA:	ascorbic acid
AGS:	automated graphene search
ARPES:	angle-resolved photoemission spectroscopy
B:	magnetic field
$\mathbf{b}_{1,2}$:	basis vector of the reciprocal lattice
BE:	beam expander
BZ:	Brillouin-zone
χ:	polarizability
χ^{-1}:	inverse compressibility
C:	capacitance
CBO:	Coulomb blockade oscillation
CCD:	charge coupled device
CLSM:	confocal laser scanning microscopy
CNP:	charge neutrality point
CNT:	carbon nanotube
CPD:	critical point dryer
CVD:	chemical vapor deposition
d_{cc}:	distance between adjacent carbon atoms in graphene, $d_{cc} = 1.42$ Å
d:	thickness
DOS:	density of states
ϵ_0:	vacuum permittivity
ϵ_r:	relative permittivity of the material
e:	electron charge
E:	energy
EBL:	electron beam lithography
f_{FD}	Fermi-Dirac distribution function
F:	filter (typically notch or edge filter)
F4-TCNQ:	tetrafluorotetracyanoquinodimethane
FET:	field-effect transistor
FQHE:	fractional quantum Hall effect
FWHM:	full width at half maximum
Γ:	Brillouin-zone center
$\mathbf{G}$:	reciprocal lattice vector
g:	system degeneracy
$\hbar$:	Planck constant
h:	hours
h-BN:	hexagonal boron nitride
HF:	hydrofluoric acid

HOPG: highly oriented pyrolitic graphite
IC: inverse compressibility
IPA: isopropyl alcohol
ITO: indium tin oxide
j: current density
$\mathbf{k}$:   wave-vector
k_B: Boltzmann constant
KOH: potassium hydroxide
LL: Landau level
μm: micrometer
μ_{ch}:   chemical potential
M: mirror
MBE: molecular beam epitaxy
MIBK: methyl isobutyl ketone
$\bar{\nu}$:   Raman shift
n: charge carrier density
NA: numerical aperture
NaOH: sodium hydroxide
ND: neutral density filter
NEP: N-ethylpyrrolidone
nm: nanometer
ω_A: frequency of an anti-Stokes scattered photon
ω_{Laser}:   frequency of a laser photon
ω_R: frequency of a Rayleigh scattered photon
ω_{Raman}:   frequency of Raman scattered light
ω_S: frequency of a Stokes scattered photon
ω_{Vib}:   frequency of a phonon
PMMA: poly(methyl metacrylate)
PMT: photomultiplier tube
PSF: point spread function
Q: charge
QHE: quantum Hall effect
ρ_{xx}:   longitudinal resistance
ρ_{xy}:   transversal resistance
RMS: root mean square
SdH: Shubnikov-de Haas
SdHO: Shubnikov-de Haas-oscillations
SET: single-electron transistor
Si: silicon
SiC: silicon carbide
SiO_2:   silicon oxide
SPM: scanning probe microscopy
T: temperature
TEM: transmission electron microscopy
UHV: ultra-high vacuum
V: voltage
V_{BG}:   back-gate voltage
V_{CNP}:   applied back-gate voltage in order to reach charge neutrality

1. Introduction

Carbon is one of the most versatile elements in nature. It possesses four valence electrons which can be hybridized in different ways. A carbon atom can form four bonds (sp^3-hybridization) but also three (sp^2-hybridization) and two (sp-hybridization) are possible. As a consequence, a cornucopia of complicated and sophisticated compounds like for instance proteins and enzymes can be realized. Carbon is the foundation for organic chemistry [1] as well as all complex life forms. Even if restricting to materials built only with carbon atoms, there exist several allotropes as shown in Figure 1.1. Amongst them are the well known three-dimensional diamond and graphite. A variety of further allotropes were synthesized in the 1980ies, the most famous are one-dimensional carbon nanotubes (CNT) [2] and zero-dimensional Buckminster fullerenes [3]. Only the two-dimensional form, graphene, was missing. Until recently, it was believed to be thermodynamically unstable [4] and, hence, only played a role as a theoretical model to explain for instance the complicated physics of CNT. Nevertheless, several groups tried to fabricate graphene. In the year 2004, A. Geim et al. succeeded and isolated single layers of graphene on a silicon substrate [5]. Their micro-mechanical cleavage technique is as simple as it is beautiful and opened the door for investigating the physical properties of graphene. The interaction between lattice and charge carriers is peculiar and yields a linear electronic dispersion relation. Unlike in most other solids, which have a parabolic dispersion relation, the charge carriers in graphene mimic chiral particles with zero rest mass. Like neutrinos and antineutrinos. This might open the door to study quantum-electrodynamic effects in a solid state experiment. Another consequence of the linear band structure is an unconventional sequence of the integer [6, 7] quantum Hall effect (QHE) [8]. The integer QHE is even observable at room temperature [9]. Graphene is a wonderful playground for theorists and basic research. But graphene is more than that: several applications exploiting various properties of graphene can be envisioned. For instance has graphene the potential to replace the scarce indium tin oxide (ITO) in solar cells and touch screens as a conducting but transparent electrode [10]. Owing to its strong in-plane bonds it furthermore is added into compounds to increase the strength of materials but not their weight. And the charge carriers high mobility makes it interesting for high frequency applications [11, 12].

One major advantage of graphene worth emphasizing that is different to most two-dimensional electron systems (2DES) is, that the 2DES is not buried at an interface inside a bulk material, but it rather is exposed at the surface. This is especially beneficial for scanning probe techniques as used in this work.
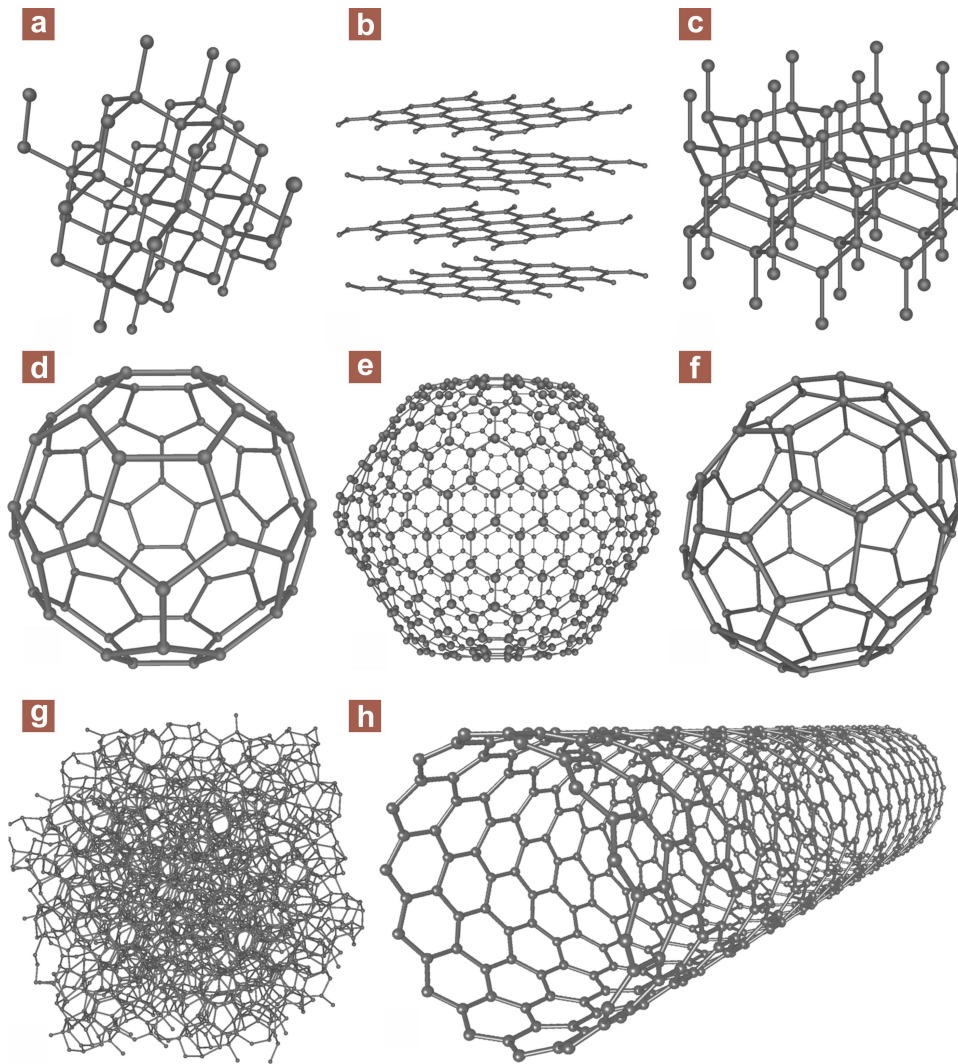
Figure 1.1.: **Some allotropes of carbon.** *(a) diamond, (b) graphite, (c) lonsdaleite, (d) fullerene C_{60}, (e) fullerene C_{540}, (f) fullerene C_{70}, (g) amorphous carbon, (h) carbon nanotube (modified from Wikimedia Commons).*

This thesis is organized in two parts. In part I we introduce the foundations necessary for the experiments covered in part II.

The first chapter is dedicated to graphene. We start by taking a closer look at the lattice structure, show the resulting electronic band structure and discuss some of its consequences. The band structure for multi-layer graphene is treated next, including Bernal stacked and twisted bilayer. As a consequence of the linear band structure of graphene, the density of states is not constant as in conventional semiconductors but increases with energy. We give the corresponding formulas. We discuss the implications for the Landau level spectrum as well as the cyclotron mass and frequency. The micromechanical cleavage method and other procedures to obtain graphene monolayers are introduced and we cover how to fabricate graphene nanostructures with electron beam lithography, etching and evaporation of metals. Finally, we end the first chapter by describing the most common way to change the carrier concentration in graphene: electric gating.

CHAPTER 2

PP. 13-36

In order to understand the mechanism behind Raman spectroscopy we start with a quantum mechanical model, before we specifically focus on the Raman spectrum of graphene. It will turn out that only one out of the three observed prominent peaks can be explained by normal vibrations. However, by introducing multi-resonance processes the other two peaks are understood as well. As this resonance process involves both phononic and electronic properties a cornucopia of information can be extracted from the Raman spectrum. We give some examples. Having established the fundamentals of Raman scattering in graphene, we end this chapter by describing the scanning confocal setup used in this thesis to measure spatially and time resolved Raman spectra.

CHAPTER 3

PP. 37-60

The second probe used to scan the graphene sample in this thesis is a single-electron transistor. We discuss the essential fundamentals in this chapter. First, we motivate why to measure the inverse compressibility and show its relation to quantum Hall states. Then, we transform the difficult task of measuring the inverse compressibility to the easier problem of measuring changes in the electrostatic potential. This can be measured with an SET with a very high sensitivity. We explain the working principle of an SET. Finally, we briefly describe the SET fabrication procedure and the scanning probe microscope which is used to measure the inverse compressibility of graphene.
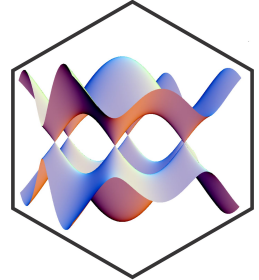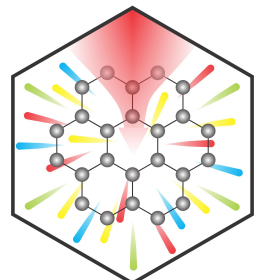
CHAPTER 4
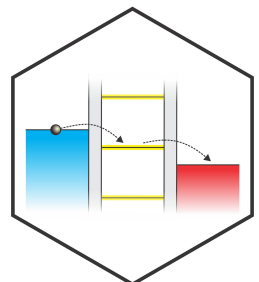
PP. 61-80

Having established the required fundamentals, the second part of the thesis is dedicated to experiments and their discussion.

CHAPTER 5
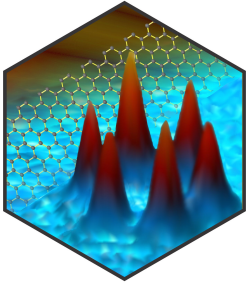
PP. 83-106

The experiment described in this chapter starts with a surprise. Although Raman spectroscopy of graphene was believed to be non-invasive, we show that laser light is not necessarily benign and modifies graphene. We combine time and spatially resolved Raman and atomic force measurements and corroborate our findings with electrical and transmission electron microscopy studies. It turns out that laser irradiation locally disassembles graphene into a network of interconnected nanocrystallites. Either the irradiation has to be dosed carefully in order to avoid these modifications or they can be exploited on purpose. The additional boundaries provide docking sites for molecular adsorbates and the reactivity can be enhanced locally.

CHAPTER 6
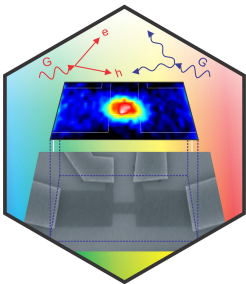
PP. 107-122

Here we show that a high current flow through a device significantly overpopulates phonon modes, which impede transport. This has an impact on device performance. For a deeper understanding, we take a closer look at the interaction between phonons and charge carriers in graphene. We explain why graphene offers a unique opportunity to control decay channels. For the experiment we use an electrically biased graphene constriction to locally increase the phonon occupation number. This allows us to entangle carrier-phonon and phonon-phonon contributions. In this context we also introduce the term "hot phonons" and its meaning. The two most important parameters in this experiment are the temperature and the interaction strength of a phonon with other quasi-particles. Both properties are measured simultaneously with Raman spectroscopy.

CHAPTER 7
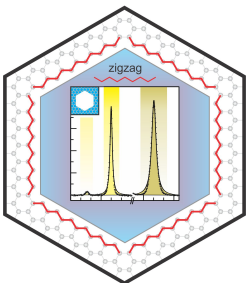
PP. 123-134

With this Chapter we add a powerful capability to the graphene toolbox: the identification of pure graphene zigzag edges with Raman spectroscopy. For this purpose we introduce an anisotropic etching procedure before we explain the theory behind Raman scattering at pure graphene zigzag edges. Here, the so-called Raman D peak serves as the litmus test. Both methods combined can be used as a straightforward technique to identify the crystallographic orientation of graphene flakes. We furthermore show how to prepare graphene constrictions, one-dimensional channels and even quantum dots which are bounded exclusively by zigzag edges. For such graphene devices, theory has predicted rich and very distinct physics.

We address the important point of the visibility of graphene on different substrates in this chapter. As with the micro-mechanical cleavage method only a minor fraction of the substrate is covered with monolayer graphene, it is necessary to find and identify these few monolayers. We explain a model based on Fresnel laws that allows to calculate the contrast of graphene on an arbitrary sandwich of materials. Using the example of indium tin oxide (ITO) as a transparent but conductive layer, for instance suited for scanning tunneling microscopy studies, we demonstrate how to choose a proper ITO thickness for maximizing the graphene contrast. The model introduced here will also be used in the next chapter.
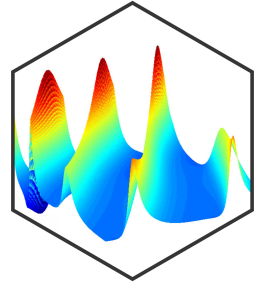
It turned out, that the substrate which supports graphene plays an important role on device performance. Up to now the measured graphene properties are inferior to the predicted intrinsic characteristics, for instance as a consequence of the substrate roughness, surface optical phonons and scattering from charged impurities inside the substrate. Here we show how to transfer graphene to hexagonal boron nitride (h-BN) as a substrate. Hexagonal-BN is atomically flat and free of dangling bonds and surface charge traps. As h-BN itself is typically only a small flake on the order of several micrometer, a micro positioning stage is used. We investigate the optical visibility of h-BN depending on its thickness by comparing experimental results with the theory developed in the previous chapter. Finally, we turn our attention to the surface roughness as a function of h-BN thickness.
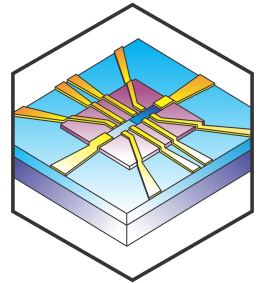
In the last experimental chapter we use a single-electron transistor (SET) mounted on a scanning microscope as a probe to image the local inverse electronic compressibility of a suspended graphene monolayer. We observe a unique pattern of incompressible fractional quantum Hall states. Between filling factor $\nu = 0$ and 1 the sequence follows the standard composite fermion picture, but between $\nu = 1$ and 2 only even-numerator fractions occur. In order to further investigate this unconventional hierarchy we extract the energy gaps as a function of magnetic field. By measuring the spatial dependence of the fractional quantum Hall states we can explain why these fragile states are observable locally with an SET but not in standard transport experiments. The fact that we see incompressible behavior at multiples of 1/3, 1/5, 1/7 and even 1/9 indicates that graphene is quickly approaching the sample quality obtained in GaAs. Thanks to graphenes massless chiral carriers, the fourfold degeneracy and the ever increasing quality of graphene devices, novel many-body effects are expected to be observed in the near future.
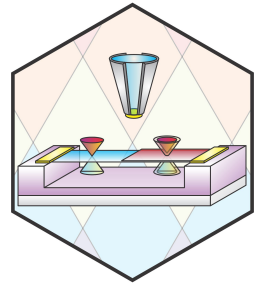
Parts of the results presented in this thesis are already published:

Peer-review journals

1. **Unconventional sequence of fractional quantum Hall states in suspended graphene**
   B. E. Feldman, B. Krauss, J. H. Smet and A. Yacoby
   Science, in press (2012) (arXiv:1201.5128).

2. **Raman scattering at pure graphene zigzag edges**
   B. Krauss, P. Nemes-Incze, V. Skakalova, L.P. Biro, K. von Klitzing, and J.H. Smet
   Nano Letters **10**, 4544 (2010).

3. **Hot phonons in an electrically biased graphene constriction**
   D. H. Chae*, B. Krauss*, K. von Klitzing, and J. H. Smet
   Nano Letters **10**, 466 (2010).

4. **Charge neutrality and band-gap tuning of epitaxial graphene on SiC by molecular doping**
   C. Coletti, C. Riedl, D. S. Lee, B. Krauss, L. Patthey, K. von Klitzing, J. H. Smet and U. Starke
   Physical Review B **81**, 235401 (2010).

5. **Electronic decoupling of an epitaxial graphene monolayer by gold intercalation**
   I. Gierz, T. Suzuki, R. T. Weitz, D. S. Lee, B. Krauss, C. Riedl, U. Starke, H., Höchst, J. H. Smet, C. R. Ast, and K. Kern
   Physical Review B **81**, 235408 (2010).

6. **Graphene on a hydrophobic substrate: Doping reduction and hysteresis suppression under ambient conditions**
   M. Lafkioti, B. Krauss, T. Lohmann, U. Zschieschang, H. Klauk, K. von Klitzing and J. H. Smet
   Nano Letters **10**, 1149 (2010).

7. **Laser-induced disassembly of a graphene single crystal into a nanocrystalline network**
   B. Krauss, T. Lohmann, D. H. Chae, M. Haluska, K. von Klitzing, and J. H. Smet
   Physical Review B **79**, 165428 (2009).

8. **Raman spectra of epitaxial graphene on SiC and of epitaxial graphene transferred to SiO$_2$**
   D. S. Lee, C. Riedl, B. Krauss, K. von Klitzing, U. Starke, and J. H. Smet
   Nano Letters **8** (12), 4320-4325 (2008).

9. **Investigation of the shift of Raman modes of graphene flakes**
   M. Haluska, D. Obergfell, J. C. Meyer, G. Scalia, G. Ulbricht, B. Krauss, D. H. Chae, T. Lohmann, M. Lebert, M. Kaemogen, M. Hulman, J. H. Smet, S. Roth, and K. von Klitzing
   Physica status solidi b **244**, No. 11, 4143-4146 (2007).

Annual reports

1. **Raman scattering at pure graphene zigzag edges**
   B. Krauss, P. Nemes-Incze, V. Skakalova, L.P. Biro, K. von Klitzing, and J.H. Smet
   Jahresbericht **2010**, Max-Planck-Institut für Festkörperforschung, selected research reports.

2. **The effect of a hydrophobic substrate on the electronic properties of graphene**
   M. Lafkioti, B. Krauss, T. Lohmann, U. Zschieschang, H. Klauk, K. von Klitzing and J. H. Smet
   Jahresbericht **2009**, Max-Planck-Institut für Festkörperforschung, selected research reports.

3. **Laser-induced disassembly of a graphene single crystal into a nano-crystalline network**
   B. Krauss, T. Lohmann, D. H. Chae, M. Haluska, K. von Klitzing, and J. H. Smet
   Jahresbericht **2008**, Max-Planck-Institut für Festkörperforschung, cover and selected research reports.

Part I.

Fundamentals

2. Graphene
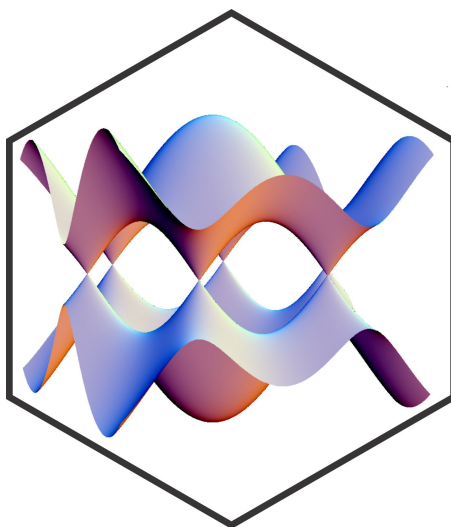
Graphene is a single two-dimensional layer of sp^2-hybridized carbon atoms arranged in a hexagonal honeycomb lattice. The basic building block for graphene is the chemical element carbon.

In graphene, the carbon atoms are sp^2-hybridized. This stipulates the lattice structure of graphene as discussed in Section 2.1. The lattice structure leads to the electronic band structure of graphene with its linear dispersion relation. This band structure and some peculiar implications are covered in Section 2.2. Stacking two graphene monolayers on top of each other strongly affects the band structure, depending on stacking order and twist angle, as will be shown in Section 2.3. Consequences of the band structure on the density of states without (Section 2.4) and with (Section 2.5) an externally applied magnetic field are discussed. The cyclotron mass and frequency for graphene is introduced in Section 2.6. In Section 2.7 we explain several methods to produce graphene mono- and multilayers including the famous "scotch tape methode" and how to fabricate graphene nanostructures like field-effect transistors or suspended graphene. We end the chapter by describing one way how to change the charge carrier concentration with electric gating in Section 2.8.

2.1. Lattice structure of graphene

Three ($2s$, $2p_x$ and $2p_y$) of the four valence electrons of carbon are in the sp²-hybridized state and form three strong in-plane σ bonds. Their uniform distribution in the plane leads to binding angles of 120° and the characteristic honeycomb lattice as shown in Figure 2.1.
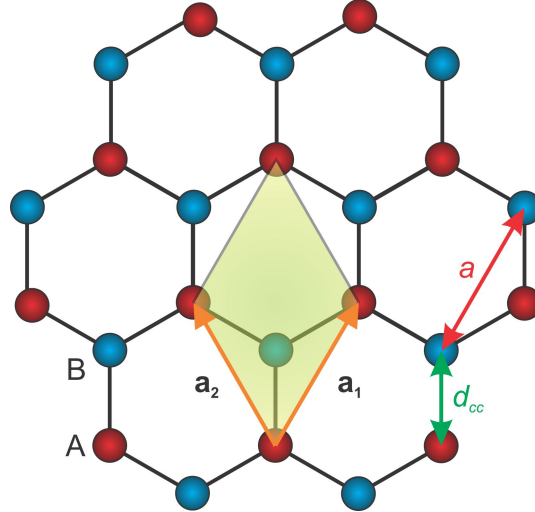
Figure 2.1.: *Lattice structure and unit cell of graphene. The unit vectors $\mathbf{a}_1$ and $\mathbf{a}_2$ are depicted as orange vectors and span the unit cell indicated by the green parallelogram. The distance between adjacent carbon atoms d_{cc} as well as the lattice constant a are shown by the respective arrows.*

The distance between adjacent carbon atoms is $d_{cc} = 1.42$ Å [13]. Although all atoms in graphene are in principal the same, there exist two inequivalent sublattices from a crystallographic point of view which are labeled as A and B (as shown in Figure 2.1). The carbon atoms related to each sublattice distinguish themselves by the orientation of their bonds and are translationally invariant. The honeycomb structure can be built by a triangular Bravais lattice with a basis of two atoms (A and B) per unit cell (indicated by the green parallelogram). The unit vectors $\mathbf{a}_1$ and $\mathbf{a}_2$ are included in Figure 2.1 as well and are given by

$$\mathbf{a}_1 = \frac{a}{2}\left(\sqrt{3}, 1\right)$$

$$\mathbf{a}_2 = \frac{a}{2}\left(\sqrt{3}, -1\right)$$

where $a = d_{cc} \cdot \sqrt{3} = 2.46$ Å is the lattice constant describing the distance between adjacent carbon atoms belonging to the same sublattice.

The basis vectors of the reciprocal lattice $\mathbf{b}_1$ and $\mathbf{b}_2$ are constructed using the relation $\mathbf{a}_i \cdot \mathbf{b}_j = 2\pi\delta_{ij}$ [14]. This yields

$$\mathbf{b}_1 = \frac{2\pi}{3a}\left(1, \sqrt{3}\right)$$

$$\mathbf{b}_2 = \frac{2\pi}{3a}\left(1, -\sqrt{3}\right)$$

which are shown by the orange arrows in Figure 2.2 (a). The reciprocal lattice is illustrated by the gray dots. The first Brillouin zone (BZ) can be constructed by drawing the
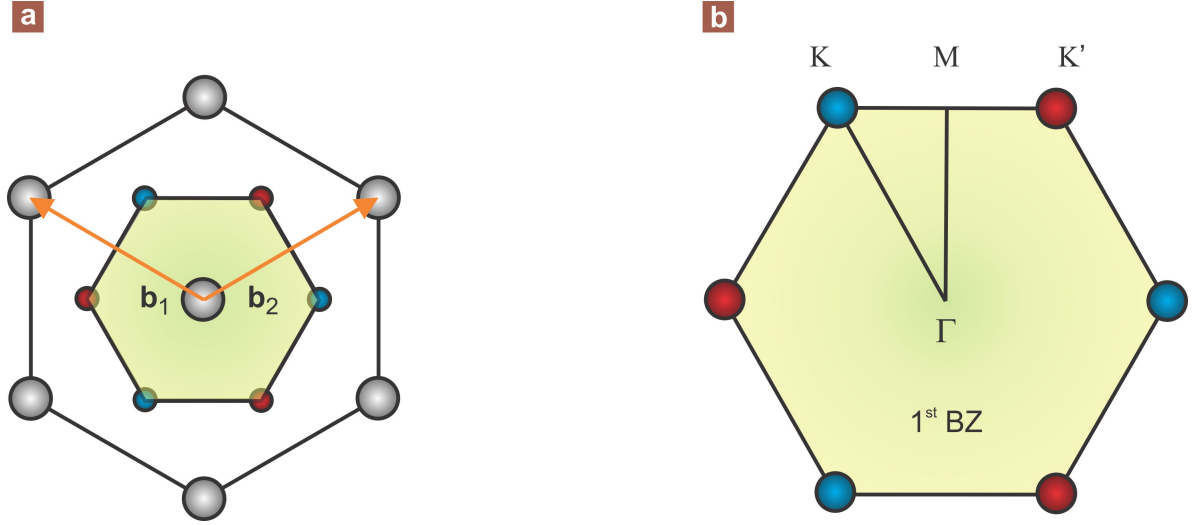
Figure 2.2.: ***Reciprocal lattice and first Brillouin zone of graphene.*** *(a) The gray dots illustrate the reciprocal lattice which is generated by the orange basis vectors* $\mathbf{b}_1$ *and* $\mathbf{b}_2$*. The first BZ is highlighted in green. (b) First BZ with the two inequivalent corners K and K' marked by the blue and red dots. Important crystallographic symmetry points are labeled.*

perpendicular bisector of the sides connecting adjacent reciprocal lattice points (Wigner-Seitz cell of the reciprocal lattice). The result is depicted in Figure 2.2 (a) by the green hexagon and as a zoom-in in Figure 2.2 (b). The symmetry of the real space lattice is mirrored in reciprocal space. The two inequivalent corners of the first BZ called K and K' are marked by the red and blue dots in Figure 2.2 (b). The center of the BZ is called Γ-point and is also included in this figure as well as the crystallographic point M in between K and K'.

Having established the fundamentals of the real and reciprocal lattice allows to derive the band structure of graphene in the next step.

2.2. Band structure of graphene

Whereas the three sp²-hybridized orbitals form the in-plane σ-band and are mainly responsible for the lattice symmetry, the remaining p_z-orbital is oriented in the out-of-plane z-direction. Each carbon atom has one of those p_z-bonds which hybridize together and form a bonding π- and anti-bonding $\pi*$-band. The electrons in these bands are delocalized which leads to a good in-plane electric and thermal conductivity. Since the bonding σ and anti-bonding $\sigma*$ bands are seperated by a large energy gap of approximately 12 eV [15], these bands are often neglected in the calculation of the band diagram and the peculiar electronic properties of graphene of interest here are mainly due to the π-bands.

The band structure of the π-bands in graphene can be calculated from a tight-binding approximation[1]. It results in an energy-momentum dispersion relation described by

$$E_{2d} = \pm\gamma_0 \left[1 + 4 \cdot \cos\left(\frac{\sqrt{3}\,k_x\,a}{2}\right) \cdot \cos\left(\frac{k_y\,a}{2}\right) + 4 \cdot \cos^2\left(\frac{k_y a}{2}\right) \right]^{1/2}, \qquad (2.1)$$

where $\gamma_0 \approx 3$ eV is the transfer integral corresponding to the nearest-neighbor hopping energy. The anti-bonding $\pi*$-band with $E > 0$ is described by the "+"-sign whereas the "-"-sign stands for the bonding $E < 0$ π-band. The band structure given by equation 2.1 is drawn in Figure 2.3.
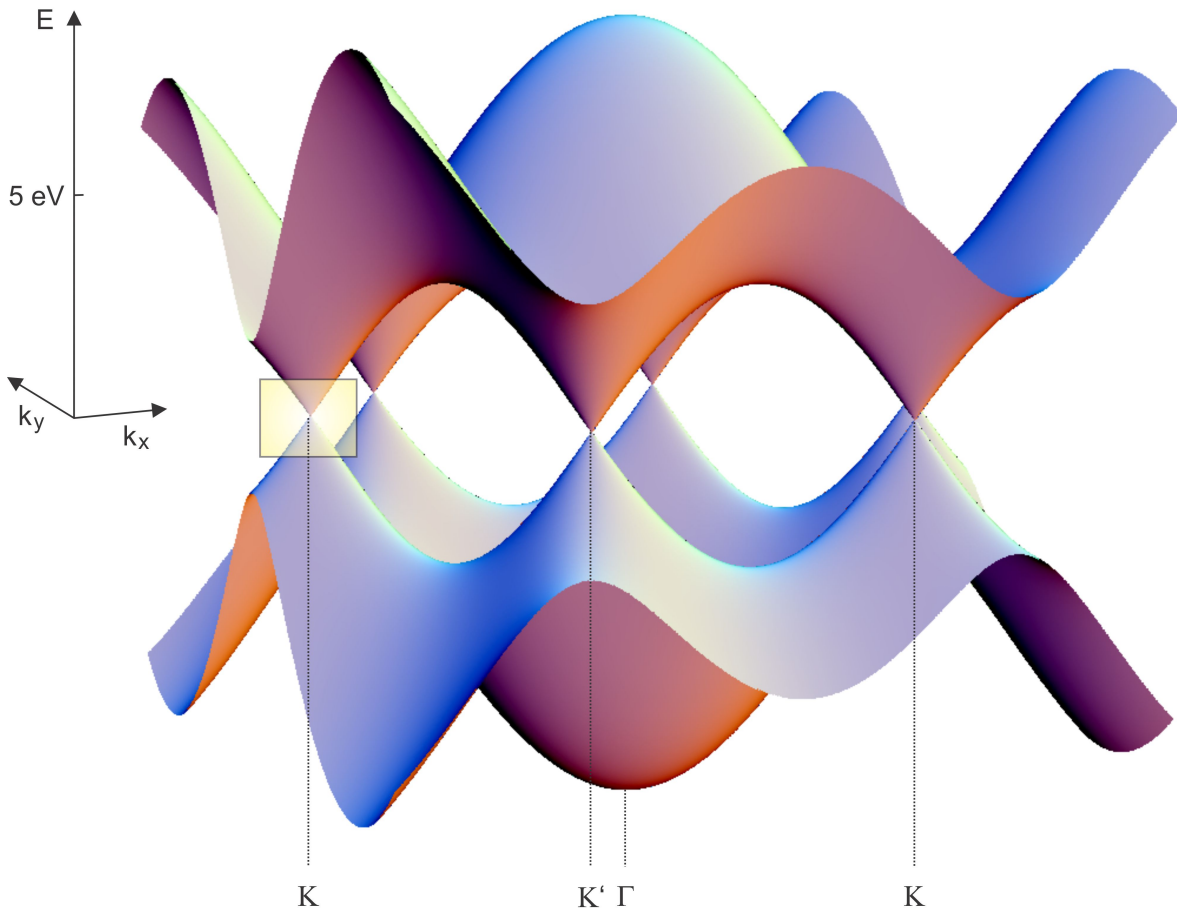
Figure 2.3.: ***Band structure of graphene.*** *This visualization is obtained by using equation 2.1. The upper band is the anti-bonding $\pi*$-band whereas the lower one is the bonding π-band. Both bands touch each other at the Fermi-energy at the K- and K′-points where the dispersion relation is linear (yellow box and Figure 2.4).*

---

[1] see Ref. [16] for a general description and Refs. [13, 17, 18] specifically for graphene.

Both bands touch at the K and K' points at the corners of the BZ. The two electrons from the unit cell completely occupy the π-band and as a consequence, the Fermi-energy is exactly where the two bands cross at K and K' (for charge neutral graphene). The density of states at the K and K' points is zero and graphene can be considered as a semi-conductor with zero energy gap.

The band structure is parabolic around the Γ-point. However, it is of special interest to note that for low energies ($E < 3$ eV) the electrons/holes at the Fermi energy E_F are located in the vicinity of the K/K'-points as indicated by the yellow box in Figure 2.3. Here, the dispersion relation is not parabolic but linear as depicted in Figure 2.4. It is described by

$$|E| = \hbar \, v_F \, |\delta\mathbf{k}| \qquad (2.2)$$

with $\delta\mathbf{k} = \mathbf{k} - \mathbf{K}$ denoting the distance between the electron wave-vector $\mathbf{k}$ and the K/K'-points. The constant v_F with units of velocity is given by

$$v_F \equiv \frac{\sqrt{3}\,\gamma_0\,a}{2\,\hbar} \approx 10^6 \, \frac{\text{m}}{\text{s}} \; . \qquad (2.3)$$
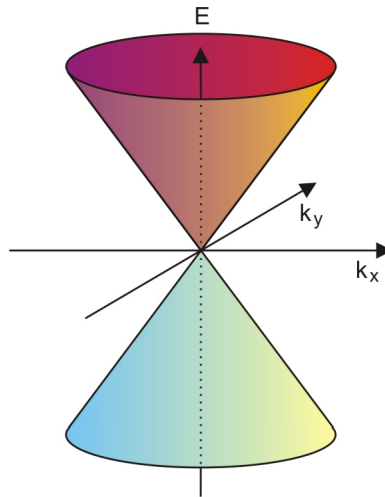
Figure 2.4.: *The band structure is linear for low energies.*

A calculation of the group velocity $v_G \equiv \left| \frac{\partial E}{\hbar \partial \mathbf{k}} \right| = v_F$ reveals that the constant v_F defined above in fact describes the group velocity. In solid state physics this velocity is often called Fermi velocity and, interestingly, in graphene it is independent of energy E and momentum.

The linear dispersion in graphene has remarkable effects on the motion of electrons. In general, the motion of electrons in a solid can be described by the Schrödinger equation with all atomic potentials included explicitly. If however, the atoms and consequently the potentials are arranged in a periodic pattern and the band structure is parabolic, the electrons can be treated as free electrons (no periodic potential from the atoms, only external forces) but with a changed mass. This so called effective mass is inversely propor-

tional to the second derivative of the energy with respect to the wave-vector. This allows a convenient description within the Schrödinger equation. Obviously, this procedure is not feasible in graphene as the effective mass would be infinite for low energies. The linear band structure in graphene is in several ways similar to that of massless relativistic particles with a constant group velocity (like photons), described by the Klein-Gordon equation for spin 1 particles. For electrons as spin 1/2 particles a modified Dirac equation [19] is used which indeed can be derived from graphenes' Schrödinger equation for small energies. The charge carriers near the six K and K' corners of the BZ mimic in this regard the behavior of massless relativistic particles, with the speed of light substituted by the Fermi velocity v_F [20]. Due to this formal analogy, the K and K' points are referred to as Dirac-points and the charge carriers as Dirac-fermions. It is also one of the reasons why graphene has received so much attention as it may be possible to investigate quantum electrodynamic effects like the Zitterbewegung [21] or Klein tunneling [22] in a solid state experiment.

Another remarkable property of charge carriers in graphene closely related to the relativistic quantum mechanical description is a quantity called pseudospin. This quantum number is analogous to but completely independent of "real" spin. In graphene, each sublattice (A and B) is responsible for one branch of the electronic dispersion (see Figure 2.5) and the pseudospin allows to differentiate between relative contributions from each sublattice. In other words, the pseudospin tells you at which sublattice the quasiparticle is located.
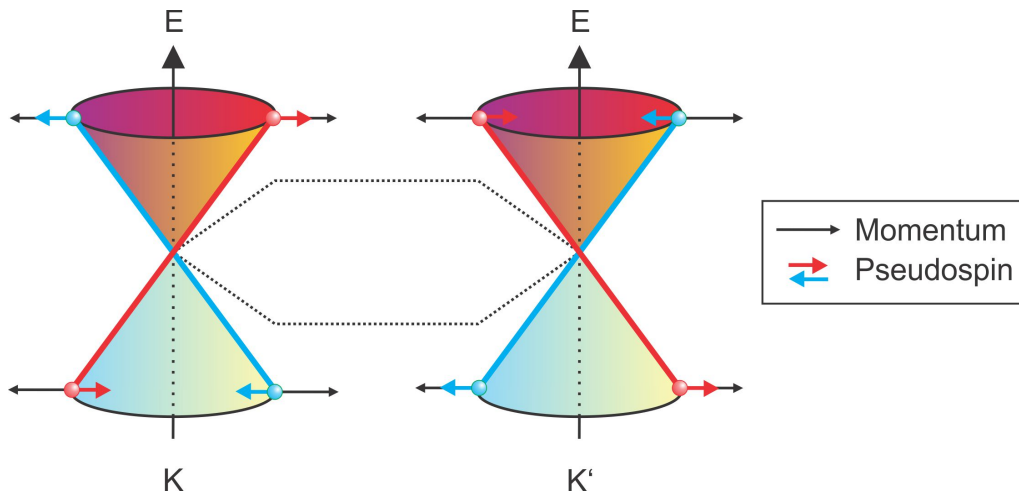
Figure 2.5.: **Pseudospin in graphene.** *The red and green line in the electronic dispersion relation indicate which of the two different sublattices is regarded to be responsible for each branch. For electrons around K momentum and pseudospin are parallel whereas for holes they are antiparallel. At K' it is the other way round.*

2.3. Band structure of multi-layer graphene

The analogy of the band structure of graphene monolayers as described in Section 2.2 with relativistic quantum mechanics is a playground for theorists as well as experimentalists. Strikingly, adding just a single second graphene monolayer on top of the first has a huge

impact on the band structure. This band structure also sensitively depends on the stacking order and relative orientation of the two layers. In the following two subsections we cover cases that are especially important: Bernal stacked bi- (and tri-)layers as well as twisted bilayers.

2.3.1. Bernal stacked bi- and tri-layer graphene

In a Bernal stacked bilayer as shown in Figure 2.6, the two single graphene layers are separated by a distance of approximately 3.35 Å [13] and stacked in such a way that a carbon atom from the upper layer either is on top of a carbon atom from the lower layer or above the center of the hexagon enclosed by the carbon atoms of the lower layer. The
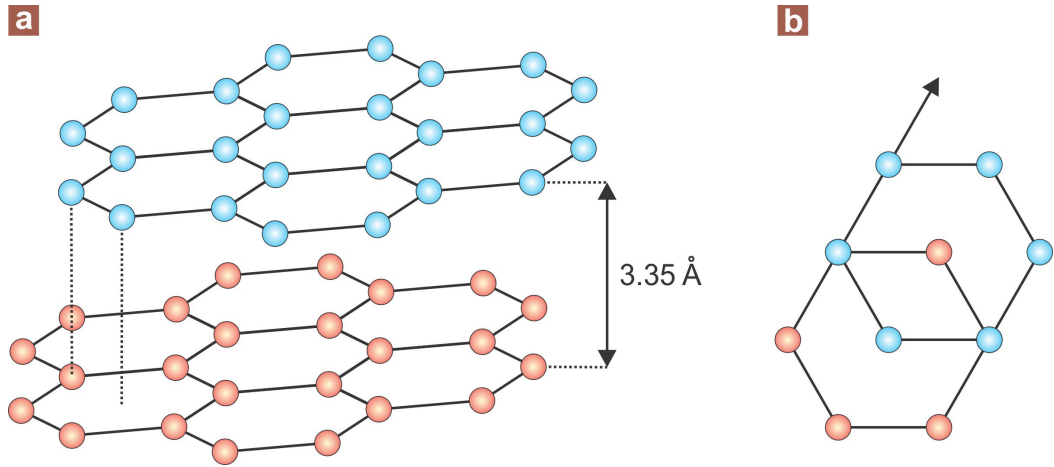
Figure 2.6.: **Bernal stacked graphene bilayer.** *(a) The seperation between two layers is 3.35 Å. (b) Top view. Shifting the upper blue layer with respect to the lower red layer by one bond length in the direction of this bond results in a Bernal stacked bilayer.*

top view in Figure 2.6 (b) illustrates that the upper layer is shifted with respect to the lower layer by a distance that equals one bond length in the direction of this bond. The band structure of this Bernal stacked (or AB stacked) bilayer can be derived using the tight-binding approximation [18]. The outcome of the calculation is depicted in Figure 2.7 (b). The second graphene layer splits the valence and conduction band in each case into two valence (shown in blue) and conduction bands (orange). The region around the K-point where the electrons reside for low energies is enlarged in the inset. The lower conduction band touches the upper valence band at the K-point. More precisely, theory predicts that there is even a small overlap of 1.6 meV. Different from the monolayer case, the bilayer has a parabolic dispersion relation like conventional semiconductors.

Figure 2.7 (c) shows the band structure of ABA stacked triple-layer graphene calculated with the tight-binding approximation. The additional, third graphene layer adds again an extra conduction and valence band. At low energies there is an overlap between the lowest conduction and highest valence band of 13.8 meV. It is interesting to note that one valence and one conduction band have a linear electronic dispersion relation, like
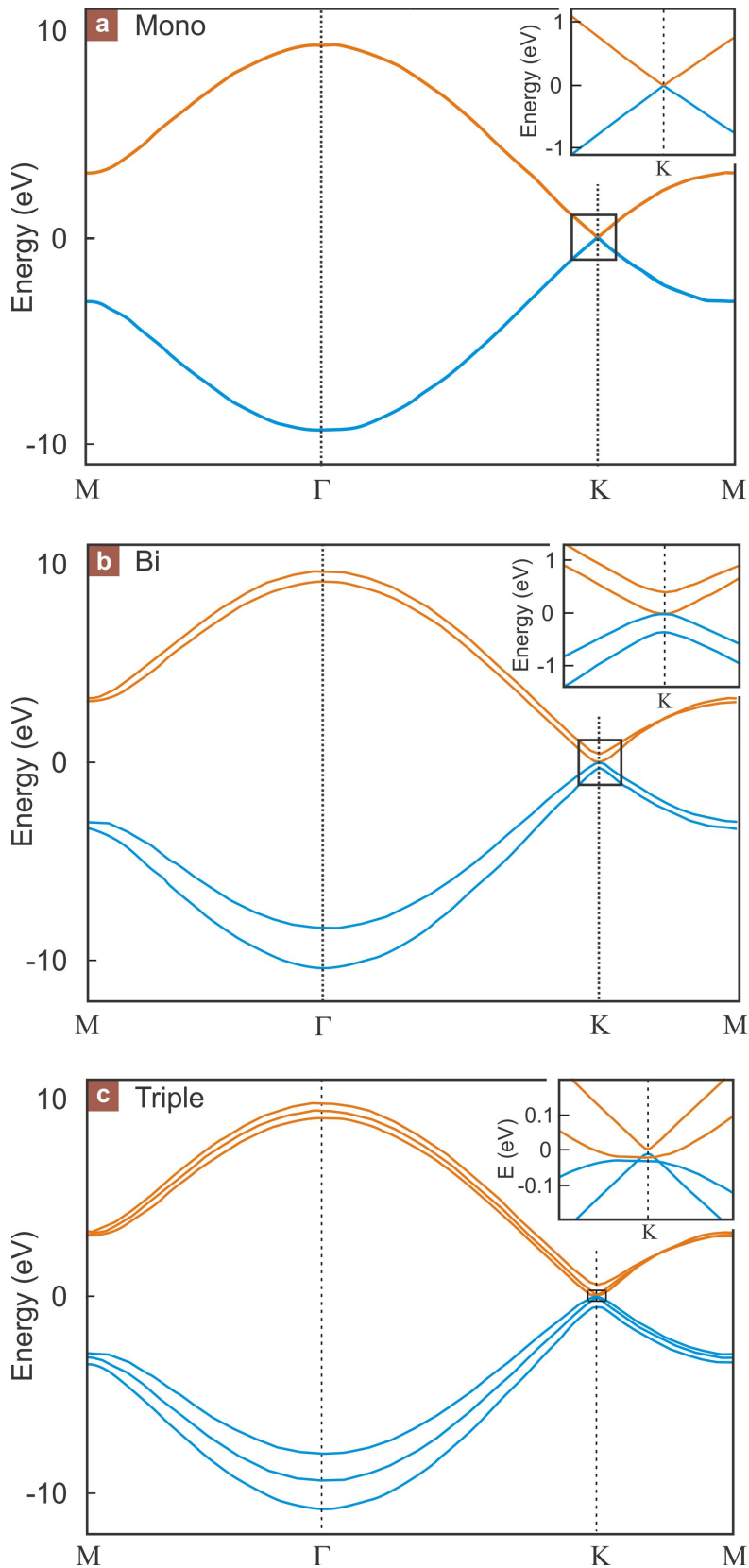
Figure 2.7.: ***Band structure of graphene (a) mono-, (b) bi- and (c) tri-layer.*** *Each extra graphene layer adds another valence and conduction band to the system. The conduction bands are shown in orange, the valence bands in blue. The insets depict an enlargement of the band structure for low energies in the vicinity of the K and K′-points. Modified from Ref [18].*

it is the case for a monolayer graphene. The other four bands follow a parabolic dispersion.

2.3.2. Twisted bilayer graphene

Bilayers that do not possess AB stacking but are rotated with respect to the Bernal configuration are referred to as twisted bilayers. Four examples are shown in Figure 2.8 with rotation angles θ between 5° and 22°.
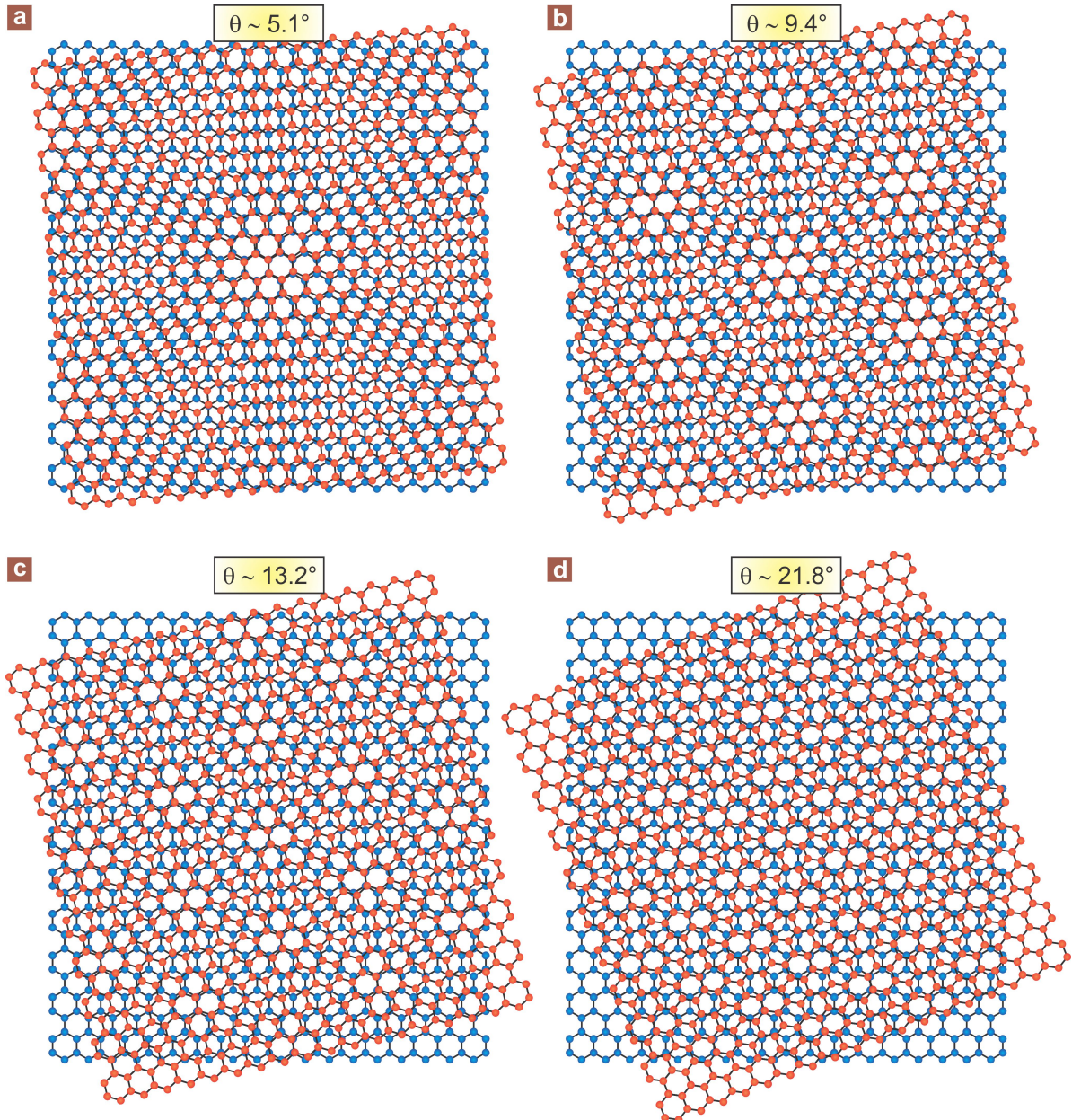
Figure 2.8.: *Moiré pattern in twisted bilayer graphene.* *The angle of rotation θ between the layer is indicated at the top of each picture. The periodicity of the resulting superlattice is largest for panel (a) and decreases as we go from (b) to (d).*

As a result of the twist a superstructure or Moiré pattern[2] appears. The lattice constant of the superlattice L_S is given by $L_S = \sqrt{3i^2 + 3i + 1}\,a$ with the graphene lattice constant $a \approx 0.246$ nm and $i = 0, 1, 2...$ being an integer. This integer i is related to the angle θ for a commensurate rotation by $\cos \theta_i = \frac{3i^2 + 3i + 1/2}{3i^2 + 3i + 1}$ [23]. Moiré patterns are observable for instance with STM [24–26] on graphite or in systems prepared by chemical-vapor-deposition (CVD) and epitaxial growth on a silicon carbide (SiC) substrate. Figure 2.9 shows a TEM image of a bilayer sample prepared by CVD growth on a copper substrate. The light blue region shows a monolayer part. The violet and dark blue colored regions show twisted bilayers with different rotation angles.

Figure 2.9.: **_TEM image of CVD grown graphene._** _A monolayer part of graphene is colored in light blue (top middle). Two twisted bilayer graphene areas with different twist angle are shown in violet and dark blue. Sample grown by Viera Skakalova. TEM image obtained by Simon Kurasch, University of Ulm. The scale bar is 1 nm._

The rotation of the two layers has a strong impact on the electronic structure. The two Dirac electron gases are coupled by the periodic interaction. Figure 2.10 (a) shows the BZ of the two twisted layers which are rotated by an angle θ. Modifications of the band structure occur mainly where the two Dirac cones of the single layers overlap each other. A simplified scheme of this is illustrated in Figure 2.10 (b). The DOS of twisted bilayer (red) is modified from the single layer graphene DOS (blue) as shown in Figure 2.10 (c).

---

[2]Another way to obtain a Moiré pattern is to superimpose two lattices with slightly different lattice constants.
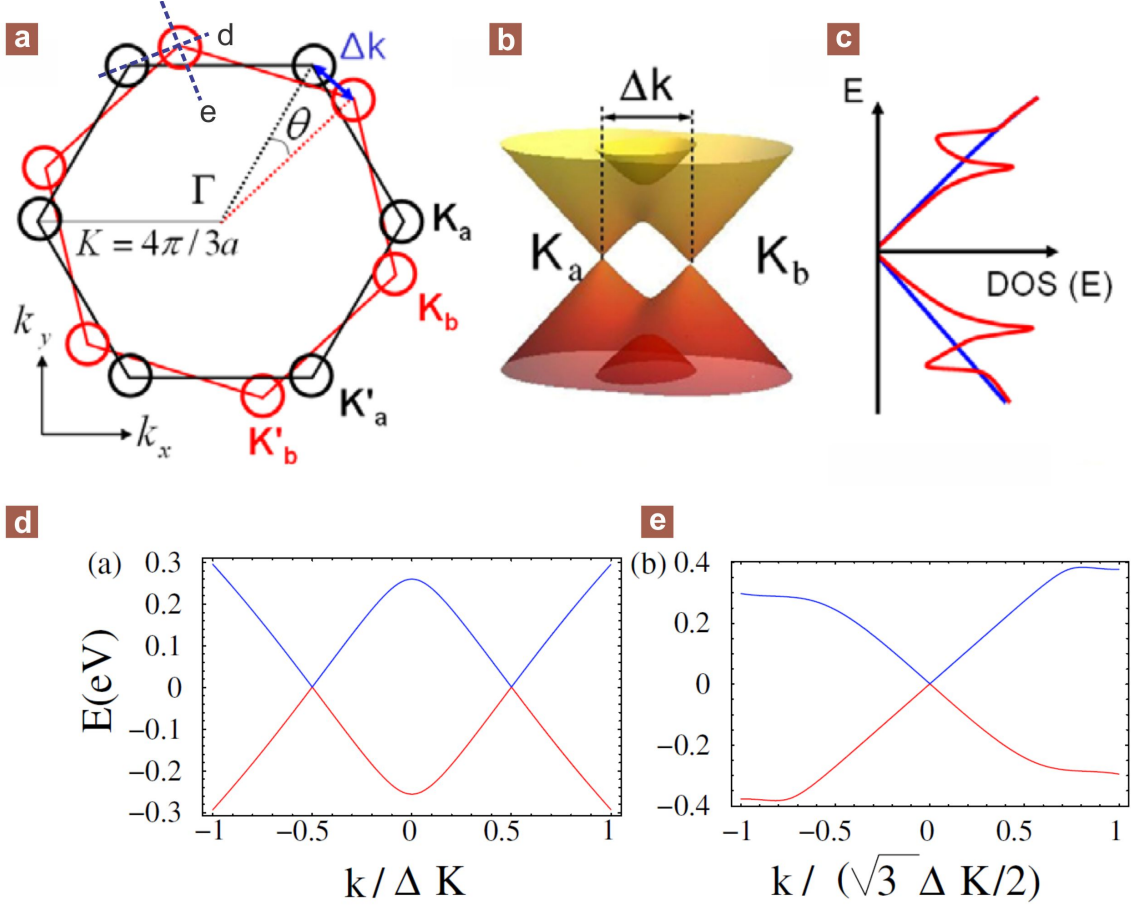
Figure 2.10.: *Electronic band structure in a rotated graphene bilayer.* (a) *BZ of the twisted bilayer graphene. The red and black circles are the Dirac cones of the two single layers. (b) Simplified energy diagram at the position where the two Dirac cones overlap and interactions occur. (c) DOS of the twisted bilayer (red) compared to single layer graphene (blue). The interaction of the two Dirac cones causes a Van Hove singularity. (d) and (e) Line cut along two specific directions as indicated in (a) for a twist angle of $\theta = 3.9°$. (d) Along the direction cutting both Dirac points of the single layers, a Van Hove singularity occurs. (e) In a direction nearly perpendicular to (d) the band structure is linear and resembles the case of a monolayer graphene. (a)-(c) modified from [27], (d)-(e) modified from [23]*

Van Hove singularities occur at energies depending on the twist angle, the smaller this twist angle the smaller the energy difference. Line cuts along two specific directions as marked in Figure 2.10 (a) by blue dashed lines are given in Figure 2.10 (d) and (e). The Van Hove singularity is visible in (d), whereas in (e) theoretical calculations [23] predict a linear energy dispersion for low energies for the combined system, similar to the case of monolayer graphene. This was confirmed by angle-resolved photoemission spectroscopy (ARPES) experiments [28]. Depending on the rotation angle, the Fermi velocity v_{bi}, given by the slope of the Dirac cones, is renormalized and can be significantly smaller than the single layer value v_{mono}. A combination of ab initio and tight-binding methods allows to calculate the band structure and Fermi velocity as a function of twist angle θ [29]. The latter is illustrated in Figure 2.11 with v_{bi} normalized to the monolayer value v_{mono}. The
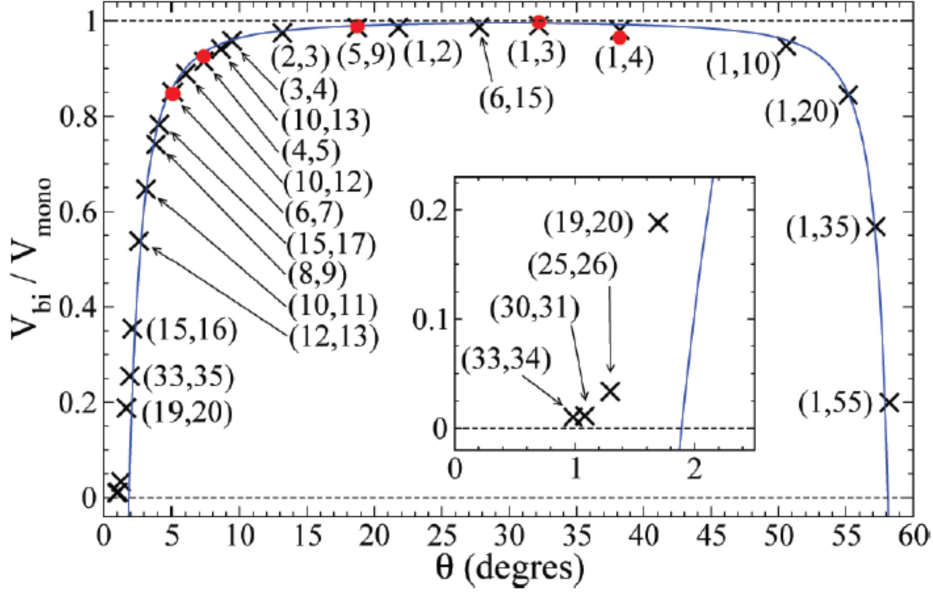
Figure 2.11.: *Fermi velocity of twisted bilayer as a function of twist angle.* *The bilayer Fermi velocity is normalized with respect to the single layer value. Adapted from Ref. [29]. The solid line is from the theory given in Ref. [23].*

renormalization of the Fermi velocity is symmetric around $\theta = 30°$. For small angles ($\theta < 15°$) the reduction of the Fermi velocity is obvious. However, we point out that for angles smaller than 3° the velocity tends to zero and localization may occur [29].

The result of the last three subsections is summarized in Figure 2.12 where we depict the lattice and band structure of monolayer graphene, Bernal stacked bilayer and twisted bilayer graphene.
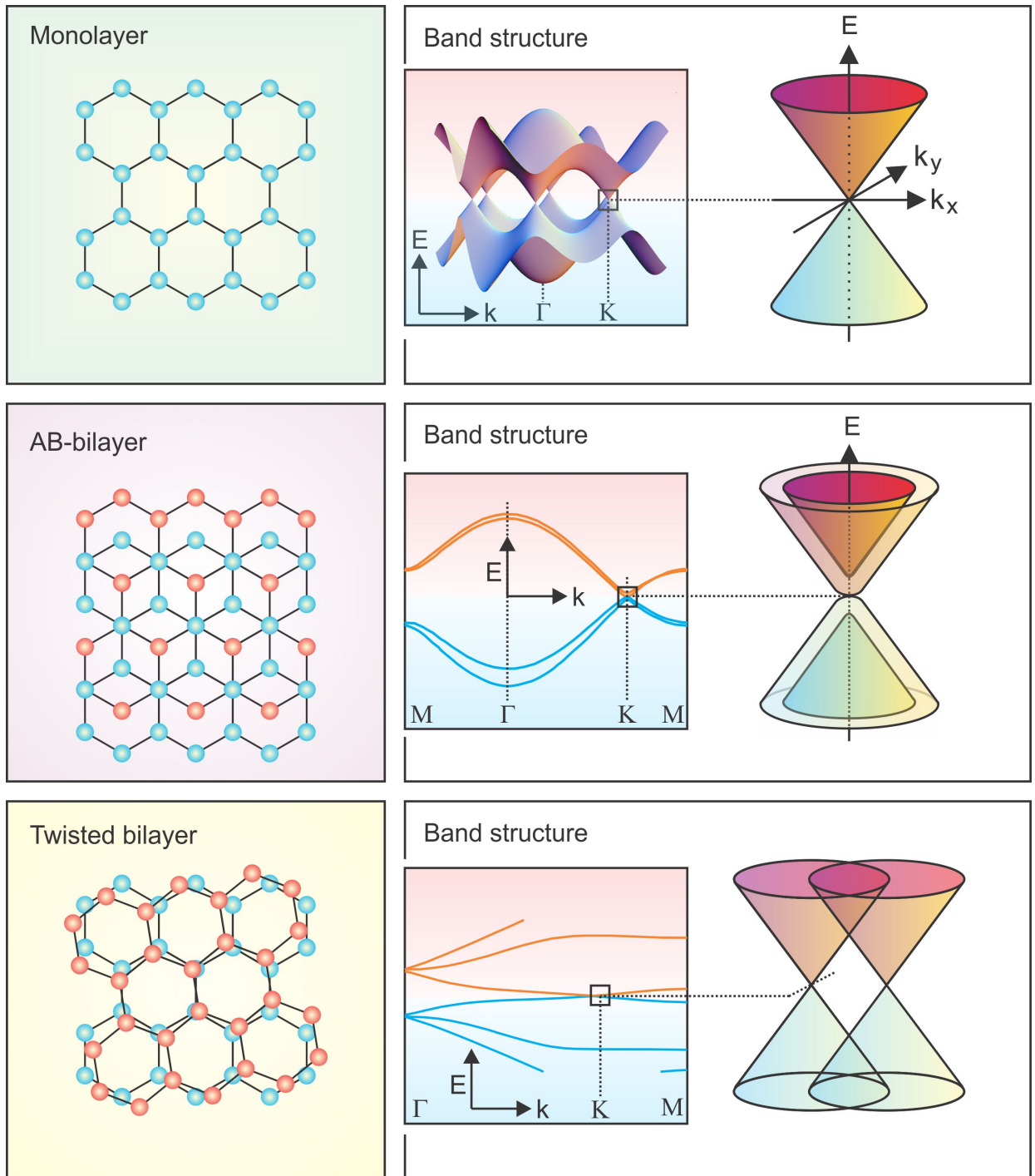
Figure 2.12.: *Overview of lattice and band structure for monolayer graphene, Bernal stacked bilayer and twisted bilayer graphene.*

2.4. Density of states

As a consequence of the linear band structure of graphene as introduced in Section 2.2, the density of states (DOS, $D(E)$) depends linearly on the energy E and is zero at the Dirac point. Including the four fold degeneracy resulting from spin and valley degrees of freedom gives

$$D_{graphene}(E) = \frac{|E|}{\pi \hbar v_F^2}$$

This behavior is different from a conventional 2DES where the DOS is independent of energy E. Here, for the spin degenerate case, the DOS is given by

$$D_{conv.}(E) = \frac{m_{eff}}{\pi \hbar^2}$$

with the effective mass m_{eff}. The DOS as a function of energy for graphene is depicted in Figure 2.13 (a) as well as for a conventional 2DES in Figure 2.13 (b). For the conventional 2DES we show the common case where the effective mass is higher for holes than for electrons.
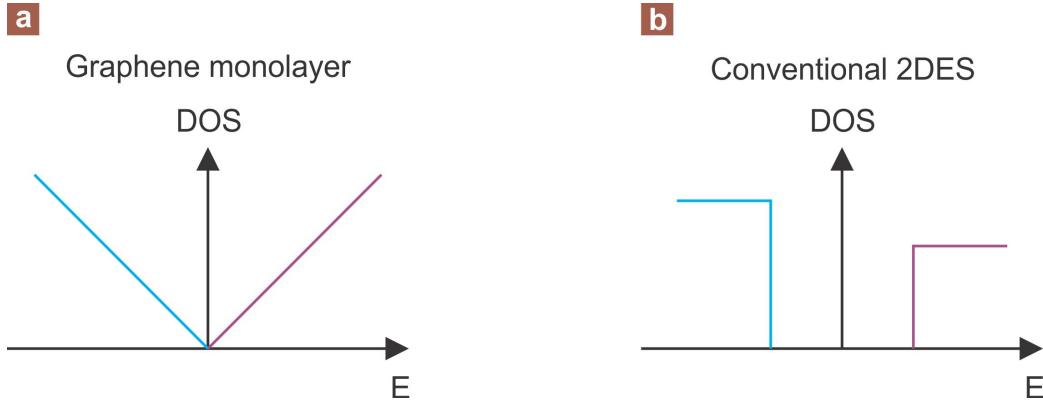
Figure 2.13.: **The Density of states** $D(E)$ **is (a) linear for graphene and (b) constant for a conventional 2DES.** *The blue branch represents holes, the purple electrons.*

2.5. Landau level spectrum

The application of a magnetic field B perpendicular to a 2DES effectively reduces the kinetic degrees of freedom from two to zero and the states of the 2DES condense into a discrete set of landau levels (LL). Each LL contains a total of $g \cdot$ (number of flux quanta threading the sample) $= geB/h$ states, with e being the electron charge, g the system degeneracy and h Planck's constant.

For a conventional 2DES with a parabolic electronic dispersion relation the LL are separated by the energy $\hbar\omega_c$, where ω_c is the cyclotron frequency (see next section). The energy E_N of the N's LL for electrons is given by [30]

$$E_N = \hbar\omega_c(N + 1/2)$$

The lowest LL $N = 0$ lies at $1/2\hbar\omega_c$ as shown in Figure 2.14 (c). Note that we define the energy relative to the conduction band edge. The energy E_N of the N's LL for holes then reads as

$$E_N = -\hbar\omega_c(N + 1/2) - E_G$$

where the spacing between LLs is smaller than for electrons due to the higher effective mass for holes (see Figure 2.14 (c)).
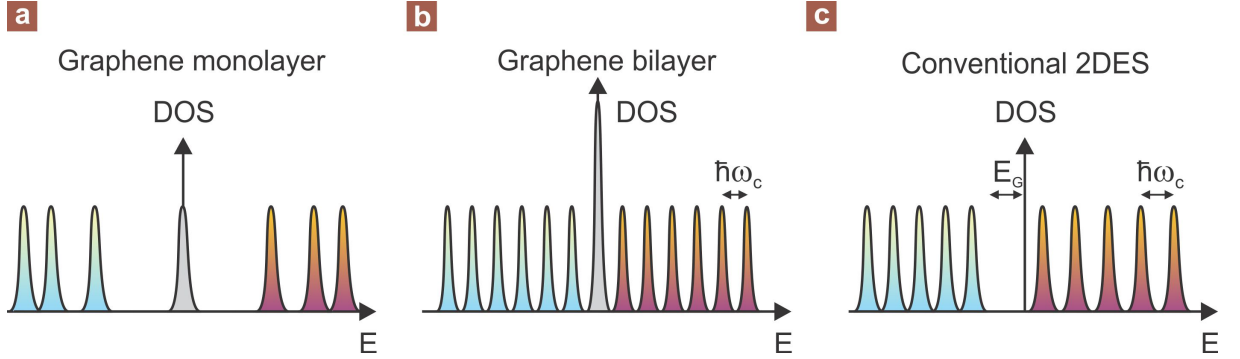
Figure 2.14.: ***The DOS exhibits discrete LLs if a perpendicular magnetic field is applied to the 2DES.*** *(a) Monolayer graphene possesses a LL at zero energy and the spacing between adjacent LLs follows a square root dependence. (b) Bilayer graphene also features a LL at zero energy. (c) Conventional 2DESs show an equidistant spacing between LLs and the lowest LL is offset by half a spacing. Electron and hole LLs are separated by the bandgap E_G.*

In a graphene monolayer with its linear relation between DOS and energy the LLs are not equidistant but rather obey a square root dependence

$$E_{N_1} = sgn(N_1)v_F\sqrt{2e\hbar|N_1|B}$$

where N_1 is the LL index for monolayer graphene. The lowest LL ($N_1 = 0$) is at zero energy $E = 0$ and contains two hole-like states and two electron-like states. A consequence of this LL spectrum is an unconventional sequence of integer Quantum Hall states [6,7,31]. Figure 2.14 (a) illustrates the discussed properties of the graphene monolayer LL spectrum. The LL energy of bilayer graphene on the other hand follows the relation

$$E_{N_2} = sgn(N_2)\hbar\omega_c\sqrt{N_2(N_2 - 1)}$$

with $\omega_c = eB/m_{eff}$ and N_2 the LL index for bilayer graphene. Like it is the case for graphene monolayer, bilayer graphene also possesses a LL at zero energy (see Figure 2.14 (b)). However, the DOS is twice as high for the zero energy LL due to an orbital degeneracy ($N_2 = 0$, 1). Typically, the energy gap between adjacent LL in monolayer graphene is many times larger than that of a bilayer graphene.

2.6. Cyclotron mass and frequency

Whereas for a conventional 2DES the cyclotron frequency ω_c is given by

$$\omega_c = \frac{eB}{m_{eff}}$$

this relation does not hold for graphene monolayer as the linear energy spectrum of fermions in graphene implies that their is no effective mass m_{eff}. However, their exists a cyclotron mass that is not zero but rather described by

$$E = m_c c^{*2} .$$

Here, c^* equals the Fermi velocity v_F. Keeping in mind the relation between energy E and carrier density n, $E = \hbar v_F k = \hbar v_F \sqrt{\pi |n|}$ leads to a characteristic square root dependence of the cyclotron mass m_c on the carrier density n:

$$m_c = \frac{\hbar \sqrt{\pi}}{|v_F|} \sqrt{n}$$

This relation was observed experimentally by measuring the inverse compressibility of graphene [32] and also from the temperature dependence of the Shubnikov-de Haas-oscillations [6]. Finally, the cyclotron frequency of graphene can be written as

$$\omega_c = \frac{eB v_F}{\hbar k}$$

The cyclotron frequency is much higher for graphene than for conventional 2DES and consequently the spacing between adjacent LL is high. One of the conditions for the QHE to occur is that the separation between LL is higher than the thermal smearing: $\hbar \omega_c >> k_B T$, where k_B is the Boltzmann constant and T the temperature. This was shown to be realizable for graphene at room temperature (300 K) with a magnetic field of 29 T [9].

2.7. Fabrication procedure

In this section we give a brief overview about the fabrication process of graphene devices and nanostructures. We start with the graphene synthesis and discuss the three most established procedures to obtain single and multilayer graphene: micro-mechanical exfoliation, thermal decomposition of silicon carbide and chemical vapor deposition on a metallic catalyst. We end the section by explaining the process of structuring and contacting graphene using electron beam lithography and introduce a way how to continuously tune the charge carrier concentration in graphene.

2.7.1. Micro-mechanical exfoliation

The micro-mechanical exfoliation technique was first demonstrated to produce single layer graphene by A. Geim et al. in Manchester. It relies on the asymmetric bond strength in graphite. On the one hand there are strong covalent in-plane bonds (in graphite this binding energy is 524 kJ/mol [33]) causing a high in-plane stability of single graphene layers. On the other hand the bond between two adjacent graphene layers is determined by weak van der Waals interactions (in graphite: 7 kJ/mol [33]). Consequently, the graphene planes can easily be moved with respect to each other and separated without destroying the single layers themselves. The micro-mechanical exfoliation process is outlined in Figure 2.15.
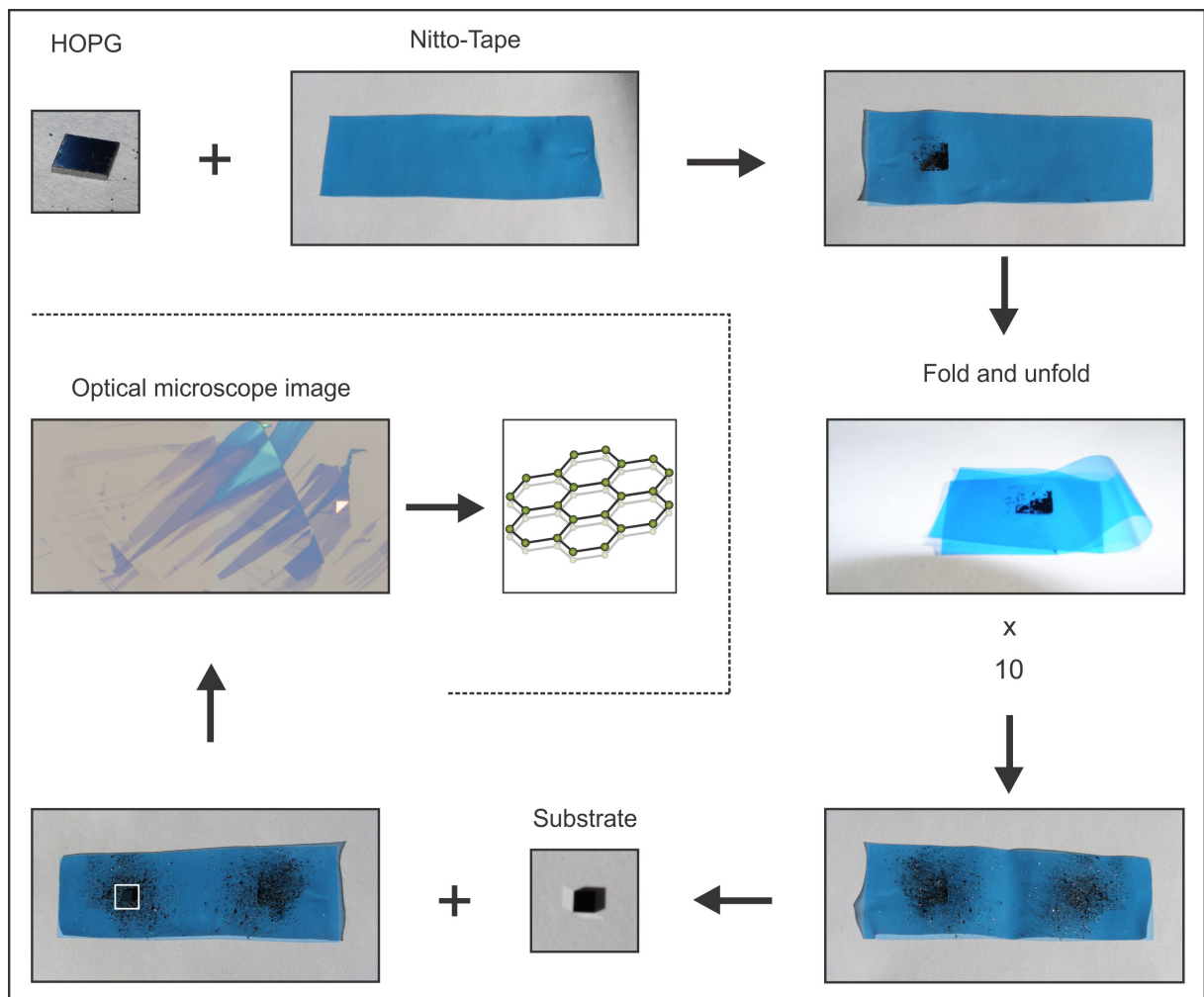
Figure 2.15.: ***Micro-mechanical exfoliation technique.*** *Starting with HOPG, several graphene layers are transferred to an adhesive tape and thinned by multiple fold and unfold sequences. Finally, few graphene layers are transferred to a substrate. Single layer are among those by chance.*

The starting material is either a piece of highly oriented pyrolitic graphite (HOPG) or natural graphite from which the top few layers are transferred to adhesive tape. The tape

is subsequently folded and unfolded several times until the initial thick graphite layer is cleaved into many thinner parts. The tape with thin graphite flakes is gently pressed onto a pre-heated highly n-doped conductive silicon substrate capped with 300 nm thermally grown silicon oxide. This transfers graphite layers from the tape to the substrate. In the next step, the tape is peeled off and the substrate is cleaned in acetone, water and isopropyl alcohol in order to remove residues from the transfer process. Finally, the substrate is dried in a soft nitrogen jet. Suitable graphene flakes on the substrate are searched for and identified with a combination of optical microscopy (see Chapter 8), Raman spectroscopy (see Section 3.2) and atomic force microscopy.

It turns out that graphene monolayers prepared by the micro-mechanical exfoliation technique have a high quality. The carrier mobilities are high and the defect densities are low. In this respect they are the material of choice for basic research and proof-of-concept devices. However, the flake size is typically limited to a few tens of micrometers in length and width only. This procedure is up to now restricted to small scale production and it is time consuming. For applications like flexible transparent transistors made out of graphene, a different approach is of great interest. The next two subsections introduce two methods that allow to produce graphene on a larger scale. However, other issues such as quality and costs become important.

2.7.2. Thermal decomposition of silicon carbide

One promising approach for graphene production on a large scale on an insulating substrate is provided by the epitaxial growth of monolayer graphene during high temperature annealing of silicon carbide (SiC) wafers in ultra-high vacuum (UHV). The crystal structure for two SiC polytypes commonly used for graphene fabrication is displayed in Figure 2.16.
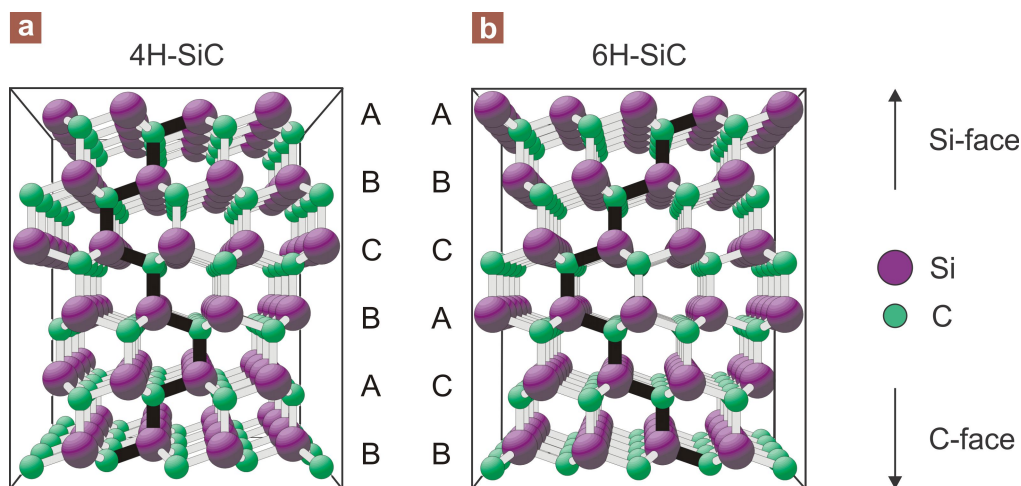
Figure 2.16.: *Crystal structure of two different SiC polytypes. Both are commonly used to produce mono- and multilayer graphene. (a) Hexagonal 4H-SiC. (b) Hexagonal 6H-SiC. The enhanced black line indicates the stacking sequence. The silicon- and the carbon-face are labeled. Modified from [34].*

The higher vapor pressure of silicon causes the silicon to evaporate at a lower temperature compared to carbon. The carbon atoms left behind form graphene layers on SiC. Typically, the quality of the surface is improved in a first step by hydrogen etching followed by heating the sample at around 1000°C (e.g. with electron bombardment) in order to remove the oxide layer. Then, the sample is heated up to around 1300°C. Depending on the temperature one to three layers of graphene form on the Si-face [35].

Heating the SiC substrate in an Argon atmosphere at 900 mbar instead of UHV conditions increases the area of continuous graphene layers drastically and reduces the surface roughness [36]. This leads to a higher mobility of the charge carriers.

Figure 2.17 illustrates the growth process in more detail. First, a so called buffer layer emerges after the top layer of Si has evaporated. STM studies proved the existence of this $(6\sqrt{3} \times 6\sqrt{3})$R30° reconstructed interface layer. It is closely linked to the underlying layer via dangling bonds. This precursor stage of graphitization is depicted in Figure 2.17 (a). Further heating of the sample results in the situation shown in Figure 2.17 (b) where the previous buffer layer transforms into the monolayer and the next layer becomes the new buffer layer. Alternatively, the buffer layer can be separated from the substrate, for instance by hydrogen-intercalation as illustrated in Figure 2.17. The buffer layer then turns into a quasi-free monolayer of graphene [37]. Note that the schematics in Figure 2.17 are oversimplified, as the process is not self-terminating and the result is only a monolayer "on average".
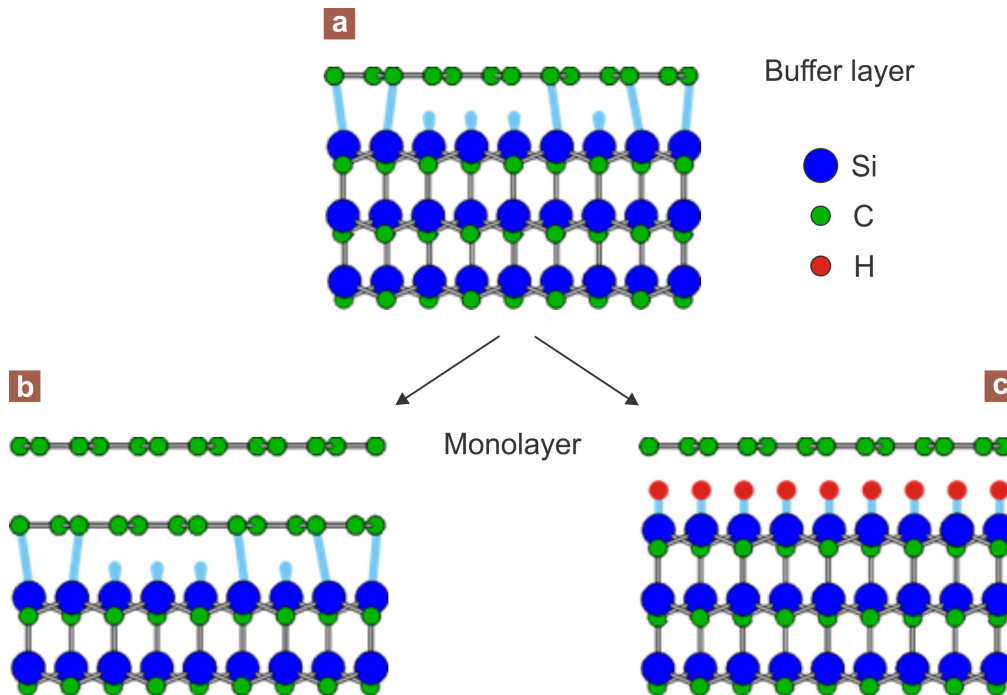
Figure 2.17.: *Side view for different stages of the graphene growth on SiC. (a) Buffer layer or "zero layer" epitaxial graphene. (b) Monolayer epitaxial graphene. (c) Quasi-free monolayer graphene after decoupling of the buffer layer by hydrogen intercalation. The dangling bonds are represented by blue clouds. Modified from [38].*

The number of graphene layers grown on SiC can be conveniently identified by the Raman 2D peak line width [39]. However, epitaxial graphene on SiC suffers from strong

intrinsic n-type doping. This excess negative charge can be compensated for by depositing for instance F4-TCNQ (tetrafluorotetracyanoquinodimethane) [40] onto graphene. A detailed study about the process of thermal decomposition of SiC as well as its characterization and manipulation is covered in Ref. [38].

2.7.3. Chemical vapor deposition

An alternative method to grow graphene on a larger scale is epitaxial growth on various metallic substrates using chemical vapor deposition (CVD) of hydrocarbons. In some cases, the growth is self-limiting so that only one monolayer of graphene will grow. In contrast with thermal decomposition of SiC, the carbon atoms are not present in the substrate yet. Therefore, carbon is supplied in gas or liquid [41] form and the metal surfaces serve as substrate and catalyst at once. Examples for metals suitable for graphene growth include

- copper Cu [42],
- nickel Ni(111) [43–45],
- platinum Pt(111) [46],
- iridium Ir(111) [47, 48],
- rhodium Rh(111) [49],
- ruthenium Ru(0001) [50] and
- cobalt Co(0001) [51].

A disadvantage of using a conducting substrate during the fabrication of graphene, is that it is necessary to transfer the graphene onto an insulating substrate [52]. A roll-to-roll process to produce graphene layers on copper with a diagonal of up to 30 inches and the subsequent transfer to a transparent and flexible substrate was successfully demonstrated [10].

2.7.4. Other methods

There exist many additional ways to produce graphene for instance by molecular beam epitaxy (MBE) [53, 54] by unzipping carbon nanotubes [55], by reduction of graphene oxide [56], by electron-beam irradiation of PMMA nanofibers [57] or by arc discharge of graphite [58]. However, the quality and mobility is by far the best in micro-mechanically cleaved graphene. The experiments described in this thesis are all conducted on graphene prepared by the micro-mechanical cleavage method.

2.7.5. Fabrication of graphene devices and nanostructures

In order to optically and electrically study the properties of graphene, it often has to be integrated in an electrically contactable device like a field-effect transistor (FET). In this subsection we describe how to manufacture suspended and electrically contacted graphene devices.

Graphene flakes obtained by the micro-mechanical cleavage method often have a random shape which is unsuited for transport experiments since the geometry factor is difficult to determine. A hall-bar geometry is more desirable for extracting the mobility from the field-effect behavior and quantum Hall effect. Figure 2.18 (a)-(e) illustrates the processing steps to produce a well defined hall-bar (the same steps are suited to obtain any other shape like a corbino structure etc.). The initially randomly shaped graphene flake (a) is covered by a thick resist (PMMA: polymethylmetacrylate) layer (b) in which the desired shape is transferred by electron-beam lithography (EBL) and development (c). The unwanted and unprotected graphene parts are subsequently removed with a reactive ion etching (RIE) step as depicted in (d). The graphene hall-bar itself is protected by the PMMA-layer and not affected by the RIE. The final step is to remove the now superfluous PMMA-layer in NEP (N-Ethylpyrrolidon) and acetone which leaves behind a well defined graphene hall-bar as shown in Figure 2.18 (e). Alternatively, the etch mask can be fabricated out of evaporated aluminum which is removed in potassium hydroxide (KOH) subsequent to the etching step. The etching of graphene can also be done in an oxygen or argon plasma.

In order to drive a current through the fabricated hall-bar and measure voltage drops at different positions, we need to electrically contact the graphene flake. The process steps used in this thesis are outlined in Figure 2.18 (f)-(j). In a first step an approximately 140 nm thick layer of 200 K 3.5 % PMMA is spin-coated (5 seconds at 3000 rpm followed by 30 seconds at 8000 rpm) and subsequently a second 60 nm thick 950 K 1.5% PMMA layer (see Figure 2.18 (g)). After each step the substrate is baked for 3 minutes on a 180℃ hotplate. The lower PMMA layer is more sensitive to electron beam irradiation which results in an undercut after EBL and development as shown in Figure 2.18 (h). For development, we immerse the sample for 120 seconds in MIBK/IPA (Methyl isobutyl ketone/Isopropyl alcohol) and 60 seconds in IPA to stop the development. After evaporation of typically 3 nm chromium (Cr) and 30 nm gold (Au) (Figure 2.18 (i)) in a vacuum chamber with a pressure below $p < 10^{-6}$ the undercut ensures an efficient lift-off in 55℃ NEP. The sample is further cleaned in acetone and IPA and dried in a nitrogen jet. The fully contacted sample in Figure 2.18 (j) is glued in a chip carrier and wedge bonded.

Etching away parts of the supporting silicon oxide underneath the graphene flake can drastically improve the quality of the device (for reasons discussed in Chapter 8 and 9). The experiments described in Chapter 10 were conducted on such a suspended graphene device fabricated as illustrated in Figure 2.18 (k)-(o). Again, a layer PMMA is spin-coated and baked (Figure 2.18 (l)). At the desired region where the substrate should be etched away a window is opened by EBL and development as shown in Figure 2.18 (m). In the next step, the substrate is etched in a buffered hydrofluoric acid (HF) solution (Figure 2.18 (n)) for 120 seconds. With an SiO_2 etch rate of 80 nm/s this corresponds to etching away 160 nm SiO_2. After cleaning the sample in de-ionized water or IPA it is transferred to either acetone or IPA and dried in a critical point dryer (CPD) (Figure 2.18 (o)). The CPD is used to circumvent possible damage resulting from surface tension during the
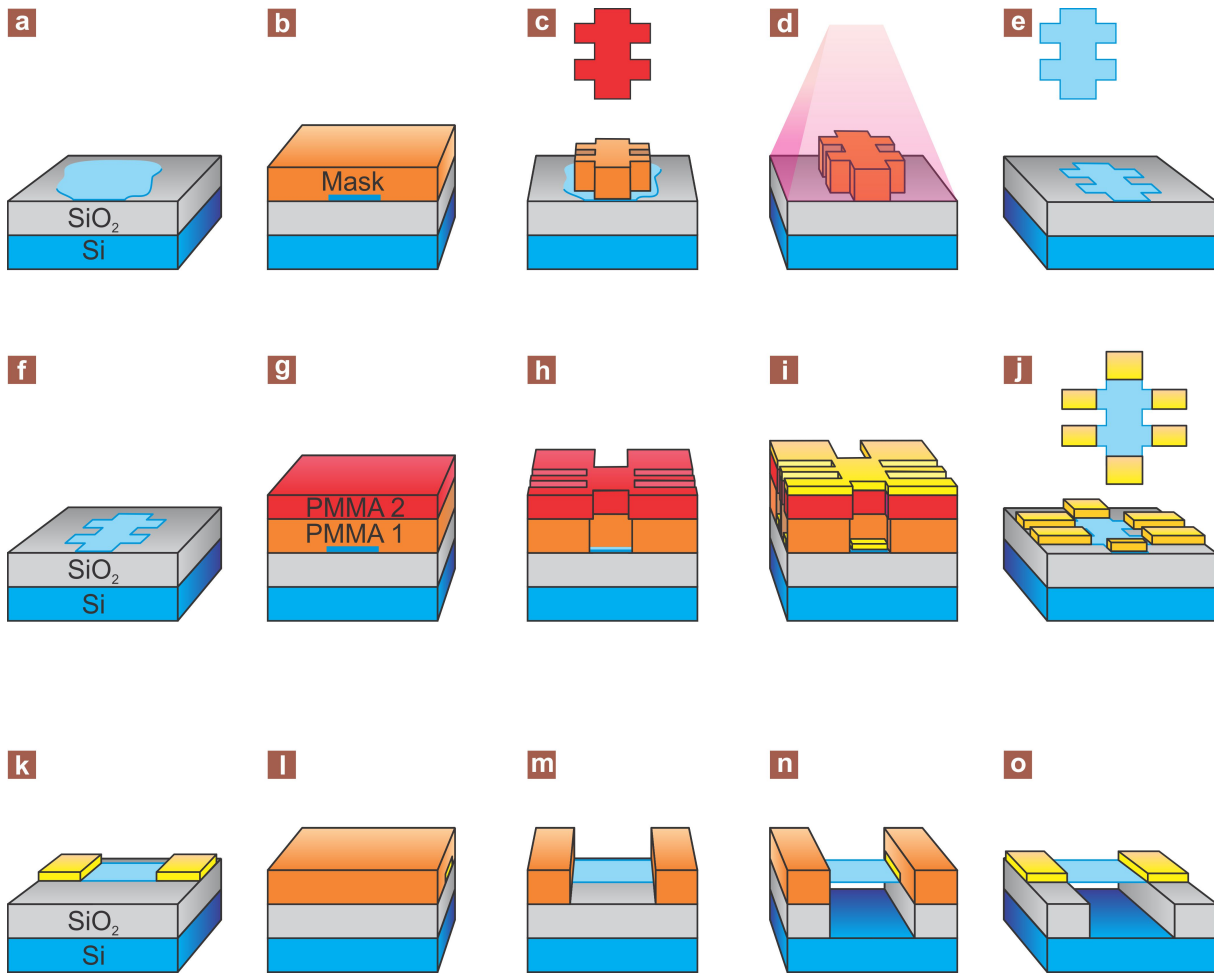
Figure 2.18.: ***Schematic fabrication steps for electrically contacted suspended graphene flakes with a well defined geometry.*** *(a)-(e) Reactive ion etching in order to obtain any desired shape. (f)-(j) Fabrication of electrical contacts to the graphene flake. (k)-(o) Producing suspended graphene flakes by hydrofluoric acid etching.*

drying process by avoiding a phase transition (liquid to gaseous). Alternatively, instead of using a PMMA mask to define an area which will be etched by HF, the contacts itself prevent that the SiO_2 is etched away underneath the contacts. Consequently, the whole substrate can be put in HF in order to obtain a suspended graphene flake.

2.8. Electric gating of graphene

Important parameters to tune in solid state experiments are for instance the temperature, an externally applied magnetic field and the number of charge carriers in the sample. One way to continuously vary the charge carrier density in graphene is the use of the field effect. In this thesis we typically use a highly n-doped silicon substrate as a backgate and 300 nm thermally grown silicon oxide as an insulator in between graphene and the silicon substrate (see Subsection 2.7.1). Figure 2.19 illustrates a generalized system with two

different insulating materials (SiO$_2$ and material x (e.g. air, boron-nitride)) separating graphene from the backgate. The thickness of material x and SiO$_2$ is d_x and d_{SiO_2}, respectively.
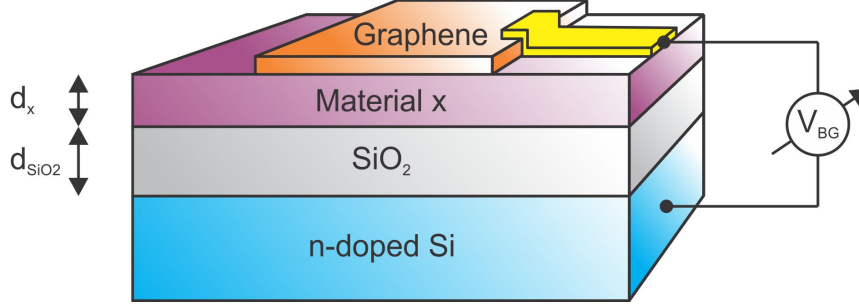
Figure 2.19.: ***Generalized schematic of backgated graphene.*** *The graphene sample is separated by two insulating materials from the conductive n-doped silicon backgate. Applying a bias between graphene and the backgate allows to tune the charge carrier concentration in graphene. It can be calculated by using a parallel capacitor model.*

The carrier concentration can either be measured (e.g. by the Hall effect) or calculated with a parallel plate capacitor model. For a parallel plate capacitor, the capacitance C is given by

$$C = \epsilon_0 \epsilon_r \frac{A}{d} \,,$$

with ϵ_0, ϵ_r, A and d being the vacuum permittivity, the relative permittivity of the material, the area and the thickness of the dielectric. The charge Q on the plate is related to the capacitance C via the applied voltage V

$$Q = C \cdot V \,.$$

Taking into consideration that the SiO$_2$ and material x are connected in series ($\frac{1}{C_{eff}} = \frac{1}{C_{SiO_2}} + \frac{1}{C_x}$) and that the carrier concentration is given by $n = \frac{Q}{A}$ yields

$$n = C_{eff}^* \cdot V_{BG} \,.$$

The charge carrier concentration is typically given in electrons or holes per square centimeter, hence $C_{eff}^* = C_{eff}/(100\text{cm})^2 \cdot e$. Note that the above equation is only valid if the graphene is charge neutral at zero applied backgate voltage. Otherwise the voltage V_{BG} has to be replace by $V_{BG} - V_{CNP}$ where V_{CNP} describes the backgate bias which has to be applied to reach charge neutrality. This model can be applied to graphene on 300 nm SiO$_2$ ($d_{SiO_2} = 300$ nm, d_x=0, Chapter 5 and Chapter 6), suspended graphene with for instance 150 nm SiO$_2$ etched away ($d_{SiO_2} = 150$ nm, $d_x = 150$ nm, Chapter 10) or graphene on 300 nm SiO$_2$ and boron-nitride ($d_{SiO_2} = 300$ nm, $d_x = d_{hBN}$, Chapter 9). Other ways to change the carrier concentration in graphene include chemical doping [59], top gating [60] or gating by an electrolyte [61, 62]. However, this is not in the scope of this thesis.

3. Raman Spectroscopy of Graphene
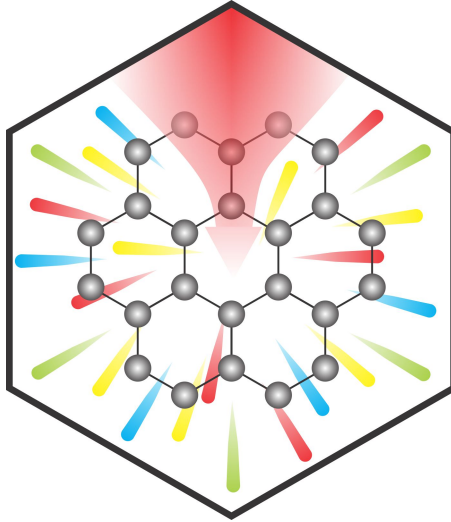
In Raman spectroscopy, the sample is illuminated with a monochromatic laser beam of known frequency ω_{Laser}. The emitted light is analyzed with respect to both wavelength and intensity. Besides the light with unchanged frequency ω_{Laser} resulting from elastic scattering (Rayleigh scattering) also light with higher and lower frequency is emitted. This so-called Raman effect [63] is a consequence of the inelastic scattering of light with elementary excitations, for instance with phonons, magnons, excitons, plasmons etc.. Due to these interactions, Raman spectroscopy is an important and widely used tool as it provides various information about the sample under study. For instance vibrational properties (phonons) are specific to the chemical bonds and symmetry of molecules which allows the identification of substances by their characteristic Raman "fingerprint". This entails possible applications, from the detection of explosives for security screening [64,65] to metabolic fingerprinting in disease diagnosis [66]. Another example is the confirmation of the predicted existence of low-frequency collective motion in proteins [67] and DNA [68] with Raman spectroscopy which stimulated extensive studies about their biological functions. In the field of solid state physics, Raman spectroscopy is often used for instance to identify the crystallographic orientation, measure temperature and evaluate material properties. Especially for characterizing carbon and its allotropes, Raman spectroscopy turned out to be an extremely fruitful tool for reasons discussed below. First, we intro-

duce a quantum mechanical model to understand Raman scattering. Then we turn our attention specifically to Raman spectroscopy of graphene and end the chapter with a brief description of the setup used for our experiments.

3.1. Quantum mechanical model for Raman scattering

Although the classical interpretation of visible light interacting with matter via the polarizability of the valence electrons [69–71] is able to successfully explain the existence of Rayleigh scattered light as well as Stokes- and anti-Stokes scattered Raman light (this is light with lower and higher frequency compared to the incoming light), the model fails to explain the observed light intensities. Furthermore, the classical model neglects the quantization of the vibrations of the atoms. The quantum mechanical treatment remedies those shortcomings. It describes the interaction of the light field (photon) with an electron of the solid which can be excited in a virtual state ψ_V. As this state is not an eigenstate of the system it is highly unstable. It will decay on a very short time scale and hereby emit light. The quantum mechanical lifetime of virtual states is dictated by Heisenberg's uncertainty principle $\Delta E \cdot \Delta t \geq \hbar/2$. A schematic energy level diagram is shown in Figure 3.1. This figure is used in order to illustrate the spontaneous Raman effect as well as Rayleigh scattering events. Here ψ_G, ψ_E, ψ_V and $\psi_{V'}$ represent the ground state, an excited state and two virtual states, respectively.

   If laser light impinges upon a sample, we have to consider different possibilities. The incoming photon may excite an electron from the ground state ψ_G to a virtual state ψ_V or from an excited state ψ_E to another virtual state $\psi_{V'}$ followed by the relaxation of the electron to a lower energy state involving the emittance of a photon. If the initial and final state have the same energy (see Figure 3.1 (b)) the process is called Rayleigh scattering and the emitted photon has the same energy as the incoming laser light. This is the most frequent process and produces the highest intensity. It can simply be described as an elastic scattering process (no change of energy) of a photon with an electron.
Stokes scattering is depicted in Figure 3.1 (a). The incoming photon first excites an electron from the ground state ψ_G into a virtual state ψ_V before the electron relaxes into the excited state ψ_E by emitting a photon with a lower energy. The energy difference between incoming and outgoing photon is equal to the energy difference between ground and excited state.
Anti-Stokes scattering as illustrated in Figure 3.1 (c) results from the excitation of an electron from the excited state ψ_E followed by its relaxation into the ground state ψ_G. The photon emitted in this process obtains a higher energy than the incoming one. Again, the energy difference of incoming and outgoing photon equals the energy difference between the ground and excited state. Stokes and anti-Stokes scattering can be described as an inelastic scattering event of a photon with a quasi-particle, for instance with quantized lattice vibrations (phonons). In this case, the photon transfers energy quanta to the phonon field (Stokes) or absorbs energy from it (anti-Stokes). Compared to Rayleigh scattering these processes are less probable by a factor of 10^6 - 10^8 [72]. However, owing to
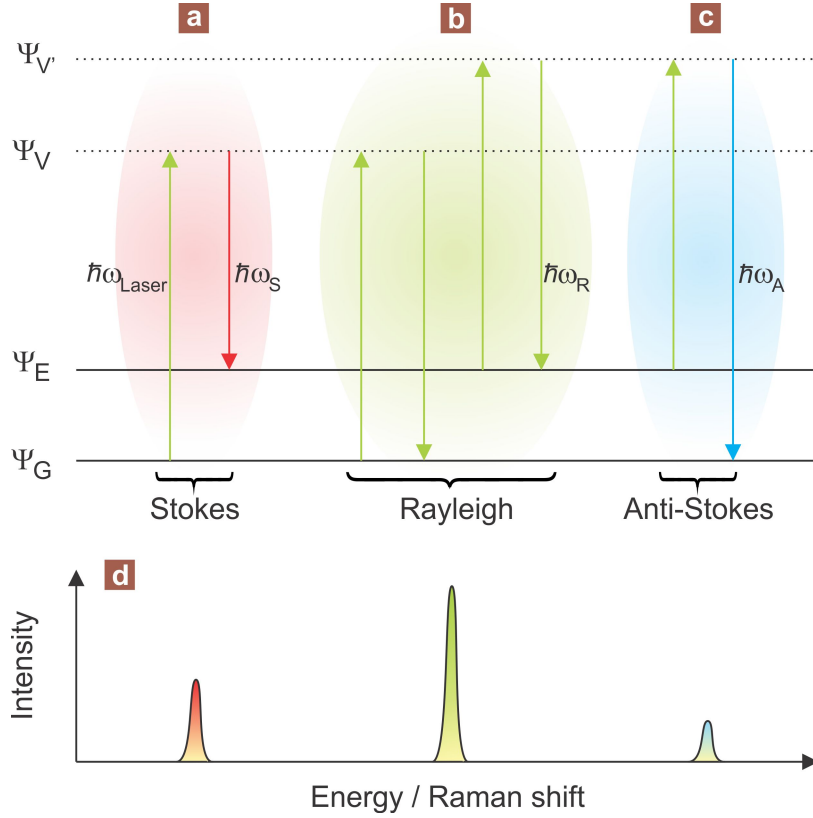
Figure 3.1.: *Quantum mechanical energy level diagram illustrating the occurrence of Raman and Rayleigh scattered light. (a) Stokes Raman light. The incoming photon with energy $\hbar\omega_{Laser}$ excites the electron from the ground state ψ_G to a virtual state ψ_V from where it relaxes to the excited state ψ_E by emitting a photon with lower energy $\hbar\omega_S$. (b) For Rayleigh scattered light the initial and final states are the same and, consequently, the energy of the emitted photon equals the energy of the exciting photon. (c) Anti-Stokes scattered Raman light is emitted if an electron from an excited state transits via a virtual state to the ground state. The emitted photon possesses a higher energy $\hbar\omega_A$ than the incoming light.*

high quality lasers, filters and spectrometers these effects are easily measurable nowadays. With respect to Chapter 6 we point out that the occupation of the ground state is higher compared to the excited state at room temperature as described by the Boltzmann distribution. Consequently, Stokes scattering is more likely to happen than anti-Stokes scattering and hence will have a higher intensity. The ratio of both intensities is related to the respective occupation numbers and provides a measure for the temperature according to:

$$\frac{I_{AS}}{I_S} = \left(\frac{\omega_{Laser} + \omega_{Vib}}{\omega_{Laser} - \omega_{Vib}}\right)^4 \exp\left(-\frac{\hbar\omega_{Vib}}{k_B T}\right) \tag{3.1}$$

Here, ω_{Vib} is the frequency of the respective vibration. We point out that this relation is only valid if the system is in thermal equilibrium. Let us imagine a case in which the different phonon modes are only weakly coupled with each other, or even not coupled at all. If the occupation number of only one phonon mode is now changed, the system is out

of thermal equilibrium. There is no longer one single temperature to describe the system but each mode has to be described by its own temperature. The phonon mode with a higher occupation number will have a higher temperature and the term hot phonons is used (see Chapter 6).

Figure 3.1 (d) schematically introduces how the Raman spectrum will look like as a result of the processes given in Figure 3.1 (a)-(c). The abscissa describes the energy of the emitted photon. In spectroscopy the energy is often given for convenience in terms of Raman shift $\bar{\nu}$. The Raman shift is defined as

$$\bar{\nu} = \bar{\nu}_{Laser} - \bar{\nu}_{Raman} \, .$$

Here, $\bar{\nu}$ is related to the wavelength via equation $\bar{\nu} = 1/\lambda$. The Raman shift is directly related to the vibrational energy via $E = hc\bar{\nu}$. The incoming photon obviously corresponds to zero Raman shift. The ordinate in Figure 3.1 (d) describes the intensity in numbers of emitted photons at a certain energy. As indicated, the intensity for Rayleigh scattered light is highest, followed by Stokes scattered light. Anti-Stokes scattered light typically shows the lowest intensity.

3.1.1. Conservation laws

The scattering processes described above have to obey the physical conservation laws. In this case the conservation of energy and momentum is especially important.

The conservation of energy dictates

$$\hbar\omega_{Laser} - \hbar\omega_{Raman} = \pm\hbar\omega_{Vib} \, .$$

Stokes scattering is described by the "+" sign and $\omega_{Raman} = \omega_S$ whereas anti-Stokes by the "-" sign and $\omega_{Raman} = \omega_A$. The term $\hbar\omega_{Vib}$ stands for the energy difference between excited and ground state. The frequency of a vibration typically depends on its momentum $\omega_{Vib} = \omega_{Vib}(\mathbf{q})$. For graphene this dispersion relation will be covered in Subsection 3.2.6. In order to formulate the conservation of momentum in a crystal, the reciprocal lattice vector $\mathbf{G}$ has to be included in the consideration due to the translation invariance of the crystal lattice. This leads to the quasi momentum conservation

$$\mathbf{k}_{Laser} - \mathbf{k}_{Raman} \pm \mathbf{q} + m \cdot \mathbf{G} = 0$$

where $\mathbf{k}_{Laser}$ is the wave-vector of the laser light, $\mathbf{k}_{Raman}$ the wave-vector of Raman scattered light, m an integer and $\mathbf{q}$ describes the momentum of the created (Stokes) or annihilated (anti-Stokes) phonon.

The wave-vector of a photon with a frequency commonly used for Raman experiments [1] is nearly five orders of magnitude smaller than the wave-vector pointing to the border of the first Brillouin-zone (BZ) in graphene and hence can be neglected. As a consequence of this and the quasi momentum conservation, only phonons from the BZ center Γ with $\mathbf{q} \approx 0$ can be measured with one phonon Raman spectroscopy. This rule does not apply for higher order Raman scattering processes. One real life example where several phonons

---

[1]This region typically ranges from UV to near IR light.

are involved will be discussed when the origin of the 2D peak is explained in Subsection 3.2.2. In the next section we specifically consider the Raman spectrum of graphene. We explain the origin of the experimentally observed peaks as well as what kind of information we can extract from the position, the full width at half maximum (FWHM) and the intensity of those peaks.

3.2. Raman spectroscopy of graphene

The chemical bonds of a material are closely linked to its vibrational properties, which can be measured in Raman spectroscopy. In the case of carbon compounds this allows for instance to distinguish between different hybridizations. The most prominent peak in linear carbon chains with strong sp-hybridization is found in the range of 1850-2100 cm^{-1} [73] whereas diamond with its sp^3-hybridization possesses a peak at 1333 cm^{-1}. Graphene and its sp^2-hybridization exhibits the characteristic peak (called G peak) at around 1580 cm^{-1}. A typical Raman spectrum of graphene is shown in Figure 3.2. Besides the G peak which will be covered in Subsection 3.2.1, two additional prominent peaks called D and 2D are visible and will be treated in Subsections 3.2.5 and 3.2.2, respectively.
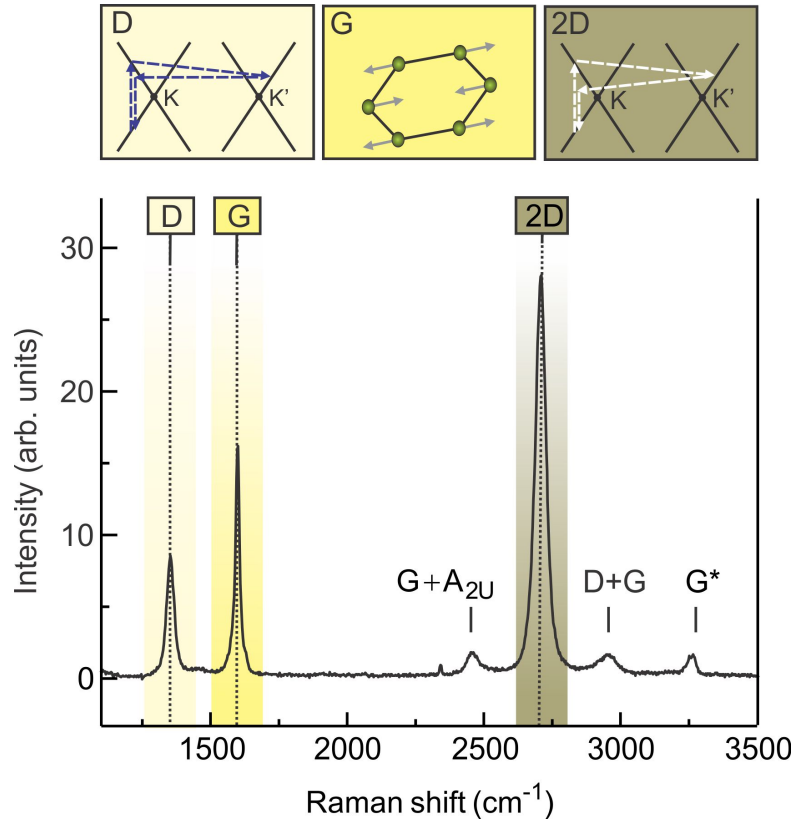

Figure 3.2.: *Stokes Raman spectrum of graphene. The three most prominent peaks, called D, G and 2D are marked and their origin is schematically depicted in the upper three insets. Three additional peaks (G+A$_{2U}$, D+G and G*) are identified and marked in the overview as well.*

41

The intensity, full width at half maximum (FHWM) and position of the three Raman main peaks of graphene (D, G and 2D) allow to deduce several important information, for instance about:

- Electronic band-structure and Fermi velocity

- Charge carrier type and concentration

- Crystallographic chirality (armchair or zigzag edges)

- Number of graphene layers

- Stacking order

- Crystallite size

- Defects

- Strain

- Electron coherence length

- Interaction of phonons with other quasi particles

- Phonon occupation number and temperature

However, one has to keep in mind that different properties may trigger the same response in the Raman spectrum. To give an example, heating the graphene will cause a red shift in the G peak position due to phonon softening. On the other hand, heating the graphene might reduce the intrinsic doping level which also leads to a red shift in the G peak position. Consequently, in order to establish a relation between temperature and G peak position one has to experimentally fix all other properties that would otherwise influence the G peak position. For graphene with three peaks, each with three parameters, this is challenging. However, once this requirement is fulfilled, Raman spectroscopy of graphene is a very fruitful tool. One reason for this richness of information lies within the double resonance mechanism for the D and 2D peak as covered in Subsection 3.2.5 and Subsection 3.2.2, respectively. First, we discuss the origin of the G peak as a "classical" Raman peak and the insights we can gain from it.

3.2.1. Raman G peak

One phonon Raman scattering takes place at the Γ-point of the Brillouin zone (BZ) due to the negligible photon momentum compared to the extension of the first BZ. Figure 3.3 and 3.4 sketch the six normal vibrations which are possible in graphene [74]:

$$A_{2u}, B_{2g}, E_{1u}, E_{2g}$$

The vibrations A_{2U} and E_{1U} describe the movement of the whole graphene plane. They both are Raman-inactive as the polarizability χ does not depend on the position x of the atoms ($\frac{d\chi}{dx} = 0$) which constitutes a necessary selection rule for Raman scattering [75].
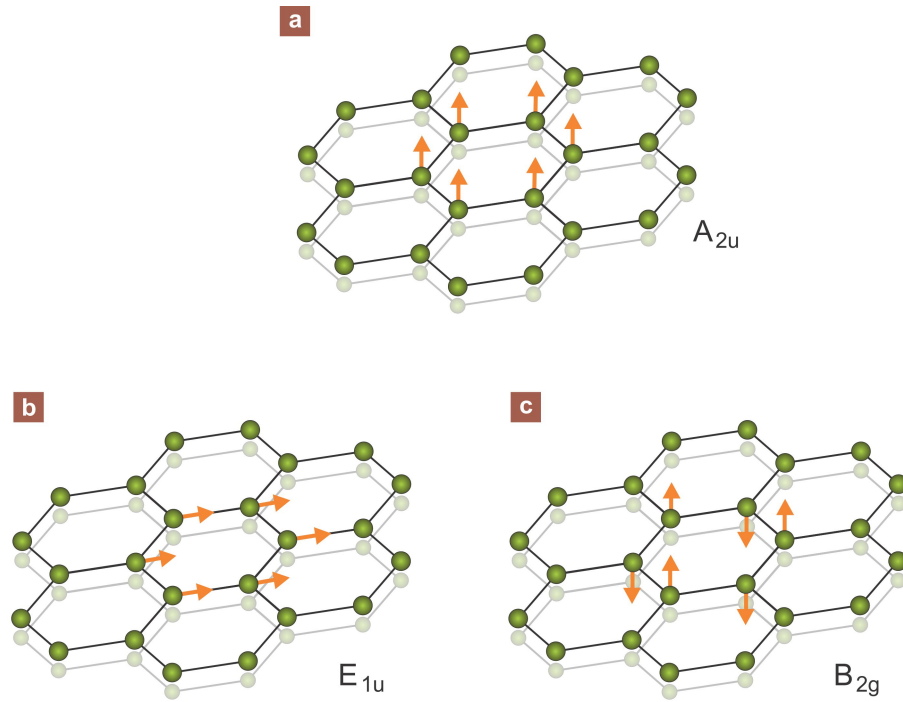
Figure 3.3.: **Raman-inactive normal vibrations of graphene.** *(a) and (b) describe a motion of the whole graphene plane whereas in (c) the carbon atoms vibrate mirror-inverted out-of-plane.*

However, as the dipole moment is changing, these two vibrations can be measured by infrared-spectroscopy [76]. Figure 3.3 (c) represents an optical phonon where the carbon atoms vibrate mirror-inverted perpendicular to the graphene plane. This vibration does not fulfill the Raman selection rule either and is also Raman-inactive. Nevertheless, as a consequence of slight rearrangement of the lattice structure at the edge of HOPG it was measured on HOPG to have a Raman shift of 867 cm^{-1} [77].
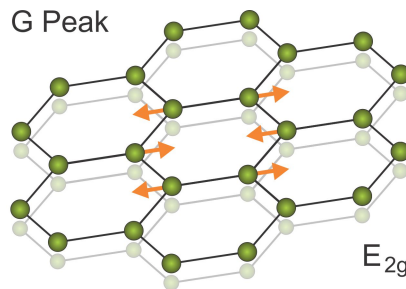
Figure 3.4.: **Raman-active in-plane stretching vibration responsible for the graphene G peak.** *This peak is characteristic for all sp^2 carbon-carbon bonds. In charge neutral graphene the G peak is found to be at 1583 cm^{-1}.*

The only Raman-active vibration expected in graphene stems from the vibration shown in Figure 3.4. The in-plane stretching vibration of the sp^2-hybridized carbon atoms leads to two degenerate optical phonons at the Γ-point. They give rise to the G peak in graphene and graphite samples and are eponymous for this peak: G like graphene/graphite. The

G peak position of charge-neutral graphene is at 1583 cm^{-1}, the corresponding energy is 196 meV. The G peak position is influenced for instance by temperature via phonon softening/hardening or by the charge carrier density via electron-phonon coupling. Additionally, the charge carrier concentration influences the FWHM (see Chapter 5). The position of the G peak also changes with the crystallite size as well as with strain applied to graphene [78].

The intensity of the Raman peaks depends (besides the power of the incoming light) on the area illuminated by the laser beam. The G peak is often used to normalize the intensity of other Raman peaks. At the edge however, the intensity of the G peak depends sensitively on the polarization of the laser beam as well as on the chirality of the edge [79, 80].

Although the G peak is the only Raman-active vibration, the experiment (see Figure 3.2) reveals a much richer Raman spectrum with several additional peaks. The origin of these peaks will be treated in the next two subsections.

3.2.2. Raman 2D peak of single layer graphene

The 2D peak is visible in all graphite/graphene samples[2] at around 2700 cm^{-1}. Considering only one phonon Raman processes is obviously not enough to explain the appearance of the 2D peak (see Figure 3.2) and its properties. A key experimental observation is that the 2D peak is dispersive [82], i.e. its position depends on the laser wavelength used. This finding cannot be explained by the model discussed so far where the Raman shift only depends on the energy of the vibration (compare to Figure 3.1). A theory involving resonances as well as a second phonon is able to shed light on the origin of the 2D peak. Furthermore, the band-structure of graphene has to be included in the consideration leading to the so-called inter-valley double (triple) resonance mechanism [83]. Resonances in the context of Raman spectroscopy mean that the energy of an incoming or scattered phonon or photon matches a real state rather than a virtual state. This drastically increases the transition matrix element and consequently the intensity of the related Raman scattered light [84]. For a double or triple resonance, two or three of the involved processes end up in real states giving rise to a pronounced Raman peak. The process is best explained by examining the schematics depicted in Figure 3.5. It shows the electronic band structure with the two Dirac cones located at the two inequivalent K and K' points at the corner of the first Brillouin zone as introduced in Chapter 2.

The inter-valley double resonance as illustrated in Figure 3.5 (a) can be described in four steps:

1. Creation of an electron-hole pair by the incoming laser photon with energy $\hbar\omega_{in}$.

2. First inelastic scattering event of the electron by a phonon with wave-vector $\mathbf{q}$.

3. Second inelastic scattering event of the electron by a phonon with wave-vector $-\mathbf{q}$.

4. Recombination of the electron-hole pair by emitting a photon with energy $\hbar\omega_{out}$.

---

[2]For a given excitation laser frequency the 2D peak may get quenched as a result of Pauli blocking at large enough carrier density. The 2D peak intensity also undergoes a severe quenching if the exciting laser frequency lies in the UV [81].
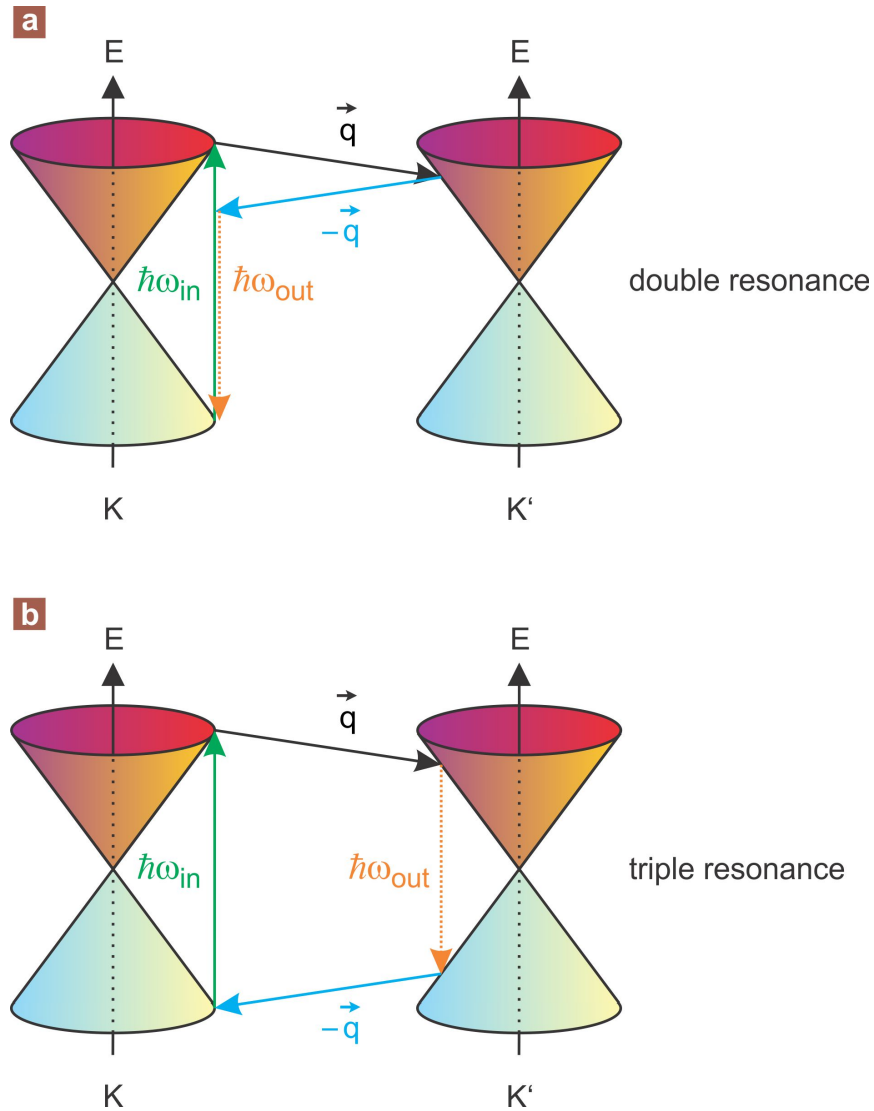
Figure 3.5.: ***Inter-valley resonance mechanism giving rise to the 2D Raman peak*** *(a) Double resonance mechanism. (b) Triple resonance mechanism. The incoming photon creates an electron hole pair which recombines and emits the Raman light after two phonon scattering events.*

To gain a deeper understanding we describe these four steps in more detail. First, the incoming laser photon with energy $E_{Laser} = \hbar\omega_{in}$ creates an electron-hole pair, as illustrated by the green arrow in Figure 3.5 (a) and (b). Owing to graphene's linear zero gap band-structure, it is always possible to create this e-h pair in resonance[3]. The transition is almost vertical due to the low photon momentum. We point out that there is not only one single point where the e-h pair can be created. Including the band structure in the consideration leads to an equi-energy circle on which's circumference the electron (and hole) can be resonantly created. This circle is drawn in green in Figure 3.6 (a) and (b) and is fixed by the energy of the incoming photon to have a radius Δk_0 around K.

The created electron can now scatter with phonons of arbitrary wave-vector. The

---

[3]Again, provided that the charge carrier concentration and excitation laser frequency are not too high.
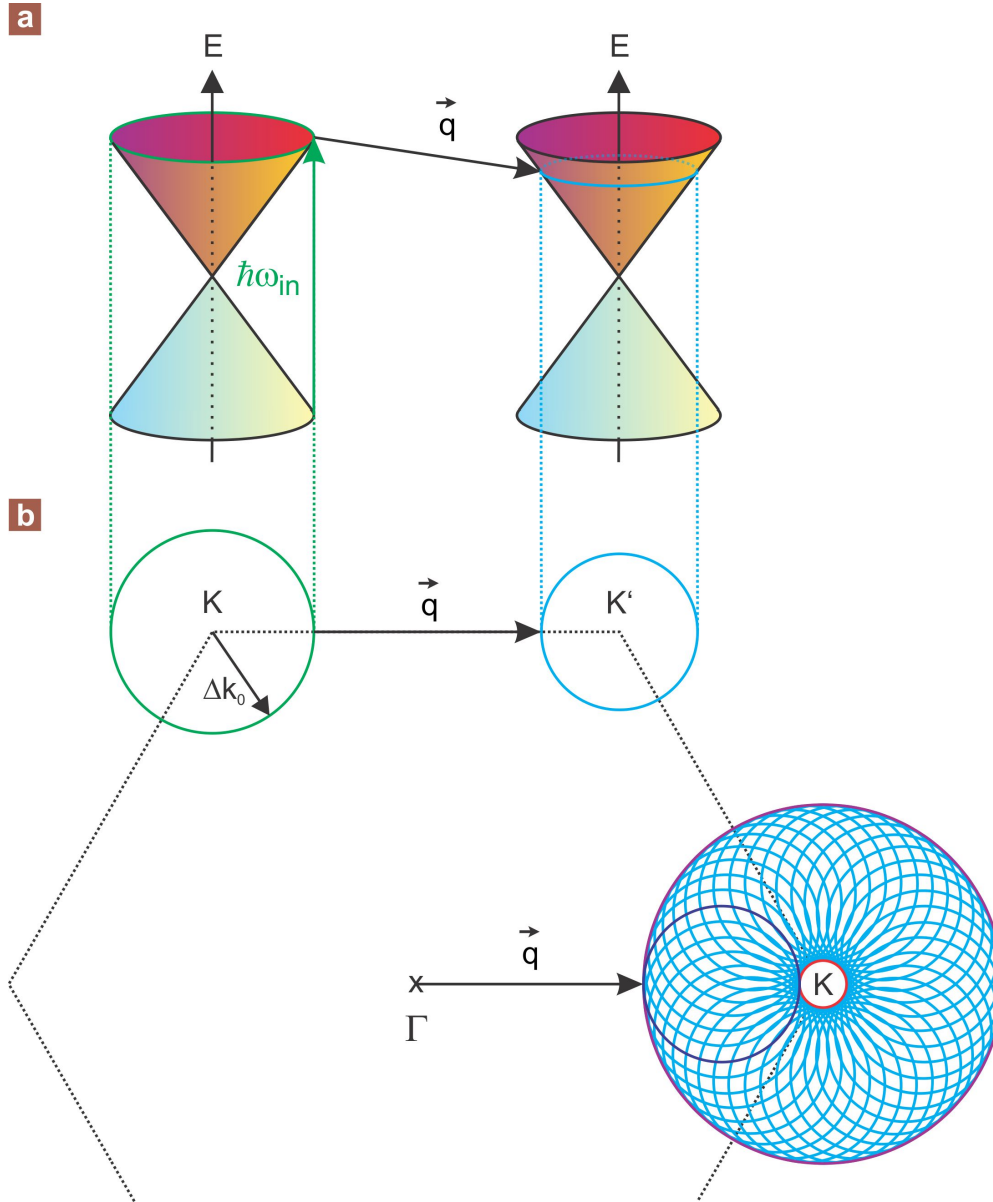
Figure 3.6.: ***Many different scattering pathways are possible in the double resonance mechanism.*** *All possible wavevectors **q** that fulfill the resonance requirements reside on the surface of the depicted annulus. The phonon density of states favors however the extremes (inner and outer circle) for the 2D peak.*

scattering rate is however drastically enhanced if the electron scatters with a phonon that contributes just such a momentum **q** that the electron ends up in a real state as illustrated in Figure 3.5 (a) and (b) by the black arrow. For a monotonically increasing phonon dispersion relation there exists always a combination of phonon momentum and energy that will satisfy the condition for this second resonance. The scattering is inelastic as energy is transfered. In analogy to the case of e-h pair creation, there is also not only one single possibility but multiple processes can satisfy the second resonance condition. They are located on a second circle around K' (light blue circle in Figure 3.6). All phonons which connect one point of the circle around K with one point around K' satisfy the double

resonance condition. Drawing all possibilities for $\mathbf{q}$ gives the annulus in Figure 3.6 (b). Although all phonons with a wave-vector pointing on the torus may contribute to the scattering, the inner (red) and outer (purple) circle dominate the Raman singal due to the enhanced phonon density of states at these extrema.

The next step for the electron is to scatter again inelastically with a phonon with the same momentum but opposite direction $-\mathbf{q}$ back to the initial valley K as illustrated by the blue arrow in Figure 3.5 (a). Finally, the electron can recombine with the hole and emit a photon with energy $\hbar\omega_{out}$. This completes the double resonance Raman round-trip. Note that everything discussed above for electrons is also valid for holes. The characteristic dispersion of the 2D Raman peak (different Raman shifts for different laser frequencies) as mentioned above and measured in experiments is explained by the resonance mechanism involving two phonons as well as the phonon dispersion relation covered in Subsection 3.2.6: Using laser light with a higher energy will create the e-h pair at a higher energy which finally results in a higher Raman shift.

Another even more favorable process is outlined in Figure 3.5 (b). In this case all the transitions end up in real states resulting in a threefold resonance:

1. The incoming photon with energy $\hbar\omega_{in}$ creates an electron-hole pair.

2. The electron is inelastically scattered by a phonon with wave-vector $\mathbf{q}$.

3. The hole is inelastically scattered by a phonon with wave-vector $-\mathbf{q}$.

4. The electron-hole pair recombines by emitting a photon with energy $\hbar\omega_{out}$.

The fact that the electronic band structure is involved in the double and triple resonance has some interesting consequences. One is, that the shape of the 2D peak depends on the number of layers. Adding only one additional layer drastically changes the shape of the 2D peak. Hence, it can be used to distinguish whether the sample is a mono- or bilayer. This is discussed in more detail in the next subsection.

3.2.3. Raman 2D peak of a graphene bilayer

When two graphene monolayers are stacked on top of each other in the commensurate Bernal configuration, the valence and conduction bands split into two (see Subsection 2.3.1). This increases the number of possible resonant inter-valley processes contributing to the 2D Raman peak. Figure 3.7 depicts the electronic band structure of a Bernal stacked bilayer around K and K'.

An incoming photon can create an electron-hole pair either in the inner conduction and valence band (process (1) in Figure 3.7) or in the outer conduction and valence band (process (2)) around K. The subsequent inelastic scattering event may end in either of the conduction bands around K' giving rise to altogether four different possible Raman lines. The Raman shift for these four lines are very close to each other and partially overlap. In addition to the processes (1) and (2) the e-h pair could also be created in the inner valence and outer conduction band or vice versa. However, theoretical calculations using density functional theory (DFT) predict that these transitions are very unlikely to happen and can be neglected [85]. In summary, the 2D peak of a Bernal stacked graphene bilayer
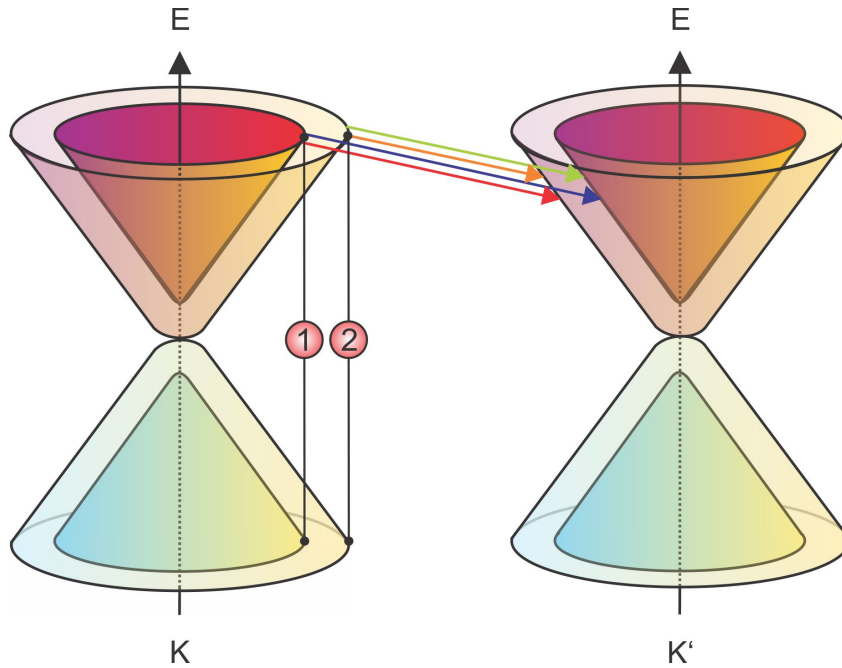
Figure 3.7.: ***Bandstructure and inter-valley double resonance mechanism in Bernal stacked bilayer graphene.*** *The electron-hole pair can either be created in the inner conduction and valence band (process (1)) or in the outer conduction/valence band (2). The subsequent inelastic scattering events (illustrated by the colored arrows) lead to a Raman 2D peak which consists of four overlapping peaks.*

consists of four overlapping peaks with different intensities. In experiments, the 2D peak indeed shows clear shoulder structures (see for instance [71]) and a fit to the data requires four Lorentzians. Monolayer data in contrast can be fitted with a single Lorentzian [85]. The analysis of the line shape of the 2D peak is a useful tool to distinguish between mono- and multilayer graphene. If, however, the bilayer is not Bernal stacked but the two layers are twisted with an arbitrary angle, the valence and conduction band are not split into two but rather resemble the monolayer case with one linear band structure under certain conditions. In this case the 2D peak will again only show one single peak. This case for a twisted bilayer is considered next.

3.2.4. Raman 2D peak of twisted bilayer graphene

In Subsection 2.3.2 we discussed the band structure of twisted bilayers. Due to the rotational fault, the coupling between the two layers is reduced and the band structure is changed significantly. Two split Dirac cones appear and the Fermi velocity is reduced. This linear band structure and reduction of the Fermi velocity has a strong impact on the Raman spectrum. The 2D peak no longer consists of four overlapping peaks as it was the case for Bernal stacked bilayer graphene but rather is comprised of one single peak. The change in the Fermi velocity affects the position of the 2D peak. Figure 3.8 depicts the energy dispersion around K for two different Fermi velocities as well as the created electron-hole pair. The slower the velocity (smaller slope) the higher the resulting Raman

2D peak position [86]. However, this model is oversimplified and only valid as long as the
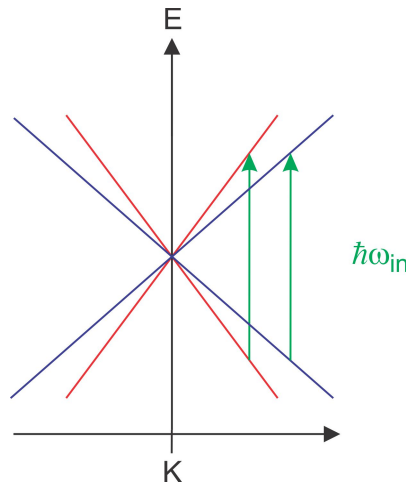
Figure 3.8.: *Electronic dispersion relation for twisted bilayer graphene with two different angles θ. A reduction of the Fermi velocity (smaller slope of the Dirac cone) leads to a change of the phonons involved in the double resonance mechanism. The resulting 2D peak is comprised of one single peak and has a higher Raman shift.*

laser excitation is smaller than the energy difference between valence and conduction Van Hove singularities, e.g. for large angles. This case is shown by the blue arrow in Figure 3.9 (b). If the laser energy equals the energy difference between Van Hove singularties, the coupling between top and bottom layer will strongly affect the Raman spectrum. Also for small rotation angles, if the laser energy is higher than than the energy difference between valence and conduction Van Hove singularities (illustrated by the black lines in Figure 3.9 (b)) the scattering path is significantly different from those of a monolayer. A tight-binding approximation provides a more quantitative explanation and resembles well experimental data [27].
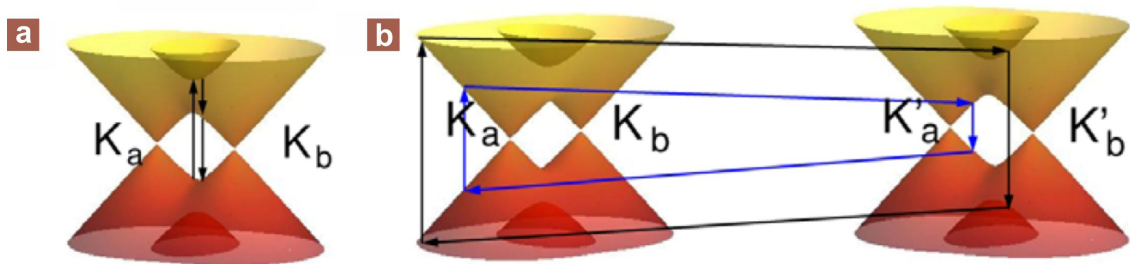
Figure 3.9.: *Raman scattering processes in twisted bilayer. (a) The G peak will also be affected by the modified band structure of twisted bilayer. A resonant Raman scattering process becomes possible between the Van Hove singularities. (b) The energy difference between the Van Hove singularities depends on the twist angle θ. If this energy is bigger than the laser energy the Raman spectrum resembles the monolayer case with a different Raman shift (blue line). For the other case (black line) or if the energies are equal, the situation is more complicated and a complete theoretical approach is needed. Modified from [27].*

It is important to realize that the 2D Raman peak of a non Bernal stacked bilayer can consist of only one single peak as a consequence of the linear Dirac cone. This fact has to be taken into consideration when identifying monolayer graphene.

3.2.5. Raman D peak

In some graphene samples the Raman spectrum exhibits another peak (see Figure 3.2) at half the Raman shift of the 2D peak. This peak is only visible in the presence of defects and it is called D peak. The correlation between the intensity of this D peak and the defect density makes this peak interesting and worthwhile to study in more detail. One early work established the connection between the D peak intensity (normalized to the G peak, ratio I(D)/I(G)) and the crystallite size. The crystallite size was determined independently from X-ray diffraction data [87]. A linear dependence of the ratio I(D)/I(G) with inverse crystallite size was found, hence a higher D peak for smaller crystallites. But not only the size of the crystallites enters the D peak intensity. Exchanging for instance some of the carbon atoms by boron atoms [88] does not change the size of the crystallites but also generated an increase of the D peak. Because boron atoms locally break the lattice symmetry, the idea was that defects and disorder in general evoke the D peak by relaxing the $q \approx 0$ selection rule. The previously prohibited A_{1g} breathing mode as illustrated in Figure 3.10 might be activated by defects and lead to the D peak.
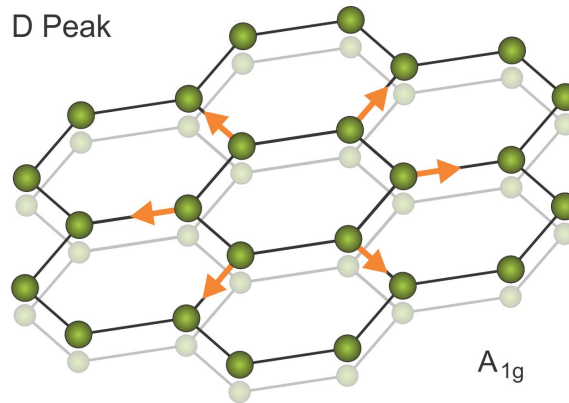
Figure 3.10.: ***Breathing mode activated by defects as a possible origin for the appearance of the Raman D peak.*** *This idea of a classical vibration does, however, fail to explain all experimentally observed facts concerning the D peak.*

Experiments using different laser wavelength caused however different Raman shifts. This dispersion is not consistent with the model of a breathing mode as the origin for the D peak. It rather points to a mechanism similar to that introduced for the 2D peak: A slightly altered inter-valley double resonance process as elucidated in Figure 3.11.

The individual steps are as follows:

1. Creation of an electron-hole pair by an incoming photon.

2. Inelastic scattering of the electron by a phonon with wave-vector q.
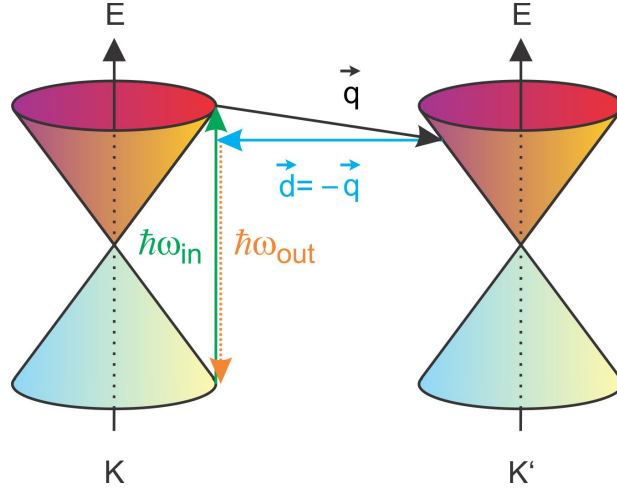
Figure 3.11.: *Intra-valley double resonance mechanism as origin of the D peak. The distinction between the 2D and D peak is the elastic scattering by a defect.*

3. Elastic back scattering of the electron by a defect with wave-vector -**q**.

4. Recombination of the electron-hole pair and emittance of a photon.

The distinction between 2D and D peak is the elastic back scattering of the electron to its original valley, only changing its momentum but not energy. Consequently, all kind of defects, disorder etc. that can provide the correct momentum transfer to the electron without changing its energy will lead to the D peak. One consequence of this is that the D peak allows to distinguish between different edge chiralities as will be discussed in Chapter 7.

We point out that the process depicted in Figure 3.11 is only one possibility out of many. The order of events 2. and 3. can be exchanged for instance (see reference [71] for more illustrated processes). Furthermore, Figure 3.6 is also valid for the D peak. The inner red circle gives rise to a weak peak at around 1250 cm^{-1} independent of the incoming laser wavelength. The outer circle (purple) yields a dispersive peak at around 1350 cm^{-1} for 488 nm exciting laser wavelength. This peak is termed D peak.

The models described here fulfill the purpose of illustrating the origin of the D and 2D peak. In order to establish quantitative statements however, a full quantum mechanical treatment of the Raman cross-section is indispensable, including interferences and non resonant processes as well [89, 90]. This is beyond the scope of this thesis.

3.2.6. Phonon dispersion relation in graphene

The phonon dispersion describes the relation between energy and wave-vector of phonons. This helps to understand most of the vibrational properties of graphene. In order to calculate the phonon dispersion, typically the displacement of each atom from its equilibrium position is considered. A certain number of neighbors is taken into account [72] (see Figure 3.12), to which the atom is coupled by longitudinal and transversal forces. As these forces only depend on the relative position of the atoms, it is possible to write and solve the Newtonian coupled equations of motion.
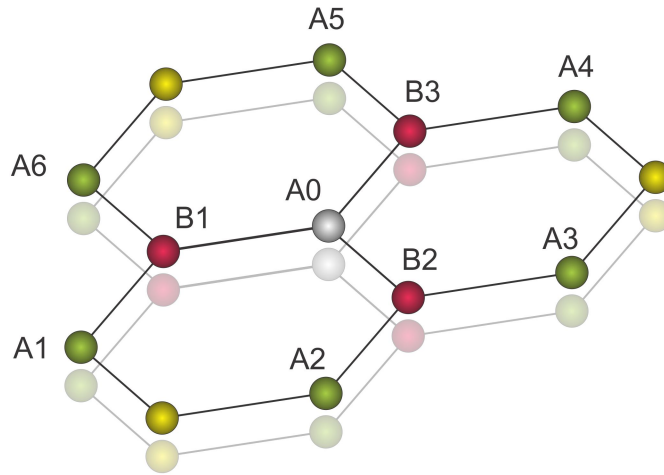
Figure 3.12.: ***Nearest- and next nearest-neighbors in graphene.*** *The gray atom A0 in the middle has three nearest-neighbors B1 - B3 (red) in a different sublattice and six next nearest-neighbors A1 - A6 (green) in the same sublattice.*

Graphene has two atoms per unit cell which leads to six phonon modes [91]. Three of those are acoustic (A) and three are optical modes (O). The possible motions of two carbon atoms A and B in the unit cell are illustrated in Figure 3.13. The atoms can vibrate perpendicular to the graphene plane (Z) and in-plane, either longitudinal (L) or transversal (T). Consequently the six phonon modes are ZA, LA, TA, ZO, LO and TO.
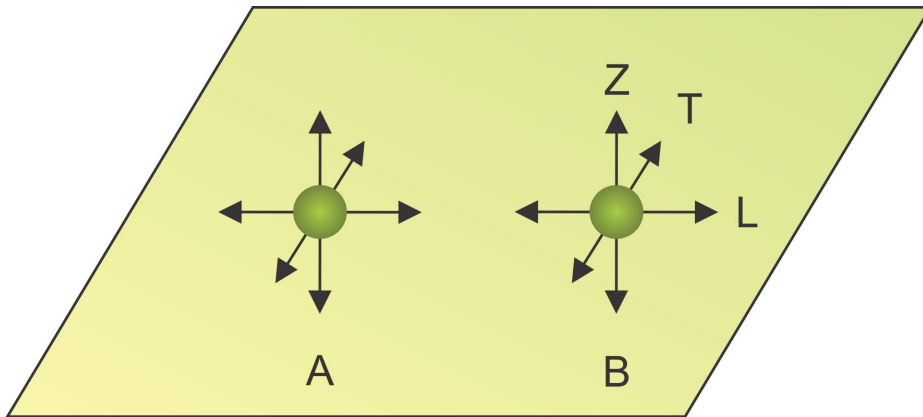
Figure 3.13.: ***Possible motions of two carbon atoms A and B in the unit cell.*** *The atoms can vibrate perpendicular to the graphene plane (Z) or in-plane longitudinal (L) or transversal (T). This leads to a total of six phonon modes.*

In the first- and second-neighbor approximation the out-of-plane vibrations ZA and ZO are often assumed to be decoupled from the in-plane modes [92]. These phonon dispersion relations are shown in Figure 3.14. They have several similarities to the electronic band structure of graphene as a consequence of the identical honeycomb lattice structure. The dispersion relation exhibits a quadratic behavior at the Γ point which is consistent with experimental data [93,94]. Similar to the Dirac cones in the electronic band structure, the phonon dispersion relation possesses a cone structure around the K and K' points. The

phonon density of states nevertheless does not vanish at these points because in-plane modes are available.
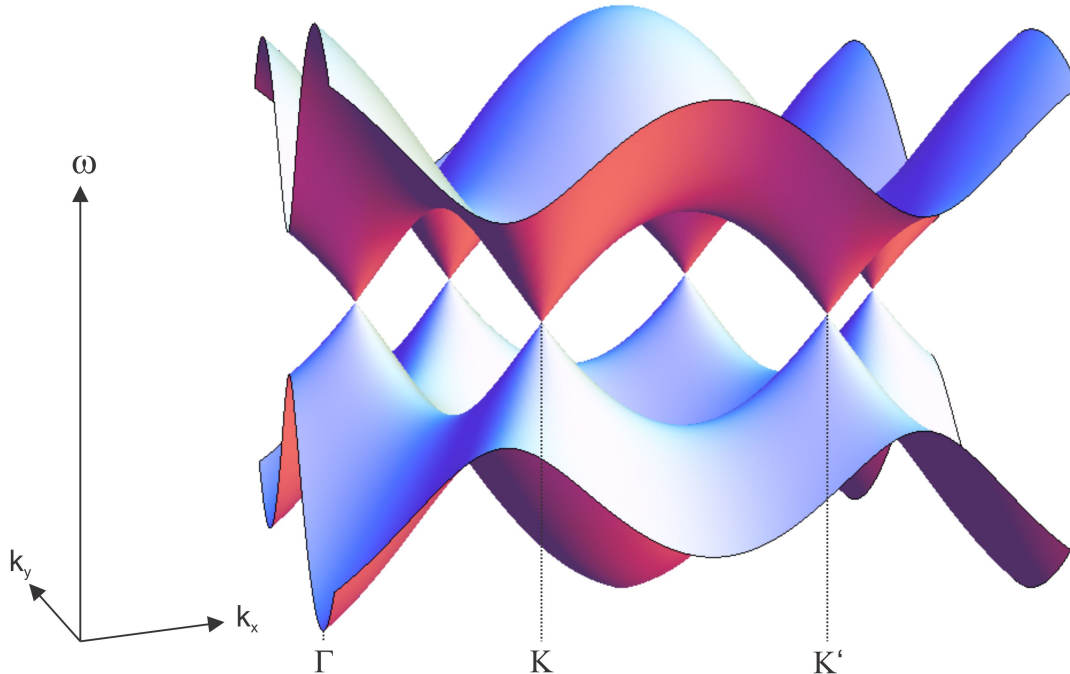
Figure 3.14.: ***Phonon dispersion from the out-of-plane phonon modes ZO and ZA.*** *The horizontal axes are k_x and k_y in momentum space, the vertical axis is the phonon frequency. The upper part depicts the out-of-plane optical (ZO) mode whereas the lower part corresponds to the out-of-plane acoustic (ZA) mode. The phonon dispersion was calculated by using the second-nearest-neighbor model and parameters for graphene as described in reference [92].*

All six phonon modes are shown in Figure 3.15. In order to compare with experiments it is more instructive to show the relation along specific surface cuts ($\Gamma \to M \to K \to \Gamma$). The in-plane modes obey a linear behavior at the Γ-point, the transverse mode closely follows the slightly higher longitudinal one. At the Γ-point the LO and TO are degenerate, causing the Raman G peak as introduced in Chapter 3.2.1. The phonon modes LA and LO touch each other at the K-point [13]. A comparison between theory and experiments on graphite including data from Raman scattering, neutron scattering, X-ray scattering, infrared absorption and electron energy loss spectroscopy is collected in Figure 3.16. Due to the weak coupling between graphene planes in graphite, the dispersion relation for single layer graphene is expected to be very similar. One phonon Raman processes are restricted to probe the phonon dispersion around the Γ-point due to quasi momentum conservation. As a consequence of the double/triple inter-valley resonance scattering mechanism in graphene it is also possible to measure phonons around the K-point with Raman spectroscopy. Having established the fundamentals of Raman
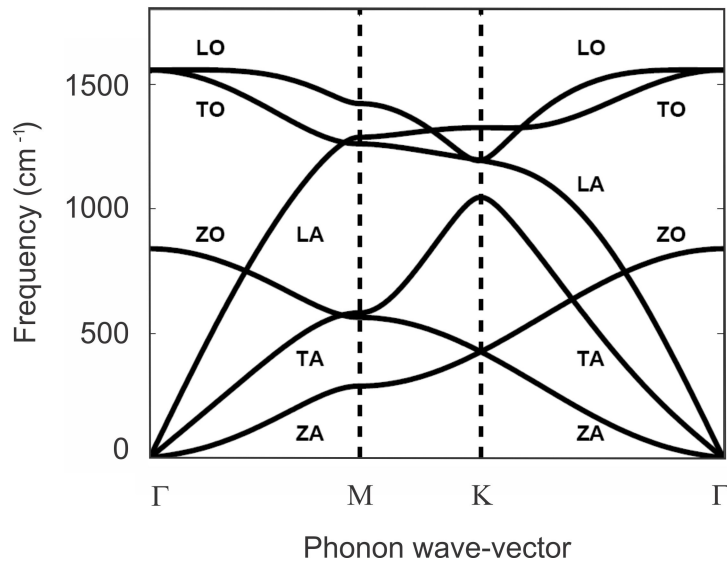
Figure 3.15.: *Calculated surface cuts of the phonon dispersion relation for graphene.* *Figure adapted from reference [92].*

scattering in graphene we are going to describe the scanning confocal setup used in this thesis to measure Raman spectra in the next section.
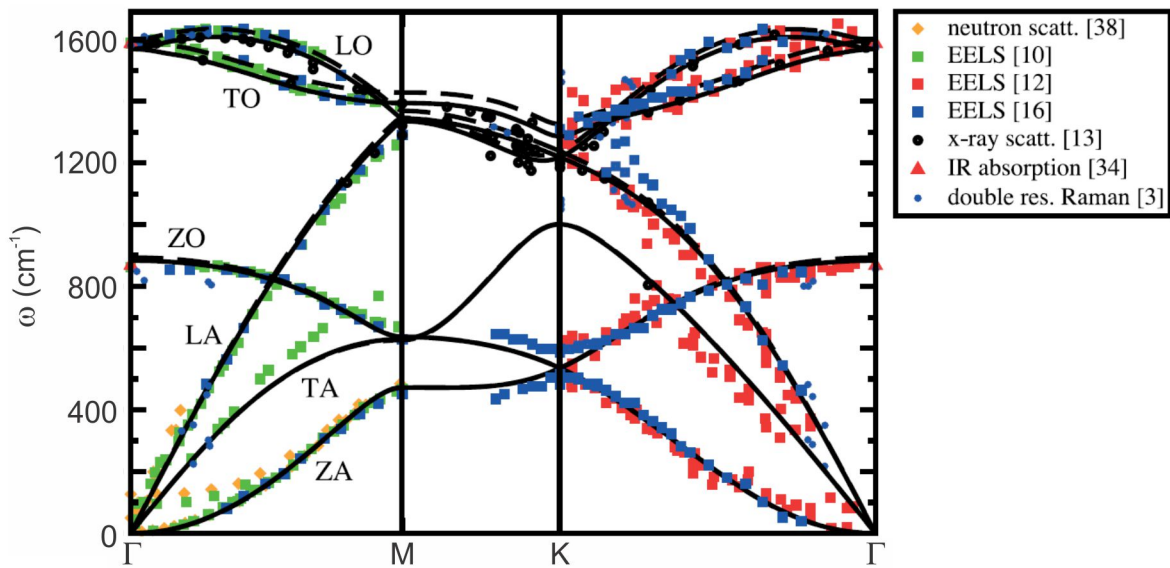
Figure 3.16.: *Experimental data points for the phonon dispersion relation of graphite.* *All phonon modes are included as well as ab initio calculations (LDA, dashed line and GGA, solid line). Modified from [94].*

3.3. Scanning confocal microscope

The principle of confocal microscopy was introduced by Marvin Minsky in 1955 in order to study the connection of neural cells in the human brain. With the invention of the laser, the confocal laser scanning microscopy (CLSM) became an important and widely used technique. It allows to obtain high-resolution images with depth sensitivity.
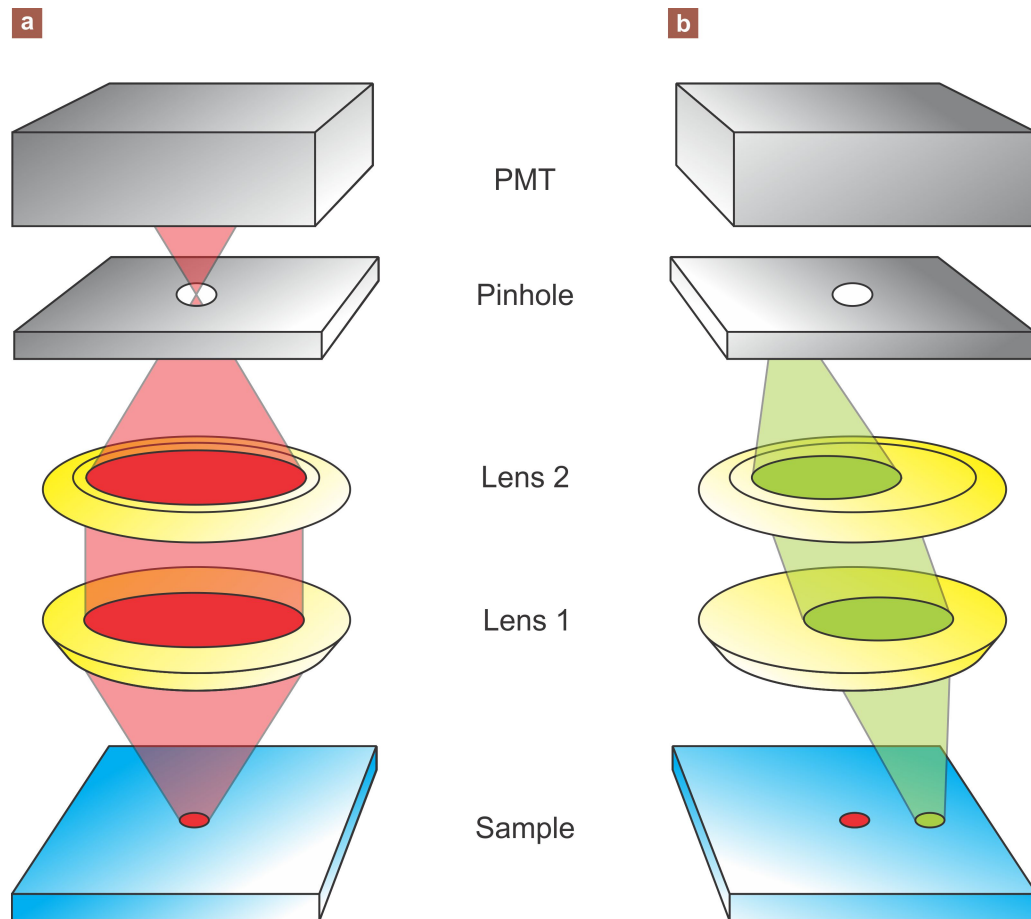
Figure 3.17.: *Principle of confocal microscopy.* *(a) Light emergent from the focal point of lens 1 is able to pass through the pinhole located at the focal point of lens 2 and is detected by, for instance, a PMT. (b) If the light originates from a point out of focus it is obstructed by the pinhole. This enhances contrast and acuity.*

The working principle of a confocal setup is depicted in Figure 3.17. It is different from conventional optical microscopy where the whole sample is illuminated and all light coming back from the sample is collected simultaneously. In a confocal setup, only light emerging from the focal point of lens 1 (see Figure 3.17 (a)) is able to pass through the pinhole, which is located at the focal point of lens 2. With the help of a photomultiplier tube (PMT) the light is converted into an electric signal and read out with a computer. Light emerging from a point out of focus is obstructed by the pinhole as shown in Figure 3.17 (b). For a confocal laser scanning microscope as shown in Figure 3.18, the probe laser is coupled into the system by a beam splitter and subsequently focused by lens 1 to

a diffraction limited spot. The surface is then scanned point-by-point and reconstructed from the PMT output with a computer. This drastically enhances the contrast and acuity compared to conventional optical microscopy as stray light from adjacent points (in all three dimensions) is reduced. Additionally, the z-direction can be scanned to obtain a three dimensional reconstruction of the sample.
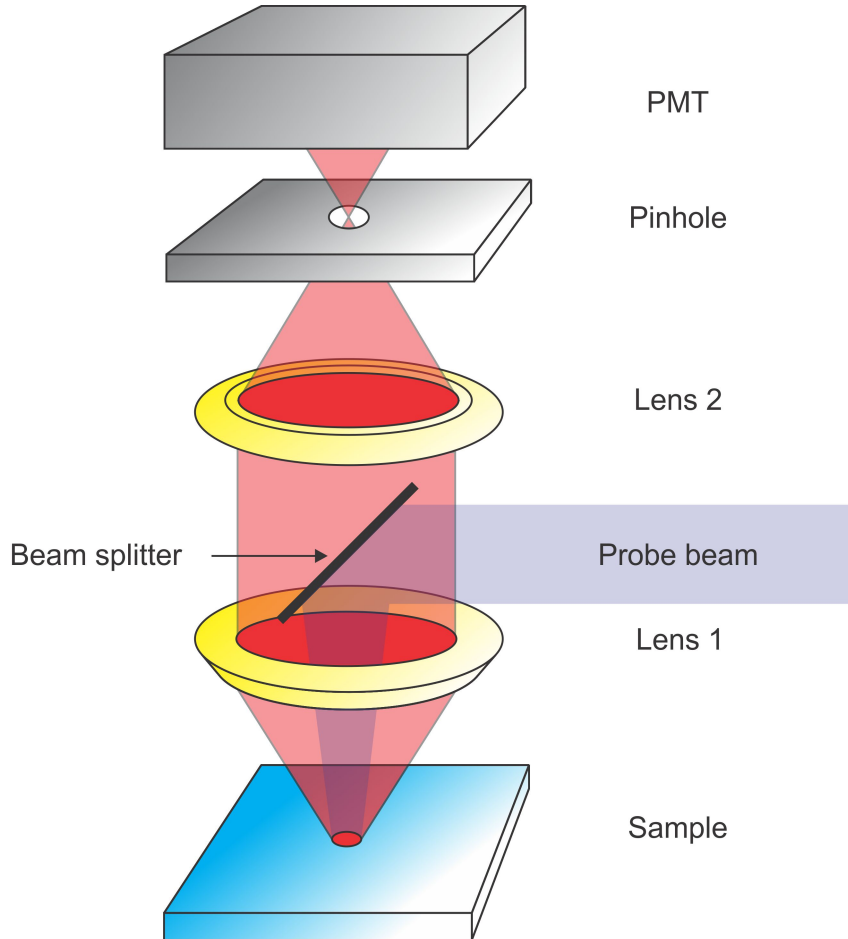
Figure 3.18.: ***Schematics of confocal laser scanning microscopy.*** *The elements of the confocal part as introduced in Figure 3.17 are highlighted here. A probe laser beam is coupled into the system and focused onto the sample to an only diffraction limited spot (see Figure 3.19). Hence, only a small part of the sample is illuminated at once. This increases further the resolution of this method.*

The focused laser spot size and the resolution in x- and y-direction is limited by diffraction of the incoming light by lens 1 and its finite size. If plane waves are focused by a lens, the spot is not infinitely sharp but rather a diffraction pattern occurs. The insets in Figure 3.19 illustrate such diffraction patterns (left hand: linear color scale; right hand side: logarithmic color scale). They consist of a bright disc in the middle (Airy disc) surrounded by dark (zero intensity) and bright rings with decreasing intensity. The radius of the inner disk is given by [95]:

$$r_{Airy} = \frac{0.61 \cdot \lambda_{Laser}}{NA}$$
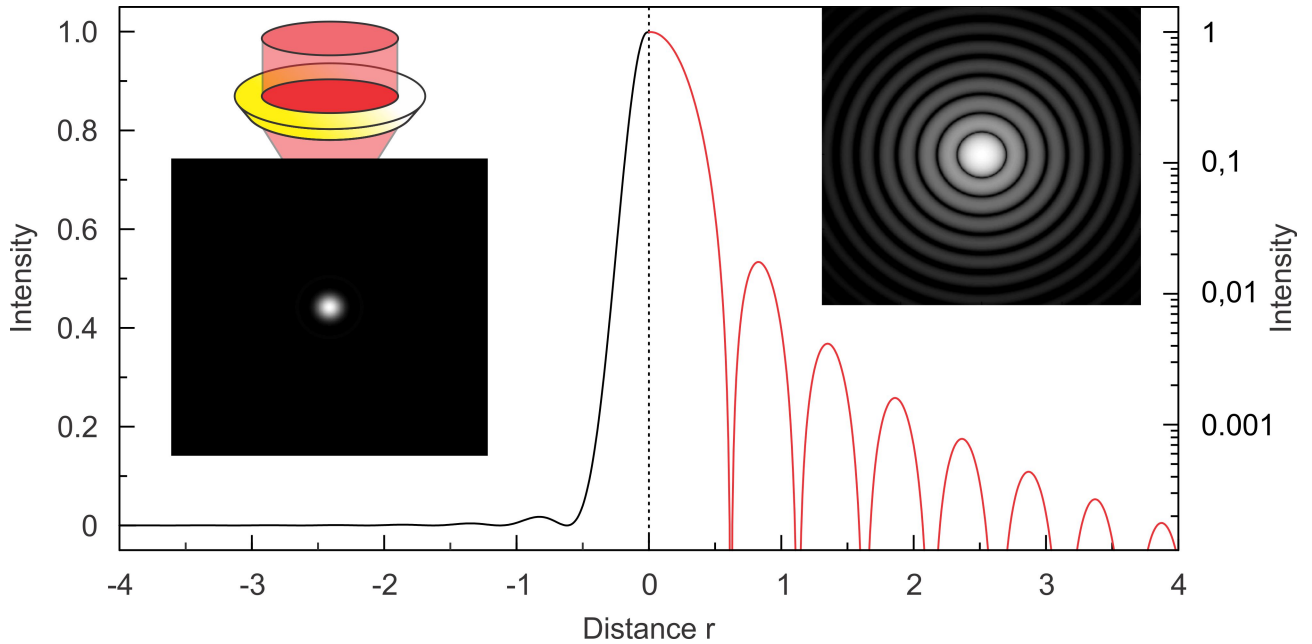
Figure 3.19.: ***Diffraction pattern as a result of focusing plane waves with a lens.*** *The black curve on the left hand side shows the light intensity (normalized to one) as a function of distance r from the center. The left inset depicts a two dimensional view. The intensity is color coded on a linear scale (black = zero, white = one). The logarithmic scale on the right hand side allows to visualize the low intensity side maxima. The color plot in the inset shows the center Airy disk surrounded by low and high intensity rings with decreasing intensity.*

where $NA = n \sin \alpha$ is the numerical aperture. It describes the ability of a lens to collect light. The angle α is half the opening angle of the collected light cone and n the refractive index of the material in between lens and sample. The first minimum of the Airy pattern appears at $r = 0.61$ and enters the equation above. Note that the second maximum has only 1.75% of the intensity compared to the main maximum. One possible way to define the spatial resolution is the Rayleigh criterion: Two points can just be resolved when the center of one Airy disk falls on the first minimum of the Airy pattern of the second point. Hence, the resolution depends on the used laser wavelength as well as on the NA of the lens and the refractive index. We typically use a wavelength of 488 nm and a lens with NA of 0.7 in our experiments. This results in a spatial resolution of 425 nm. Replacing the air in between the lens and the sample by for instance oil would improve the resolution below 300 nm. Extending the considerations for the x- and y-direction to the z-direction yields a full description of the diffraction pattern in all three dimensions via the point spread function PSF. A typical resolution in z-direction is about 1 μm. For our experiments on two-dimensional graphene this, however, does not play a role.

As a last point, we note that the PSF has to be applied to the incoming laser beam when focused by the lens as well as to the back-scattered light when collected by the lens. This twofold application of the PSF further improves the spatial resolution, the contrast and the signal-to-noise ratio. Compared to conventional optical microscopy the spatial resolution is improved by about 40%.
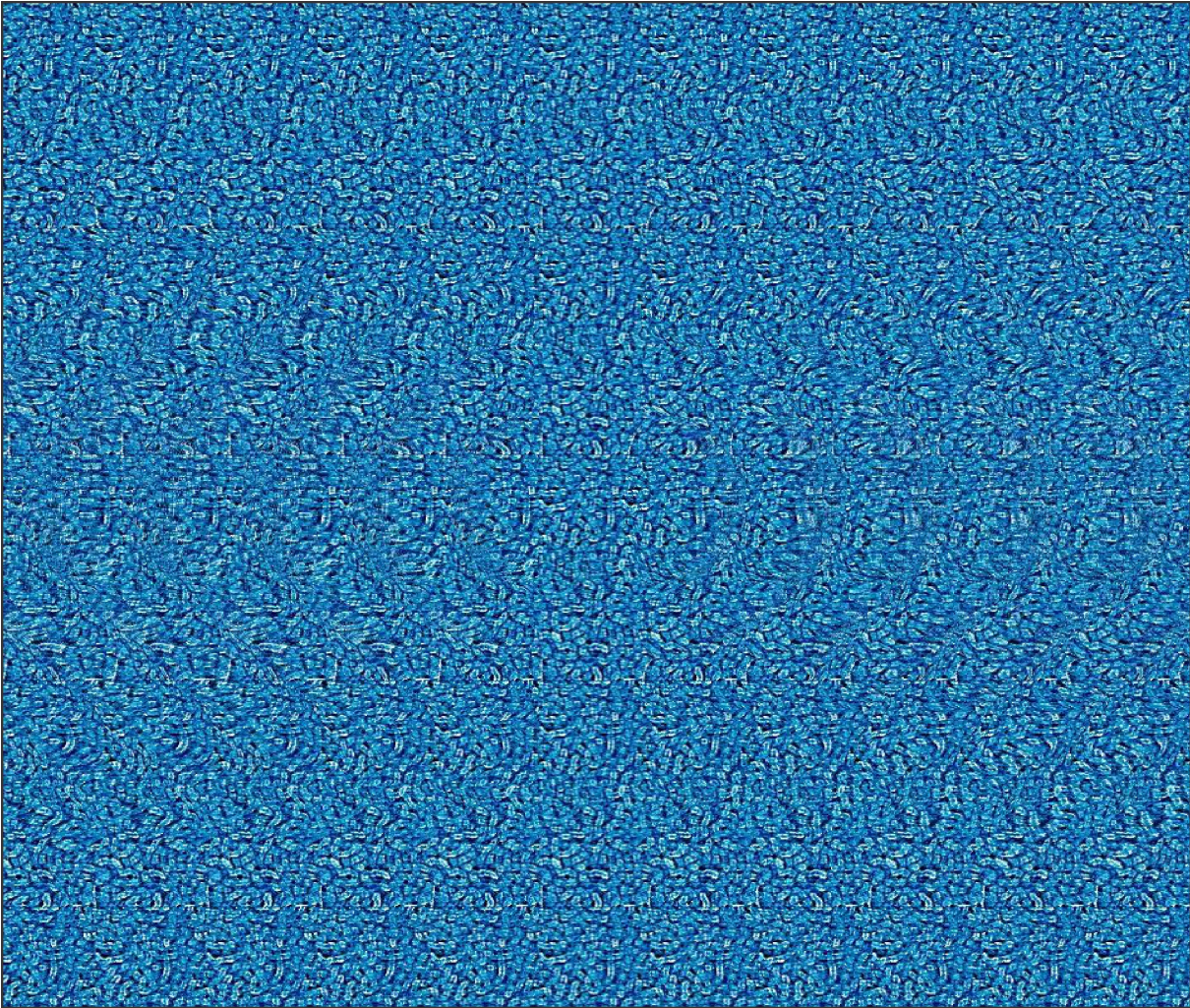
Figure 3.20.: *Three dimensional representation of the Airy diffraction pattern.*

3.3.1. Setup for scanning confocal microscope

The previous subsection introduced the basic theoretical aspects of confocal microscopy. This subsection deals with the experimental setup used in this thesis. One crucial ingredient for a scanning confocal microscope is the capability to realize a relative motion between stage and laser beam. This can either be accomplished by moving the sample stage underneath the fixed laser beam or by scanning the laser beam with respect to the stationary sample. Both motions are performed with piezo-crystals which change their shape when an external voltage is applied. The elongation of the piezo-crystal is capacitively monitored. With a feedback-loop it is possible to increase the spatial precision.
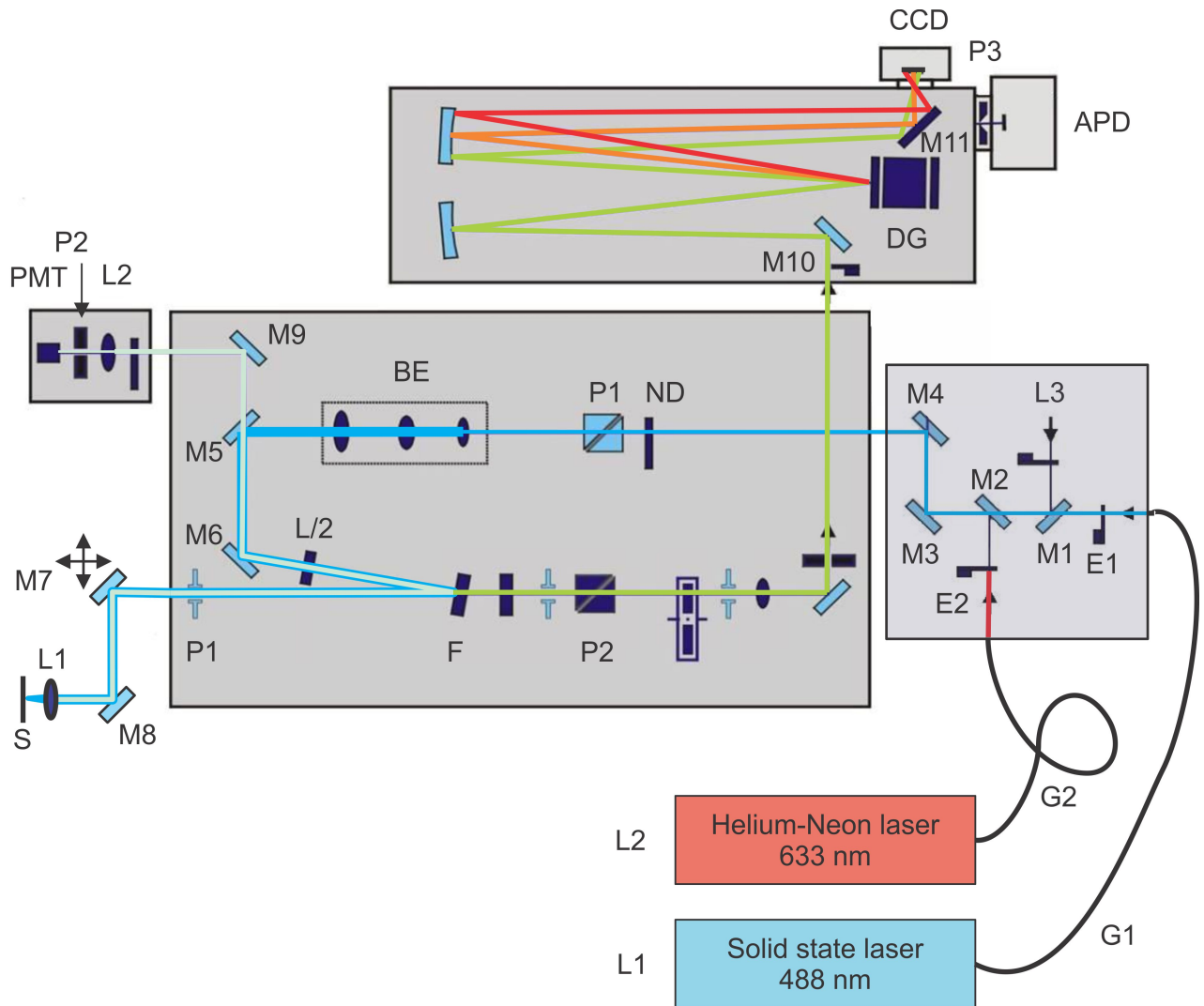
Figure 3.21.: ***Schematic of the optical setup for confocal laser scanning microscope and scanning confocal Raman spectroscopy.*** *Two lasers with different wavelengths can be used as a source. The elastically scattered Rayleigh light is detected with a PMT. The inelastically scattered Raman light is dispersed in a monochromator and the spectrum is acquired with a CCD. The confocal setup allows to obtain two-dimensional maps of the sample.*

The optical part of the setup is shown in Figure 3.21. Two lasers with 633 nm or 488 nm wavelength are coupled into the setup via glass fibers. Mirror M1 - M4 are used to overlay the two laser beams before their intensity is adjusted with a neutral density filter (ND). Subsequently, the polarization of the light can be adjusted to be, for instance, linearly or circularly polarized. The beam expander (BE) consists of a system of three lenses and is used to increase the diameter of the laser beam to exploit the full NA of the focusing lens (see Figure 3.18). This ensures the highest possible spatial resolution and intensity. The light is guided by mirrors M5 and M6 to a filter (F) which totally reflects light with either 488 nm or 633 nm wavelength. Finally, the light is guided through a pinhole P1 and focused onto the sample with lens L1. Mirror M7 can be moved in two orthogonal

directions so that the beam can be scanned with respect to the sample in the x- and y-direction. The back-scattered light (consisting out of Rayleigh and Raman scattered parts) is collected with lens L1. The filter F reflects the Rayleigh scattered light. This light subsequently is guided via several mirrors to lens L2, then through a pinhole P2 and finally it is detected with a photomultiplier tube (PMT). This completes the optical setup for the CSLM which detects light that is elastically scattered from the sample. In addition to this elastically scattered light, the sample emits inelastically scattered light (Raman light). It is also collected by lens L1. However, filter F (typically an edge or a nodge filter) is transparent for those wavelengths. The light is transmitted, its polarization analyzed (P2) and finally it passes through the spectrometer. The spectrometer consists of a rotatable diffraction grating with different numbers of lines per millimeter (l/mm) on each side. The number of lines per millimeter determines the spectral resolution as well as the bandwidth. The incoming beam is dispersed by the grating with angles depending on the frequency. The light is recorded using a Peltier cooled charge coupled device (CCD). This yields the Raman spectrum. Scanning the sample enables us to measure a complete Raman spectrum at each spatial point. Analyzing for instance the position or intensity of a certain peak allows to construct a two-dimensional map of the Raman features.

4. Scanning Single-Electron Transistor
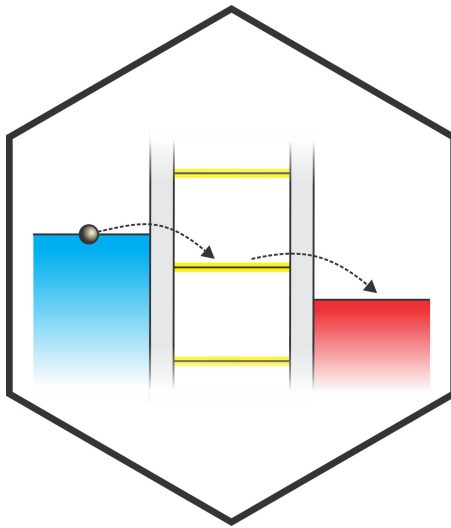
The fundamental building block in todays integrated circuits is the field-effect transistor (FET). A gate allows to control the density of charge carriers and hereby the conductivity of the region between source and drain. In contrast to an FET where many electrons may pass the device simultaneously, the single-electron transistor (SET) can be tuned in such a way that only one electron at a time passes through the device. The working principle of an SET relies on the discrete nature of charges. This causes the Coulomb blockade effect, which will be described below. First, we motivate why to measure the inverse compressibility and give its relation to the density of states and the Landau level spectrum. We show how the inverse compressibility can be measured with an SET. In a next step, we briefly describe the fabrication process of the SETs used in this work and the experimental setup. The experimental results obtained from a high quality suspended graphene monolayer in a scanning probe microscope (SPM) with an SET tip will be described in Chapter 10.

4.1. Inverse compressibility

The inverse compressibility (IC) χ^{-1} is a measure for the change in the chemical potential $\partial\mu^{ch}$ if the number of charge carriers n in the sample is changed by ∂n multiplied with n^2:

$$\chi^{-1} = n^2 \cdot \frac{\partial\mu^{ch}}{\partial n}$$

In a single particle approximation the compressibility χ is equal to the density of states (DOS). For instance, an insulator with a gap in its energy spectrum is completely incompressible, as the DOS in the gap is zero.

First, we schematically illustrate the relation between inverse compressibility (IC), chemical potential μ_{ch} and the underlying density of states (DOS) as well as the longitudinal (ρ_{xx}) and transversal resistance (ρ_{xy}) measured in transport experiments. The DOS in an applied external magnetic field is illustrated in Figure 4.1 (a). It exhibits Landau levels (LLs, see Section 2.5) with the related monolayer filling factors at $\nu = 2$, 6 and 10 lying in between the LL. The expected longitudinal resistance is schematically drawn in Figure 4.1 (b) and shows Shubnikov-de Haas peaks at positions where a high DOS is present. In between two adjacent LLs the longitudinal resistance is zero whereas the transversal resistance displays plateaus with values quantized in units of e^2/h. The jump from one plateau to another occurs in regions with a high DOS. The chemical potential (Figure 4.1 (c)) is constant while the LL is being filled and jumps to a higher value once a LL is completely filled. The jump in chemical potential is equal to the energy gap between the two corresponding LLs. The derivative of the chemical potential with respect to the carrier density finally yields the inverse compressibility shown in Figure 4.1 (d). Incompressible behavior occurs in between the LLs at filling factors $\nu = 2$, 6 and 10 and consequently are a convenient way to measure quantum Hall states.

Above we introduced the inverse compressibility as a measure for the change in chemical potential if the number of charge carriers is changed. Changing the carrier density is possible as described in Section 2.8. However, we cannot measure the chemical potential directly. We bypass this problem as shown in the next Subsection.

4.1.1. Local chemical potential

In thermodynamic equilibrium the sum of the chemical potential μ^{ch} and the local electrostatic potential φ equals the electrochemical potential μ^{elch}. The electrochemical potential is determined by the voltage applied to the graphene sample. If we keep this voltage constant any change in the chemical potential $\Delta\mu^{ch}$ is compensated by an equal but opposite change in the electrostatic potential $\Delta\varphi$

$$e \cdot \Delta\varphi = -\Delta\mu^{ch}$$

Using this relation we transform our problem of measuring the IC to the much easier task of measuring the local electrostatic potential. Here, we use an SET as an electrometer with a very high sensitivity. We describe its working principle next.
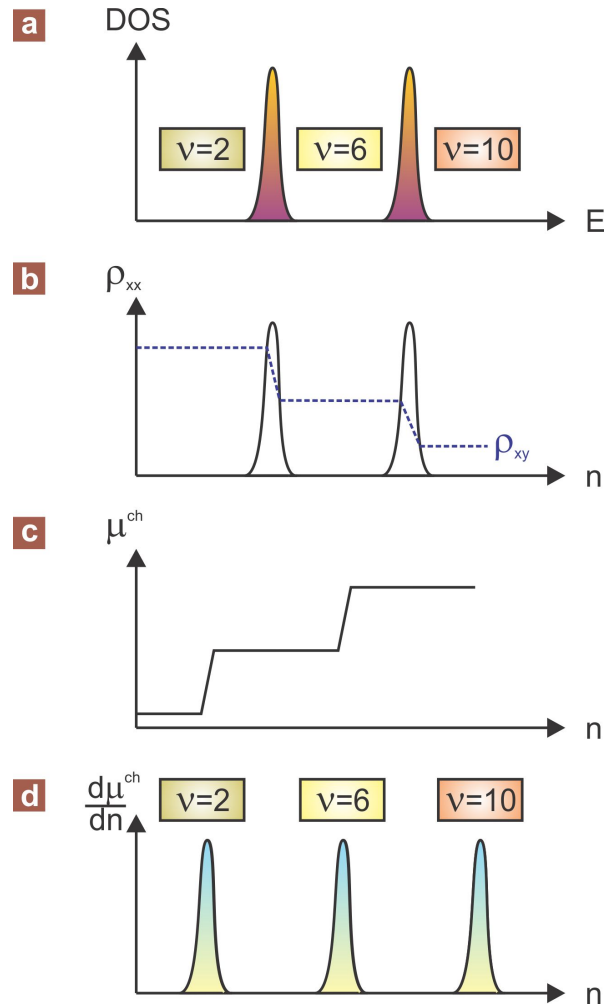
Figure 4.1.: ***Relation between (a) density of states (DOS), (b) longitudinal and transversal resistance, (c) chemical potential and (d) inverse compressibility.*** *The filling factors 2, 6, 10 etc. are situated in between the regions of high DOS (LLs). At these fillings plateaus appear in ρ_{xy} and ρ_{xx} vanishes. The chemical potential (c) jumps when a LL gets completely filled and the system becomes incompressible (d).*

4.2. Single-electron transistor

The SET used in this work consists of a small metallic island which is capacitively coupled to two metallic leads (called source and drain) through tunnel junctions. Figure 4.2 (a) and (b) sketch the basic elements of an SET and the corresponding electric circuit diagram. Given a fixed bias between source and drain, the amount of current that flows through the device is set by the electrostatic potential of the island. This potential can be influenced by a gate that couples capacitively to the island. In the experiment described below the graphene itself will be used as the gate.

In order to add an electron to the neutral island a certain charging energy E_{charge} has
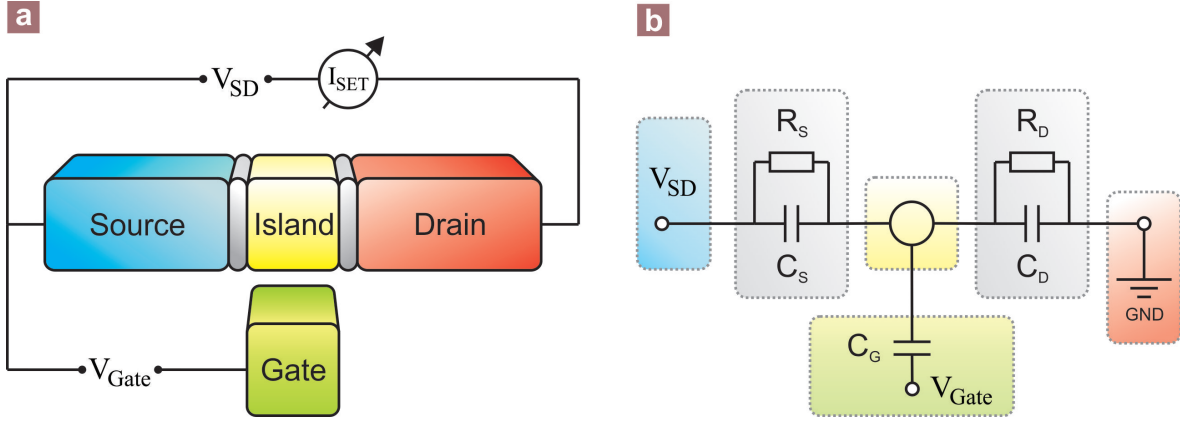
Figure 4.2.: *(a)* ***The basic elements of an SET.*** *Metallic source (blue) and drain (red) contacts are connected to a small metallic island (yellow) via tunnel barriers (grey regions). The tunnel junctions are represented in the electric circuit (diagram (b)) by an effective resistance R and a capacitance C in parallel. The capacitive coupling of the gate modifies the internal levels of the island.*

to be payed due to the capacitive coupling of the island to the source, drain and gate:

$$E_{charge} = \frac{e^2}{2C}.$$

Here, $C = C_S + C_D + C_G$ where C_S, C_D and C_G are the capacitances between island - source, island - drain and island - gate, respectively. The same energy E_{charge} is needed in order to extract one electron from the neutral island and hence the allowed states on the island can be described by a ladder of discrete levels. The energy diagram is displayed in Figure 4.3.
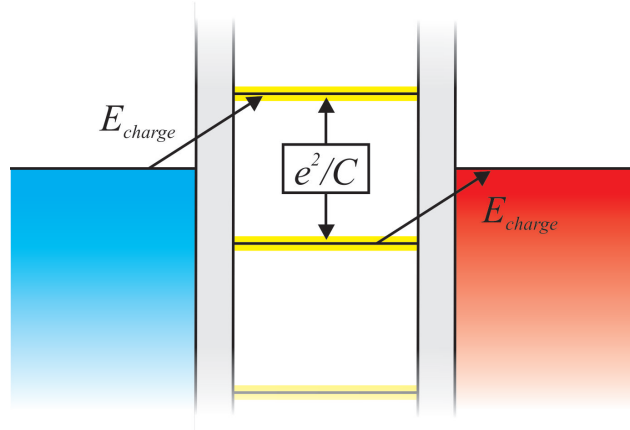
Figure 4.3.: ***Energy diagram for adding or extracting an electron to/from the island.*** *The energy spacing between adjacent states is twice the charging energy and we can describe this by a ladder of discrete states on the island.*

The charging energy only plays a role if it is larger than the thermal energy of the electrons ($E_{charge} > E_T = k_B T$ with k_B being the Boltzmann constant and T the temperature). In this case, tunneling is suppressed if the next available energy state in the island

is higher in energy than the electrochemical potential of the electrodes. By shrinking the size of the tunnel barriers the source and drain capacitance can be reduced and hence the charging energy increased. Note, that the tunnel resistance depends exponentially on the thickness of the tunnel barriers whereas the capacitance only linear. The capacitance of the tunnel barriers is also defined by their area.

In order for a current to flow through the SET, an electron has to jump from one lead to the island and subsequently to the other lead. Figure 4.4 (a) shows an example where this process is energetically forbidden. No current flows in this case despite the applied source-drain bias. This suppression of the current is referred to as Coulomb blockade effect.
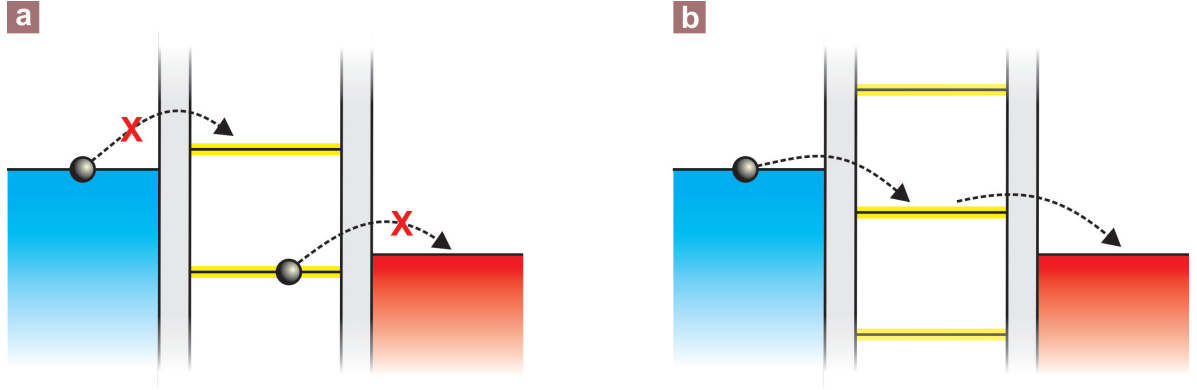
Figure 4.4.: *Schematic level diagram for forbidden (a) and allowed (b) electron transport through the island leading to the Coulomb blockade oscillations.* (a) The energy of the electron on the blue side is not sufficient to populate the next available state on the island. Simultaneously, no electron from a lower lying state can leave the island due to the lack of energy. Hence no current flows through the SET (Coulomb blockade). If, however, the ladder of discrete states is shifted by applying a gate bias, it becomes possible for an electron to flow from the blue to the red lead via the island (b).

However, the electrostatic potential of the gate can be tuned such that the energies of the states on the island with N and $N+1$ electrons are degenerate. N or $N+1$ electrons on the island are equally likely and the charge on the island can fluctuate. Consequently, current can flow. Whether current can flow through the SET or not sensitively depends on the electrostatic gate potential (Coulomb blockade oscillations, CBO). We utilize this fact by employing the graphene sample itself as a gate: Changes in the current through the SET are monitored and by knowing its dependence on the gate potential we can directly read out the electrostatic potential underneath the SET tip. Figure 4.5 summarizes the charge transport through an SET and shows the full charge stability diagram in (a) when varying both source-drain and gate bias. The patterns are referred to as Coulomb diamonds and the capacitances C and C_G can be determined from the diamond size as indicated in the figure.

Figure 4.5 (c) shows an energy diagram where N or $N-1$ electrons can occupy the island (see Figure 4.5 (a)) and hence current flows. The corresponding linear I_{SET}-V_{SD}-curve is given in (e) and leads to a maximum in the CBO illustrated by the red dot in (b). When changing the gate voltage eventually only N electrons can be on the island
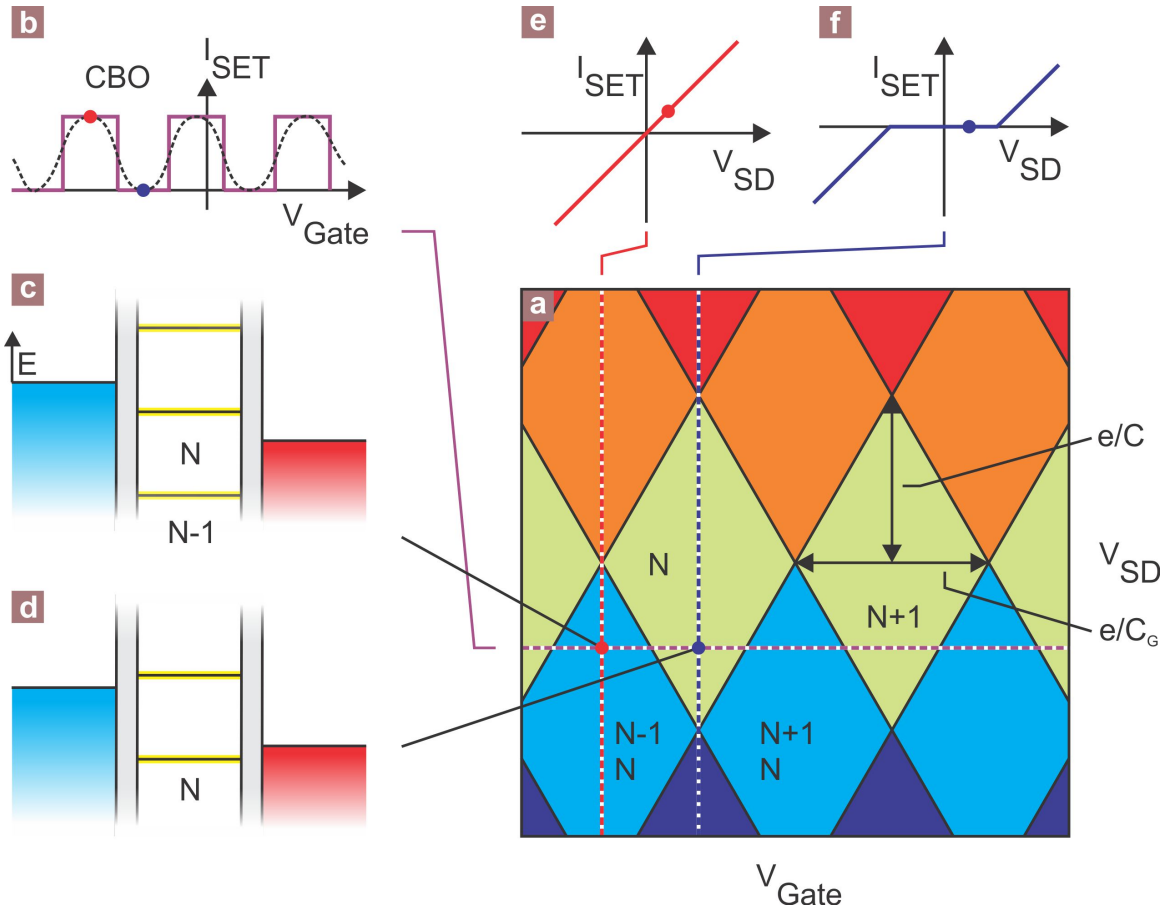
Figure 4.5.: *Charge transport through an SET and full charge stability diagram.* *(a) The SET current as a function of gate V_{Gate} and source - drain bias V_{SD}. Two distinguished points at fixed V_{SD} and V_{Gate} where charge transfer is allowed (c) and forbidden (d) are tagged at the corresponding positions in (a). A cross section at fixed V_{SD} intersecting these points is depicted in (b) and shows the CBOs. The dashed line is a more realistic trace including thermal smearing. Cuts along fixed V_{Gate} can feature linear IV characteristic (e) or show regions of suppressed current (f).*

(d). In this case the $I_{SET}V_{SD}$-curve (f) has a flat region and no current can flow through the SET (Coulomb blockade). This regime is exemplified by the blue dot in (b).

Now that we have established how the SET can serve as a very sensitive electrometer, we come back to our original idea to use the SET in order to determine the inverse compressibility, which is closely linked to the screening capability of the electrons. If the compressibility of a system is large, it is able to screen well an applied backgate voltage. An SET placed on top will not be affected by the field generated with the backgate. The opposite holds, if the electronic system turns incompressible. We introduce a small carrier density change in graphene by applying a backgate voltage V_{BG} and then measure the resulting change in the current through the SET. The factor, to normalize the obtained current with the gain can be measured simultaneously by introducing a second small voltage modulation directly to the graphene sample and again measure the

resulting change in SET current. For convenience we drop the prefactor n^2 in the inverse compressibility χ^{-1} and find:

$$\chi^{-1} = \frac{\partial\mu^{ch}}{\partial n} \overset{(1)}{=} \frac{\partial\mu^{ch}}{\partial V_{BG} \cdot C_{eff}} \overset{(2)}{=} -\frac{e \cdot \partial\varphi}{\partial V_{BG} \cdot C_{eff}} \overset{(3)}{=} -\frac{e \cdot \partial I_{SET}^{V_{BG}}/a}{\partial V_{BG} \cdot C_{eff}} \overset{(4)}{=} -\frac{e \cdot \partial I_{SET}^{V_{BG}}}{\partial V_{BG} \cdot C_{eff}} \cdot \frac{\partial V_{2D}}{\partial I_{SET}^{2D}}$$

1. A change of the carrier density in the graphene sample ∂n is induced by wiggling the backgate voltage with an amplitude ∂V_{BG} at a fixed frequency $f_{V_{BG}}$. The relation between the applied voltage and the resulting change in density is given in Section 2.8:
   $\partial n = \partial V_{BG} \cdot C_{eff}$.

2. As discussed in 4.1.1, any change in the chemical potential $\Delta\mu^{ch}$ is compensated by an equal but opposite change in the electrostatic potential $\Delta\varphi$:
   $\Delta\mu^{ch} = -e \cdot \Delta\varphi$.

3. A change in the electrostatic potential $\Delta\varphi$ is mirrored in the current through the SET:
   $\Delta\varphi = \partial I_{SET}^{V_{BG}}/a$
   where a is the local slope of the CBO.

4. This local slope of the CBO can be simultaneously determined by wiggling the electrochemical potential of the graphene sample with an amplitude ∂V_{2D} at a second incommensurate fixed frequency $f_{V_{2D}}$ and measuring the resulting ac current through the SET at this frequency.
   $a = \frac{\partial I_{SET}^{2D}}{\partial V_{2D}}$

In summary, the inverse compressibility is calculated from

$$\chi^{-1} = -\frac{e}{C_{eff}} \cdot \frac{\partial V_{2D}}{\partial V_{BG}} \cdot \frac{\partial I_{SET}^{V_{BG}}}{\partial I_{SET}^{2D}}$$

The electrical measurement setup to extract the IC is given in Figure 4.6. For the measurements shown in this thesis we used the following values for the ac modulation frequencies: $f_{V_{BG}} = 77.05$ Hz and $f_{V_{2D}} = 42.05$ Hz. Further details concerning the scanning SET setup can be found in Ref [96].

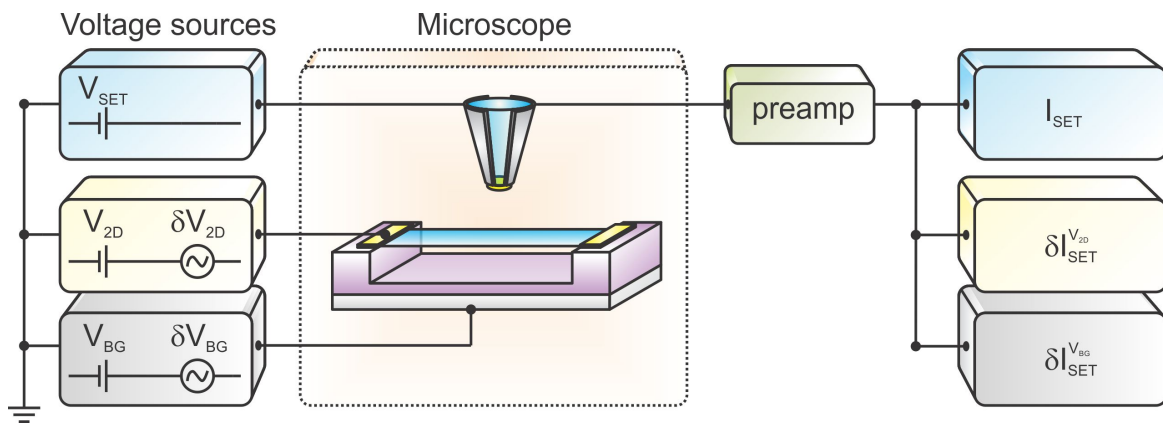**Figure 4.6.**: **Setup for measuring the chemical potential and inverse compressibility.** *The carrier density is modulated with a periodic voltage applied to the backgate. The resulting change in current through the SET is measured with a lock-in. In parallel the sensitivity of the SET is measured with a second periodic voltage applied to the graphene and detected in the SET current with a second lock-in.*

4.3. Experimental setup

In this section we will briefly describe the experimental setup, starting from the fabrication of the smallest part, the SET tip, and zooming out until the whole system is assembled.

4.3.1. SET fabrication

The SET is fabricated at the end of a tapered quartz rod as this geometry is well suited for scanning probe experiments. Quartz has a low thermal expansion coefficient, it is easy to handle and it is rather rigid. The tapered quartz rods are fabricated by clamping a glass fiber onto two puller bars of a fiber puller, heating the center area with a laser beam with a specific power and applying a certain pulling force to both puller bars. Eventually, the fiber is ripped apart and two conical tips are formed at either end. Further details and parameters are described in [96]. In the next step, the metals constituting the SET (source, drain and island) are evaporated under UHV conditions. The evaporation is done in three steps from different angles as elucidated in Figure 4.7. The tip holder is built to allow the rotation of two axis and the angular adjustment can be verified with a laser diode. Additionally, the resistance between the source and drain contacts can be measured in situ.
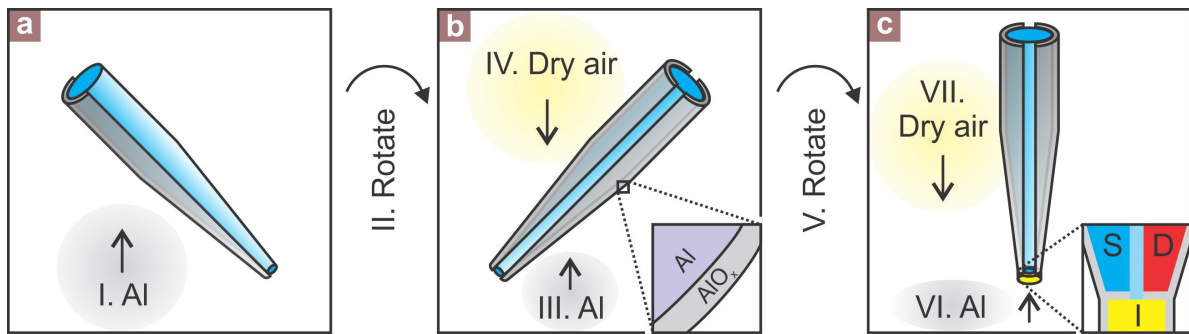
Figure 4.7.: **Scheme of three angle evaporation and oxidation to form an SET tip.** *After evaporation of the first layer of aluminum (Al) (a) the tip is rotated and a second layer of aluminum (b) is evaporated on the other side of the quartz taper followed by an oxidization step in which the surface of the aluminum is oxidized (inset in (b)). Subsequent to a second rotation a third structure is evaporated (c), again followed by an oxidization step. The inset shows how the evaporated structure makes up the different elements of an SET, namely source S and drain D coupled by a tunnel junction to the island I.*

In the following we give some details on the individual process steps.

1. The first electrode of aluminum (e.g. source) (thickness $\approx$ 16 nm) is evaporated under a certain angle as shown in Figure 4.7 (a) once the vacuum reaches the 10^{-7} mbar range. The evaporation rate is 0.2 nm/s.

2. The second electrode (e.g. drain) is evaporated after rotating the tip holder (see Figure 4.7 (b)). Again 16 nm of aluminum is evaporated with a rate of 0.2 nm/s.

3. After a certain cool down time, the vacuum chamber is filled with dry air until a pressure of approximately $2 \cdot 10^{-1}$ mbar is reached. Within the next 30 seconds the aluminum is oxidized to aluminum oxide as illustrated in the inset of Figure 4.7 (b). Different from aluminum, which is a metal (superconducting at low temperatures), aluminum oxide is an insulator. After these 30 seconds the evaporation chamber is evacuated again.

4. The last evaporation step is used to create the island of the SET. Therefore, the tip is aligned parallel to the evaporation beam as shown in Figure 4.7 (c). The evaporation rate is increased to 0.4 nm/s and 6 nm aluminum is evaporated on the tip. From now on it is crucial that the SET tip is grounded at any time unless the resistance is to be measured.

5. The final step again is the oxidization of aluminum with dry air.

It can be seen from the inset in Figure 4.7 (c) how the end of the tapered fiber constitutes an SET as introduced above and in Figure 4.2. The resistance of the SET should be in the range of 100 $k\Omega$ at room temperature. The tip is now all set to be mounted in the tip holder. In order to confirm that the fabricated tip really works as an SET we measure the transport characteristics in the cryostat at base temperature. Figure 4.8 shows a representative example of the SET current I_{SET} when sweeping the gate voltage V_{Gate} over a wide voltage range. Several CBOs are visible. The measured full SET characteristics as depicted in Figure 4.9 (c) features characteristic Coulomb diamonds and fits to the theoretical expectation (a). The regions where Coulomb blockade governs is easily discernible in the three dimensional representation in Figure 4.9 (b) as flat zero current regions. For the sake of completeness cross sections at certain source-drain biases are depicted in Figure 4.9 (d). As discussed above, it is this sensitive dependence of the SET current on the gate potential (visible in (d)) that we will exploit in order to extract the inverse compressibility.
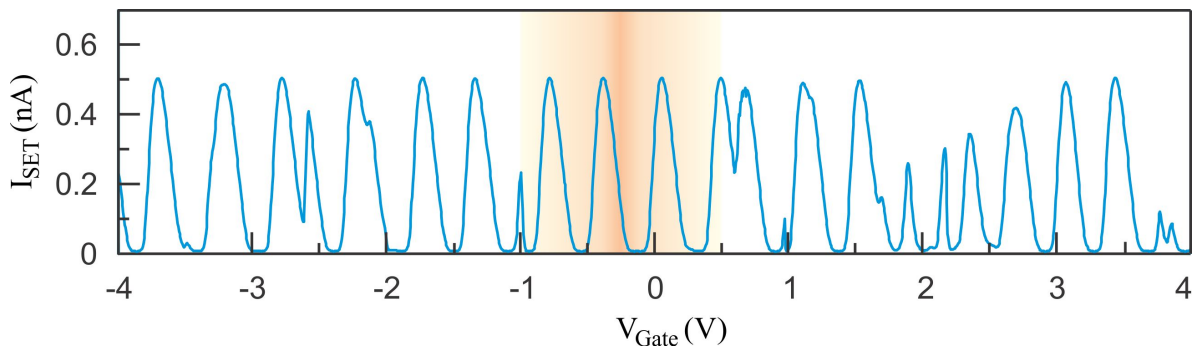
Figure 4.8.: *Coulomb blockade oscillations of an SET tip measured at base temperature when sweeping back-gate voltage.* *The CBOs confirm the existence of an SET at the end of the tapered quartz as desired. A full characterization of the highlighted region is shown in Figure 4.9.*
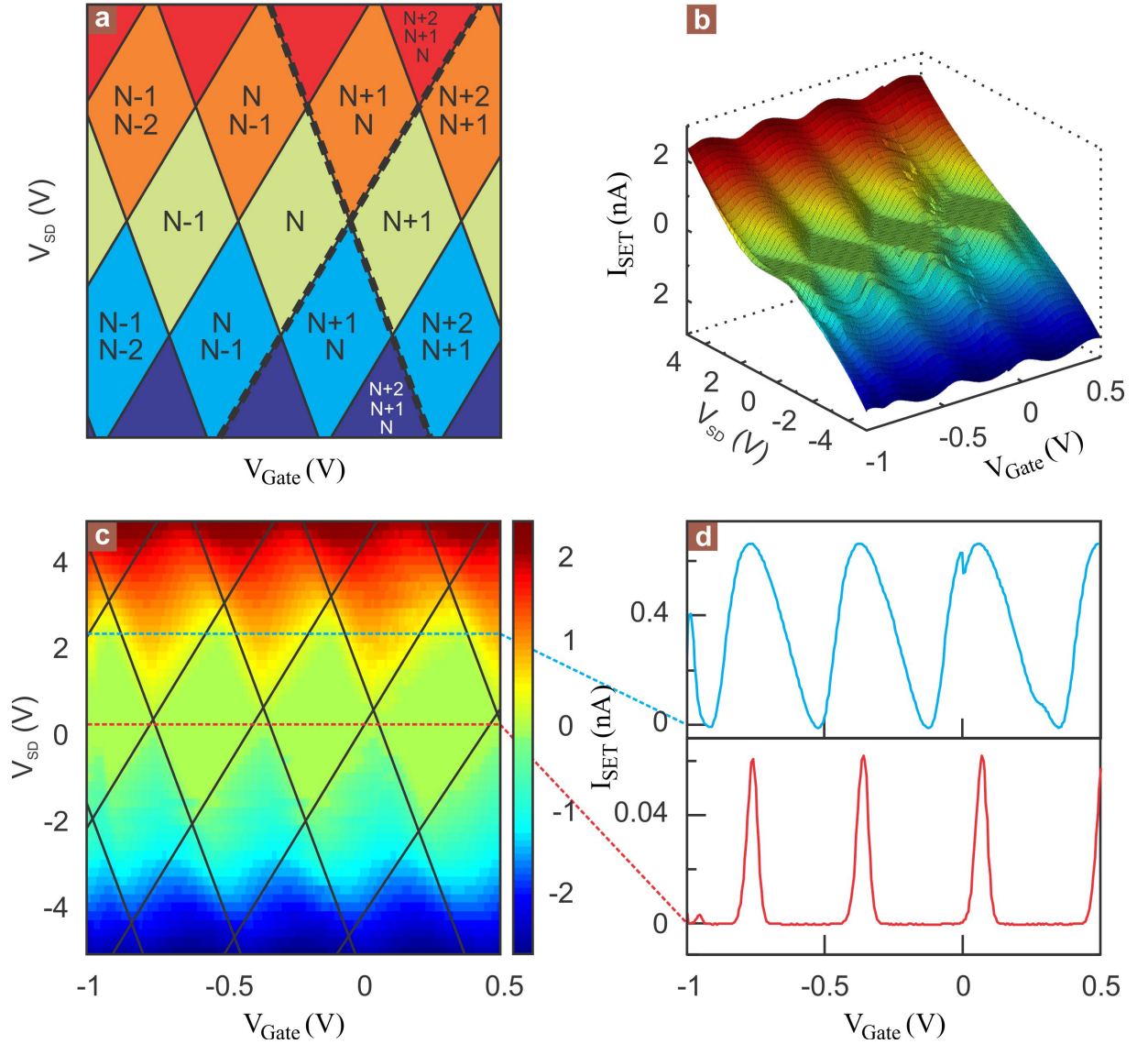
Figure 4.9.: *Full charge stability diagram of the tip exhibiting the characteristic SET features. The theoretical model in (a) describes well the measured SET current color coded in (c) and (b) as a function of gate and source-drain bias. CBOs like those shown in (d) will be used to measure the inverse compressibility.*

4.3.2. Microscope setup

Figure 4.10 (a) shows an optical image of the tip holder in which the SET tip is mounted. The tip holder itself is mounted at the lower end of a sample rod (Figure 4.10 (c)) and is movable in x- and y-direction by means of stick-slip motion. This coarse motion allows to move the tip with respect to the sample in the range of up to millimeters. The graphene sample is fixed on top of the sample holder illustrated in Figure 4.10 (b). The sample holder provides the electrical connections to the system as well as a coarse motion in z-direction (blue piezo stacks). Furthermore, it contains a piezo tube enabling the fine motion in all three directions for the scanning probe measurements. After being equipped
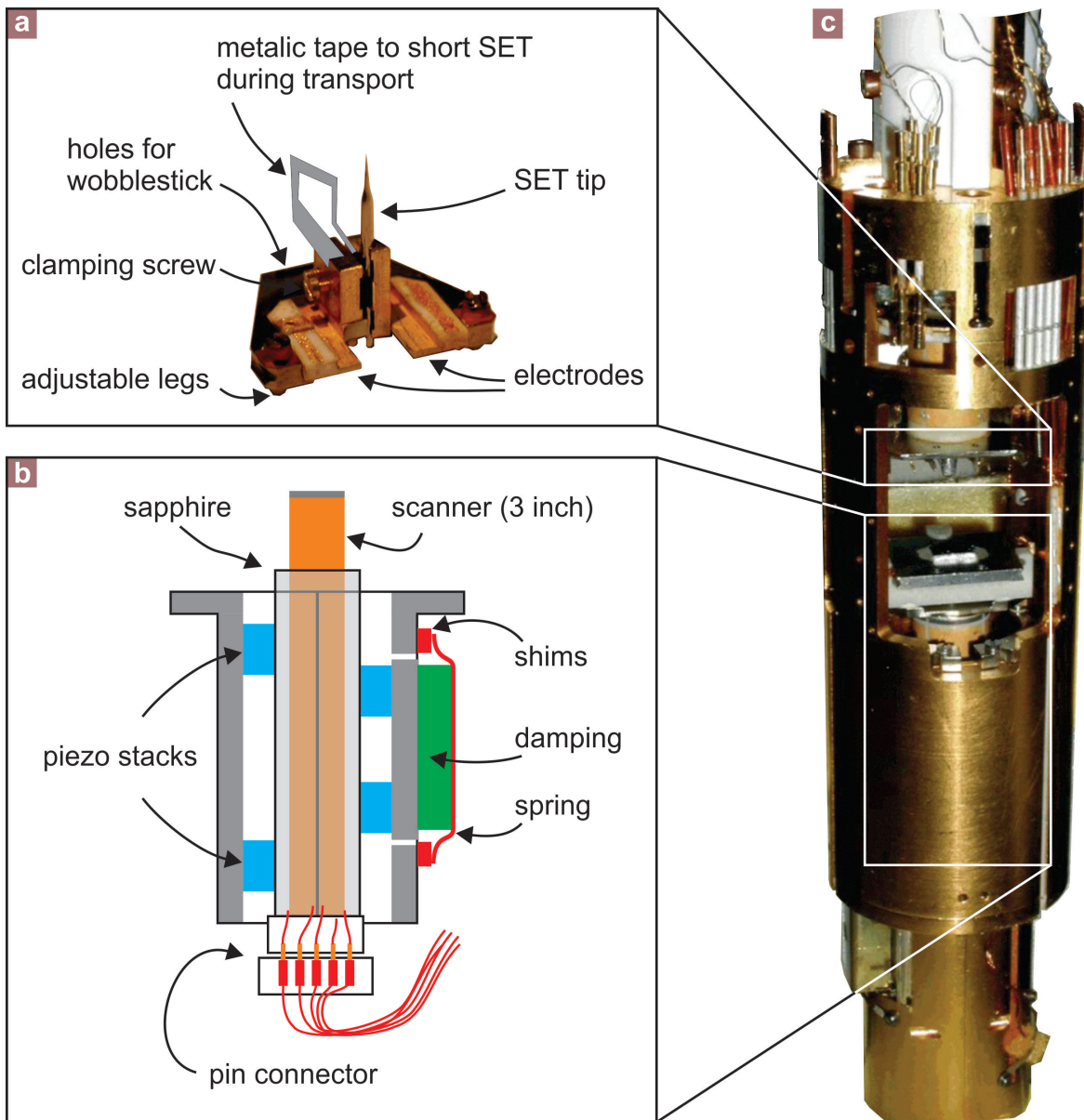
Figure 4.10.: *The scanning part of the microscope is located at the lower end of a sample rod. The tip holder (a) fastens the tip and provides electrical contacts to source and drain. Furthermore it allows the coarse motion in x- and y-direction. The graphene sample is connected to the sample holder (b) which allows coarse motion in z-direction as well as fine motion in all three dimensions. Additionally it provides the electrical contacts to the graphene sample. Tip and sample holder are both located at the end of the sample rod (c) and are lowered into a ^{3}He fridge.*

with the graphene sample and the tip, the whole sample rod is lowered into a ^{3}He fridge with a base temperature of approximately 450 mK and a magnetic field up to 12 Tesla. A schematic of the fridge and the exterior is shown in Figure 4.11.

In order to perform scanning probe measurements it is crucial to damp vibrations. Although due to the large tip-sample distance (typically 50 nm - 100 nm) SET measurements are in principle less sensitive to vibrations (compared to for instance AFM or STM) the
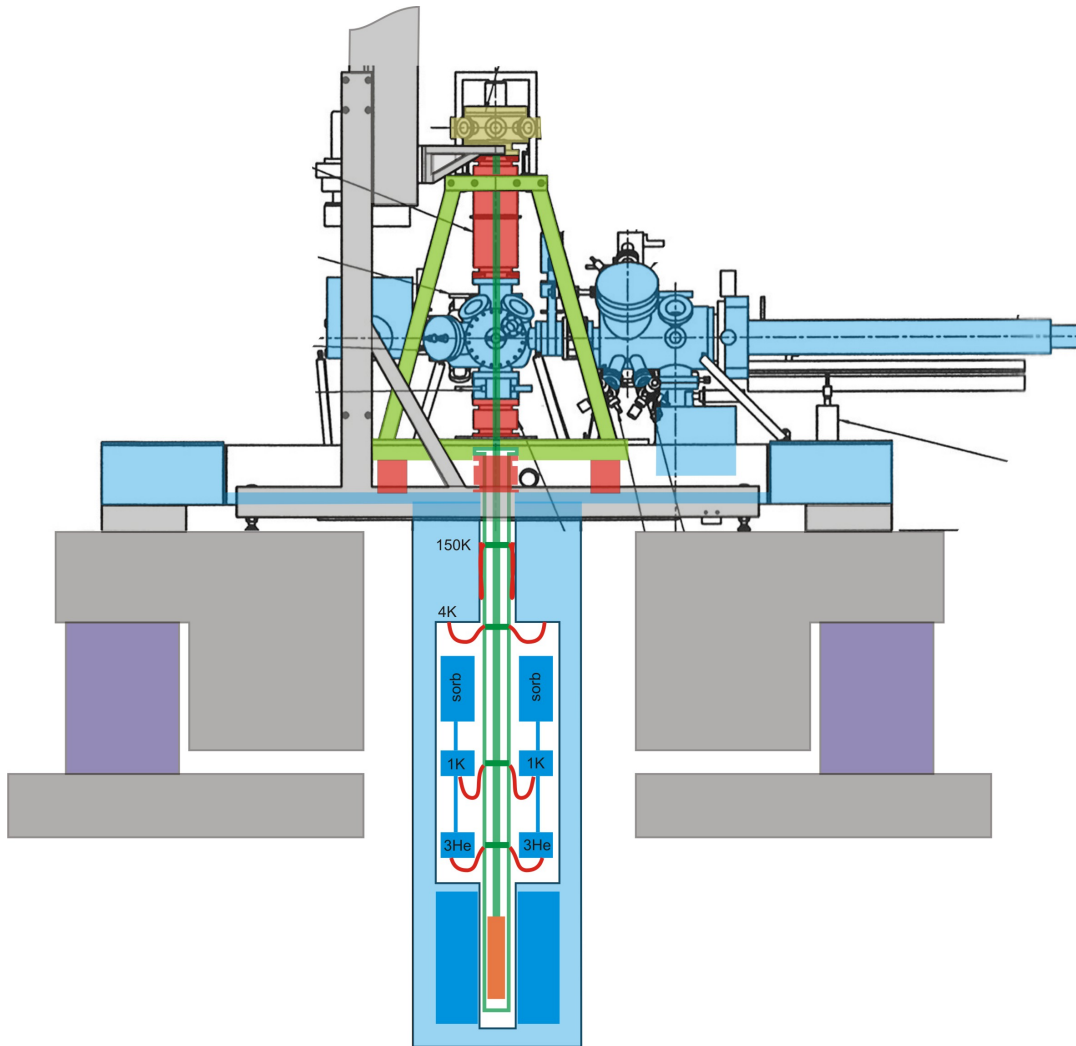
Figure 4.11.: ***Schematic of the experimental setup.*** *The scanning probe micro-scope part at the end of the sample rod is lowered into a ^3He fridge. The transfer chamber provides UHV conditions. Several active and passive dampening frames are deployed as well as a massive concrete stage to prevent vibrations and possible crashes of the SET tip into the graphene sample.*

lack of an active height feedback mechanism requires a low level of vibrations to keep the tip in a safe distance away from the sample. Therefore, the whole system is fixed on a massive concrete block and is equipped with three active and passive vibration dampening frames. Some pictures of the setup are shown in Figure 4.12. For further details (and there are many) we refer to [96].

4.3.3. Approach

Before we can start to measure, for instance, the inverse compressibility we have to po-sition the SET tip typically 50 nm above the graphene sample. The approach procedure consist of four parts:
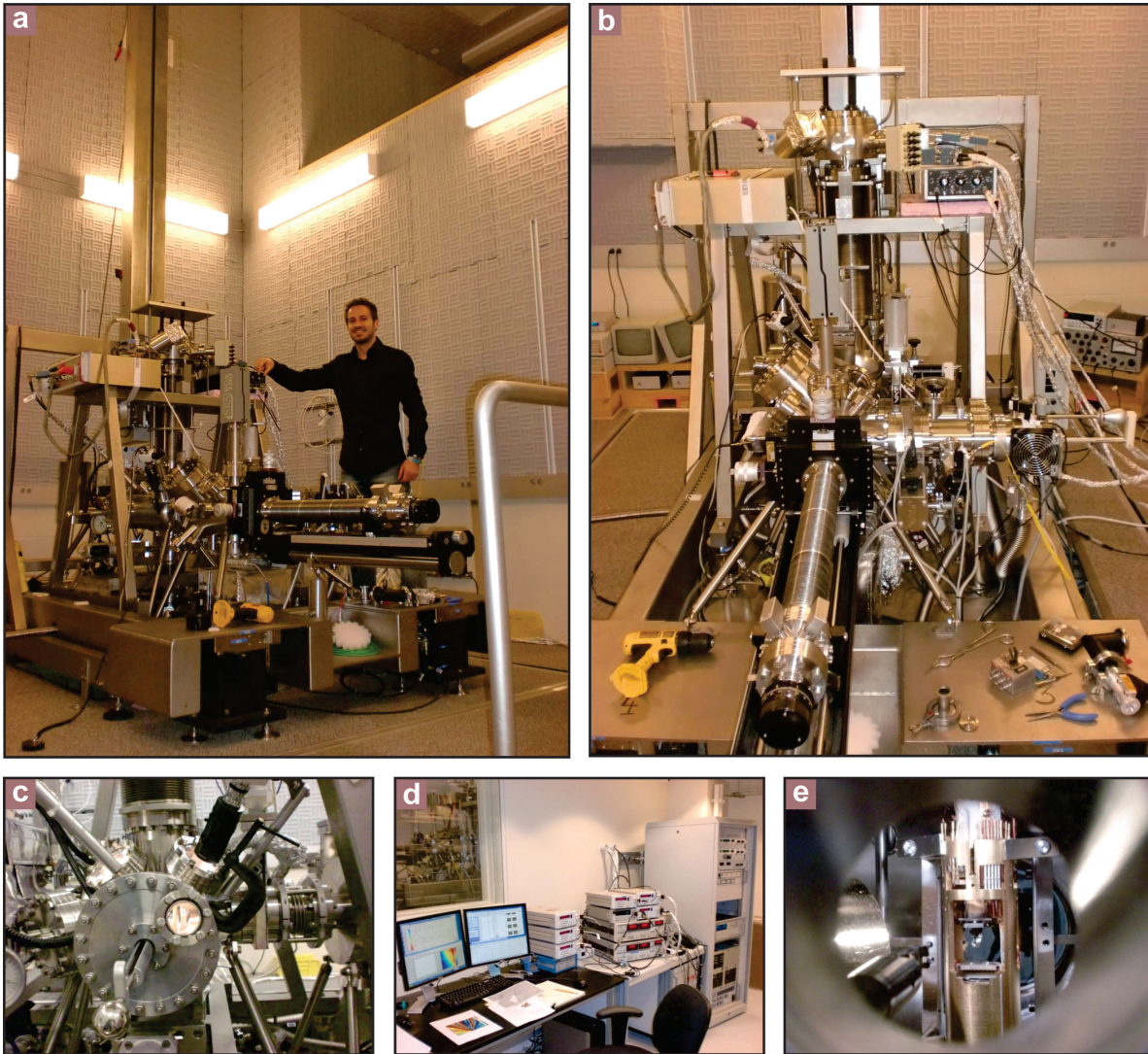
Figure 4.12.: *Optical images of the scanning SET setup. The upper part of the scanning probe microscope is shown in (a) and (b). The fridge is located underneath those parts and not visible here. The control room (d) is separated from the microscope in order to avoid vibrations. The lower part of the sample rod as described in Figure 4.10 is visible in (e).*

1. Coarse positioning of the SET tip in close vicinity of few micrometer to the graphene sample in x-, y- and z-direction.

2. Approaching the tip to the surface (z-direction).

3. Finding the flake in x- and y-direction.

4. Fine positioning of the tip above the graphene sample and adjusting local coordinates.

1) Coarse positioning of the SET: The coarse positioning of the SET tip can be done at room temperature (sample rod lifted out of the fridge) with an optical microscope

when the SET tip is still far away from the surface. The reflection of the SET tip at the SiO_2 surface (see Figure 4.13) is used to determine the position of the tip it will have after approaching. Note that the position in x- and y-direction as well as in z-direction will change while cooling down. Therefore, it is important not to approach too close to the surface yet as a crash would destroy the SET. Next, the sample rod is lowered into the fridge and cooled down to base temperature.
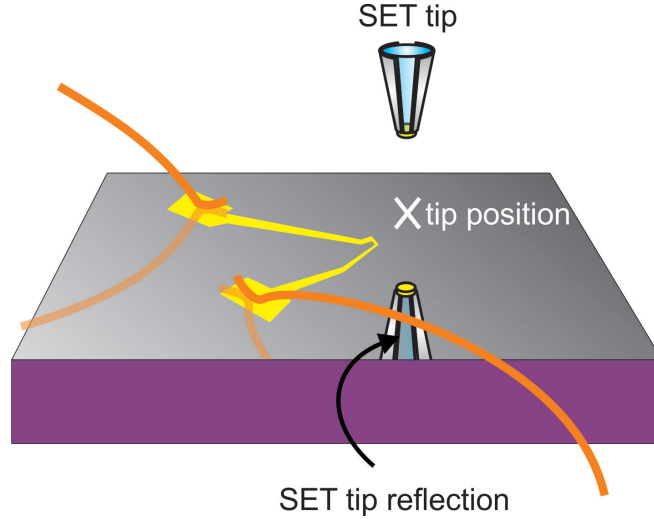
Figure 4.13.: ***Coarse positioning of the SET tip in close vicinity to the graphene sample at room temperature.*** *The reflection of the tip at the SiO_2 surface is monitored with an optical camera and used to assess the position of the tip relative to the sample after approaching.*

2) Approaching the tip to the surface: We need to determine the distance between the tip and the sample. Once the system reached base temperature it is possible to record Coulomb blockade oscillations which provide a measure for the tip-sample distance: The period between adjacent CBO peaks when sweeping the V_{Gate} bias is given by the effective capacitive coupling C_{eff} to the gate:

$$\Delta V_{Gate} = \frac{e}{C_{eff}}$$

Assuming a parallel-plate capacitor for the tip-sample system is a reasonable ansatz. The capacity C_G then depends inverse of the tip-sample distance d

$$C_G \propto \frac{1}{d}$$

Including an unknown capacitive coupling to the environment C_0 as a capacity in parallel to C_G finally allows to extract the real distance between tip and sample. Figure 4.14 (a) clarifies the procedure by showing the current through the SET as a function of back-gate bias V_{Gate} (CBO) and z piezo voltage. The piezo voltage translates into a well defined change in tip - sample distance (1V = 45 nm) where a higher piezo voltage means
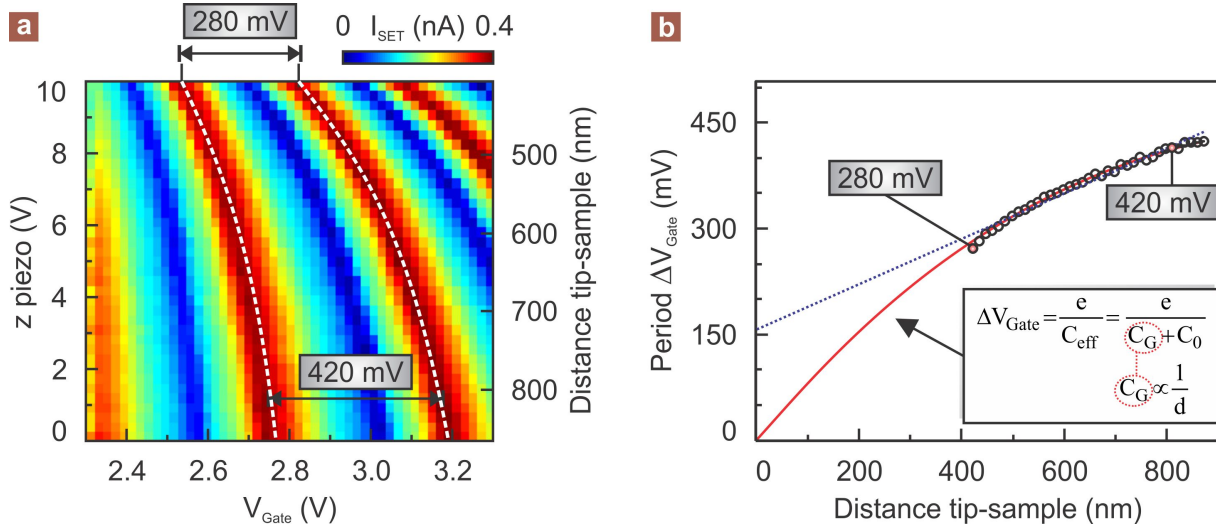
Figure 4.14.: *Determining the tip-sample distance.* *(a) The color coded SET current as a function of backgate bias and voltage at the piezo (higher voltage means that the tip is closer to the sample) shows a decrease in CBO period when approaching the sample. Tracing the CBO peaks allows to extract the CBO period as a function of tip sample distance (b). A best fit to this curve using a parallel-plate capacitor model (see text) reveals the real tip-sample distance.*

a smaller distance. However, the offset is so far unknown. Reducing the distance between tip and sample (applying a positive piezo voltage) leads to a reduction in the CBO period as apparent from Figure 4.14 (a). This change in period with reducing distance can be traced by following the CBO peaks as exemplified by the white dashed lines and is summarized in Figure 4.14 (b) by the encircled data points. A best fit to the data with the model described above (red line) finally allows to extract the real distance between tip and sample by associating zero period with zero distance. The algorithm now consists of iteratively measuring the tip sample distance and approaching closer to the surface with stick-slip motion until the desired distance of 50 nm - 100 nm is reached.

3) Finding the flake: Once the tip is approached close enough to the surface it is possible to acquire surface potential maps. Random potential variations due to contaminations are convenient because they allow to orient oneself. With coarse stick-slip motion one moves in the direction of the graphene sample and navigates in a controlled manner. In order to work out in which direction we have to move we exploited the so called "needle scan": Figure 4.15 depicts two examples of needle scans where the current through the SET is color coded as a function of applied back-gate bias V_{BG} and sample bias V_{Sample}, one far away from the sample and the connecting contacts (a) the other one close to the sample (b). If the graphene sample is far away from the tip, the applied sample bias will only have a minor influence on the SET current as visible in (a). If the tip on the other hand is in close proximity to the sample or even above it the SET current will also strongly be influenced by the sample bias as discernible in Figure 4.15 (b). Obtaining four of those needle scans, one at each corner of the scan window finally will point in the

direction to the sample/contacts like the needle of a compass.
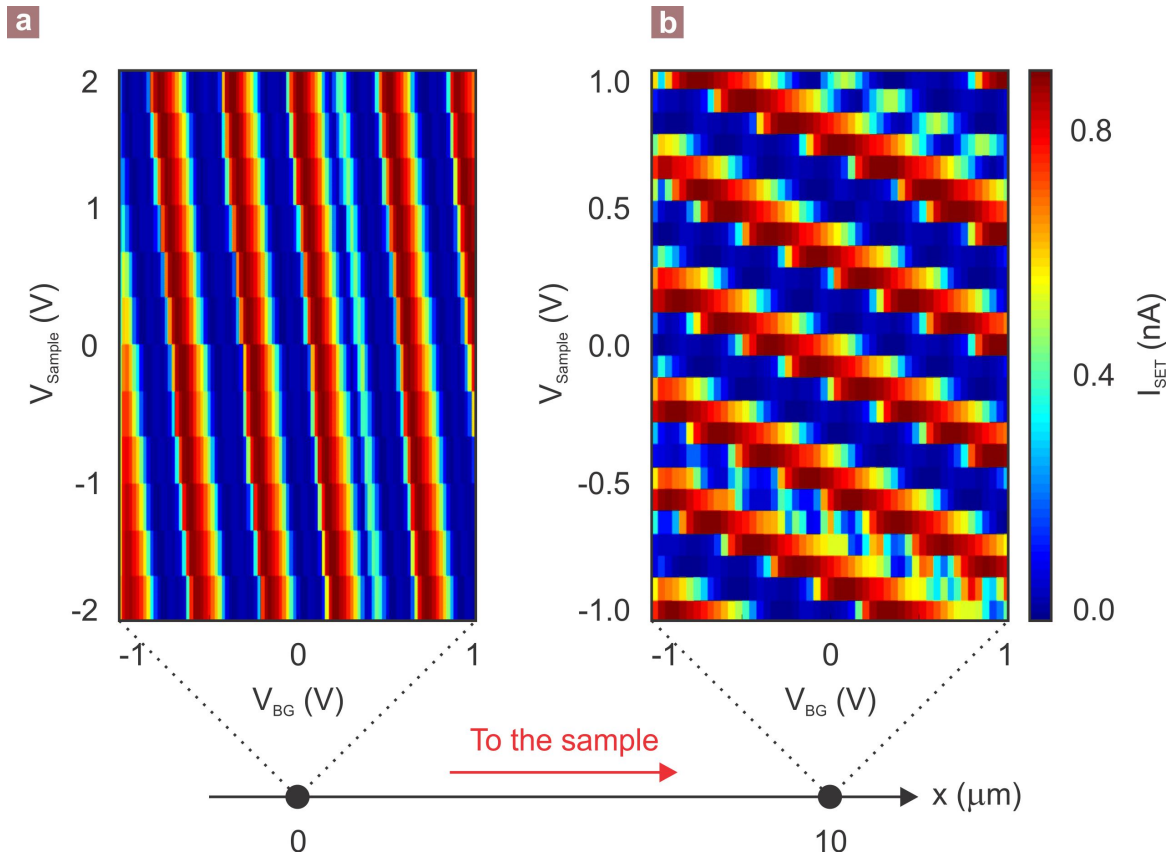
Figure 4.15.: **The needle scan acts like the needle of a compass and points the way to the graphene sample.** *Panel (a) is obtained far away from the sample whereas (b) is measured very close to the sample. The current through the SET in (a) is controlled mainly by the backgate bias V_{BG} as the sample is too far away to show any huge impact in contrast to (b) where also the sample bias V_{Sample} drastically affects the SET current.*

It is helpful to apply different bias voltages to the back gate and to the electrodes attached to the graphene once the SET is close to the graphene as the CBO will pass several peaks and the potential map will show fringes along the contact. An example of such a surface potential map close to the graphene contact is shown in Figure 4.16 (b) and (c) where the contacts are clearly visible.

4) Fine tuning: The final steps include the fine positioning of the tip above the graphene sample, setting up local coordinates (scan window parallel to the graphene edge), approaching down to 50 nm and calibrating the x-, y- and z- dependence with magnetic field. If an applied external magnetic field changes the period of the CBO it means that the z-coordinate is not constant. This can be measured and compensated for in the software. A possible change in the x- and y-direction is also measured and compensated with the help of surface potential maps as demonstrated in Figure 4.17. The change in position of local potential extremes can be traced and compensated for each

77
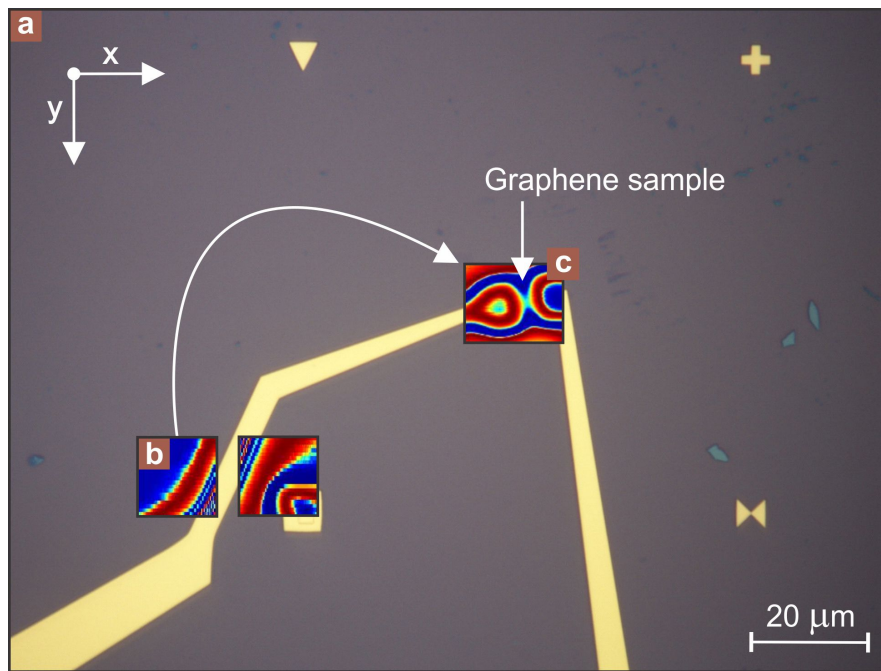
Figure 4.16.: ***Surface potential maps close to the contacts and the sample.*** *(a) An optical image of the device is used as background and illustrates how the surface potential maps (b) and (c) mirror the real structures. The suspended graphene sample is visible in (c).*

magnetic field value. The system is now all set to measure the inverse compressibility and chemical potential. The outcome of this experiment is discussed in Chapter 10.
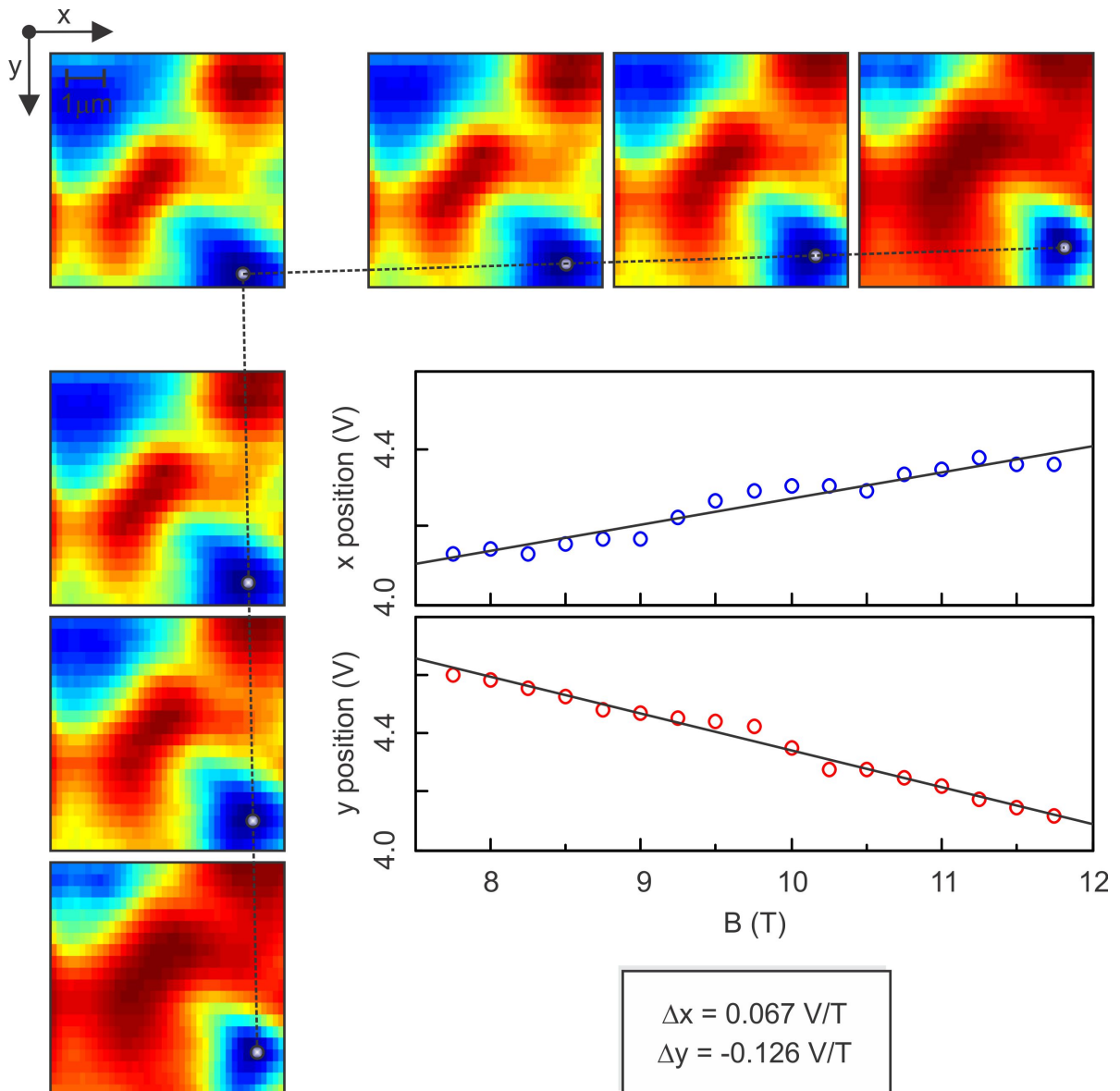
Figure 4.17.: **Surface potential maps used to calibrate the x- and y-coordinates with an applied external magnetic field.** *Tracing local potential extremes allows to measure and compensate for possible magnetic field induced changes in the x- and y- position.*

Part II.

Experiments and Discussion

5. Laser-induced Disassembly of a Graphene Single Crystal into a Nanocrystalline Network
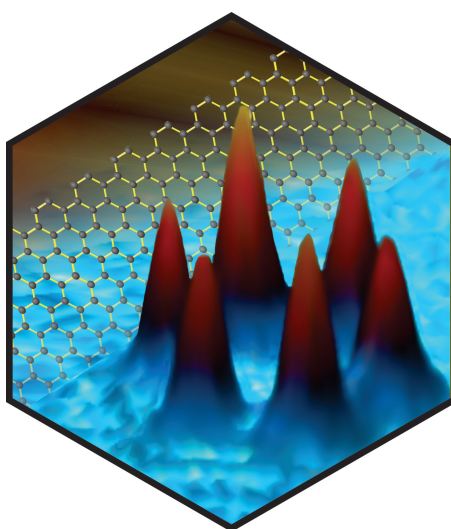
The importance of Raman scattering as a spectroscopic tool to investigate various properties of graphene has already been introduced in Chapter 3. Although the interaction of the incoming laser beam with graphene is restricted to a single plane only one atom thick, the intensity of the Raman scattered light is surprisingly sufficient to be easily detected with a common spectrometer. This is mainly due to the double resonance for the D and 2D peak as well as multiple reflections resulting from the substrate [97]. However, if one wants to resolve for instance extremely weak peaks [98, 99] or slight changes in the position of a peak one needs to increase the signal to noise ratio. Another example where it is crucial to have a high signal to noise ratio is the measurement of anti-Stokes scattered light for temperatures below 500℃ (compare to Chapter 6). Here the occupation number of excited states and hence the signal itself is very low. There are mainly four possibilities to increase the signal to noise ratio:

1. Using a probe laser with a lower wavelength

2. Optimizing the optical path

3. Increasing the laser power

4. Increasing the time of accumulation

A lower wavelength and hence a higher frequency yields a higher scattering probability [70]. However, the graphene 2D Raman peak intensity is severely quenched already at UV wavelength [81] which constitutes a lower limit for the wavelength. Optimizing the optical path is an important task but also inevitably reaches a limit where no further improvement can be achieved. The last two points however seem to be exploitable without restrictions. This chapter deals with the consequences resulting form increased laser power and irradiation time. The investigations will show that Raman spectroscopy of graphene is not as benign as the community believed and can be invasive. Either the irradiation has to be dosed carefully or on purpose can be used to locally modify graphene and for instance enhance the reactivity to molecular adsorbates or remove those adsorbates in a controlled manner.

5.1. Overview

The black line in Figure 5.1 shows a typical Raman spectrum obtained on a freshly prepared flake with a diffraction-limited 1 mW laser spot of 488 nm wavelength after an acquisition time of 30 s.

The following Raman features can be distinguished (see Chapter 3): the first observable peak appears at 1590 cm^{-1} and is associated with the zone-center in-plane longitudinal optical phonons (middle inset in Figure 5.1 and Ref. [74]). This well-known G peak is characteristic for sp^2-hybridized carbon-carbon bonds. The second prominent peak is located at 2700 cm^{-1}. This 2D peak originates from a double-resonance process ([83] and Subsection 3.2.2).The incoming laser light creates an electron-hole pair and after two inelastic-scattering events involving phonons with opposite momenta Raman light is emitted during recombination (right inset in Figure 5.1). If defects are present, one of the two scattering events can occur elastically (left inset in Figure 5.1). This yields the defect or D peak. The D peak exhibits only half the Raman shift. An increase in the number of defects, would result in an increase of the D peak intensity and a concomitant drop in the intensity of the 2D peak. The D peak is not observable in our pristine flake, which attests the good crystalline quality and undetectable small concentration of defects. A shape analysis of the 2D peak has been successfully used to distinguish single layers from bilayers or multilayers [85]. For monolayer graphene the 2D peak can be fitted to a single Lorentzian while the multiple bands in multilayer graphene give rise to a more complex peak structure that requires for instance fitting to 4 Lorentzians for bilayers. Here, the 2D peak clearly indicates that the flake is a monolayer. Additional smaller features in the Raman spectrum have been identified as well and were labeled in Figure 5.1, but are not relevant for the remaining discussions (G* at 3250 cm^{-1}, which results from an intravalley double-resonance scattering process, and the G+A$_{2U}$ peak at 2460 cm^{-1}).
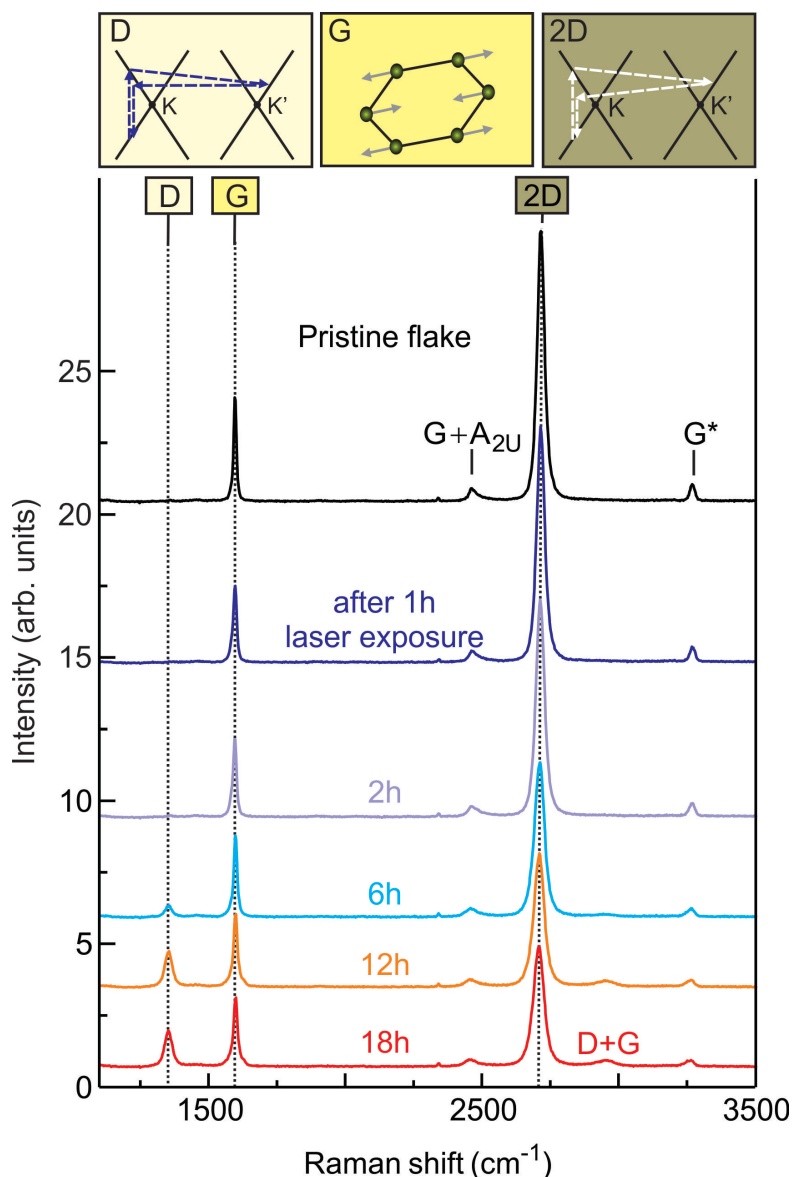
Figure 5.1.: ***Laser induced change in the Raman spectrum.*** *The black line (offset in intensity for clarity) is the spectrum of a pristine monolayer. Other Raman spectra were obtained after laser exposure with 1 mW for the time interval indicated near each trace. Comparing the Raman spectrum after 18 hours laser exposure (red line) with the spectrum of the pristine flake reveals dramatic changes. The appearance of the D peak as well as the decrease in the G and 2D peak intensities are signatures of structural modifications.*

Figure 5.1 also plots Raman spectra after the graphene flake has been exposed to the diffraction-limited focused laser spot with an intensity of 1 mW for different time intervals. The Raman spectrum changes drastically with time. After 18 hours (h) (bottom red line in Figure 5.1) a strong D peak at 1350 cm^{-1} has emerged which was completely absent in the pristine flake. It indicates a large increase in the number of broken sp^2 carbon-carbon bonds [87]. Concomitantly, a peak has appeared at approximately 2950 cm^{-1} or a Raman shift equal to the sum of the G and D peak Raman shifts. This combined D+G peak is in

85

general only observed in the vicinity of defects. We also note the drop in intensity of the 2D peak. The presence of defects also allows the double-resonance mechanism with only one inelastic event and the D peak grows at the expense of the 2D peak, which involves two inelastic events. The 2D peak of the treated flake remains composed of a single Lorentzian despite the apparent local structural modifications of the flake. We point out that the Raman spectrum obtained after 18 h of laser exposure is very different from that of amorphous carbon [100], sp^3-bonded diamond [101] and graphite oxide [102].

5.2. Time-resolved Raman measurements

In order to gain more insight into these laser induced modifications, we have performed time-resolved Raman measurements. The laser power was again set to a moderate level of 1 mW and the laser was focused down to a spot size of around 500 nm. A Raman spectrum was recorded every 30 s. During a time interval of 18 h spectra were acquired. These spectra were analyzed with respect to the intensity and location of the three most prominent features: the G, D and 2D peaks. To improve the signal-to-noise ratio, a signal-averaging procedure was applied to the extracted data traces. It consisted of a fast Fourier transform (FFT) followed by the removal of high-frequency components via a parabolic low-pass filter. The data were then back transformed. Figures 5.2 (a) and 5.2 (b) display the time dependence of the G peak intensity and position.

The intensity initially exhibits a rapid drop. So does the peak position. Both traverse a local minimum after 2 h. After 5 h the intensity decreases monotonously, while the location of the G peak continues to rise. We will argue that two processes, which occur simultaneously but on different time scales, can account for this behavior. Laser-induced heating is held responsible for the removal of dopants. It causes a drop of the G peak position and dominates the Raman spectrum initially in the region denoted as regime I in Figure 5.2 (b) and (e). Previously, it was shown that laser irradiation may cause heating of the electronic system [103]. This should be distinguished from the removal of adsorbants due to laser heating as described here. While dopants continue to be removed, the longer term behavior is mainly attributed to sp^2 carbon-carbon bond breaking and the gradual disassembly of the macroscopic single graphene crystal into a network of interconnected graphene nanocrystallites at the location of the laser spot (regime II in Figure 5.2 (b)). The time evolution of other Raman features also corroborates this interpretation as will be discussed below.

5.3. Influence of doping on the Raman spectrum

We first consider the influence of removing doping adsorbates on the Raman spectrum. It has been demonstrated previously through the field effect that the G peak undergoes a redshift as the carrier density drops [104]. In graphene the adiabatic Born-Oppenheimer approximation is not valid. The charge carrier density n enters the electron phonon coupling [105] and causes phonon softening when n decreases. The initial behavior of the G

peak (see Figure 5.2 (b)), i.e., both the sign and magnitude of the change in the Raman shift, is consistent with a drop in the charge-carrier density due to the removal of dopant molecules. Laser heating is presumably responsible for the dopant removal. The behavior is analogous to the influence of heating with a resistor in close thermal contact under vacuum conditions as shown in Figure 5.3 by combining Raman studies with transport studies on a sample with patterned Ohmic contacts (see also Figure 5.10 (a)).

The initial doping level of the as prepared graphene flake without special treatment was determined from the charge neutrality point at 63 V to be about $5 \cdot 10^{12}$ holes/cm^2 when measuring the field-effect transport characteristic (Figure 5.3 (a), solid black line). Subsequently, the G and 2D Raman features were recorded (Figures 5.3 (b) and (c), solid black line). The carrier density, i.e., dopant concentration, was determined again after removing dopants by evacuating the sample chamber during a time period of 90 min. The carrier density dropped to $7 \cdot 10^{11}$ cm^{-2} (red dashed line in Figure 5.3 (a), the back-gate voltage at the charge neutrality point now equals around 9 V). The Raman spectra around the G and 2D features are again plotted in Figures 5.3 (b) and (c) (red dashed lines) and exhibit a redshift. Finally the sample was heated in vacuum up to 110 °C. It reduced the doping concentration further until the Dirac point was close to zero back-gate voltage. This additional reduction in the carrier density is again reflected in the Raman spectrum as a redshift (blue dotted traces in Figures 5.3 (b) and (c)). The peak positions are listed in Table 5.1. They are obtained from fitting the experimental data with Lorentzians. The G peak position and its shift with density agree well with the experimental data based on field-effect tuning of the density previously reported for instance in Ref. [106]: 1589.5 ± 0.8 cm^{-1} for $n = 5 \cdot 10^{12}$ cm^{-2} and 1583.5 ± 1.2 cm^{-1} for $n = 7 \cdot 10^{11}$ cm^{-2}.

	n (cm^{-2})	G peak (cm^{-1})	2D peak (cm^{-1})
Pristine	$4.9 \cdot 10^{12}$	1588.7 ± 0.1	2709.3 ± 0.1
Vacuum	$7.0 \cdot 10^{11}$	1583.6 ± 0.7	2704.4 ± 0.2
Heated	$7.8 \cdot 10^{10}$	1582.3 ± 2.0	2702.0 ± 0.3

Table 5.1.: **Raman peak positions of the G and 2D peak depending on the charge-carrier density n.** *The values are extracted from the measurements shown in Figure 5.3*

Figure 5.3 also shows that a drop in the carrier density causes a redshift of the 2D peak as well. This behavior of the G and 2D peaks associated with the removal of dopants is also seen in the experiment of Figure 5.2 (h) when the graphene flake is exposed to laser radiation. Since the flake is measured under ambient conditions water and oxygen are believed to be among the dominant doping species. The intensity ratio of the 2D peak and the G peak I(2D)/I(G) is related to the charged impurity concentration in graphene [107–109]. The higher the graphene is doped, the lower is this ratio. For regime
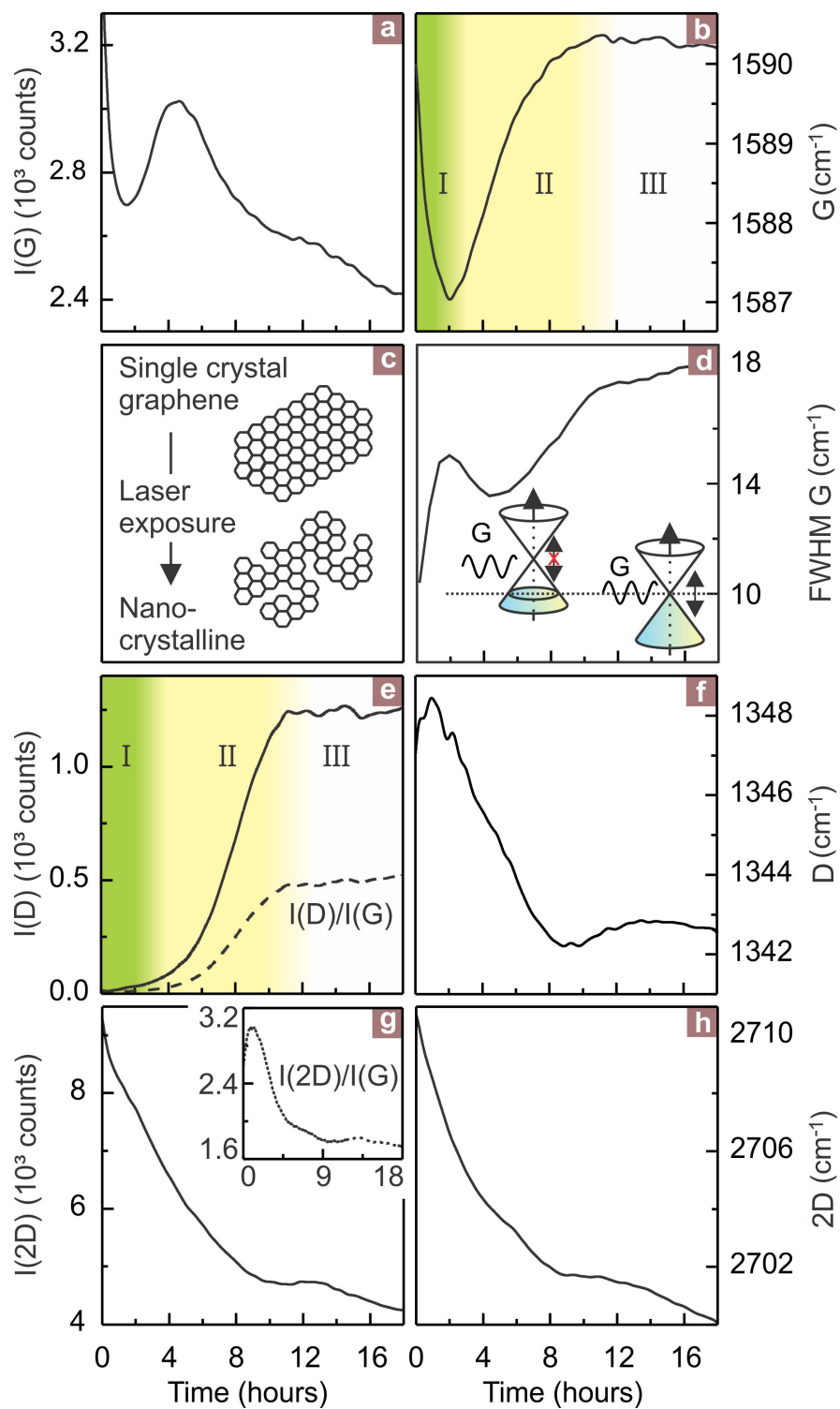
I, we find that I(2D)/I(G) increases. This further corroborates that dopants are removed by the laser beam in regime I.

Additional evidence that the initial rapid time dependence of the Raman features is caused by dopant removal comes from the time evolution of the full width at half maximum (FWHM) of the G peak shown in Figure 5.2 (d). At time zero the FWHM equals approximately 10.5 cm^{-1}. It ascends steeply within the first 2 h of laser exposure up to 15.2 cm^{-1}. This rise in the FWHM is correlated with the drop of the G peak position. The left inset schematically highlights the case with large p-doping. At high doping levels, the energy of the G phonon ($\approx$ 200 meV) is insufficient to create an electron-hole (e-h)-pair as there are no occupied states available. Consequently, the phonon has a long life time and the Raman peak is expected to be narrow [110]. In the case of low doping (right cone in Figure 5.2 (d)) the phonon can decay rapidly in an e-h-pair and the FWHM will grow as the charge-carrier density drops. This behavior is indeed born out in the experimental data of Figure 5.2 (d).

For exposure times longer than 2 h, the FWHM varies more slowly. There is an overall but much slower tendency to increase. Its value remains within a band of 2 cm^{-1} of the value reached after the initial steep ascend. Most of all, the correlation between the behavior of the G peak position and its FWHM is expected when variations in the charge-carrier density would dominate is absent. The G peak moves to larger values, which suggests an increase in the carrier density, but this blueshift is neither accompanied by a corresponding drop in the line width nor by a blueshift of the 2D peak. Hence, at long exposure times ($>$ 2 h) other mechanisms predominantly govern the time-dependent Raman behavior.

5.4. Disassembly due to bond-disruption

During the first few hours of laser exposure the amplitude of the D peak (regime I, Figure 5.2 (e)) remains small. It suggests that only few carbon-carbon sp^2 bonds are broken. For longer laser beam exposure (regime II in Figure 5.2 (e), t $>$ 3 $-$ 4 h) however, the D peak intensity rises and eventually a substantial amount of sp^2 carbon-carbon bonds

Figure 5.2. (preceding page): ***Time evolution of the G, D, and 2D Raman peaks.*** *Panels (a), (e), and (g) show the intensity of these peaks as a function of time during laser exposure with 1 mW of power and a wavelength of 488 nm. For each data point on these curves a Raman spectrum was acquired in the range from 1024 to 3770 cm^{-1} with a 30 s integration time. In panel (e) also the intensity ratio between the D and G peaks has been included as well as the intensity ratio between the 2D and G peak (inset in panel (g)). Panels (b), (f), and (h) display the time development of the position of each of these Raman peaks. The FWHM of the G peak is given in (d). The observed changes with time suggest a structural modification of a single crystal of graphene into a network of graphene nanocrystallites as depicted in a cartoonlike fashion in panel (c).*
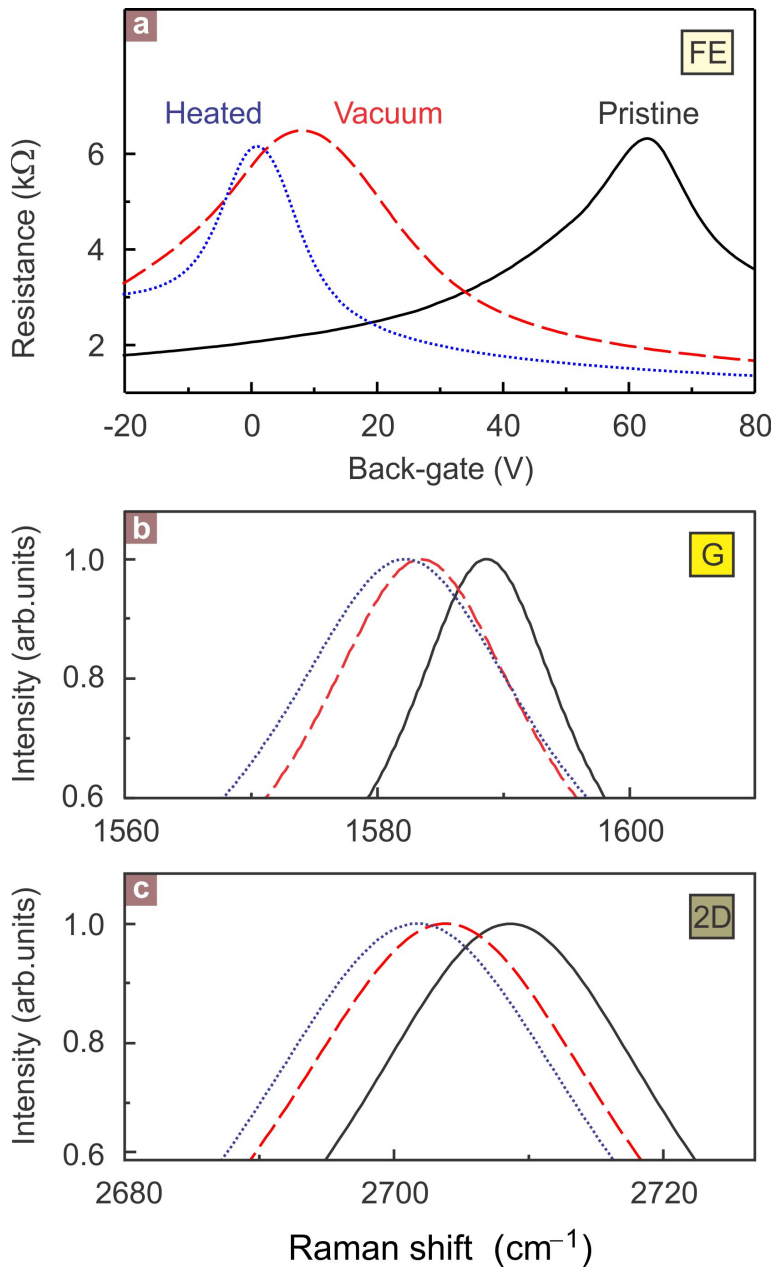
Figure 5.3.: *Influence of removing dopants on the Raman spectrum of graphene.* (a) field-effect curve, (b) G Raman peak, and (c) 2D Raman peak of the as prepared flake (black solid lines), after evacuating the sample for 90 min (red dashed lines) and after heating the sample to 110 °C in vacuum (blue dotted trace). Removal of dopants causes a redshift of the G as well as 2D peak.

apparently get cracked. We assert that the single crystal of graphene is gradually disassembled underneath the laser spot and the graphene crystal is after long laser exposure converted from a single crystal into a network of interconnected graphene nanocrystallites due to bond disruption as schematically illustrated in Figure 5.2 (c). Since the photon energy is smaller than the binding energy, two photon processes might be responsible for bond breaking. The long-time scale indicates a low probability for bond breaking.

After 10 h of laser exposure the intensity of the D peak saturates (regime III in Figure 5.2 (b)). The bond breaking apparently decelerates or terminates. Tuinstra and co−workers [87] have carried out Raman investigations on pellets composed of single crystals of graphite. The crystallite size was determined from x-ray diffraction. Their studies revealed that the characteristic length scale d of the crystallites and the ratio between the D and G peak intensity are in inverse proportion $I(D)/I(G) \propto 1/d$. It simply reflects that the Raman intensity of the D peak is proportional to the percentage of 'boundary' in the sample. Based on the reported data, we would conclude from the $I(D)/I(G)$ ratio observed in the experiments here (Figure 5.2 (e), dashed line) that the Raman signal of the laser treated graphene flake is equivalent to that of graphene nanocrystallites with a characteristic size which saturates at an average value of approximately 10 nm. Since the intensity of the G peak is now strongly affected by the crystallite size, the ratio of the 2D peak intensity and the G peak intensity no longer serves as a measure for the amount of charged impurities. Next we will show that this picture of nanocrystallite formation is impressively confirmed by the behavior of the G peak position (Figure 5.2 (b)).

The increase in the D peak intensity is accompanied by a rise of the G peak position. If due to carbon-carbon bond disruption the graphene flake locally disintegrates into a network of nanocrystalline graphene patches, it is natural to attribute this shift of the G peak to phonon confinement [111]. In the pristine graphene flake, the incident photons only interact with phonons that have essentially zero momentum $q \approx 0$ in order to fulfill momentum conservation [72]. For nanocrystallites with size d, the Heisenberg uncertainty principle relaxes this momentum selection rule and also phonon modes with a nonzero momentum up to $\Delta q \approx 2\pi/d$ contribute to the Raman intensity [112]. For an average crystallite size of 10 nm, we obtain a maximum momentum transfer $\Delta q \approx 0.6/$nm. The Raman-active zone-center phonon mode exhibits a positive dispersion when moving away from the zone center ([113] and Figure 5.4). Due to the lack of experimental phonon-dispersion data for graphene, we resort to reported inelastic x-ray scattering data of graphite to estimate this energy dispersion. A linear approximation yields a slope of $S(LO,\Gamma) \approx 13$ nm/cm. For 10 nm crystallites, phonon modes with an energy larger by at most 8 cm^{-1} (see green and red doted line in Figure 5.4 (b)) compared with the zone-center phonon energy (blue dotted line) may contribute to the Raman G peak. Since all phonons with Δq between 0 and $\approx 0.6/$nm take part, the G peak will broaden. This relation is illustrated in Figure 5.4 (b). The estimated maximum blueshift is compatible with our experimental observations. We start from a highly p-doped flake with a G peak position close to 1590 cm^{-1} and remove dopants by laser irradiation. The G peak position of undoped graphene is approximately 1583 cm^{-1}. The phonon confinement is expected to cause a blueshift of less than 8 cm^{-1}, so that the G peak should not exceed 1591 cm^{-1} in the limit of long exposure times. This agrees well with the data in Figure 5.2 (b). It is purely fortuitous that the initial and final G peak positions are so close.
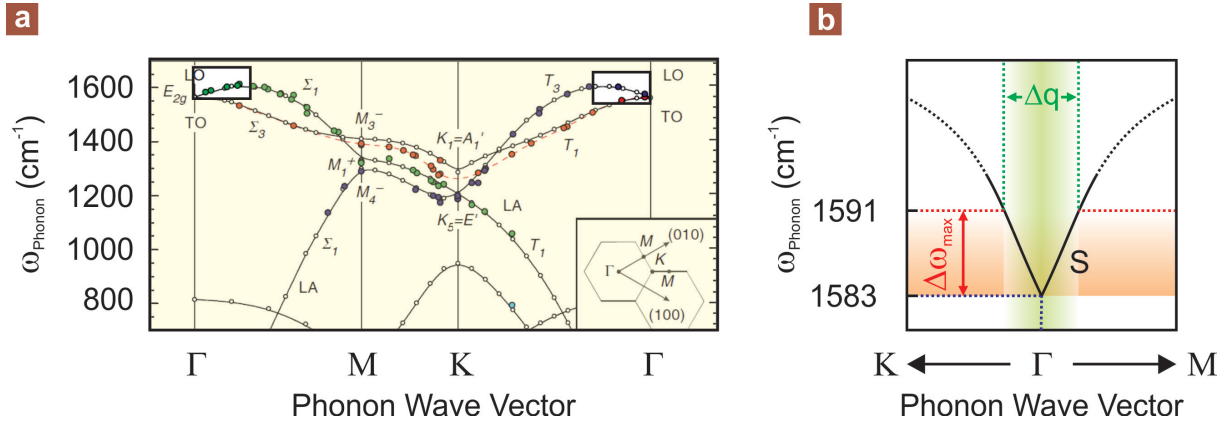
Figure 5.4.: ***Phonon dispersion and momentum relaxation.*** *(a) Phonon dispersion of graphite modified from Ref. [113]. The highlighted regions are magnified in (b): The relaxation of the momentum conservation (green area) allows phonon modes with higher energy (red area) to contribute to the G peak. Overall the G peak will appear at higher energies and has a higher FWHM.*

5.5. Seperation of laser-induced Raman effects

In order to separate the two effects of removing dopants by laser heating and bond disruption which converts single crystal graphene into a network of graphene nanocrystallites, some flakes were prepared and treated so their charge neutrality point was close to zero back-gate voltage prior to laser treatment in order to minimize the influence of dopant removal. Dopants can be removed effectively either by chemical treatment of the substrate during flake preparation [114] or by heating the flake under vacuum conditions. These procedures to shift the charge neutrality point close to zero back-gate voltage were tested on a large series of samples and were verified by recording field-effect characteristics. Both treatments were used and led to the same results. Here we will focus on a flake annealed under vacuum conditions. The pristine sample was heated in vacuum for several hours and subsequently kept under argon atmosphere during the time-dependent Raman experiment. The argon atmosphere ensures comparable thermal conditions as in air. The outcome of this experiment is displayed in Figure 5.5.

The laser exposure time serves as abscissa. Left panels show the time dependence of the Raman intensity of the G, D, and 2D peaks (Figures 5.5 (a), (e), and (g)). The Raman shift of the G, D, and 2D peak as a function of time is displayed in the right panels (Figures 5.5 (b), (f), and (h)). The measurement and evaluation of the data were performed in the same manner as for collecting the data plotted in Figure 5.2. One exception is the incident laser power. It was increased from 1 mW to 12 mW. A factor of 2 is lost in the Raman signal intensity when the sample is mounted in a chamber with a window. Hence, compared with Figure 5.2 the data in Figure 5.5 were effectively recorded for a six times higher intensity. The 3 h time scale in Figure 5.5 is therefore comparable to the 18 h in Figure 5.2.
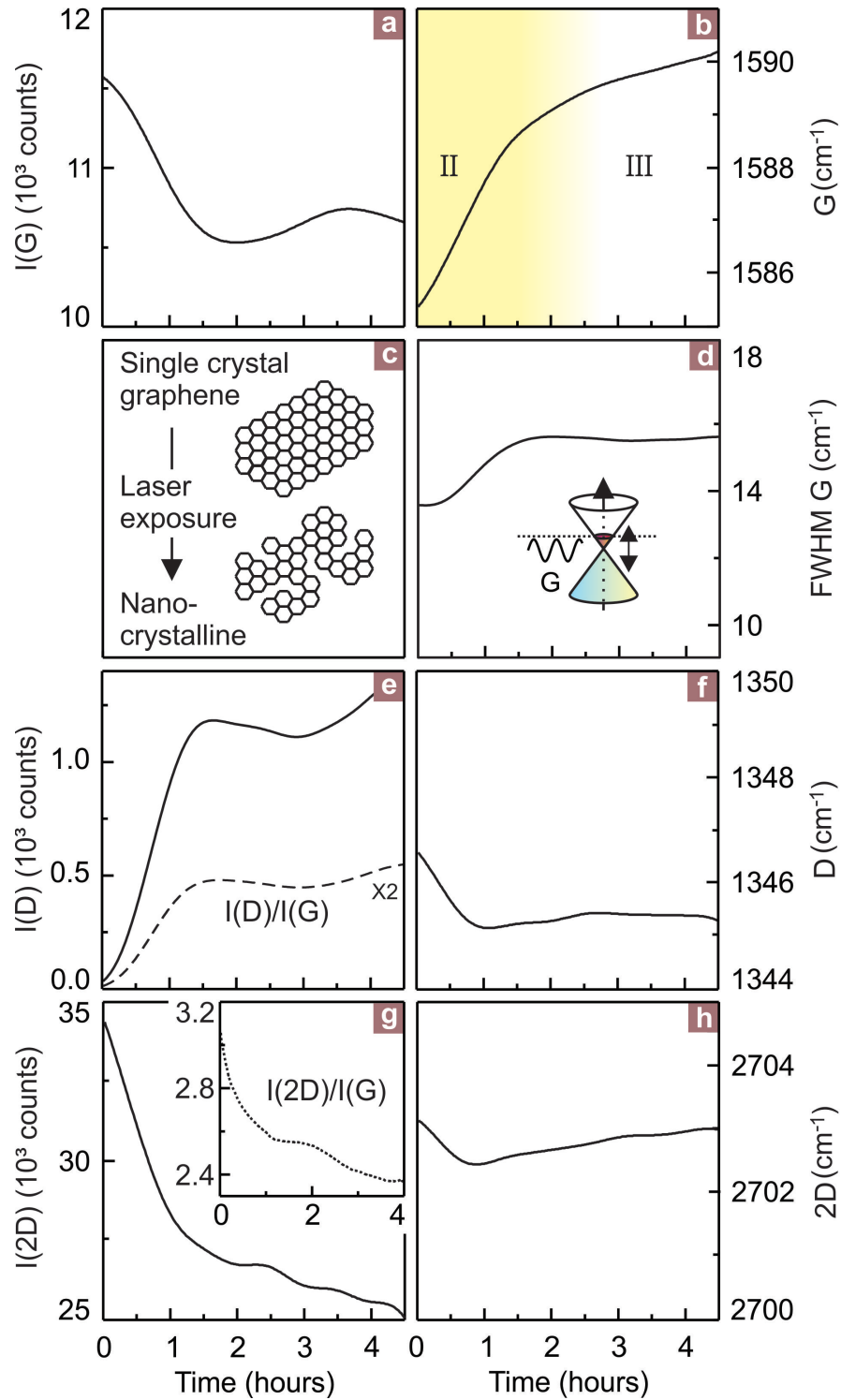
Figure 5.5.: *Time evolution of the G, D, and 2D Raman peaks under laser exposure where dopants have been removed beforehand by heating and pumping.* *Compared to Figure 5.2 all features attributed to the laser induced removal of dopants (regime I) are absent. The time evolution points to the disassembly of single-crystal graphene into a network of graphene nanocrystallites.*

All the time-dependent features previously attributed to the removal of dopants such as the redshift of the G, D, and 2D peaks as well as the strong increase in the FWHM of the G peak have vanished almost entirely (regime I in Figure 5.2). Furthermore, the ratio I(2D)/I(G) does not increase. This again strongly supports our assertion that the Raman behavior in regime I of Figure 5.2 is related to the removal of dopants by laser heating. What remains are mainly those modifications in the spectrum previously attributed to sp^2 carbon-carbon bond breaking (regime II in Figure 5.2 and Figure 5.5):

1. a blueshift of the G peak due to phonon confinement,

2. an increase of the D peak intensity due to the creation of additional boundaries,

3. a decrease in the 2D peak intensity, which is closely linked to (ii) as well as

4. a reduction in the G peak amplitude as a result of the drop in the number of intact carbon-carbon bonds.

The intensity ratio of the D and G peak in Figure 5.5 (e) (regime III, dashed line) is approximately 1/4 from which an average crystallite size of 20 nm can be estimated [87]. The resulting phonon confinement allows phonons with an energy larger by 4 cm^{-1} to contribute to the G peak. This fits well with the experimental data in Figure 5.5 (b). Also the G peak is broadened due to the relaxed momentum selection rule. For the sake of completeness, we point out that some small influence from adsorbates remains present in the data of these pretreated flakes. The small decrease in the position of the D and 2D peaks during the first hour is likely associated with adsorbate removal.

5.6. Spatially resolved Raman spectroscopy

Figure 5.6 displays spatial Raman maps of the D, G, and 2D peak intensities. The panels on the left are Raman maps for the pristine flake while panels on the right side were recorded after 18 h of laser exposure. In these experiments, the laser spot was defocused to enlarge the spatial extent of the modified area. The spot size was measured separately. It was equal to 1.5 μm and hence the laser irradiated area can be spatially resolved with confocal Raman spectroscopy. A complete Raman spectrum was recorded for each location (step size 200 nm in both spatial directions) and the intensity was evaluated for the three peaks. Apart from the inevitable blurring due to the diffraction limit, the modifications in the Raman spectrum are indeed spatially confined to the laser spot size.

5.7. Atomic force microscopy

5.7.1. Height study

A more accurate estimate of the affected region can be obtained by recording the topography with atomic force microscopy. To minimize the influence of the tip, such measurements were performed in tapping mode. Figure 5.7 (a) depicts an AFM image of
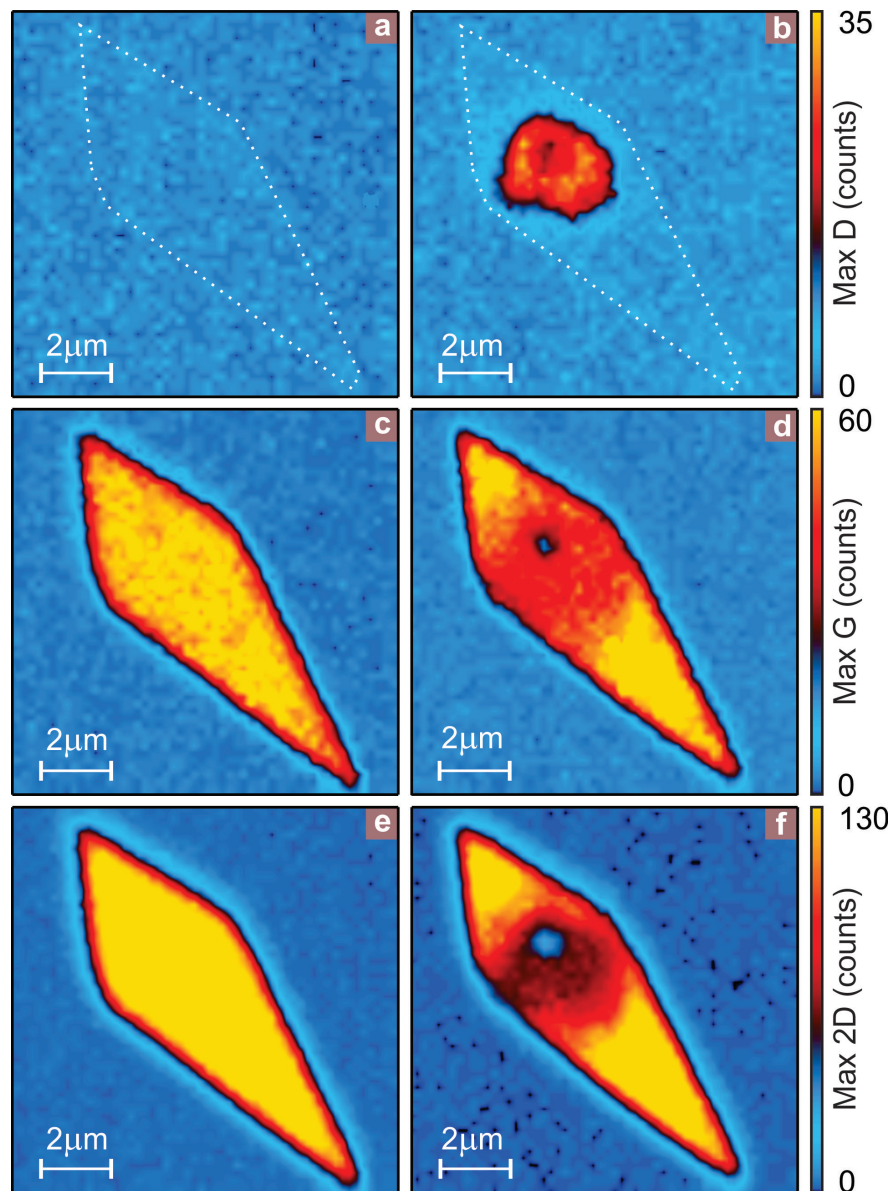
Figure 5.6.: ***Intensity maps of the D, G, and 2D Raman peaks before (left panels) and after laser exposure (right panels).*** *(a) On the pristine flake there are virtually no defects and hence the D peak is not observable. The white dashed line is a guide to the eye and corresponds to the border of the graphene sheet where a few defects are located. (b) Inside a circle with a diameter of approximately 1.5 μm, the intensity of the D peak is irreversibly enhanced after laser exposure. The size and position of the spot with a large D count coincide with the laser spot. (c) Before the laser treatment, the intensity of the G peak is nearly identical across the entire graphene sheet. It confirms the high crystalline quality of the flake. (d) After laser treatment, the intensity of the G peak is reduced.*

a freshly prepared monolayer. The measured height of the flake is about 1 nm instead of 0.335 nm expected for a monolayer. This discrepancy has been reported previously and is attributed to adsorbed molecules on top of the graphene surface or in between the graphene layer and the substrate [115]. Note that in the tapping mode the AFM 'height' may also contain a chemical contrast contribution. After laser exposure the irradiated region shows an additional even higher elevation of approximately 1.5 nm (Figure 5.7 (b)). The disruption of carbon-carbon bonds offers additional docking sites for adsorbates. We associate this height increase with the adsorption of additional molecules from ambient air when the laser is turned off. This assertion is proved in transport experiments described in Section 5.8.
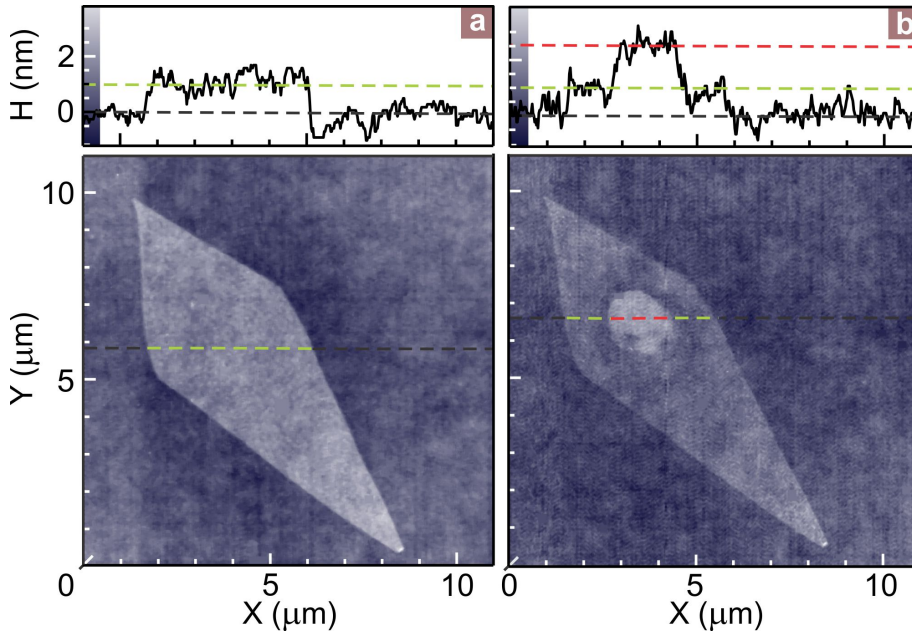
Figure 5.7.: *AFM image of a graphene monolayer before and after laser exposure recorded in tapping mode. (a) AFM height image of a pristine graphene flake. The top panel shows a height scan along the dashed line. The height H of the substrate and the graphene surface are marked by the dashed black and green lines, respectively. The measured height difference is approximately 1 nm. (b) AFM height image after exposing one spot on the sample for 18 h with a 1 mW defocused 488 nm laser beam. An elevated area has appeared where the laser spot was positioned. In the top panel, the red dashed line marks its height. The difference with respect to the pristine graphene surface is approximately 1.5 nm. The diameter of the modified region coincides with the diameter of about 1.5 µm of the defocused laser spot.*

5.7.2. Time dependence of the topography

To gain more insight into the topographical changes as the single graphene flake is decomposed into nanocrystallites, we have performed time-resolved AFM measurements. One way to do this would be to irradiate the flake with laser light for a certain time interval, obtain an AFM image, and continue with the laser irradiation at the same location. To

circumvent the potential influence of the AFM tip, we have chosen a different route. Multiple spots, spatially apart by a sufficiently large distance to ensure no mutual influence, were irradiated with the laser for different time intervals. The laser power was set to 12 mW in all cases. After all spots were 'written' just a single AFM image was recorded in tapping mode. The AFM image is depicted in Figure 5.8 (a).
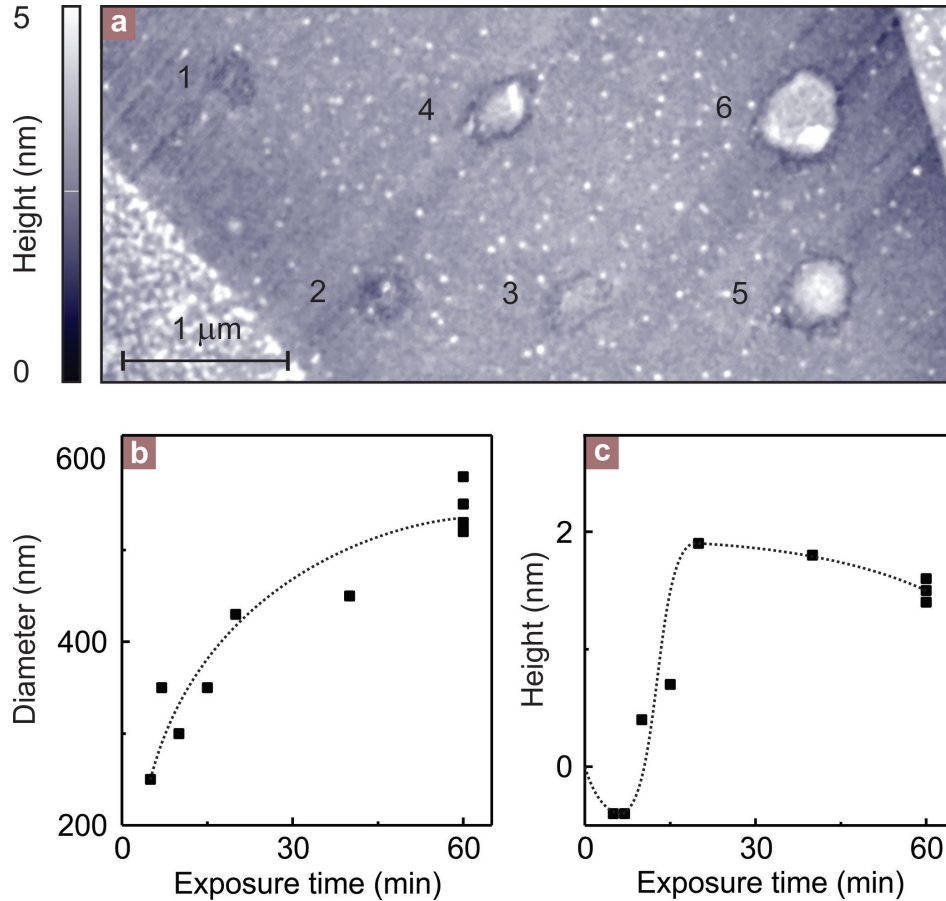
Figure 5.8.: **_Time resolved AFM measurements._** _AFM measurement on a graphene flake on which multiple laser spots with different exposure time have been written. (a) Height image of the laser treated areas. Laser treated areas are numbered. A large number corresponds to a longer exposure time. (b) Analysis of the diameter of the laser treated spots in (a). The modification of graphene occurs first in the middle of the laser spot where the laser intensity has its maximum. (c) Analysis of the height as a function of the exposure time. After a small decrease in height (removal of dopants) the height grows until it reaches a maximum. The increased height is attributed to the attachment of ambient species after the laser has been turned off._

The results of the image analysis are summarized in Figures 5.8 (b) and (c). In panel (b), the diameter of the modified area is plotted as a function of the exposure time. The modification occurs first in the middle, where the laser intensity has its maximum. After 1 h, the modified area has grown into an area equal in size to the focused, diffraction-limited laser spot. The modified region does not expand further at longer exposure times. Also addressed in Figure 5.8 (c) is the time evolution of the height of the modified region. The indicated height is obtained from a histogram which plots the counts for each height

contour. During the first 10 minutes, there is a slight decrease in the height. This corresponds to the removal of adsorbates initially present on the pristine flake. We note that a chemical contrast contribution may be contained in tapping mode images and hence when we refer to a change in height it also includes a potential change in the chemical contrast. The height decrease fits well with the observed red-shift of the Raman G and 2D peaks. Subsequently, the height increases as the crystalline flake is locally converted into a nanocrystalline network. As time progresses, sp^2 carbon-carbon bonds are broken up. These broken bonds provide additional docking sites for molecular adsorbates such as water from the ambient atmosphere. That additional adsorbates appear after laser treatment is unambiguously confirmed in field-effect experiments which will be described below in Section 5.8. The increase in height is attributed to these additional adsorbates. It is well-known that it is not possible to properly identify monolayers, bilayers, or multilayers of graphene using AFM images. The height of a monolayer of graphene (identified unequivocally using optical contrast, Raman spectroscopy or magnetotransport) typically ranges from 0.8 - 1.3 nm in an AFM image even though the actual graphene layer thickness is only 0.33 nm. Adsorbates on top of the flake or in between the substrate and the flake are held responsible for the discrepancy between the measured height and the true graphene thickness [115]. Hence, it is plausible to attribute the height increase upon laser irradiation to the larger number of attached adsorbates seen in field-effect studies. The height increase eventually slows down or terminates. This saturation coincides with the Raman data in which the D peak intensity no longer increases. No additional defects, i.e., broken bonds, are created. Hence, the accumulation of additional adsorbates stops and the height remains nearly constant. Note that the time scale for saturation in Figure 5.8 is much shorter than for instance in Figure 5.2, because the sample was irradiated with 12 mW of laser power instead of 1 mW for the data acquired in the experiment of Figure 5.2.

5.7.3. Topography near graphene edge

To confirm that the observed changes in AFM images (increased height) and the Raman measurements are intimately connected with the presence of graphene, we have irradiated a graphene flake near its edge so that laser light is simultaneously incident on graphene and an uncovered piece of the underlying SiO_2 substrate. The edge region was exposed again to 12 mW of laser light for 1 h.

Figure 5.9 displays the AFM image after irradiation. On the bare SiO_2 substrate, laser irradiation has little influence. A slight decrease in height is visible in the irradiated region. Presumably this is due to the removal of molecular adsorbates. Even when irradiating the bare substrate for a much longer time period, no increase in height is observed. On the graphene flake however, the height has increased due to the gradual disassembly of crystalline graphene and the adsorption of a larger number of molecules. The border of the graphene flake does not wash out, instead the sharp boundary to the uncovered SiO_2 substrate is maintained. For the sake of comparison, we show on the left side of Figure 5.9 the disk shape which forms when the laser light is entirely incident on the graphene monolayer.
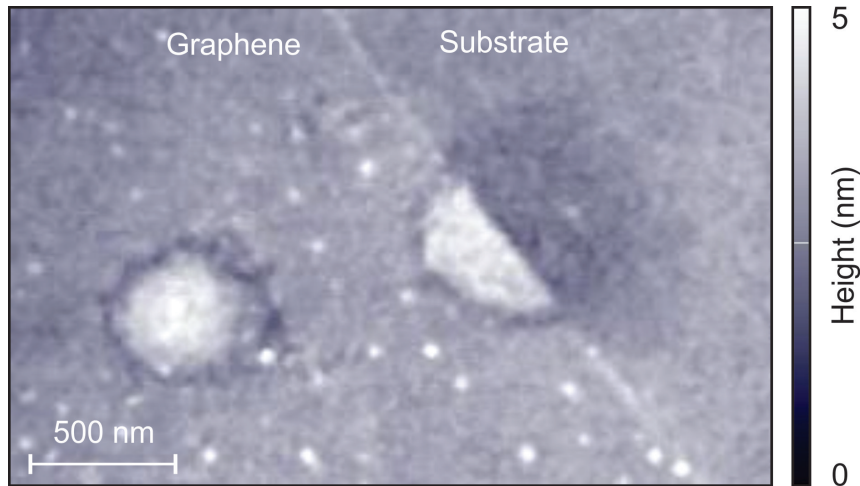
Figure 5.9.: ***AFM image of a flake which has been treated by laser light at the edge.*** *Only the graphene itself shows an elevated height. For the sake of comparison also a spot located entirely within the flake has been 'written'.*

5.8. Transport characteristics after laser treatment

It is known from noncontact scanning force microscopy studies [116] that on graphite crystals water nanodroplets preferably attach to steps. The laser treatment of graphene creates many additional edges (see the D peak behavior in Figures 5.1, 5.2, and 5.5). They provide additional docking sites for instance for water droplets from the surrounding ambient air. Also other constituents from the surrounding atmosphere (e.g., O_2) may attach to the flake. Water as well as oxygen transfer charge and act as p - type dopants on graphene. This p-type doping can be observed experimentally by recording the field-effect transport curves after different times of laser irradiation. Field-effect data were recorded after the laser was switched off for 60 seconds.

Figure 5.10 (a) shows an AFM image of a typical device used for recording these field-effect characteristics. The bright stripes are the Cr/Au contacts, the dark brown color is the SiO_2 substrate. At the end of each contact lead, the AFM image is brighter, because in these regions the graphene monolayer is located underneath. This causes a slight height increase. The width of the contacts as well as the distance between adjacent contacts is approximately 600 nm. The incident laser beam has been schematically included as a transparent blue ray. Prior to modifying the flake we acquired a scanning confocal laser image, which enables us to position the laser spot precisely on the graphene in between the contacts.

The four terminal longitudinal resistance is plotted as a function of the applied back-gate voltage in Figure 5.10 (b) with the laser irradiation time as the parameter. As before a laser power of 12 mW has been used in this experiment. For short exposure times, the removal of the dopants which were already present on the as prepared flake dominates. It appears as a large shift of the charge neutrality point to smaller back-gate voltages during
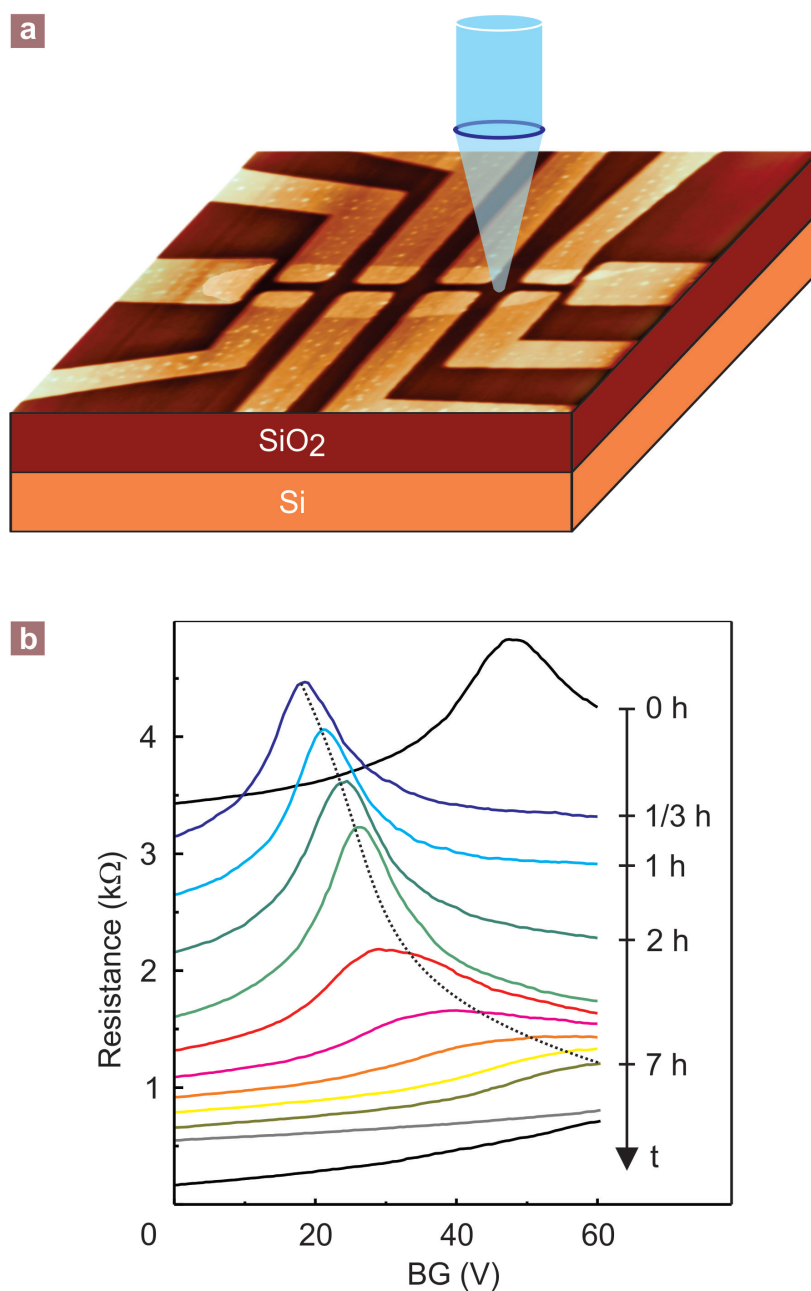
Figure 5.10.: ***Field-effect curves recorded on a graphene flake which has been exposed to laser irradiation.*** *(a) AFM image of a typical device. (b) Field-effect characteristics for different laser exposure times. Before recording this transport data, the laser was switched off for 60 seconds. The removal of the dopants on the as prepared flake causes an initial shift of the charge neutrality point to lower back voltages, i.e., the carrier concentration drops (first 20 minutes). As sp^2 bonds get cracked, the reactivity of graphene is locally enhanced and more dopants from the ambient can adsorb after the laser light has been switched off. This results in an increase of p-type doping.*

the first 20 minutes (faster than for Figure 5.2 as a result of the increased laser power). The amount of boundary, i.e., the number of broken sp^2 carbon-carbon bonds continuously increases with time. This enhances the reactivity. After switching off the laser, dopants easily attach to the flake and p dope it. After 7 h, the charge neutrality point is already higher than 60 V when the laser is switched off. By pumping and heating the dopants can be removed again and the charge neutrality point returns to lower back-gate voltages. Subsequent exposure to ambient air shifts the charge neutrality point reversibly back to the high doping state. This controlled enhancement of the reactivity of nanocrystalline graphene may be helpful to trim or tune for instance the properties of graphene based gas sensors [117]. It can also be exploited to generate spatially varying doping patterns as will be shown next in Section 5.9.

5.9. Lithography

In order to demonstrate the ability to spatially modify graphene and its properties with laser irradiation in a controlled manner we 'write' the six corners of a hexagon as a test structure on a monolayer. The model is rendered into coordinates and subsequently transfered to the sample by either moving the stage or the laser beam. AFM images after the laser exposure are depicted in Figure 5.11 (a) and (c). The elevated regions of the modified graphene can clearly be seen. A color rendition of the intensity of the Raman D peak is shown in Figure 5.11 (b) and (d). The resolution of the modified structures is only limited by diffraction. The written shape is not restricted to circles but can be extended to arbitrary patterns like lines etc.

5.10. Transmission electron microscopy studies

In the last part of this chapter we address transmission electron microscopy (TEM) studies with atomic resolution of modified graphene. The aim is a microscopic understanding and visualization of the modification. Furthermore the TEM data is used to corroborate the conclusions drawn from Raman, AFM, and electric measurements as discussed in the previous sections.

For TEM measurements graphene is prepared on a special TEM grid as shown in Figure 5.12 (c) and (d). The monolayer is visible by optical microscopy in the blowup in Figure 5.12 (b). The laser irradiated and imaged part of the monolayer is enclosed by a red circle. Low magnification TEM image of the modified area already confirm that dopants are removed as the graphene is cleaner at irradiated areas compared to non irradiated parts of the sample. This agrees well with the results from Raman spectroscopy in Section 5.3 and electric transport measurements in Section 5.8. One example of such a clean area is shown in Figure 5.12 (a) where the atomic structure of defect free graphene is visible. It was obtained from one of the spots labeled by 'G' in Figure 5.12 (e).
However, as can be seen from Figure 5.12 (e), there are not only these clean areas (blue 'G') but furthermore residual contaminations (yellow 'c') and holes (red crosses) are visible.
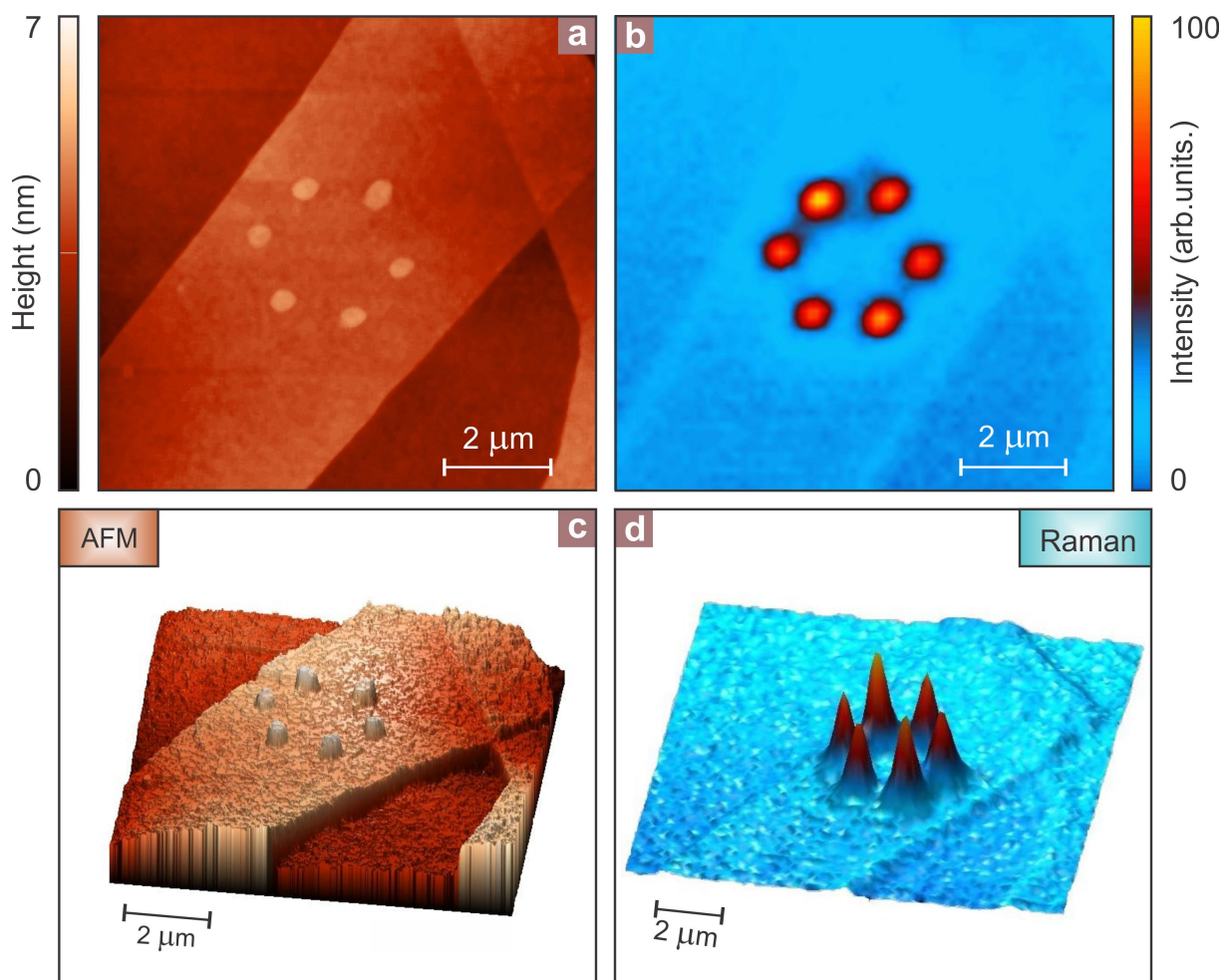
Figure 5.11.: *'Lithographene': (a) and (c) depict AFM images of the graphene flake after writing the six corners of a hexagon with a laser beam focused to the diffraction limit. (b) and (d): color rendition of the Raman D peak intensity.*

All the data from the previously described measurements pointed towards a laser-induced disassembly of a graphene single crystal into a nanocrystalline network by disrupting sp^2 carbon-carbon bonds. This is indeed confirmed by the TEM images as several holes (marked by red crosses in Figure 5.12 (e)) can be distinguished from clean areas by their slightly higher black-white diffraction contrast. The measured size of the observed holes is a few tens of nanometers and verifies the predictions from Raman spectroscopy. Higher magnification images of those holes shown in Figure 5.13 (c) and (d) impressively confirm the increased reactivity of dangling bonds and endorse that contaminations preferably attach to the edge of those holes. Additionally, several point defects were found on the irradiated area, some examples are encircled in black in Figure 5.13 (b). Consecutive images of the same area reveal that these point defects are chemically active and able to catch ad-atoms for short but multiple times. Vacancies are created by the laser beam which are subsequently occupied by other atoms from the ambient air for instance nitrogen. One example of a such a vacancy (blue) and a nitrogen substitution (red circel and inset) is shown in Figure 5.13 (a).
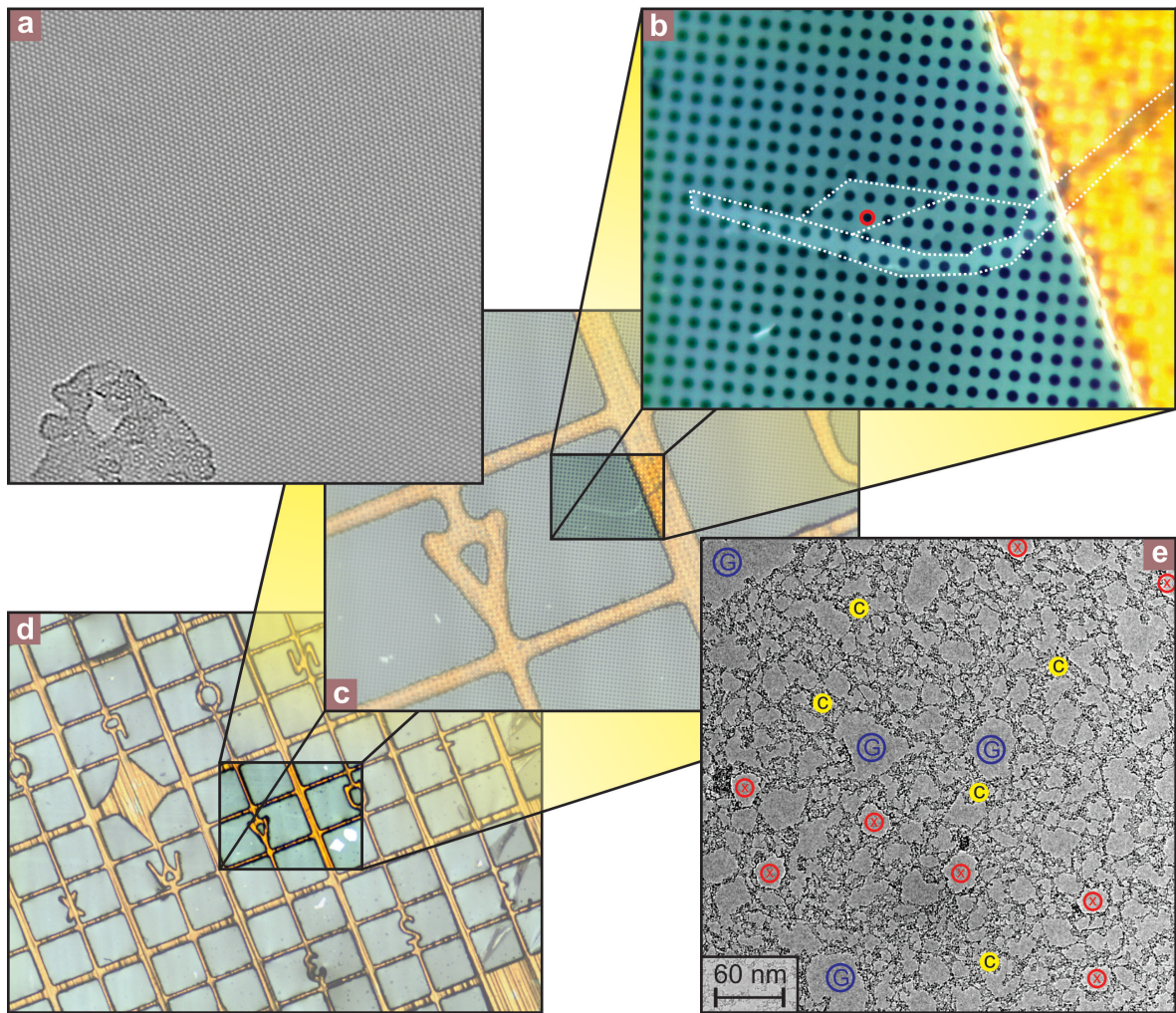
Figure 5.12.: ***TEM grid and TEM images of a modified graphene flake.*** *(d), (c), and (b) are optical images of the TEM grid (increasing zoom) with the attached graphene sample visible in (b). The white dotted line sketchs out the boundary of the flake. The hole in the TEM grid enclosed by a red circle demarcates the position where the laser beam is focused to and where the TEM images were recorded. (e) TEM overview. Key regions are marked, 'G' denotes clean and defect free areas of graphene, red crosses denote holes and in regions labeled with 'c' contaminations are found. (a) Defect free graphene can be found in large areas marked with 'G' in (e).*

We finally turn our attention to the chirality (see also Chapter 7) of the edges surrounding the observed holes. The crystallographic directions for the following analysis are obtained from the atomic resolution image depicted in Figure 5.13 (c). Unfortunately, as mentioned above, the real atomic structure of the edge is concealed as open edges tend to trap contaminations on a short time scale. However, if we consider the overall tendency (as exemplified in Figure 5.13 (d)) and average over many holes we find an approximately equal number of edges with armchair and zigzag orientation. Hence, we conclude that under the present conditions of laser irradiation the two edge chiralities have a similar

stability and no crystallographic direction is preferrentially affected by the laser beam.
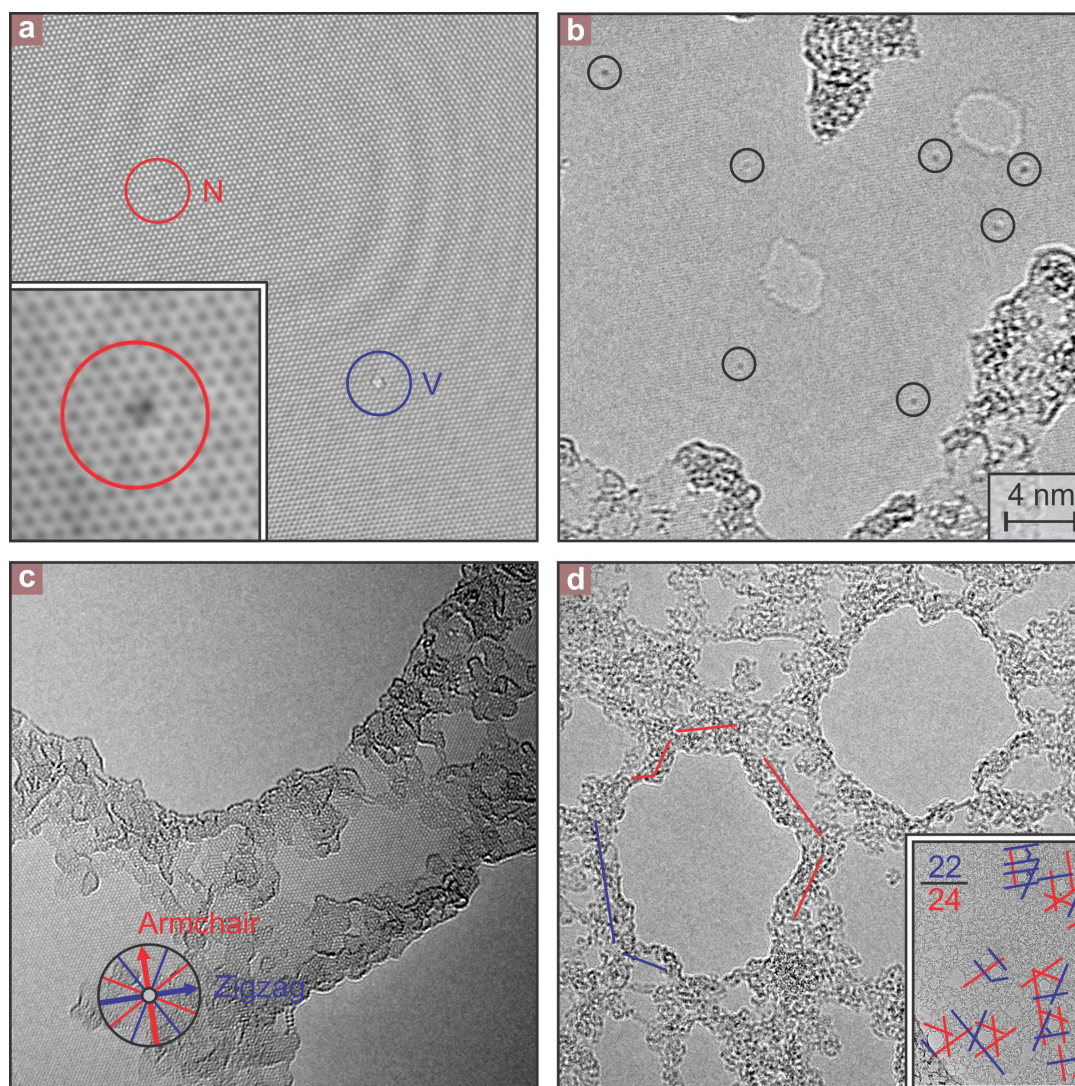
Figure 5.13.: *Atomic resolution TEM images of laser irradiated graphene.* *Several point defects (black circles in (b)) are found to be chemically active. They trap and release for instance nitrogen (red circle in (a) and inset). No preferred edge chirality is found in (c) and (d) but the enhanced reactivity of dangling bonds at the edge is confirmed by the fact that contaminations primarily are visible at the edge.*

5.11. Summary

In summary, we have demonstrated with a combination of spatially- and time-resolved Raman, AFM and TEM as well as transport measurements that laser irradiation of graphene can be invasive and may induce controllable structural modifications. Long laser exposure locally disassembles a single crystalline layer of graphene into a network of interconnected graphene nanocrystallites. Their characteristic size saturates at approximately 10 nm in

the limit of long exposure times. The additional boundaries provide docking sites for molecular adsorbates, so that the reactivity can be locally enhanced.

6. Hot Phonons in an Electrically Biased Graphene Constriction
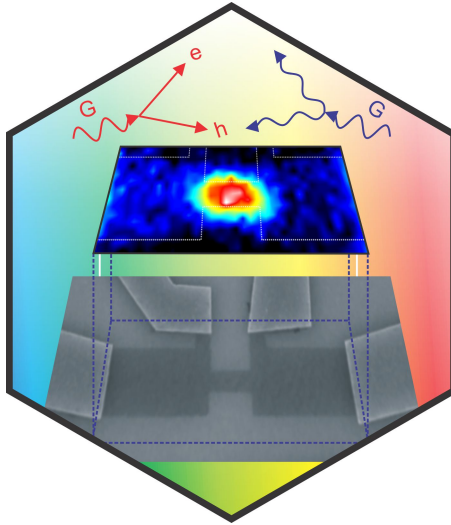
Interactions between phonons and charge carriers can have significant impact on device performance. These interactions can be probed by measuring the phonon lifetime, which reflects the interaction strength of a phonon with other quasi-particles, in particular charge carriers as well as its companion phonons. The carrier-phonon and phonon-phonon contributions to the phonon lifetime can be disentangled from temperature-dependent studies. Here, we address the importance of phonon-carrier interactions in Joule-heated graphene constrictions in order to contribute to the understanding of energy dissipation in graphene-based electronic devices. We demonstrate that gapless graphene grants electron-phonon interactions uncommon significance in particular at low carrier density. In conventional semiconductors, the band gap usually prevents the decay of phonons through electron-hole generation and in metals or other semimetals the Fermi temperature is excessively large to enter the regime where electron-phonon coupling plays such a dominant role as in graphene in the investigated phonon temperature regime from 300 to 1600 K.

6.1. Introduction

The prospect of carbon-based electronics has triggered a strong interest in understanding the scattering processes of charge carriers supporting current flow through these devices. High currents may induce a significant overpopulation of phonons [118–123]. Calculating the phonon temperature from the population number via the Bose-Einstein distribution leads in such a case to high temperatures and we therefore speak of hot phonons. These phonon modes may in turn impede transport and enhance scattering with electrons as a result of strong electron-phonon interactions [118–120, 123–125]. For instance, Yao et al. [118] have reported a dramatic drop in the ballistic conductance in carbon nanotubes under large applied bias voltages which would deteriorate the performance of carbon nanotube based interconnects. Here we exploit the local generation of hot phonons in Joule-heated graphene constrictions with high-energy electrons to investigate phonon decay mechanisms and especially the electron-phonon scattering as a function of temperature. The main tool is scanning confocal Raman spectroscopy of the in-plane carbon stretching mode (G-mode). Line widths associated with phonons immediately reveal scattering rates, and the Stokes and anti-Stokes counterparts allow extracting the phonon population number and even its spatial dependence along the constriction. The temperature dependence of the phonon line width is nonmonotonic and decreases with temperature for some temperature range at sufficiently low carrier densities. This is very distinct from the monotonically increasing line width of optical phonons due to anharmonic phonon-phonon scattering, which dominate in the large majority of other materials [126–128] in the investigated temperature regime.

6.2. Method

A scanning electron microscope picture of a typical device geometry is shown in the left inset of Figure 6.1 (a). It consists of a monolayer graphene flake with an etched constriction at its center with a width of 0.6 μm and a length of 1.5 μm. This geometry offers the advantage of concentrating the heat dissipation locally at the constriction. Graphene flakes were peeled off from highly oriented pyrolytic graphite with adhesive tape and transferred on a degenerately doped Si substrate with a 300 nm thermal SiO_2 on top (see Subsection 2.7). Monolayer graphene was identified using the contrast difference on 300 nm SiO_2 with optical microscopy ([5] and Chapter 8). The line shape and position of the 2D peak from Raman spectroscopy were utilized as an unequivocal check ([85] and Subsection 3.2.2). The constrictions were produced by first patterning an etch mask with electron-beam lithography and evaporation of 25 nm of Al. The uncovered graphene was etched away with the help of an Ar plasma. The Al etch mask was subsequently dissolved in 1 M KOH solution. Finally, Cr/Au (5 nm/50 nm) electrodes were deposited after a last e-beam lithography step (see also Subsection 2.7).
The left inset of Figure 6.1 (a) depicts schematically the scanning confocal Raman setup. Raman measurements were performed with a bias voltage applied across the graphene constriction in a backscattering geometry using a He-Ne laser at 632.8 nm with a diffraction-limited spot size of approximately 500 nm. The incident laser beam is deflected by a piezo-driven mirror to obtain a scanning confocal optical image of the sample in order to
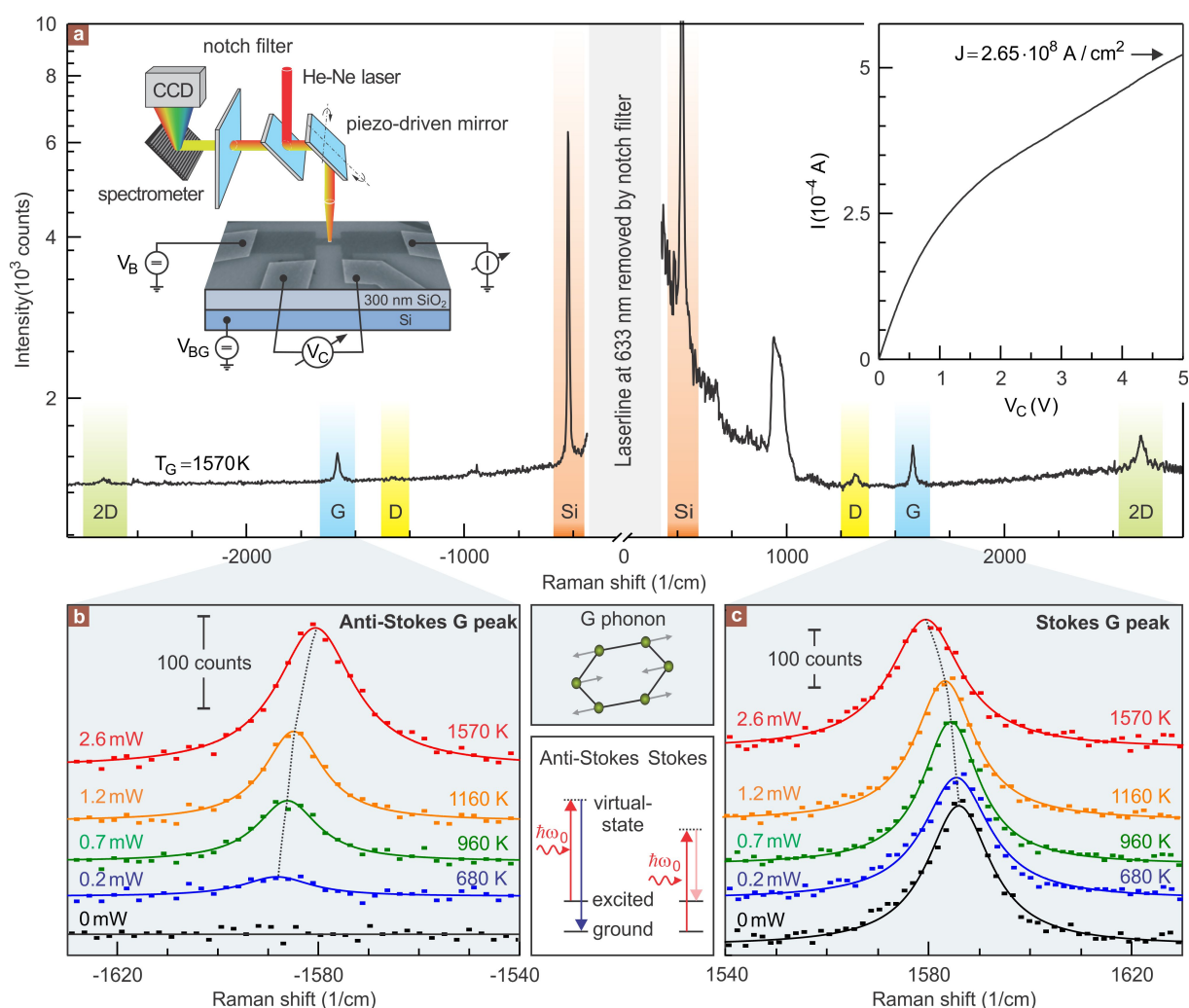
Figure 6.1.: *Overview over Raman spectra of an electrically biased graphene constriction.* (a) Stokes and anti-Stokes Raman spectra taken when 2.6 mW of electrical power is dissipated in the constriction. The prominent Raman peaks of graphene (G, D, and 2D modes) are marked as well as the Si peak around 520 cm^{-1}. The left inset depicts the measurement arrangement. It consists of a scanning confocal Raman spectrometer and a typical graphene constriction with a width of 0.6 µm and a length of 1.5 µm. The right inset shows the current-voltage characteristic measured at zero backgate voltage across the constriction. (b) Anti-Stokes and (c) Stokes peaks of the G-mode acquired for zero up to 2.6 mW of dissipated electric power at the constriction. The spectra are fitted with Lorentzians (solid lines). They were shifted vertically for clarity. The effective temperature of the G-phonon was extracted from the intensity ratio of the Stokes and anti-Stokes lines. This temperature has been included near each curve. The upper central inset displays the in-plane stretching eigenmode (G-phonon) in graphene. The bottom inset contains schematic diagrams for the Stokes and anti-Stokes Raman scattering processes.

find the constriction and precisely position the laser spot. With the same method, spatially resolved Raman spectra were acquired. All measurements were carried out at room temperature in vacuum with a pressure below $3 \cdot 10^{-6}$ mbar to avoid unintentional contamination. Stokes and anti-Stokes Raman spectra were measured simultaneously using a notch filter. The power of the incident laser light was optimized and fixed at 2.7 mW in order to simultaneously obtain an acceptable signal-to-noise ratio and avoid excessive heating of the graphene by the laser beam itself. For the recorded spectra the typical integration time was 60 seconds.

6.3. Experiment

The data displayed in Figures 6.1, 6.2, 6.4 and 6.5 are recorded on one and the same device. Altogether three devices were measured. They showed the same generic features. Prior to the Raman experiments, the graphene devices were cleaned by current annealing [129] in order to remove molecular adsorbates and contaminants due to the fabrication procedure and exposure to the ambient. Apart from the source and drain contacts, the geometry includes voltage probes at either end of the constriction to monitor the voltage drop V_C across the constriction. The current-voltage characteristic $I - V_C$ at zero back-gate voltage is plotted in the right inset of Figure 6.1 (a). Note that the four-terminal configuration ensures that the calculated dissipated power IV_C does not include the unsolicited power dissipation due to the contact resistances at the source and drain. According to field effect measurements, charge neutrality is reached close to a back-gate voltage of -8 V which corresponds to an electron density of $n \approx 5.7 \cdot 10^{11}$ cm^{-2} and a Fermi energy of $\approx$ 90 meV.

Figure 6.1 (a) shows the Stokes and anti-Stokes Raman spectrum measured across the accessible spectral range for laser excitation at a wavelength $\lambda_0 = 632.8$ nm. It has been recorded at the center of the constriction for an electric power dissipation of 2.6 mW. Here, we will focus on the optical G-phonon Raman peak. It is attributed to an in-plane stretching mode of the carbon atoms ([74] and Subsection 3.2.1) as shown in the upper cartoon between panels (b) and (c) of Figure 6.1. Figure 6.1 (b) illustrates the behavior of the anti-Stokes G peak as a function of the dissipated electric power IV_C. The corresponding spectra for the Stokes G peak are plotted in Figure 6.1 (c). From the intensity ratio of the Stokes (I_S) and anti-Stokes (I_{AS}) G peak, it is possible to extract the occupation number of the G-phonons or alternatively the effective temperature T_G describing their Bose-Einstein distribution probability using the following equation:

$$\frac{I_{AS}}{I_S} = \left(\frac{\omega_0 + \omega_G}{\omega_0 - \omega_G} \right)^4 \exp \left(-\frac{\hbar \omega_G}{k_B T_G} \right)$$

Here $\hbar\omega_0$, $\hbar\omega_G$, $\hbar$ and k_B are the energy of the incident photons, the G-phonon energy, and the Planck and Boltzmann constants. The temperature T_G is obtained by fitting the Stokes and anti-Stokes lines to Lorentzians, taking into account the wavelength-dependent sensitivity of the detection system for the Raman peaks which we determined for each wavelength by comparing the spectrum from a calibrated tungsten light source with that of the theoretical black body curve and calculating the intensity ratio according to the

above equation for a photon energy $\hbar\omega_0 = 1.959$ eV. The temperature value has been included near each curve in panels (b) and (c) of Figure 6.1. An anti-Stokes line can be observed starting from about 500 K. The absence of an anti-Stokes feature in the bottom trace of Figure 6.1 (b) for zero electric power confirms that the incident laser light for recording the Raman data does not raise the local temperature of the G-phonons above 500 K. The temperature of the Si bulk substrate, located 300 nm below the flake, was calculated from the Si lines [126] at $\pm$ 520 cm^{-1}. It was approximately 300 K independent of the incident laser power up to the maximum of 2.7 mW. At the highest electric power dissipation in the constriction, the temperature of the Si substrate underneath rises by about 10 K.
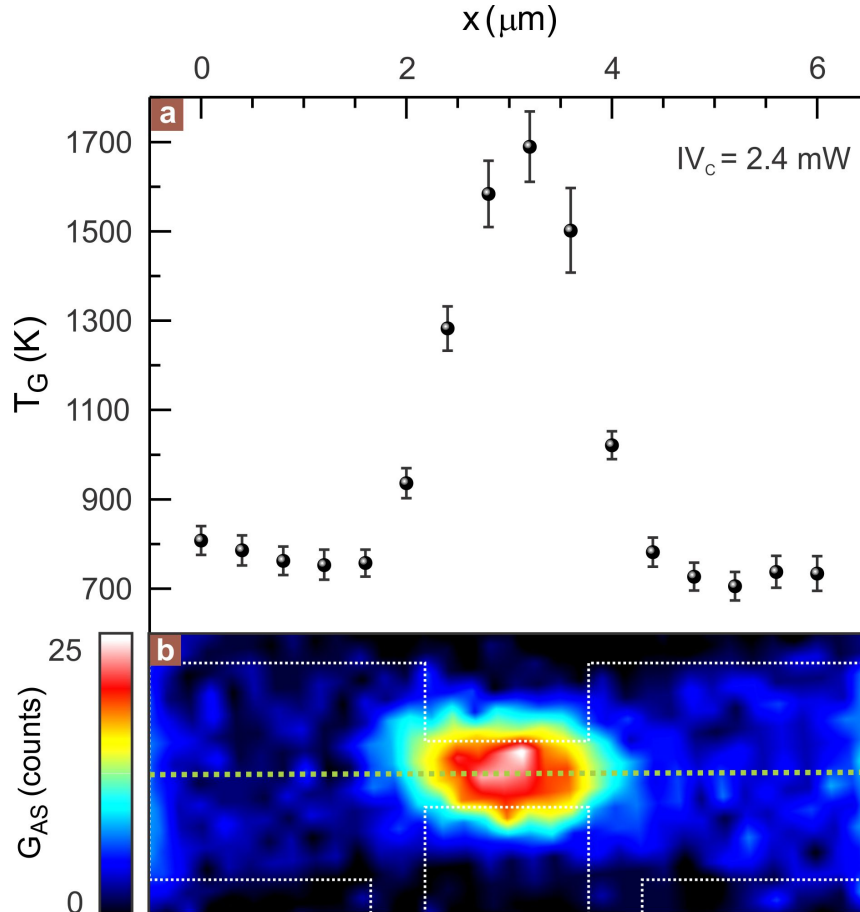
Figure 6.2.: *Spatial profile of the effective G-phonon temperature T_G across the device and the anti-Stokes spatial Raman map.* (a) Crosssectional profile of the effective temperature of the G-phonons T_G at a dissipated power of 2.4 mW. The effective temperature at the center is significantly higher than in the wide graphene regions close to the electrodes. The maximum value is larger than 1600 K. (b) Color map of the anti-Stokes G-mode intensity acquired at a dissipated power of 2.4 mW. Red (blue) corresponds to a high (low) intensity value and hence high (low) temperature. The white dotted line demarcates the etched graphene flake.

The spatial profile of T_G along the constriction for 2.4 mW of electric power dissipation was obtained by recording Raman spectra as a function of position with a spatial resolution of 400 nm. The outcome of this experiment is depicted in Figure 6.2 (a). At

the center of the constriction T_G is raised above 1600 K, indicating that it is possible to generate a large nonequilibrium population of G-phonons with electrical biasing. Outside of the constriction region, T_G is nearly position independent and equal to 750-800 K. By comparing the current density in this region to the measured data at the constriction, we expect a temperature around 600-700 K. This indicates that the elevated temperature outside of the constriction is also mainly caused by Joule heating. A spatial map of the anti-Stokes G peak intensity is plotted in Figure 6.2 (b). This color rendition was recorded on a 0.2 μm spatial grid with an integration time of 10 s for the same electric power dissipation of 2.4 mW. A hot spot is clearly visible at the constriction and confirms that power dissipation mainly takes place in this region.

On another device with the same constriction geometry (constriction width of 0.6 μm and a length of 1.5 μm) but only two terminals, experiments were carried out up to breakdown. Figure 6.3 (a) depicts the IV characteristics. During the acquisition of the IV curve, optical microscope images of the device were captured with a CCD camera and white source illumination. Inset (b) in Figure 6.3 shows an initial reference snapshot taken with low power applied to the device schematically pictured in inset (d) with the electric contacts (yellow) and the etched graphene constriction (blue). When ramping up the voltage the constriction starts to glow and emit visible radiation above a current density of $j \approx 1.4$ mA/μm (this corresponds to $J \approx 4 \cdot 10^8$ A/cm^2 with a monolayer thickness of 0.35 nm) as shown in inset (c) at a voltage of about 10 V. The current through the device eventually saturates at high bias voltage and finally the graphene constriction burns out as signaled by the sharp current drop when an even higher voltage is imposed. Comparable to the high current densities reported for carbon nanotubes [118], the maximum current density sustained by the graphene constriction prior to breakdown was larger than 1.6 mA/μm (J $> 4.5 \cdot 10^8$ A/cm^2).

Figure 6.4 (a) plots the G-phonon temperature as a function of the dissipated electric power at the center of the graphene constriction. Data points extracted from the Raman spectra displayed in panels (b) and (c) of Figure 6.1 are shown in the same color as these spectra.
The intensities of the Stokes and anti-Stokes G peak are affected by power dissipation, and also the position and the full width at half-maximum (FWHM) of these Raman modes change. We first address the position of these Raman features. Figure 6.4 (b) plots, for instance, the shift of the Stokes G peak position G_S as a function of the calculated G-phonon temperature T_G. G_S shifts downward with increasing T_G or equivalently with increasing IV_C. The temperature-dependent shift in Figure 6.4 (b) is qualitatively consistent with previous experimental results [130] and theoretical predictions [131]. According to theory [131], the thermal lattice contraction in graphene leads to a minor shift. Furthermore, this shift would be in the opposite direction. The dominant contribution to the line shift comes from anharmonic effects, which include three and four phonon scattering processes [131]. In covalent semiconductors [126], semimetals [128], and metals [127] the anharmonic phonon contribution prevails. For the sake of completeness, we note that also the charge carrier density influences the position of the G_S-line [104,105]. Adsorbates may be removed as the flake gets heated (Chapter 5 and [132]). However, field effect measurements recorded after each experiment at a different value of IV_C show that charge
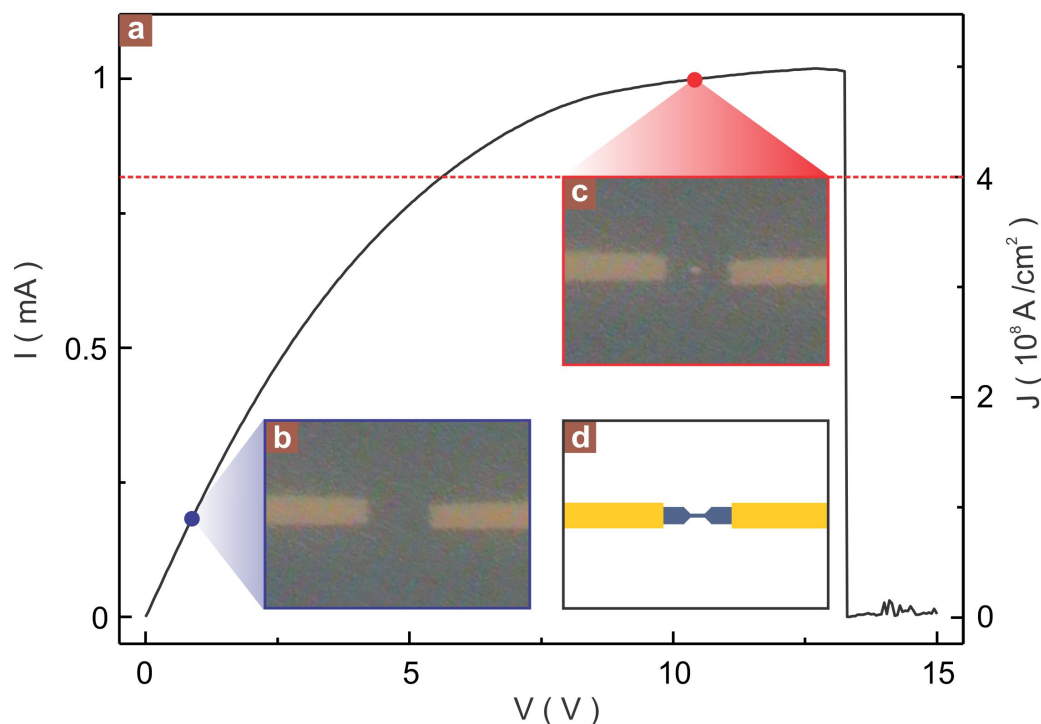
Figure 6.3.: ***Voltage-current characteristic of a graphene constriction up to breakdown.*** *A schematic of the device with the electrodes (yellow) and the graphene constriction (blue) is depicted in inset (d). The electrodes are recognizable in the optical image in inset (b) captured at a low voltage. The initially linear IV-curve deviates and becomes sub linear for higher voltages before it eventually saturates at a constant current. Once the current density is higher than $j > 1.4$ mA/μm the constriction starts to glow and emit visible radiation as shown in inset (c). Imposing an even higher voltage leads to the destruction of the constriction as signaled by the sudden drop in current. The maximum current density sustained by the graphene constriction prior to breakdown exceeded 1.6 mA/μm.*

neutrality remains at the same back-gate voltage and no further dopants are removed. Most dopants were already removed during the annealing step prior to the experiments. Unintentional electrostatic gating when applying a large source-drain bias voltage may also modify the carrier density; however the effect was found to be negligible. Extended exposure to intense laser light may also produce changes in the G peak position (Chapter 5 and [132]). To exclude that this effect occurred under the conditions of the present experiment, Raman spectra were compared at zero dissipated electric power before and after each measurement. No changes were observed. Quantitatively, the decrease of G_S for a given ΔT_G is much smaller than that for an equilibrium experiment in which an identical temperature change is accomplished by heating the entire substrate with an electrical current as depicted in Figure 6.4 (c) and (d). The data collected during such an experiment using another graphene flake are plotted in Figure 6.4 (d). The Stokes line red shifts linearly at a rate of approximately 3.2 cm^{-1} for a temperature change of 100 K. The discrepancy between the experiment with a heated substrate and the experiment with local power dissipation in the constriction reflects the nonequilibrium character of
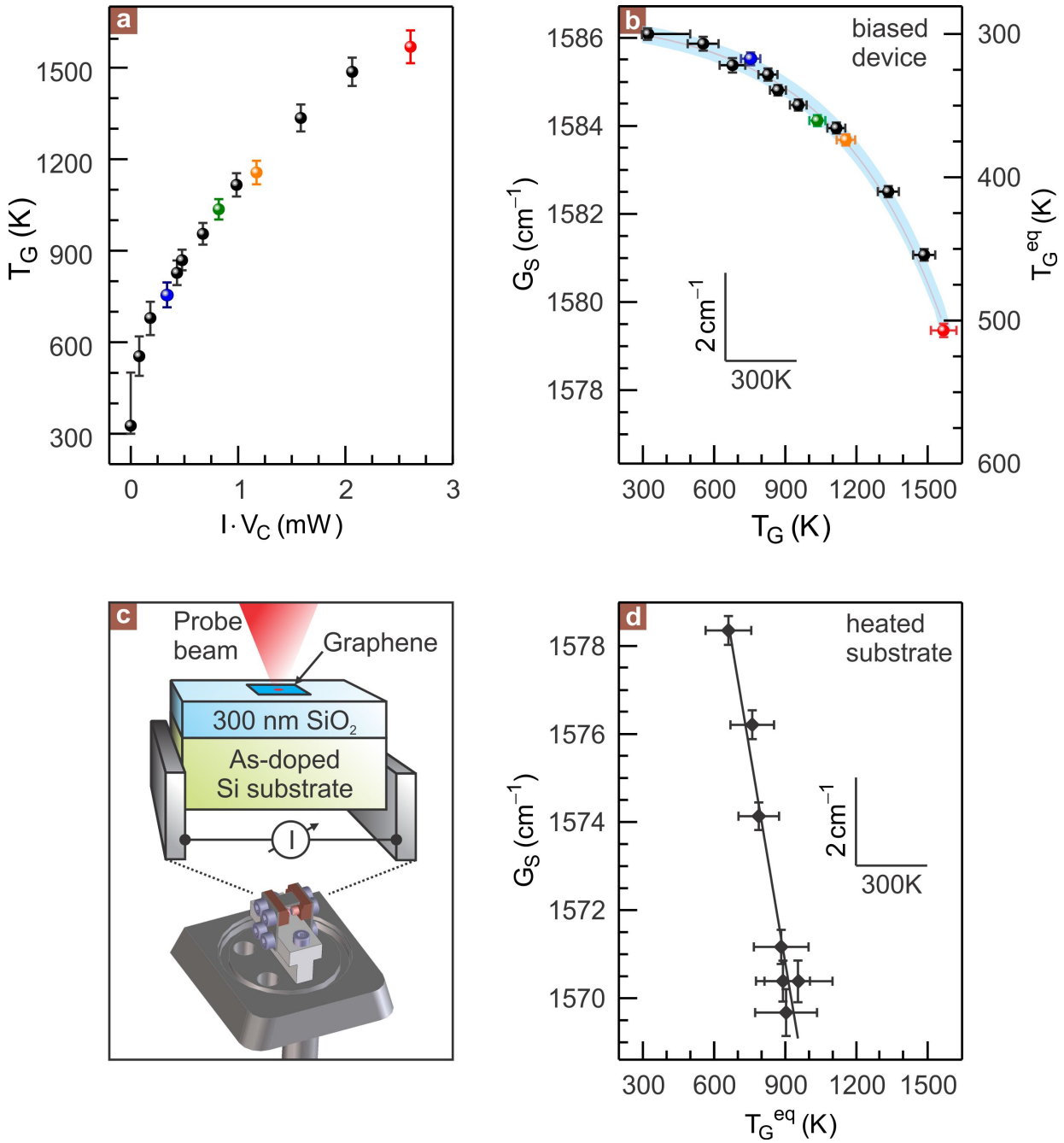
Figure 6.4.: *Power dependence of the effective G-phonon temperature and Raman shift of the Stokes G-mode as a function of T_G or T_G^{eq}. (a) Effective temperature of the G-phonons at the center of the graphene constriction as a function of the dissipated electrical power IV_C. (b) Shift of the G_S-line as a function of T_G (left and bottom axes) for local heating at the constriction. T_G is determined from panel (a). T_G^{eq} (right ordinate, determined from panel (d)) gives the equilibrium temperature required to obtain the same G_S shift. The color-coded circular data points in (a) and (b) are extracted from the Raman spectra displayed in panels (b) and (c) of Figure 6.1. (d) Shift of the Stokes G peak as a function of the equilibrium temperature T_G^{eq}. In this experiment, the entire sample is heated by driving an electrical current through the conducting Si substrate without backside metalization (c) and the temperature is determined from the Stokes to anti-Stokes ratio of the G peak.*

the G-phonon population near the constriction. It is instructive to determine the required equilibrium flake temperature in order to obtain the same G_S-line shift as for the nonequilibrium experiment. This temperature T_G^{eq} has been plotted as the right ordinate in Figure 6.4 (b).

We now turn our attention to the behavior of the FWHM of the G_S-line with increasing electric power dissipation or equivalently increasing T_G. The experimental data are summarized in Figure 6.5 (a). The FWHM slightly increases by 0.5 cm^{-1} for a T_G up to about 700 K. Then it decreases by as much as 2 cm^{-1}, and finally it starts to grow again for T_G above $\approx$ 1000 K. The anti-Stokes G-mode also shows a similar dependence. This nonmonotonic temperature dependence of the G-line width is the key experimental observation. The decrease of the FWHM is distinct from the monotonous increase of the FWHM of optical phonons observed in semiconductors [126], other semimetals [128], and metals [127]. As we will show below, this anomalous change of the G-line width is attributed to the electron-phonon coupling in graphene, which is able to compete with anharmonic phonon coupling up to high temperatures. The intrinsic FWHM of the G-mode describes the decay rate of the G-phonons [131]. This decay rate is composed of an electron-phonon and a phonon-phonon scattering contribution denoted as γ_{e-ph} and γ_{ph-ph}. In principle also extrinsic broadening of the FWHM should be considered. For instance, the extrinsic broadening, γ^*, can be attributed to the inhomogeneity of the charge carrier density in the form of electron-hole puddles [32] or the spectral resolution limitation of the detection system. The overall FWHM γ can then be written as follows:

$$\gamma = \gamma_{e-ph} + \gamma_{ph-ph} + \gamma^*$$

The electron-phonon coupling is described by Landau damping. G-phonons annihilate by creating electron-hole pairs. This process is possible even in the limit of absolute zero temperature, provided the chemical potential is positioned within an energy window, which is centered around the Dirac point and whose size is defined by the G-phonon energy (≈ 0.2 eV). The decay rate γ_{e-ph} of the G-phonons is given analytically from Fermis golden rule in the vicinity of the K point of the Brillouin zone under the assumption of a linear energy-momentum dispersion of the charge carriers [133]

$$\gamma_{e-ph}(\mu, T_e) = \gamma_{e-ph}^0 \left(f_{FD} \left(-\frac{\hbar\omega_G}{2} \right) - f_{FD} \left(\frac{\hbar\omega_G}{2} \right) \right) \tag{6.1}$$

Here $f_{FD}(E) = 1/(e^{(E-\mu)/k_B T_e} + 1)$ is the Fermi-Dirac distribution function. γ_{e-ph}^0, μ and T_e denote the FWHM at zero temperature, the chemical potential, and the electronic temperature, respectively. When the chemical potential is located outside the energy interval $\left[-\frac{\hbar\omega_G}{2}, \frac{\hbar\omega_G}{2} \right]$ this decay process is prohibited (at least at absolute zero temperature) by the Pauli exclusion principle and the requirement of energy and momentum conservation. This Pauli blocking results in a long lifetime of phonons and, hence, a small FWHM. The charge carrier density enters γ_{e-ph} via the chemical potential μ. Recently, the influence of the carrier density on the FHWM of the G_S-peak was verified with Raman studies by tuning the carrier density in a field effect device [104, 105]. Here, however the density is fixed and hence does not contribute to a change in the FWHM. As mentioned previously, the amount of chemical doping is not altered during the experiment and the
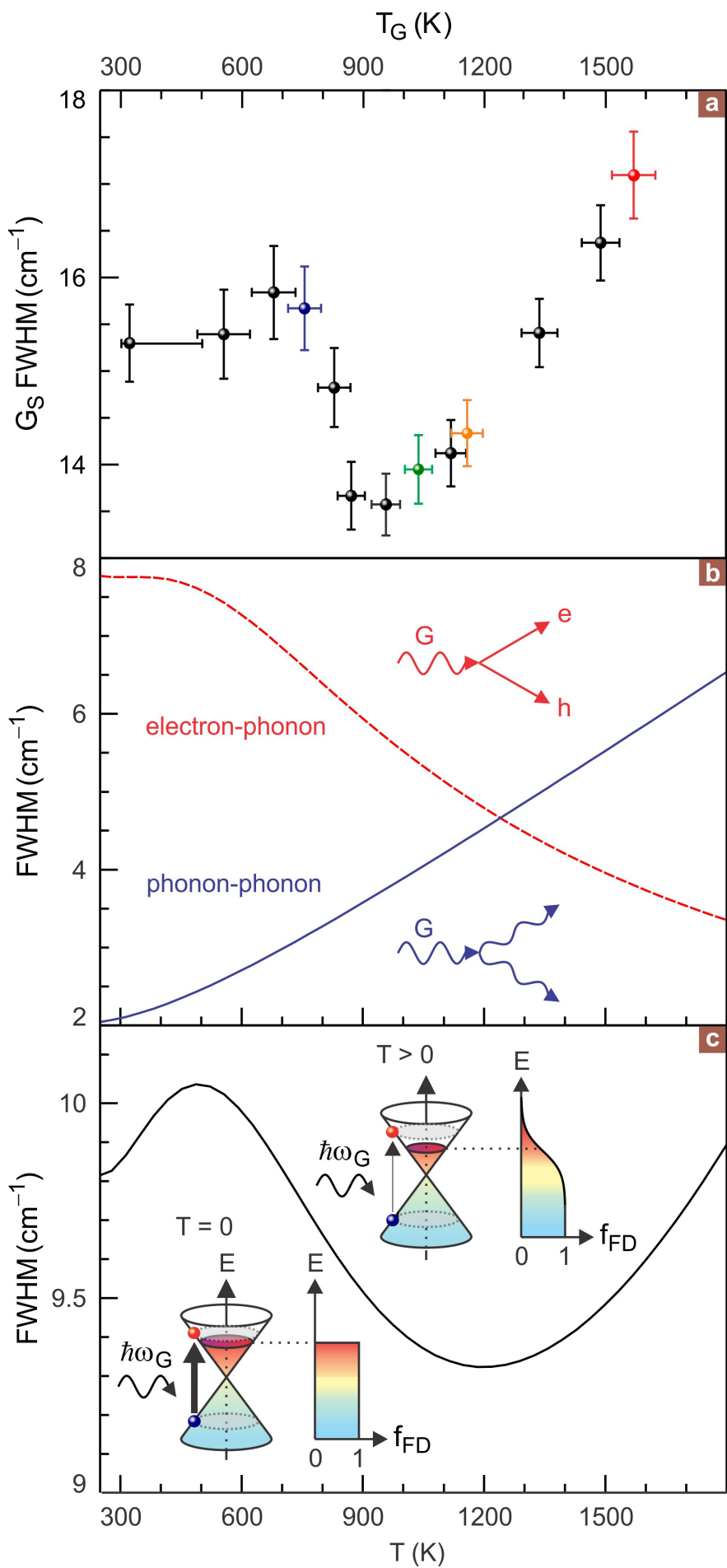
influence of electrostatic gating as a result of the applied source-drain bias voltage remains limited even at the highest electric power dissipation. The observed behavior of the FWHM should therefore be attributed solely to a change of temperature. In our Joule-heated graphene constriction, the electronic temperature T_e is unknown. T_e will increase with increasing power dissipation, but the precise relation with T_G remains inaccessible. Electrons and G-phonons are likely to adopt similar temperatures through rapid mutual scattering if electron-phonon coupling is strong [123, 134]. When μ is located close to the Dirac point, thermal broadening will reduce the number of occupied electronic states near $-\hbar\omega_G/2$ and also the number of empty states near $+\hbar\omega_G/2$. The probability for the generation of electron-hole pairs will drop accordingly with increasing T_e. This case is illustrated in the inset to Figure 6.5 (c). At higher temperatures, however,γ_{ph-ph} will gain in strength and will eventually dominate [131]. In the simplest scenario, G-phonons will decay into two lower energy acoustic phonons [135]. More sophisticated higher order anharmonic processes were considered theoretically [131]. Phonon-phonon coupling produces a monotonic increase of the FWHM as the temperature grows. The competition between electron-phonon coupling and phonon-phonon coupling and the different temperature regimes where these mechanisms prevail can account for the observed nonmonotonic behavior of the Raman G_S-line width.

Figure 6.5 (b) plots the γ_{e-ph} and γ_{ph-ph} contributions separately, while Figure 6.5 (c) shows the sum of both to illustrate that it is possible to obtain the qualitative behavior of the experimental data in Figure 6.5 (a). For simplicity, we consider an equilibrium case where the lattice or phonon temperatures and the electronic temperature are all equal (T). The red dashed curve represents γ_{e-ph} according to equation 6.1. Here, a γ_{e-ph}^0 of 11 cm^{-1} was adopted as determined from density functional theory [131]. The chemical potential was calculated for charge neutrality at a back-gate voltage of -8 V. However, as the density of states is not constant but scales linear with the energy in graphene, a temperature-dependent shift of the chemical potential due to the thermal redistribution of charge carriers [136] was taken into account. This shift is not negligible in the temperature regime covered here. In order to calculate the chemical potential we assume that the net charge carrier density q_0 remains fixed independent of temperature so that $n - p = q_0$

Figure 6.5. (preceding page): *__Line width of the Stokes G-mode as a function of the effective G-phonon temperature.__ (a) Nonmonotonic T_G dependence of the FWHM of the Stokes G-mode. The color-coded data points are obtained from the Raman spectra plotted in the same colors in parts (b) and (c) of Figure 6.1. (b) The electron-phonon (dashed red line) and phonon-phonon (solid blue line) decay contributions to the intrinsic FWHM of the G-mode as a function of temperature. No back-gate voltage is applied, and charge neutrality is reached at -8 V back-gate voltage. (c) The sum of the above two contributions qualitatively predicts the nonmonotonic T dependence of the FWHM seen in the experiment. Note that the extrinsic broadening of the line width due to for instance density inhomogeneity and spectral resolution was not taken into consideration here. The right inset shows the thermal broadening of the Fermi-Dirac distribution at higher temperatures while the left inset shows the corresponding distribution at zero temperature. A temperature increase suppresses the decay of G-phonons into electron-hole pairs.*

where n and p follow from

$$n = \int_0^\infty \rho(\epsilon) f_{FD}(\epsilon, \mu, T_e) d\epsilon = -2 \frac{k_B^2 T_e^2}{\pi \hbar^2 v_F^2} Li_2 \left(-e^{\mu/k_B T_e}\right)$$

$$p = \int_0^\infty \rho(\epsilon)(1 - f_{FD}(\epsilon, \mu, T_e)) d\epsilon = 2 \frac{k_B^2 T_e^2}{\pi \hbar^2 v_F^2} Li_2 \left(-e^{-\mu/k_B T_e}\right)$$

Here, ρ is the density of states for graphene and f_{FD} is the Fermi-Dirac distribution function. $Li_2(x)$ stands for the dilogarithm polynomial function $Li_2(x) = \sum_{j=1}^\infty (x^j/j^2)$. Figure 6.6 depicts the calculated temperature dependence of the chemical potential for $q_0 = 5.7 \cdot 10^{11}$ cm^{-2} which corresponds to the net charge carrier density of the graphene flake when charge neutrality is reached at -8 V back-gate voltage. At zero temperature this corresponds to a chemical potential of 88 meV which drops below 30 meV for temperatures higher than 1000 K.
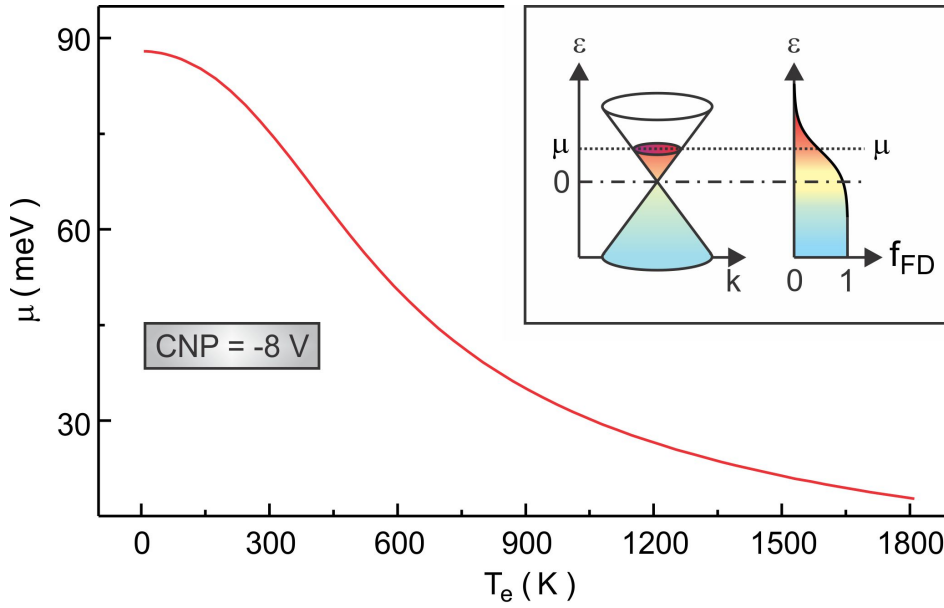

Figure 6.6.: *Temperature dependence of the chemical potential due to thermal redistribution of charges.* *The charge neutrality of the device is reached at -8 V and the corresponding net charge carrier density of $5.7 \cdot 10^{11}$ cm^{-2} is assumed to remain fixed. As the density of states in graphene is not constant but scales linear with energy the thermal redistribution of charge carriers with increasing temperature leads to a decreasing chemical potential as visible in the outcome of the calculation (see text).*

For the anharmonic contribution to the temperature-dependent shape of the Raman line width, we restrict ourselves to an oversimplified model applicable when an optical phonon decays into two acoustic phonons [135]

$$\gamma_{ph-ph} = \gamma_{ph-ph}^0 \left(1 + \frac{2}{e^{\hbar \omega_G / 2 k_B T} - 1}\right).$$

The behavior described by this expression is plotted by the solid blue curve in Figure 6.5 (b). We have used 2 cm^{-1} for γ_{ph-ph}^0 [131]. A theoretical treatment considering more ad-

ditional phonon-phonon decay channels available in graphene was covered theoretically in Ref [131]. Despite the simplifying assumptions, the shape of the temperature-dependent line width depicted in Figure 6.5 (c) qualitatively agrees with the experimental data shown in Figure 6.5 (a). Not only the drop of the line width, but also the small initial increase of the line width is captured by this model. The initial increase stems from phonon-phonon coupling. At intermediate temperatures, the thermal redistribution of charges suppresses the electron-phonon decay channel and the line width drops. At elevated temperatures, phonon-phonon coupling dominates again and imposes a line width increase as the temperature grows. We note that a drop of the line width upon raising the temperature is not always seen in graphene. This only occurs if the chemical potential remains close to the Dirac point and within the energy window of size $\hbar\omega_G$ centered around the Dirac point. For graphene doped at a level higher than $7 \cdot 10^{11}$ cm^{-1}, corresponding to a chemical potential larger than $\hbar\omega_G/2$ the line width drop has vanished. This can easily be understood within the above model. An example is shown in Figure 6.7 (a) where the blue diamonds represent the experimental data corresponding to a carrier density of $\approx 1 \cdot 10^{12}$ cm^{-2} and hence the chemical potential at room temperature is larger than $\frac{\hbar\omega_G}{2}$. The line width no longer shows the clear drop with increasing T_G. The decay of G-phonons through the creation of electron-hole pairs is suppressed as a result of the Pauli exclusion principle and the need for energy and momentum conservation. For comparison the red dots in Figure 6.7 (a) show the situation where charge neutrality is reached at -8 V so that the chemical potential is located inside the window $\pm\frac{\hbar\omega_G}{2}$ and the pronounced drop in line width is apparent. For the sake of completeness we consider theoretically the temperature-dependent behavior of the G peak line width as a function of doping level in Figure 6.7 (b) and (c) within the framework outlined above. Figure 6.7 (b) depicts the electron-phonon scattering contribution for different values of the carrier density (colored lines) as well as the monotonically increasing phonon-phonon contribution (black line) to the G-line width. The carrier density is specified in terms of back-gate voltage and Fermi energy, i.e. the chemical potential at absolute zero temperature. The sum of both contributions is plotted in Figure 6.7 (c) and visualizes the transition from monotonic to nonmonotonic behavior when the chemical potential crosses $\frac{\hbar\omega_G}{2}$.

6.4. Conclusion

The G peak line width drop in graphene is a dramatic manifestation of electron-phonon coupling. It occurs because of graphene's unique properties. It is gapless, the chemical potential can be tuned below half the optical phonon energy $\hbar\omega_G/2$, and local temperatures comparable to $\hbar\omega_G/2$ can easily be reached. In semiconductors, for instance, the band gap usually exceeds the energy of optical phonons and electron-phonon decay remains inactive. In metals and other semimetals, the accessible temperature in experiment is usually 2 orders of magnitude below the Fermi temperature. Thus, the experiments on graphene in this chapter offered a possibility to access a regime where thermal redistribution of charge carriers influence the decay process of optical phonons due to the electron-phonon coupling.
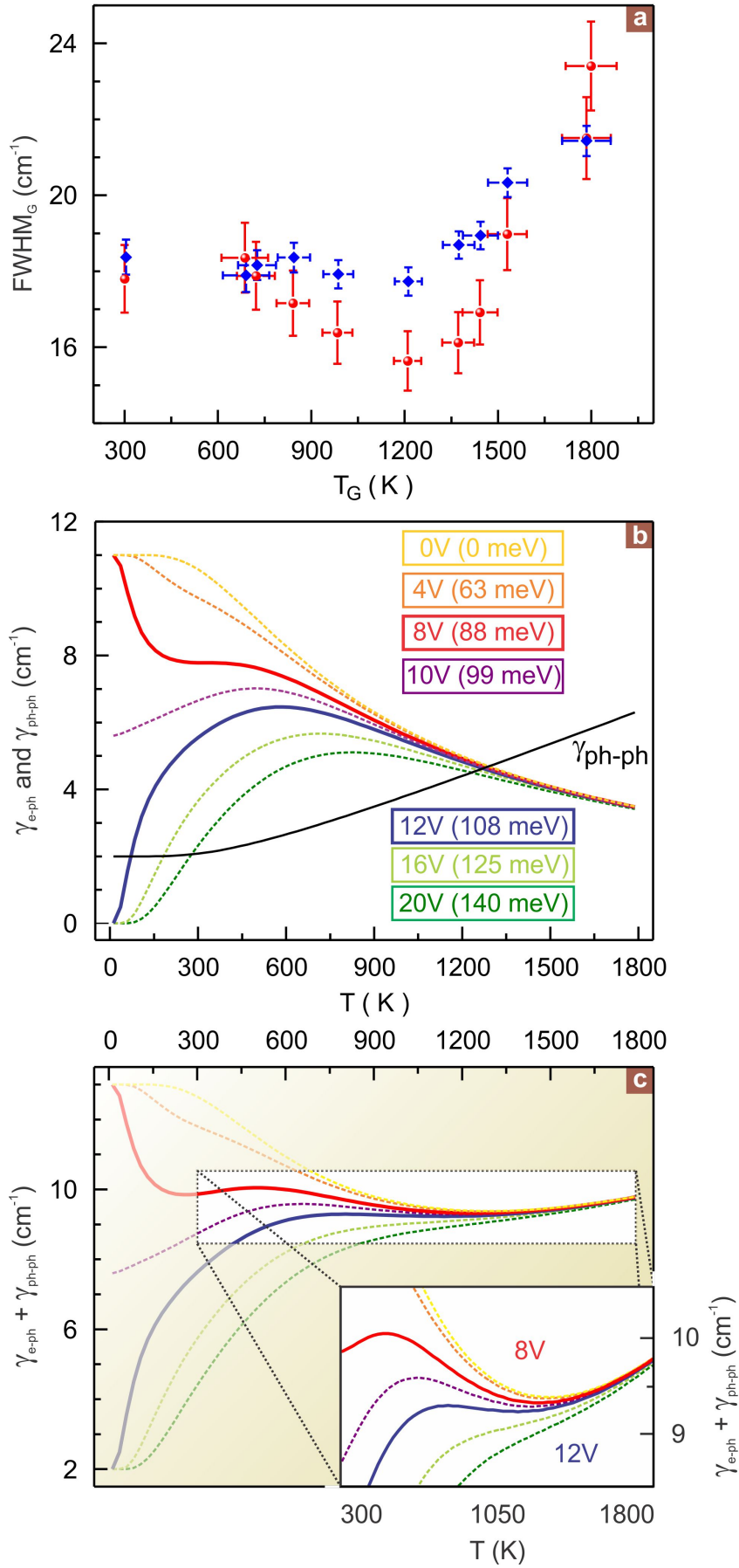
Figure 6.7. (preceding page): ***Theory and experiment for different chemical potentials.*** *(a) Measured line width for two different chemical potentials, one outside (blue diamonds) and one inside (red dots) the energy window $\pm\frac{\hbar\omega_G}{2}$. Only the red dots show the clear drop with increasing T_G. (b) Theoretical electron-phonon and phonon-phonon scattering contributions to the line width for various chemical potentials as denoted in the graph. The sum of the two contributions is given in (c) and resembles the experimental data.*

7. Raman Scattering at Pure Graphene Zigzag Edges
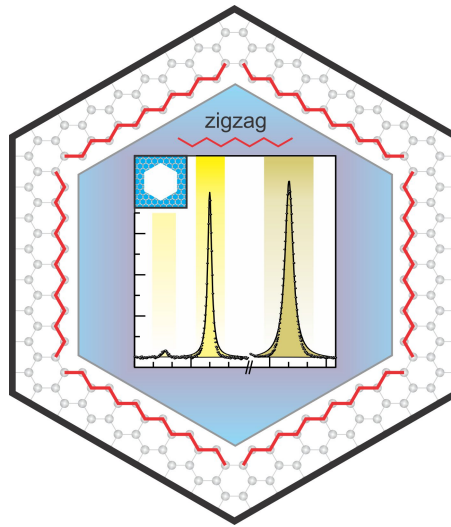
Theory has predicted rich and very distinct physics for graphene devices with boundaries that follow either the armchair or zigzag crystallographic directions. A prerequisite to disclose this physics in experiment is to be able to produce devices with boundaries of pure chirality. Exfoliated flakes frequently exhibit corners with an odd multiple of 30°, which raised expectations that their boundaries follow pure zigzag and armchair directions. The predicted Raman behavior at such crystallographic edges however failed to confirm pure edge chirality. Here, we perform confocal Raman spectroscopy on hexagonal holes obtained after the anisotropic etching of prepatterned pits using carbothermal decomposition. The boundaries of the hexagonal holes are aligned along the zigzag crystallographic direction and leave hardly any signature in the Raman D peak intensity map indicating unprecedented purity of the edge chirality. This work offers the first opportunity to experimentally confirm the validity of the Raman theory for graphene edges.

7.1. Introduction

The electronic states associated with a graphene edge have been the focus of intense theoretical research [137–141] even before the experimental isolation of graphene [142,143]. The edge is either formed by carbon atoms arranged in the zigzag or armchair configuration as displayed in Figure 7.1 (a). Zigzag edges are composed of carbon atoms that all belong to one and the same sublattice, whereas the armchair edge contains carbon atoms from either sublattice. This distinction has profound consequences for the electronic properties of the edge states. For instance a ribbon terminated on either side with a zigzag edge has an almost flat energy band at the Dirac point giving rise to a large peak in the density of states. The charge density for theses states is strongly localized on the zigzag edge sites [144]. Such localized states are entirely absent for a ribbon with armchair boundaries. A plethora of different effects associated with the distinct electronic structure of these graphene edges has been predicted by theory including an anomalous quantum Hall effect [145], superconductivity [146] and magnetism [147]. Devices with pure edge chirality to exploit the specific properties of each edge configuration have been put forward. Armchair devices have been proposed as particularly suitable candidates for spin quantum bits [148]. They may offer long coherence times because of the lifted valley degeneracy and the convenient coupling between qubits via Heisenberg exchange. For zigzag ribbons electrostatically controllable valley filter and valves have been dreamed up as devices exploiting the unique features of graphene [149].

To unlock this physics at the edge of graphene, one should first be able to produce devices that possess boundaries with a pure edge chirality and to identify that they have high chiral purity. The observation that mechanically exfoliated flakes frequently exhibit corners with angles that are an odd multiple of 30° initially raised hopes in the community that one edge at such a corner is of the pure zigzag type, while the other possesses the armchair configuration. Atomic resolution scanning tunneling microscopy (STM) and transmission electron microscopy (TEM) at first sight seem predestined to demonstrate that this statement is correct. In practice, however, TEM at the edge is too invasive [150]. The edge is modified in situ and becomes decorated with unintentional dirt (see Section 5.10). STM was successfully used to produce and visualize edges on highly oriented pyrolitic graphite (HOPG) [151]. However, these edges are not of pure chirality and since flakes are commonly produced on an insulating SiO_2 layer STM is hampered.

7.2. Raman scattering at the edge

Inelastic light scattering has been put forward as a potential technique to unequivocally distinguish clean armchair and zigzag edges [152]. The so-called defect or D peak serves as the litmus test. This peak originates from a double resonance process ([83] and Chapter 3). One of the possible processes [153] is elucidated in Figure 7.1 (b) and (c) in momentum space. An electron-hole pair is created (illustrated by the green arrow) by an incoming photon with energy $\hbar\omega_{in}$ in one of the valleys located at the K-point (or K') of the Brillouin zone boundary. The electron (or hole) is then inelastically scattered

by a large momentum ($\vec{q}$) zone boundary phonon (black arrow) to an inequivalent Dirac valley at the K'-point (or K-point). An elastic backscattering event returns the electron (or hole) to the original valley, where it completes its Raman roundtrip transition by recombining with its companion hole (or electron) in the course of emitting Raman light at frequency ω_{out}. In view of the small photon momentum, Raman emission occurs only if the elastic backscattering process involves a momentum transfer equal to $-\vec{q}$ (both in absolute value and direction) in order to fulfill overall momentum conservation. This cannot be accomplished by a zigzag edge. Along the crystallographic edge direction, momentum remains conserved. Backscattering can only proceed in a direction perpendicular to the edge. For a zigzag edge the momentum can only be transfered in a direction $\vec{d_z}$ which does not allow the electron to return to the original valley in reciprocal space (Figure 7.1 (a) and (c) red arrow). Conversely, an armchair edge can convey momentum in the proper direction ($\vec{d_a}$). Summa summarum, only an armchair edge would contribute to the Raman D peak. A zigzag edge would remain invisible in the D peak.

Several Raman studies were reported on flakes exhibiting corners that are odd multiples of 30°. In all cases, the Raman D peak from both edges showed similar intensities. The disparity was less than a factor of 2 and the D peak certainly did not vanish for one of the sides as expected and predicted by theory [153–156]. An example is shown in Figure 7.1 (d). Here, the Raman measurements were performed with a scanning confocal setup using a solid state laser with a wavelength of 488 nm and an intensity of 7 mW focused to a diffraction-limited spot size of approximately 400 nm. To record Raman maps, the position of the laser spot remains fixed and the sample is raster scanned on a grid with a step size of 200 nm. At each position the backscattered light is dispersed in a monochromator and detected with a Peltier cooled charge coupled device (CCD) with an accumulation time of 1 s. This short accumulation time ensures that no laser induced increase of the D peak occurs due to the gradual disassembly of the graphene flake (see [132] and Chapter 5). Such inadvertent laser induced modifications of the graphene flake are excluded by comparing Raman spectra recorded before and after scanning the sample. The incident laser light can be linearly or circularly polarized. For linearly polarized light the matrix element for the edge assisted Raman transition is maximum when the polarization vector is aligned with the edge and falls as $cos^2\theta$ when it is at angle θ. To avoid this angular dependence and the need for adjustment of the polarization direction, the experiments were carried out with circularly polarized light. From these experiments on mechanically exfoliated flakes either one of two conclusions must be drawn: the theory on the inelastic light scattering at the graphene edge is flawed or neither of the edges microscopically consists of pure zigzag chirality even though the average direction aligns with the zigzag crystallographic orientation. Most likely, the second scenario holds, and both edges are composed of a mixture of both zigzag and armchair sections [154]. Note that there are no geometrical constraints which would prevent forming an edge solely out of armchair terminated sections with a different orientation so that on average the edge follows the zigzag crystallographic direction.
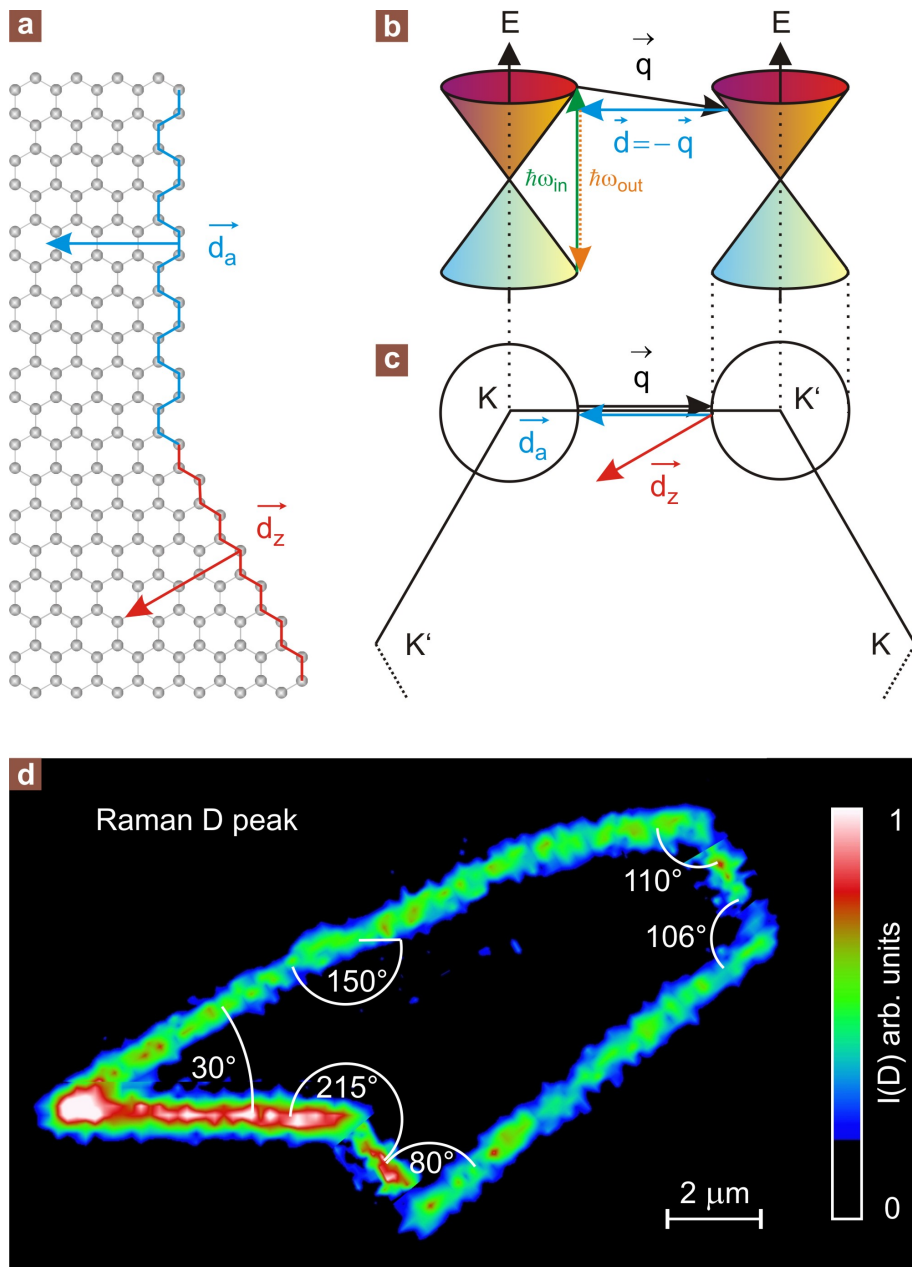
Figure 7.1.: *Raman double resonance mechanism in graphene and at the edge. (a) Atomic structure of the edge with armchair (blue) and zigzag (red) chirality. The edge can transfer momentum along the defect wave vector $\vec{d}_a$ and $\vec{d}_z$ (blue and red arrows, respectively). (b) Schematic illustration of the double resonance mechanism responsible for the defect induced D peak (see text). (c) First Brillouin zone of graphene and the double resonance mechanism in top view. Only the armchair edge supports elastic intervalley scattering of the electrons or holes. (d) Spatially resolved Raman D peak intensity of a micromechanically cleaved graphene sample. The angles were determined from an AFM image (not shown).*

7.3. Anisotropic etching of graphene

This observation has stimulated the search for anisotropic etching procedures [157] that rely on the distinct chemical stability and reactivity of both edge types (there exist plenty theoretical calculations, see for instance [158–163]). Recently two experimental techniques have emerged. The first method relies on the dissociation of carbon exposed at the graphene edge into Ni nanoparticles, which subsequently act as catalysts for the hydrogenation of carbon at a temperature of approximately 1000°C [164–166] and Figure 7.2. This procedure cuts a network of trenches with a width equal to the metallic particle size. This network is random since it was not possible to guide the nanoparticles along specific trajectories. In the case of graphene, up to 98 % of these trenches are at angles that are an even multiple of 30° suggesting that these align nearly all along equivalent crystallographic directions of either the zigzag or the armchair type.
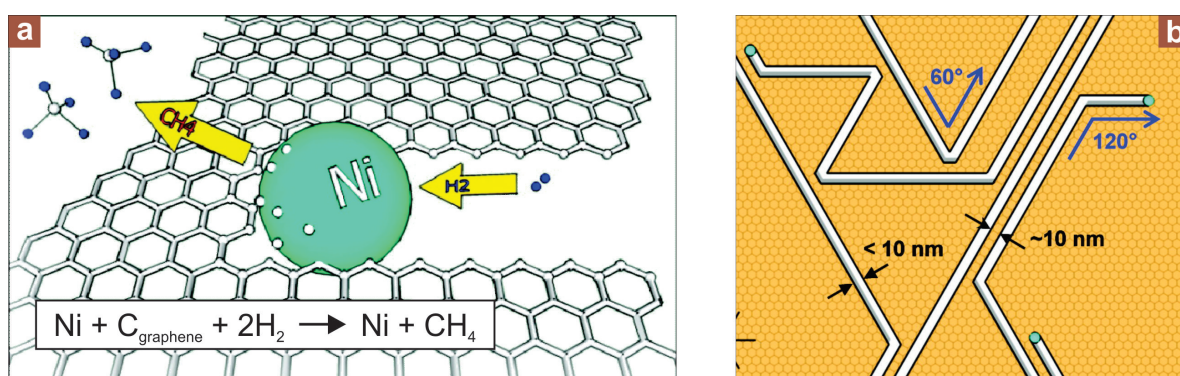
Figure 7.2.: ***Cartoon of a Ni particle etching a graphene sheet (a) and the resulting pattern (b).*** *Modified from [166].*

A second method is based on the carbo-thermal reduction of SiO_2 to SiO which consumes carbon from the edge in the process [167]. Also, residual oxygen from the ambient is involved in the reaction. A summary of the different reactions is shown in Figure 7.3. The reaction is done in argon at a temperature around 700°C. It converts unintentional defects or prepatterned round holes into hexagons all of which have their sides aligned along the same crystallographic orientation. The orientation of the flake was verified using atomic resolution STM images away from the edge but in the vicinity of the etched holes and the edge direction was confirmed to be along the zigzag direction. An example of these hexagons is displayed schematically in Figure 7.5 (c) and atomic force microscopy images (AFM) are depicted in Figures 7.4 (d) and 7.6 (d). From these results one can conclude that carbon atoms forming an armchair edge have a higher reactivity rate under these experimental conditions and hence boundaries with carbon atoms arranged along the zigzag crystal orientation remain. For the work presented here the graphene samples were prepared by micromechanical cleavage on a silicon substrate with a 90 nm thick SiO_2 layer. Two types of samples were fabricated. One set with round etch pits were produced by annealing graphene at 550°C for 30 minutes in a quartz tube oven in a constant flow of Ar (99.999%) and O_2 (99.9995%) gases. The flow rates of the gases were 1050 ml/min and 1200 ml/min for the Ar and O_2, respectively. Samples with hexagonal etch pits were obtained with a two step procedure:
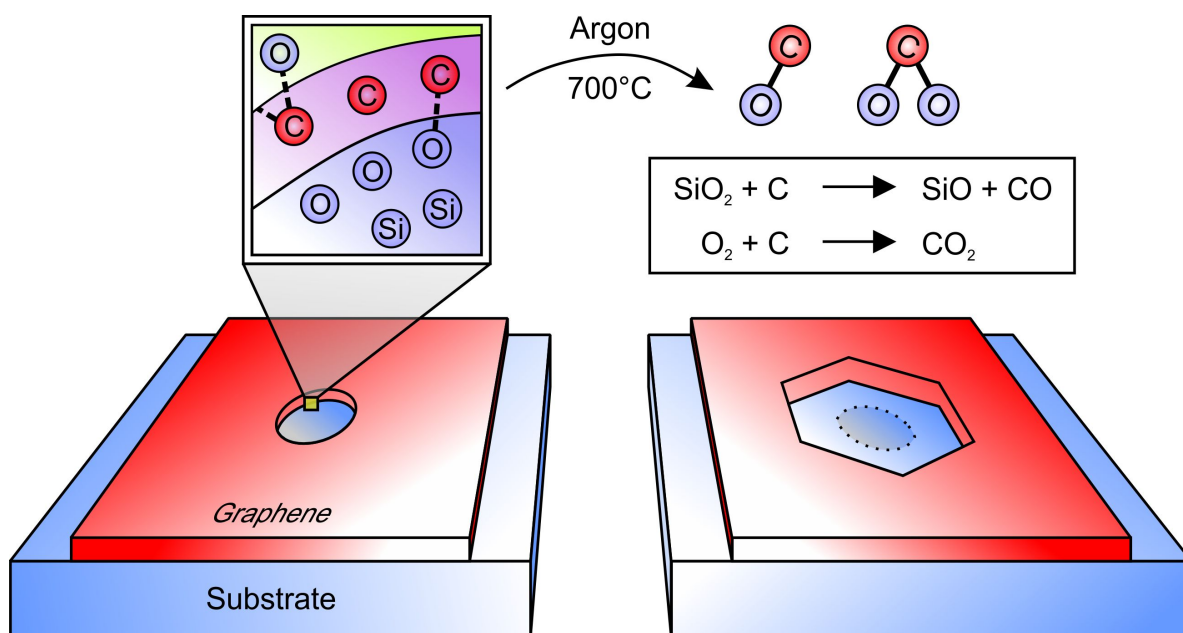
Figure 7.3.: ***Schematic of anisotropic carbothermal etching.*** *Carbon from the edge of a prepatterned hole in graphene reacts at a temperature around 700°C in an argon atmosphere with the oxygen from the substrate as well as with residual oxygen from the argon gas. The reaction rate for carbon atoms forming an armchair edge is slightly higher under these conditions. Consequently, a hexagonal hole forms with carbon edge atoms arranged along the zigzag direction.*

1. An AFM tip was used to carve small holes in the graphene layer by indentation (Figure 7.4 a).

2. These holes serve as seeds for the growth of the hexagonal etch pits during the carbo-thermal reduction.

The reaction takes place at 730°C under a constant flow of Ar (1050 ml/min) for a total time of 4 hours and 45 minutes.

7.4. Experiment

The Raman investigations were carried out on samples prepared with this carbo-thermal method producing hexagonal holes. For the sake of comparison we also examine edges of round holes in graphene obtained under conditions where etching is isotropic (see Section 7.3). For round holes such edges consist inevitably of a mixture of armchair (blue) and zigzag (red) sections as depicted in a cartoon-like fashion in Figure 7.5 (a). Figure 7.6 displays Raman maps of the D peak intensity in (c) and (f) as well as the G peak intensity in (b) and (e) for the round (top panels) and hexagonal holes (bottom panels). The G peak associated with the zone-center in-plane stretching eigenmode [74, 85] reveals sp^2 carbon-carbon bonds. White and black corresponds to high and zero intensity, respectively. Obviously, the intensity is low inside the round and hexagonal holes as can be
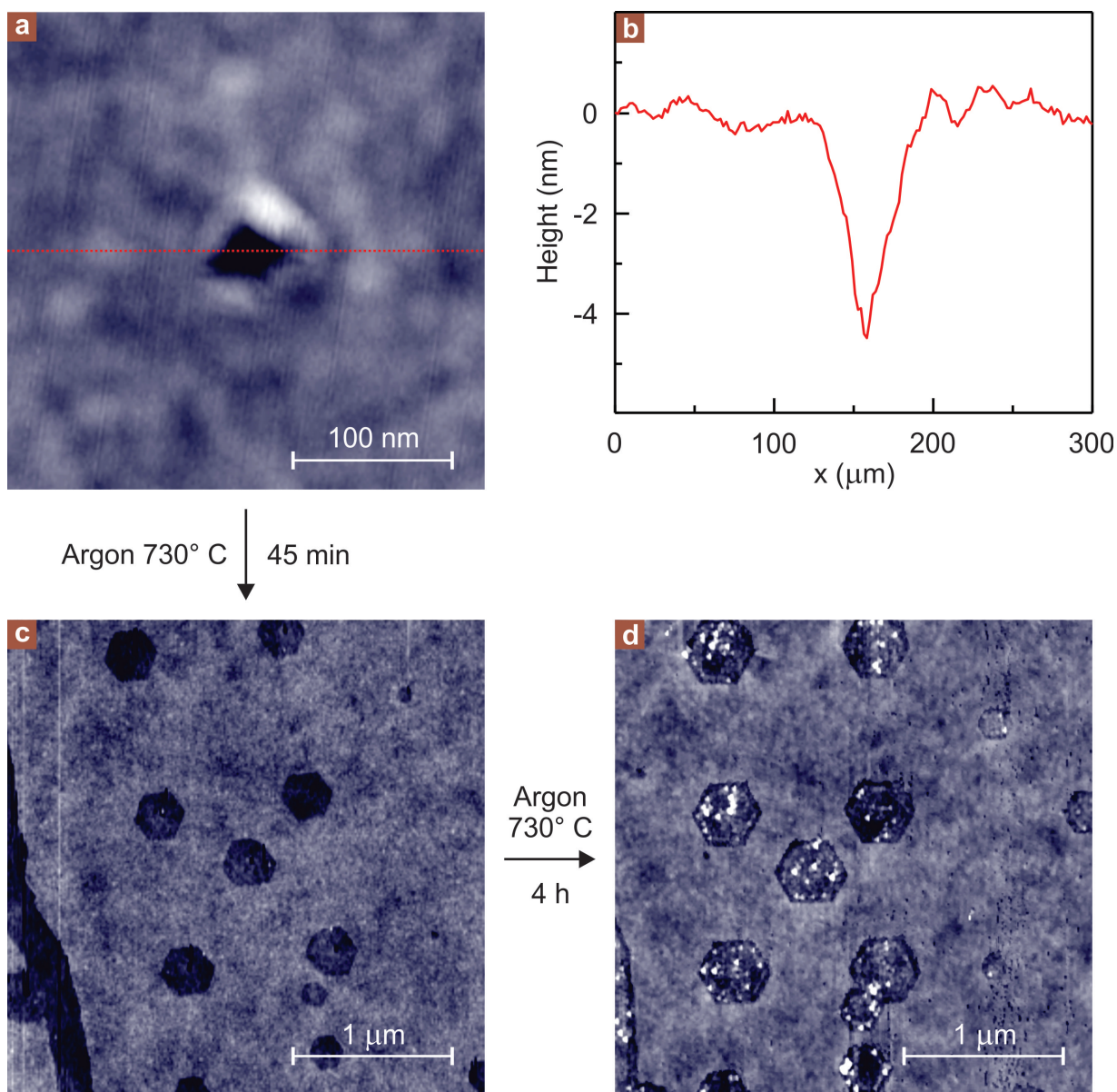
Figure 7.4.: ***Successive steps in the fabrication process of hexagonal holes.***
(a) 4 nm deep AFM indentation mark on the graphene layer. Such indentation marks rupture the graphene layer and serve as starting points for the carbo-thermal reaction. (b) Cross-section of the indentation mark obtained at the red dashed line in (a). AFM images of the hexagonal etch pits at different stages of etching are displayed in (c) for the initial 45 minutes of etching and (d) the same region of the sample, after additional 4 hours of etching. The pits increase in diameter and the hexagonal structure becomes more pronounced.
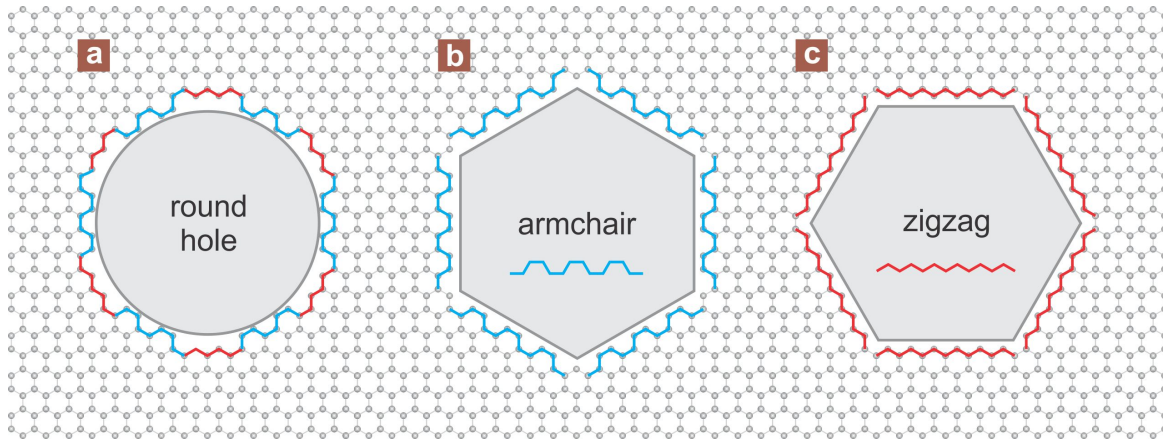
Figure 7.5.: ***Lattice model for the edges of round and hexagonal holes.*** *(a) The edge of a round hole is bound to consist of a mixture of zigzag (red lines) and armchair (blue lines) sections. Holes fabricated by oxygen treatment have rough edges. For the hexagonal holes two cases are possible: the circumference is built from either (b) armchair or (c) zigzag segments only.*

verified by comparing with the AFM images on the left. The intensity does not vanish because the diffraction limited laser spot is comparable in size with the etched holes. The D peak intensity is large near the round holes (Figure 7.6 (c)). The important result can be seen in Figure 7.6 (f) in the D peak intensity map of the sample with hexagonal holes. The intensity is homogeneous across the sample, and no maxima appear near the edge of the hexagonal holes as it is the case for round holes. Figure 7.7 compares the full Raman spectrum recorded at the round hole marked with the red square in Figure 7.6 (a) with the spectrum obtained from the hexagonal hole demarcated in blue in Figure 7.6 (d). As the intensity of all Raman peaks also depends on, e.g., the amount of graphene probed, laser intensity etc., it is common not to look at the absolute intensity but rather at the ratio of two peaks. Here we focus on the ratio of the D to the G peak intensity I(D)/I(G). The G peak intensity is normalized to 1 in this and all other Raman spectra. The D peak intensity then reflects immediately the ratio I(D)/I(G). From Figure 7.7 (b) and (f) it is obvious that the D peak intensity for the hexagonal hole is one order of magnitude smaller than that for the round hole (26%). Some statistics are collected in Figure 7.8. It displays the measured ratio for seven round holes (red region) and for the seven hexagonal holes displayed in Figure 7.7 (e) (blue region). Also included in the plot is the D peak intensity for regions without holes (bulk). It is not zero but approximately equal to 0.02 (see Figure 7.7 (c) and (g)). We attribute this to some imperfections generated during the preparation of the sample [168]. This background is also visible in the Raman map in Figure 7.6 (c) and (f) and is indicated in Figure 7.8 with the dashed black line. The laser beam exposes part of the bulk region, and the exposed surface represents a large fraction in comparison with the one-dimensional edge. Therefore this background should be subtracted from the measured peak intensities. Taking this into account the ratio I(D)/I(G) for the boundaries of the hexagonal holes is up to a factor of 30 smaller than for the edges of round holes. It points to a strong discrimination between the different crystallographic chiralities.

The attachment of functional groups to graphene may affect the D peak intensity, as these
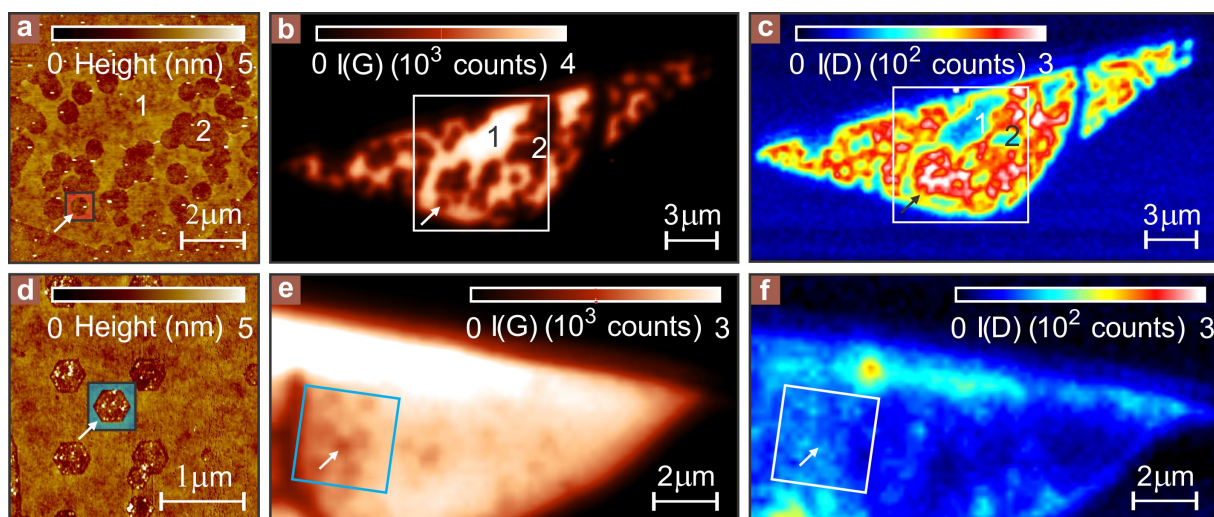
Figure 7.6.: ***AFM images and Raman maps of graphene flakes containing round or hexagonal holes*** *(top or bottom panels, respectively). (a) and (d): AFM images of the round and hexagonal holes. (b) and (e): Intensity map of the Raman G peak. The G peak intensity is uniform across each flake except at the locations of the holes. These holes appear black (no graphene). The region where the AFM image was taken has been demarcated by a square. (c) and (f) Intensity map of the disorder-induced D peak. The D peak intensity is high in the vicinity of round holes (c). On the contrary, the D peak intensity is not enhanced near the hexagonal holes in (f).*

groups can alter the hybridization of carbon atoms from sp^2 to sp^3 or disrupt the lattice symmetry. Since processing steps for the fabrication of round and hexagonal holes differ, the question rises whether the observed differences in the D peak intensity at the edges originate from a different number or type of functional groups, such as for instance hydrogen or oxygen, attached at the edge. This can however be ruled out, since the Raman cross section at visible light excitation for carbon sp^3 bonds is minor compared to the resonance enhancement for C-C sp^2 bonds. In the literature for instance, Raman studies have been reported for hydrogenated graphene [169]. The attachment of hydrogen atoms caused an increase of the D peak intensity. In this case, hydrogen is not only attached at the edge but at the majority of all carbon atoms making up graphene. Despite this large number of sp^3 bonds, the D peak intensity only becomes comparable to the G peak intensity. The area probed in the confocal Raman experiment has a diameter of approximately 1 μm. The sp^3 bonds at the edge only represent a minute fraction of the total number of sp^3 bonds. If hydrogen attachment is restricted to carbon atoms located at the boundaries, it would not be possible to resolve these C-H bonds. The same arguments can be invoked for sp^3 bonds involving oxygen. Here we can also eliminate a possible influence of oxygen by carrying out an experiment in which the graphene edges are chemically reduced if oxygen is available using a solution of 1 mmol ascorbic acid (AA) in 1 liter of water. AA is a nontoxic reducing agent and was demonstrated to successfully reduce graphene oxide [170]. In order to prevent oxygen from reattaching to the graphene sample, the measurements were carried out with the sample still kept in solution. The Raman spectra for the round and hexagonal holes after 24 hours of AA treatment are
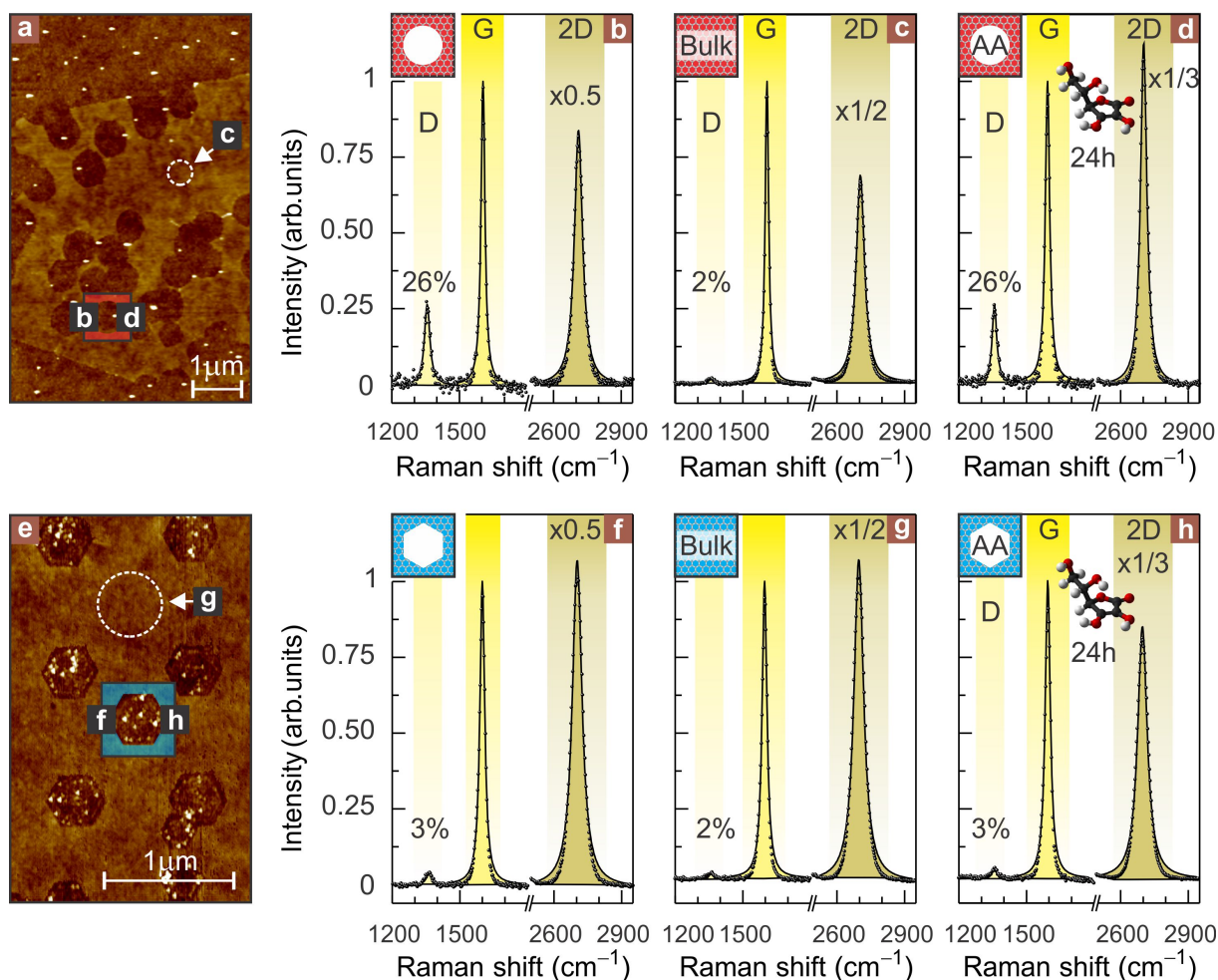
Figure 7.7.: **Raman spectra obtained from a sample with round holes (upper panel) and hexagonal holes (lower panel).** *(a) and (e): AFM images demarcating the positions where the Raman spectra on the right-hand side were obtained. (b) The Raman spectrum of a round hole has a strong D peak, whereas the D peak for a hexagonal hole (f) is minimal and only slightly higher than the surrounding bulk value shown in (c) and (g). The ratio of the D to G peak intensities is included in percentage for each spectrum. (d) and (h): The influence of attached functional groups was ruled out by reducing the samples with ascorbic acid. The Raman spectra resemble the ones before treatment.*

displayed in Figure 7.7 (d) and (h). The spectra were obtained at the same position as for the data recorded in Figure 7.7 (b) and (f). The I(D)/I(G) ratio after this chemical treatment has been included in Figure 7.8 (measurement 9). No change in the I(D)/I(G) ratio occurred. It proves that the edge geometry (zigzag or armchair) is the dominating parameter and that it is not the functional groups attached at the edge.
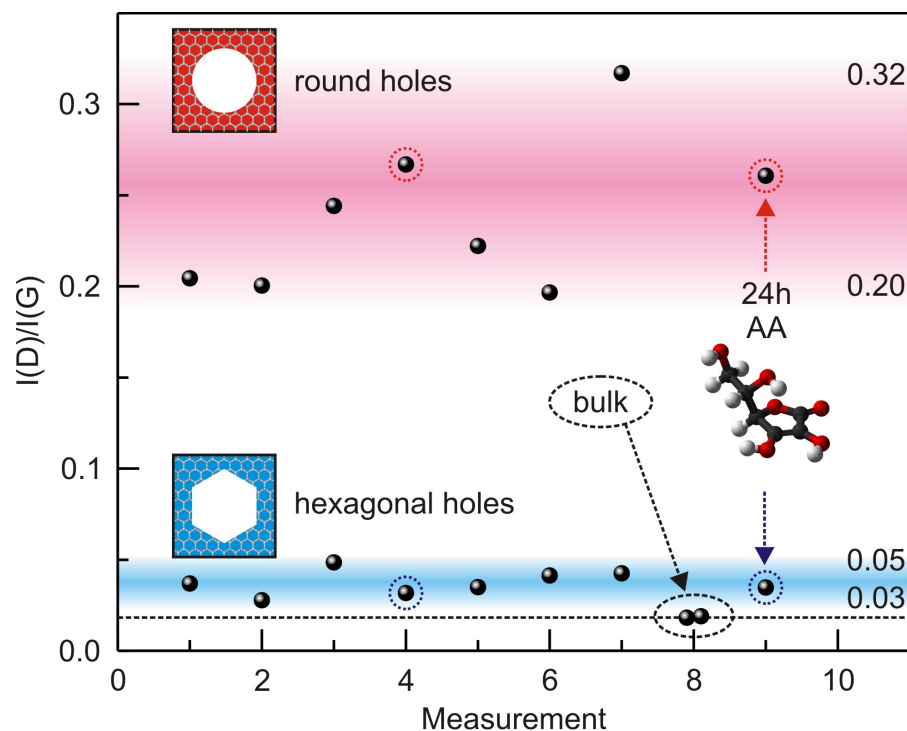
Figure 7.8.: ***Statistics for the I(D)/I(G) intensity ratio.*** *I(D)/I(G) for seven round holes and for the seven hexagonal holes in the AFM image in Figure 7.7 (e). The encircled values (measurement 4) are obtained from the Raman spectra displayed in Figure 7.7 (b) and (f). The dashed horizontal line is the average D peak intensity in the bulk of the sample (0.02, measurement 8 and Figure 7.7 (c) and (g)) and can be considered as a background. Measurement 9 was taken on the same holes as measurement 4 after treating the samples for 24 h in ascorbic acid (Figure 7.7 (d) and (h)).*

7.5. Summary and outlook

In summary, we have demonstrated that hexagonal holes obtained by anisotropic etching are bounded predominantly by zigzag edges which do not contribute to the D peak in Raman spectroscopy. Conversely, the absence of a significant D peak near such edges supports a posteriori the validity of the Raman theory which has been developed for graphene edges but could not be confirmed on the corners of mechanically exfoliated flakes. The fabrication of edges with a clean zigzag configuration represents a powerful additional capability in the graphene toolbox. It may be used as a straightforward technique to identify the crystallographic orientation of graphene flakes. By appropriate prepatterning, hexagons may be arranged so as to form constrictions or one-dimensional channels terminated on either side by pure zigzag edges. Also more advanced low-dimensional structures, such as quantum dots bounded exclusively by zigzag edges are conceivable. Two examples of such structures, one forming a nanoribbon as well as a small island connected to the leads on either side by nanoribbons are shown in Figure 7.9.
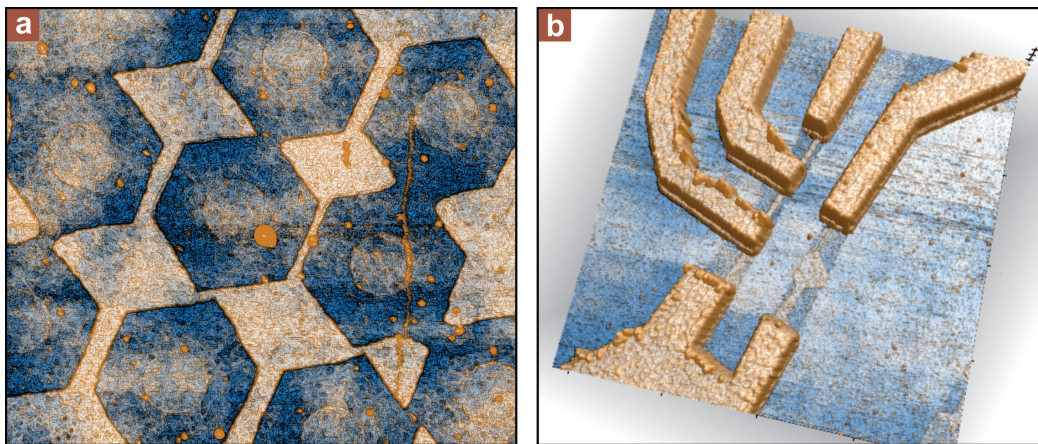
Figure 7.9.: ***AFM images of nanostructures bounded solely by zigzag edges.***
(a) By prepattern arrays of round holes followed by carbo-thermal etching small constrictions and nanoislands can be manufactured. A contacted example of such a nanostructure is depicted in (b). Even more complex and sophisticated structures can be envisioned. Modified from [171].

134

8. Visibility of Graphene on Different Substrates
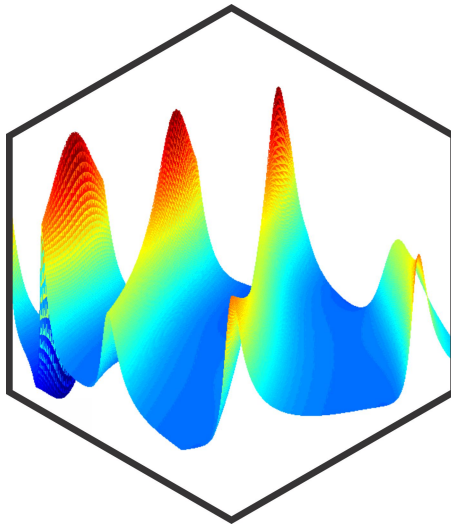
The success of graphene research and its vast proliferation has to be accredited to a large extent to the conducting silicon (Si) substrate capped with a silicon oxide (SiO_2) layer. If the thickness of the SiO_2 layer is set to be in a certain range it not only allows to visualize and identify single layer graphene with an optical microscope but simultaneously it enables us to apply a backgate voltage and change the carrier density in situ (see Section 2.8). However, graphene devices fabricated on SiO_2 substrates exhibit high disorder and the measured properties are inferior to the predicted intrinsic characteristics of perfect graphene. The charge carrier mobility is for instance limited by

- the substrate surface roughness [115, 172, 173],

- surface optical phonons [174, 175] and

- scattering from charged impurities inside the SiO_2 and at the graphene-substrate interface [175–179].

The graphene sample is often highly doped and the 2DES consists of an inhomogeneous network of random electron-hole puddles at the charge neutrality point [32]. The fabrica-

tion of suspended devices by etching away parts of the SiO_2 layer improves the situation and the quality indeed can be very high as we will show in Chapter 10. However, due to electrostatic reasons[1] the accessible density range is drastically reduced. It is desirable to combine the high density tunability of substrate supported graphene with the high quality of suspended devices.

First we will review the visibility of graphene in Chapter 8 and extend it to arbitrary layer material and arrangement. Using the example of indium tin oxide (ITO) as a transparent and conductive supporting layer for graphene we will demonstrate how to choose a suitable thickness such that the monolayer still can be seen with an optical microscope after micro-mechanical cleavage. In Chapter 9 we introduce a method to fabricate graphene devices on single crystal hexagonal boron nitride (h-BN) substrates.

8.1. Introduction

With the micro-mechanical cleavage method (see Subsection 2.7.1) only a minor fraction of the substrate is covered with monolayer graphene. Finding and identifying those few and small monolayers is an inevitable challenge and prerequisite in order to study them. The interest, however, is not solely restricted to monolayer graphene. Also double- and few-layer systems have appealing properties and increasing effort is put in the investigation of such multilayers [18, 180–183]. An easy, reliable and fast way to find and discriminate between samples with different numbers of layer is highly desirable. As shown in Ref. [71] only a combination of optical microscopy, atomic force microscopy and Raman spectroscopy is able to fulfill all requirements. Nevertheless, once carefully calibrated, the optical microscopy turned out to offer a reliable and efficient way to find and identify mono- and few-layers (<5 layers) of graphene[2]. In this chapter we will discuss a model based on Fresnel laws to explain why it is possible at all to see a layer that is only one single atom thick. Furthermore, this model allows us to experimentally adjust free parameters (especially the thickness of the materials) in order to maximize the contrast and hereby the visibility of graphene on a substrate.

The visibility of graphene on silicon substrates capped with silicon oxide has been studied previously [184–188]. We extend this analysis by (i) using a more precise wavelength dependent refractive index for graphene [189] and (ii) adding an extra layer in between graphene and the silicon oxide. For the experiment, we use ITO[3] (90 % In_2O_3 and 10 % SnO_2) as an additional transparent and conductive layer which opens the door to scanning tunneling microscopy of graphene edges. The fundamental interest in graphene edges and the difficulties in atomically resolving them has already been introduced in Chapter

---

[1] The electrostatic force between flake and substrate when applying a backgate voltage increases with this voltage and finally leads to a destruction of the device.

[2] We successfully set up a microscope, which is able to autonomously capture optical images of the substrate and locate graphene mono- and few-layers using a suitable algorithm based on the optical contrast of graphene. Further details about the automated graphene search (AGS) can be found in [171].

[3] The ITO layer was sputtered at the University of Stuttgart, Institut für Bildschirmtechnik by Mr. Bauer.

7. Whereas TEM at the edge is too invasive, STM as a powerful tool to characterize structural as well as electronical properties on an atomic scale is hampered since the graphene flakes are often micro-mechanically cleaved on the insulating SiO_2 substrate. Hence, adding a conductive and transparent layer like ITO and prepare graphene on top of it allows to exploit the capabilities of STM while still being able to proceed as normal in order to find and identify monolayer graphene. The model described below is not restricted to ITO but works for every kind of material. Only the thickness and refractive index enters the equation.
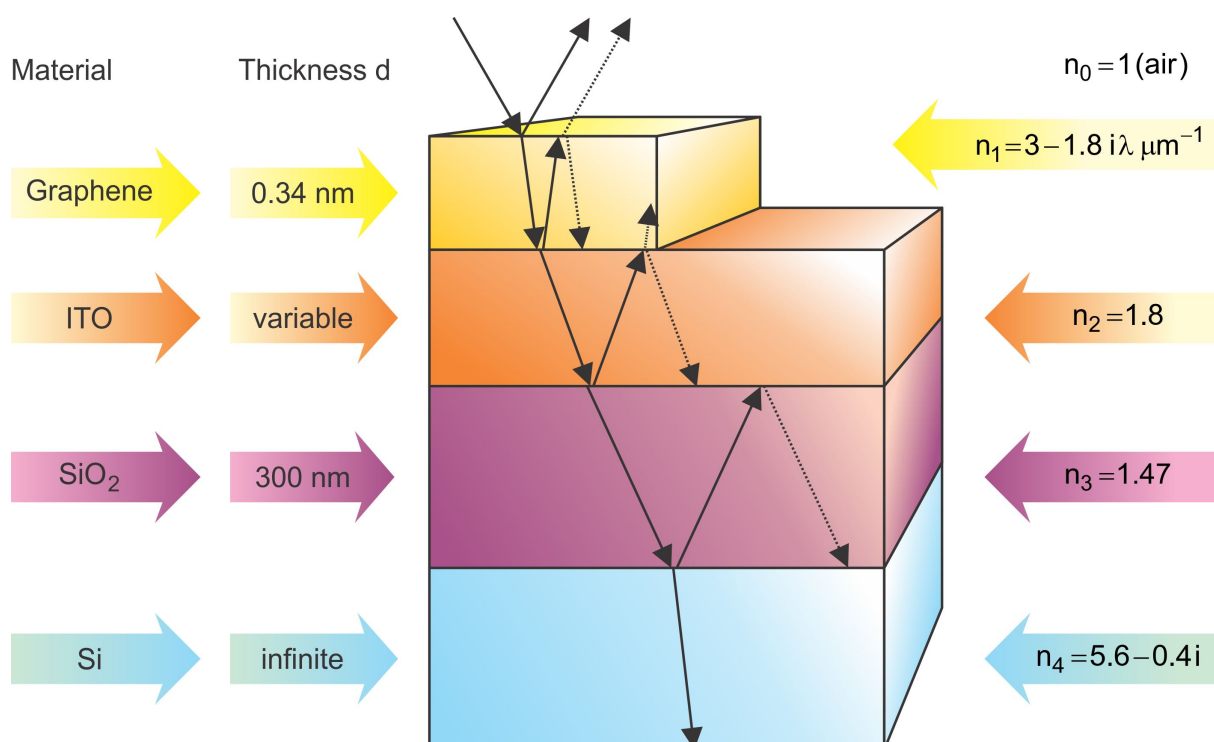
8.2. Model

Figure 8.1.: ***Overview of the five layer model for calculating the contrast of graphene.*** *The material, its thickness and refractive index is included. Also shown are schematic light rays representing some of the possible trajectories.*

The geometry used for the analysis is shown in Figure 8.1 and consists of 5 layers: the silicon substrate (Si) is capped with the silicon oxide (SiO_2) below an ITO layer and the graphene monolayer on top. The corresponding thicknesses and refractive indices are included in the figure as well as schematic light rays (black arrows) exemplifying some of the possible light trajectories. Under the assumption that all layers are (i) parallel and (ii) homogeneous we can calculate the reflectance if we know the thicknesses and refractive indices.

We start the analysis with only two interfaces (Figure 8.2) where three different optical media meet each other. The light is partly reflected and transmitted at the two interfaces
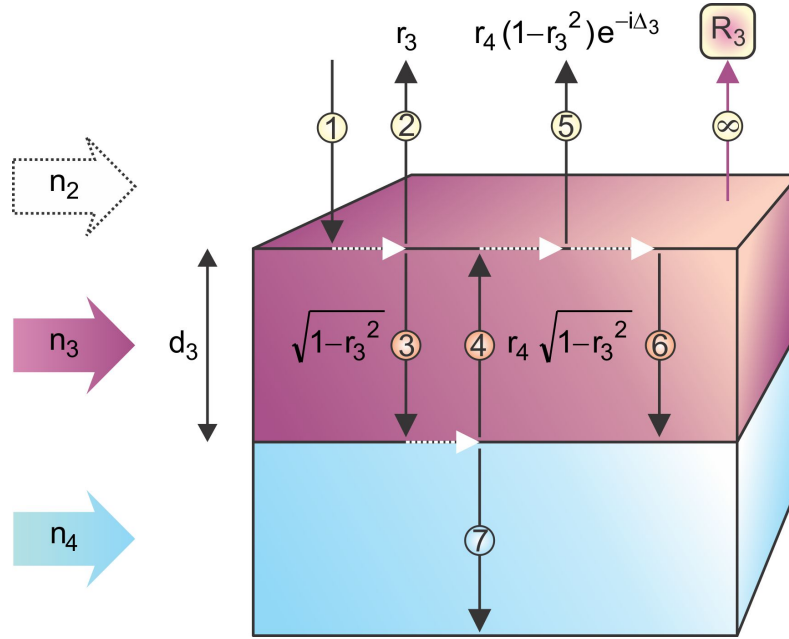
Figure 8.2.: ***Two interface model to derive the overall reflectance of the bottom two layers.*** *The arrows representing the light beams overlap each other in reality but are shifted horizontally for better visibility. The incoming light is partly transmitted and reflected at both interfaces several times. In order to calculate the overall reflectance, it is necessary to include phase shifts gained by the light.*

[190]. The incoming plane wave (1) with unity amplitude hits the first interface and the fraction (amplitude)

$$r_3 = \frac{n_2 - n_3}{n_2 + n_3}$$

is directly reflected (2) [191]. The remaining light is transmitted into the first medium (3) with an amplitude $\sqrt{1 - r_3^2}$.
At the second interface a fraction of

$$r_4 = \frac{n_3 - n_4}{n_3 + n_4}$$

is reflected (4) and hence a wave with an amplitude $r_4 \sqrt{1 - r_3^2}$ is going back to the first interface where it is partly transmitted (5) and reflected (6). The transmitted part (5) is once more reduced by a factor $\sqrt{1 - r_3^2}$ so that finally a wave with an amplitude $r_4 \cdot (1 - r_3^2)$ exits the first interface (5). This wave has traveled twice the distance d_3 and consequently has gained a phase shift of

$$\Delta_3 = \frac{2\pi}{\lambda} \cdot n_3 \cdot 2 \cdot d_3$$

with respect to the first directly reflected wave (2). The amplitude and phase of these two waves (2) and (5) have to be summed up:

$$R_3 = r_3 + r_4 \cdot (1 - r_3^2) \cdot e^{-i\Delta_3} + \dots \tag{8.1}$$

The wave transmitted at the second interface (7) will not enter the equation as the thickness of the silicon substrate is much higher than the other layers and everything transmitted into this medium will be completely absorbed. Nevertheless, we still have to take care of the wave (6) reflected at the first interface with $-r_3 \cdot r_4 \cdot \sqrt{1 - r_4^2}$ which itself from now on follows exactly the scheme introduced for wave (3). This adds another term to equation 8.1 so that the reflectivity R_3 now reads as

$$R_3 = r_3 + r_4 \cdot (1 - r_3^2)e^{-i\Delta_3} - r_3 \cdot r_4 \cdot (1 - r_3^2)e^{-i2\Delta_3} + ... \tag{8.2}$$

Repeating this procedure an infinite number of times will add each time another term to the equation and finally describe the overall reflectivity. This equation can be expressed in a geometric series[4]. It simplifies to[5]:

$$R_3 = \frac{r_3 + r_4 \cdot e^{-i\Delta_3}}{1 + r_3 \cdot r_4 \cdot e^{-i\Delta_3}} \ . \tag{8.3}$$
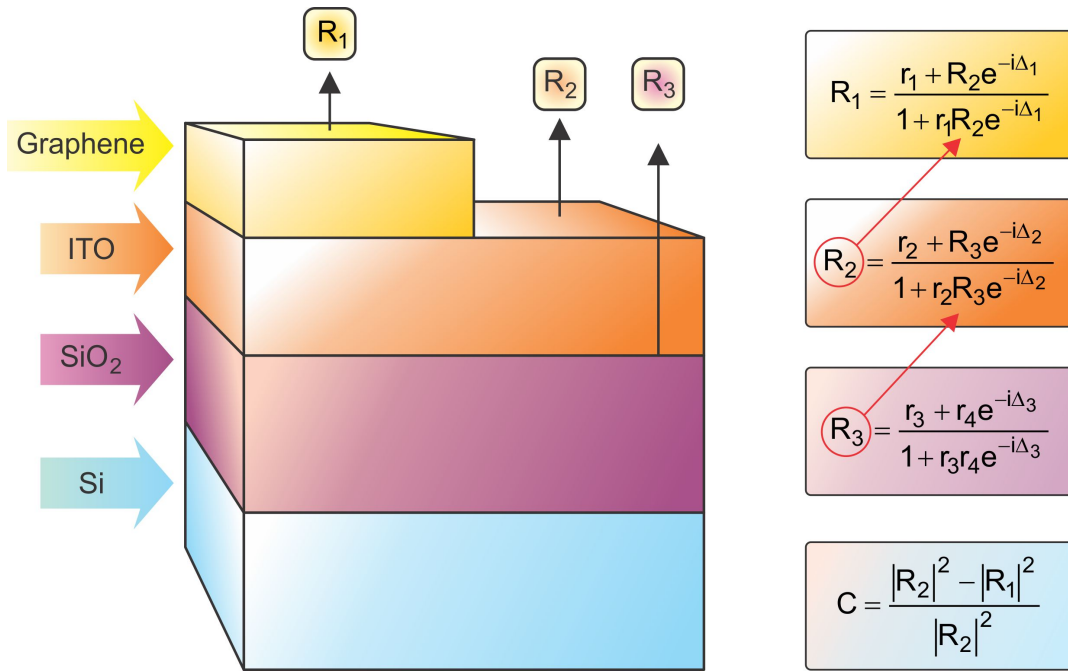

Figure 8.3.: **Rouards method.** *Following the idea of Rouard the two lowest layers can be treated as one layer with the reflectivity R_3. Repeating the same procedure as used for determining R_3 allows to calculate R_2 in the same way. Finally the last three layers are combined and graphene is added on top.*

---

[4]The geometric series has the form $a + ax + ax^2 + ax^3...$ and sums up to $S = \frac{a}{1-x}$ with $a \equiv r_4 \cdot (1 - r_3^2) \cdot e^{-i\Delta_3}$ and $x \equiv -r_3 \cdot r_4 \cdot e^{-i\Delta_3}$.

[5]Although it has no implications for the present work, it is worth noting the following two consequences which can be derived from this formula: (a) The reflectivity will be zero if the refractive index of the upper layer equals the geometrical mean of the other two refractive indices $n_3 = \sqrt{n_2 \cdot n_4}$ for the wavelengths obeying $n_2 \cdot d_2 = \lambda/4, 3\lambda/4, 5\lambda/4...$ (b) The reflectivity will also be zero if $n_2 = n_4$ for the wavelength $n_2 \cdot d_2 = \lambda/2, 3\lambda/2...$

Having established a method to calculate the reflectance of two layers, the next step is to add a third layer. In principle it is possible to repeat the same scheme and tenaciously add up all the contributions of all possible waves to the amplitude and phase. However, it is far more elegant to use the way described by Rouard et al. [192–198]: The bottom two layers can be treated as one single layer with the reflectance R_3 from equation 8.3. It is straightforward to add the next layer on top and repeat the same analysis to extract R_2 as demonstrated in Figure 8.3. In this example the final layer is graphene and R_1 the corresponding reflectance[6]. We define the contrast C as the difference in reflectivity without graphene $|R_2|^2$ and with graphene $|R_1|^2$ normalized to the background $|R_2|^2$:

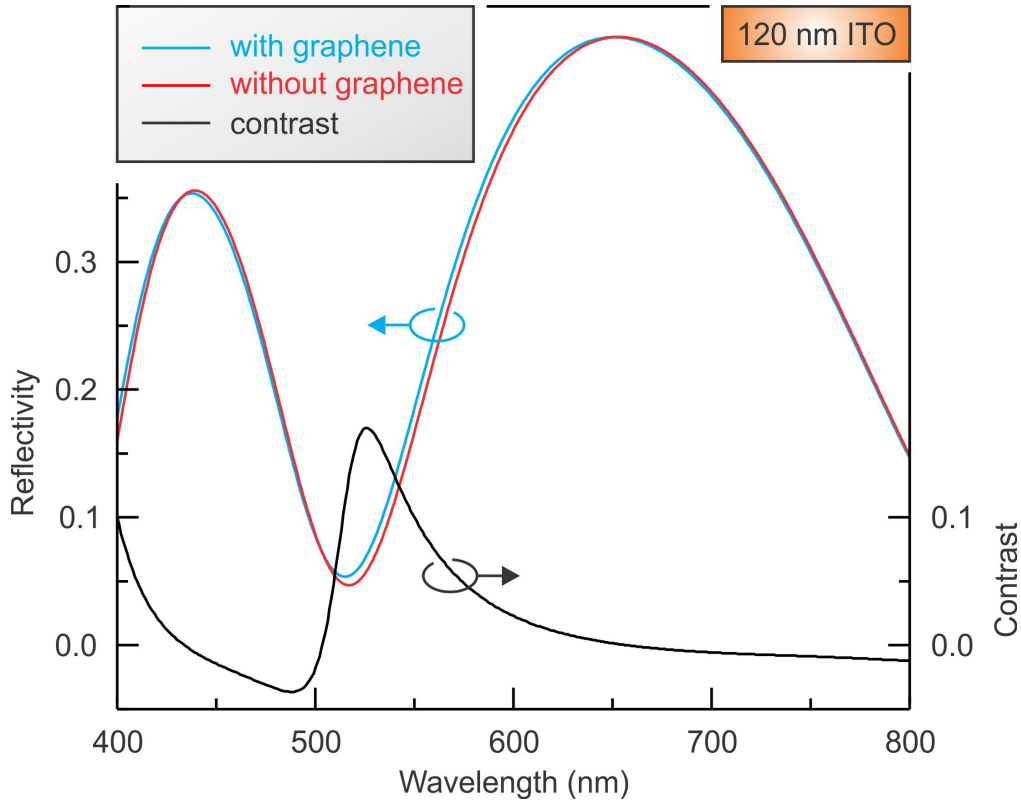$$C = \frac{|R_2|^2 - |R_1|^2}{|R_2|^2}$$

8.3. Results

Figure 8.4.: ***Reflectivity and contrast of graphene on 120 nm ITO as a function of wavelength.*** *The contrast can be positive or negative depending on the wavelength and shows a maximum at the region where the reflectivity is lowest.*

[6] $R_1 = (r_1 + r_2 \cdot e^{-i \cdot 4 \cdot \pi \cdot n_1 \cdot d_1 / \lambda} + r_3 \cdot e^{-i \cdot 4 \cdot \pi / \lambda \cdot (n_1 \cdot d_1 + n_2 \cdot d_2)} + r_4 \cdot e^{-i \cdot 4 \cdot \pi / \lambda \cdot (n_1 \cdot d_1 + n_2 \cdot d_2 + n_3 \cdot d_3)} + r_1 \cdot r_2 \cdot r_3 \cdot e^{-i \cdot 4 \cdot \pi / \lambda \cdot n_2 \cdot d_2} + r_1 \cdot r_3 \cdot r_4 \cdot e^{-i \cdot 4 \cdot \pi / \lambda \cdot n_3 \cdot d_3} + r_1 \cdot r_2 \cdot r_4 \cdot e^{-i \cdot 4 \cdot \pi / \lambda \cdot (n_2 \cdot d_2 + n_3 \cdot d_3)} + r_2 \cdot r_3 \cdot r_4 \cdot e^{-i \cdot 4 \cdot \pi / \lambda \cdot (n_1 \cdot d_1 + n_3 \cdot d_3)}) / (1 + r_1 \cdot r_2 \cdot e^{-i \cdot 4 \cdot \pi \cdot n_1 \cdot d_1 / \lambda} + r_1 \cdot r_3 \cdot e^{-i \cdot 4 \cdot \pi / \lambda \cdot (n_1 \cdot d_1 + n_2 \cdot d_2)} + r_1 \cdot r_4 \cdot e^{-i \cdot 4 \cdot \pi / \lambda \cdot (n_1 \cdot d_1 + n_2 \cdot d_2 + n_3 \cdot d_3)} + r_2 \cdot r_3 \cdot e^{-i \cdot 4 \cdot \pi / \lambda \cdot n_2 \cdot d_2} + r_3 \cdot r_4 \cdot e^{-i \cdot 4 \cdot \pi / \lambda \cdot n_3 \cdot d_3} + r_2 \cdot r_4 \cdot e^{-i \cdot 4 \cdot \pi / \lambda \cdot (n_2 \cdot d_2 + n_3 \cdot d_3)} + r_1 \cdot r_2 \cdot r_3 \cdot r_4 \cdot e^{-i \cdot 4 \cdot \pi / \lambda \cdot (n_1 \cdot d_1 + n_3 \cdot d_3)});$

Figure 8.4 depicts the outcome of the model for the reflectivity with (blue curve, $|R_1|^2$) and without graphene (red curve, $|R_2|^2$) as a function of wavelength for a fixed ITO thickness of 120 nm. The contrast defined as the normalized difference is included in black. Interestingly, the contrast is highest where the reflectivity is low. We point out that, depending on the wavelength, the contrast can be positive as well as negative.
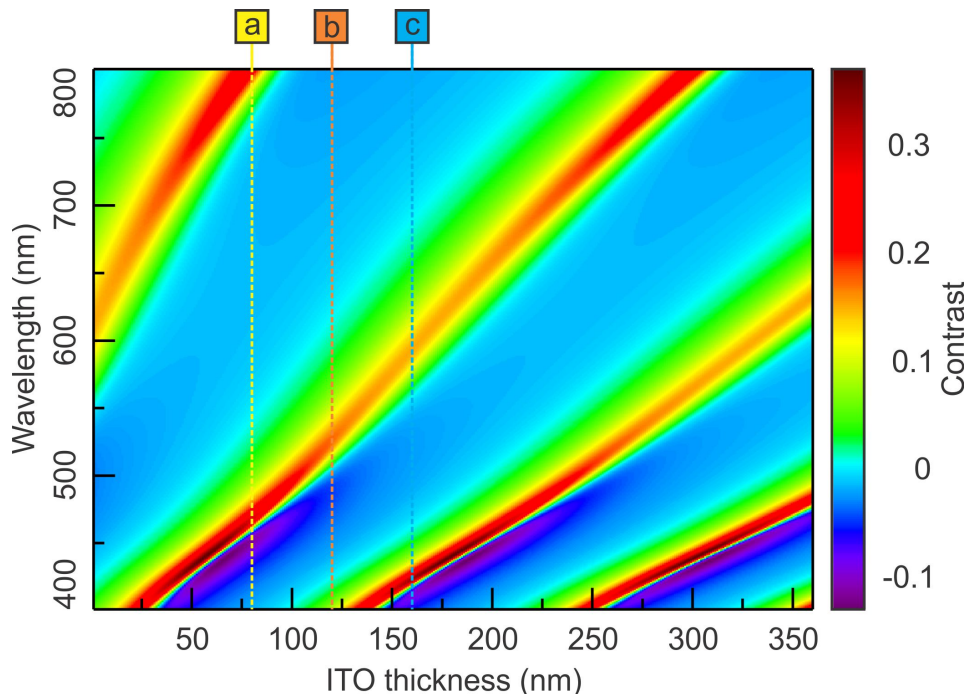

Figure 8.5.: *Color coded contrast of graphene on top of a thin ITO layer as a function of ITO thickness and wavelength.*

A color coded picture of the contrast as a function of the thickness of the ITO layer and wavelength is shown in Figure 8.5. This figure helps to either choose a specific wavelength filter most appropriate for maximum contrast for a fixed ITO thickness or to determine the most suitable ITO thickness for a white light microscope. Here we are interested in choosing the ITO thickness with maximum contrast for white light microscopy. Technical limitations impose in our case the boundary condition that the ITO thickness can only be a multiple of 40 nm. Three cuts along 80 nm, 120 nm and 160 nm ITO are given in Figure 8.6. The human eye is most sensitive for wavelengths around 550 nm (green) and a high contrast in this region is desirable. From Figure 8.6 we read that 80 nm and 160 nm ITO have nearly zero contrast at a wavelength of 550 nm (green dotted lines in Figure 8.6), whereas an ITO layer with 120 nm thickness has approximately 10% contrast. An ITO thickness of 120 nm is used for further studies. Also included in the curve for 120 nm ITO are experimentally measured contrast values for two fixed wavelengths obtained with scanning confocal laser microscopy with a He-Ne laser (633 nm) and an Argon-ion laser (488 nm) which both fit the theoretical expectations very well. The graphene for theses measurements was prepared by micro-mechanical cleavage on top of the 300 nm SiO_2 substrate capped with 120 nm ITO and identified to be a monolayer with Raman spectroscopy and optical microscopy.

The model can be extended to bi-, tri- and few layer graphene systems as shown in
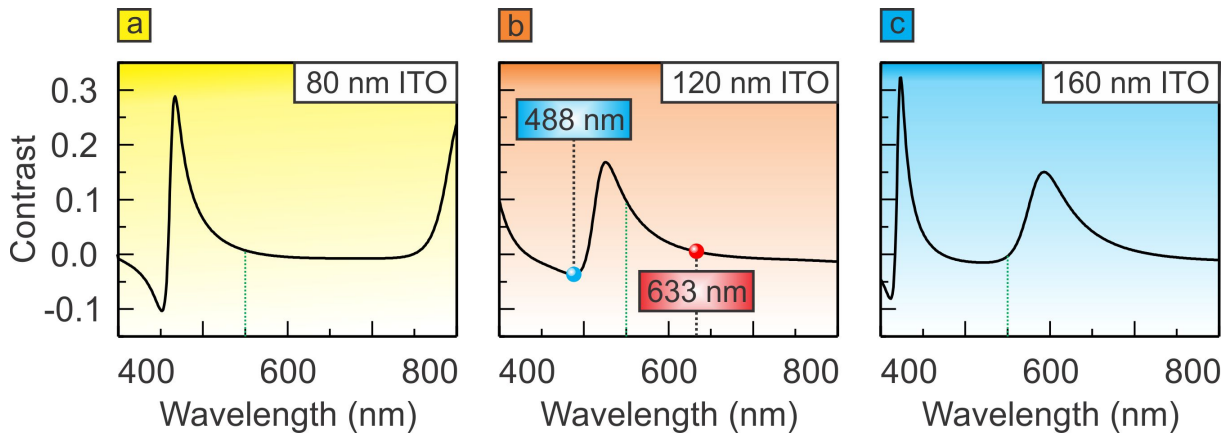
Figure 8.6.: ***Contrast of graphene on top of (a) 80 nm, (b) 120 nm and (c) 160 nm of ITO as a function of wavelength.*** *Only 120 nm thick ITO features a high contrast in the region of the human eyes highest sensitivity (green doted lines). The dots represent experimentally measured values and agree well with the theory introduced above.*
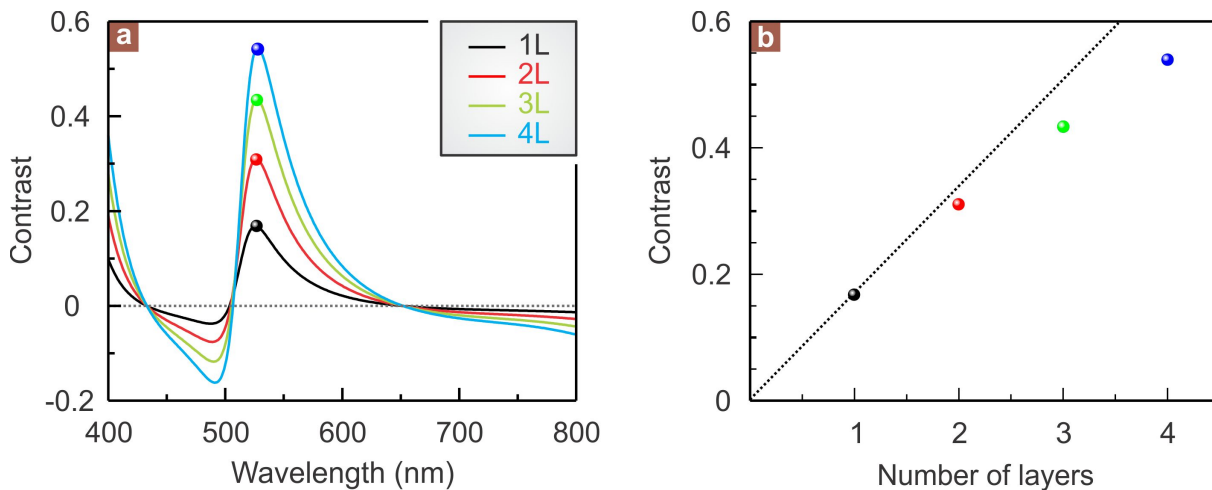

Figure 8.7.: ***Wavelength dependent contrast for few layer graphene on 120 nm ITO.*** *(a) The maximum contrast appears at a similar wavelength independent of the graphene thickness but the amplitude increases with increasing number of layers. (b) The maximum contrast as a function of layers shows a sub-linear behavior and consequently is not just the sum of the single layer value.*

Figure 8.7 (a). The maximum contrast as a function of number of graphene layers is shown in Figure 8.7 (b) and reveals a sub-linear dependence. As a consequence it becomes more and more difficult to extract the precise number of layers only from optical microscopy with an increasing number of layers.

In summary, we introduced a model that allows to calculate the contrast of graphene and multilayer graphene on top of an arbitrary three (or even more) layer substrate. We prepared graphene with the micro-mechanical cleavage method on a transparent and

electrically conductive substrate (ITO) suitable for STM measurements and demonstrated how to determine the proper ITO thickness for maximum visibility. In the next chapter we will introduce yet another method to prepare graphene on arbitrary substrates, even if the new substrate itself has a size of only a few micrometer squared.

9. Graphene on Hexagonal Boron Nitride
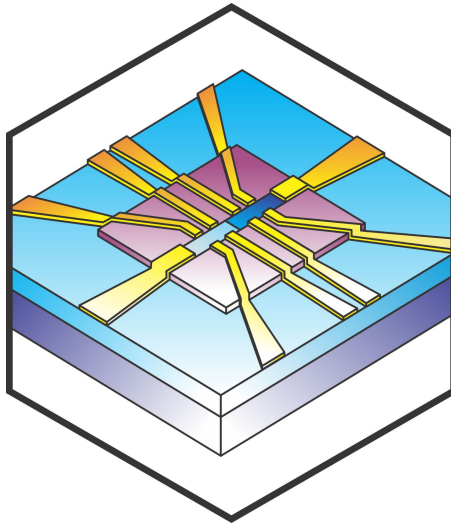
Combining the advantages of a high charge carrier density tunability of substrate supported graphene with the superior quality of suspended devices led to the search of novel substrates to host graphene. One promising candidate is hexagonal boron nitride (h-BN) which is atomically flat and insulating with a band gap of 6 eV [199]. Its strong in-plane ionic bonding of the planar lattice makes it inert and free of dangling bonds and surface charge traps. Recently it has been shown [200] that mono- and bilayer graphene devices on h-BN have mobilities and carrier inhomogeneities that are almost an order of magnitude better than devices on SiO_2. Furthermore, STM studies revealed that graphene conforms to h-BN as evident from the presence of Moiré patterns [201]. However, due to the misalignment of the two lattices this did not lead to a sizable band gap contrary to predictions [202, 203]. The electron-hole fluctuations are drastically reduced and several fractional quantum Hall states could be observed [204].

We start by introducing a method how to prepare graphene on h-BN flakes by a transfer mechanism. The relation between thickness and visibility of h-BN on our conventional Si/SiO_2-substrates as well as the substrate roughness is discussed in a next step.

9.1. Preparation of graphene on hexagonal boron nitride

The fabrication process is outlined in Figure 9.1. It starts with the conventional micromechanical cleavage of HOPG on silicon substrates covered with 300 nm silicon oxide (Figure 9.1 (a)) and the identification of monolayers by optical microscopy and Raman spectroscopy. In the next step the whole substrate is covered with a layer of spin coated PMMA (Figure 9.1 (b)) which itself is attached for easier handling to a glass frame with a through-hole (the glass frame is not shown in the figure). In order to achieve a stable layer of PMMA, able to support graphene and withstand the fabrication procedure, we use the resist 950 K 5 % and spin coat it with 3000 rpm for 1 min. This gives an approximately 700 nm thick layer after bake out. Subsequently, the substrate is put for 15 minutes in a 80° C hot 5% potassium hydroxide (NaOH) solution obtained by dissolving 20 g NaOH pellets in 380 ml of water. This solution etches away the SiO_2 but leaves behind the graphene monolayer attached to the PMMA as illustrated in Figure 9.1 (c). After thoroughly rinsing the sample in water and blowing it dry with nitrogen the sample is ready for the actual transfer process.
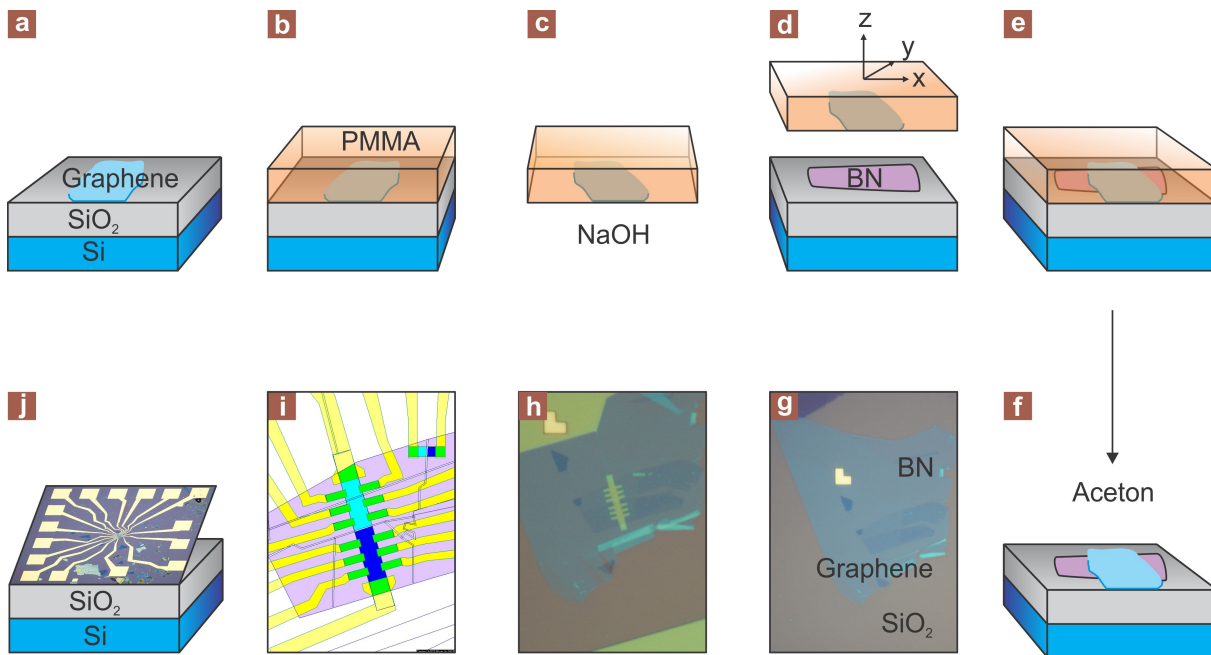
Figure 9.1.: **Fabrication process for graphene on h-BN devices.** *(a)-(f) Schematic outline of the mechanical transfer process. (g)-(j) Design and optical images of a graphene on h-BN sample.*

An h-BN flake that will eventually host the graphene is exfoliated from ultra pure h-BN single-crystals [205] to the Si/SiO_2-substrate in a similar manner in which graphene is exfoliated. Suitable h-BN flakes are identified and characterized by a combination of optical contrast microscopy and AFM. Both methods will be discussed below in more detail. It will turn out that thickness and surface roughness are the crucial parameters here. Hence, AFM measurements are needed in order to choose the best available flake.

The graphene flake attached to the PMMA is positioned directly above the host h-BN flake with a micro precision stage (Figure 9.1 (d)) and subsequently approached to the h-BN until both parts meet (9.1 (e)). The key component in this step is the parallelism between graphene plane and h-BN plane. The PMMA layer, only needed for the transfer process is superfluous now and is carefully removed in acetone vapor. This leaves behind the graphene monolayer on top of the h-BN as shown schematically in Figure 9.1 (f) and in the optical microscope image in (g). Here the SiO_2 is shown in grey, h-BN in light blue and graphene in darker blue. AFM images of graphene flakes transfered to h-BN revealed that large parts of the graphene flake are wrinkled and have a high surface roughness. Nevertheless, some parts of the graphene are found to conform to the surface of the h-BN and feature a low curvature. Etching as described in Figure 9.1 (i) helps to isolate and contact only those regions with a low surface roughness of the graphene. Transferring the design (etch mask (h) and contact layout (i)) with electron beam lithography to the sample and evaporating the contact material works similarly as described in Subsection 2.7.5. The fully contacted sample is ready to be measured in magneto-transport experiments.

9.2. Optical visibility of h-BN

Optical microscopy has proven to be a helpful tool in identifying monolayer graphene on different substrates by its contrast, especially on Si/SiO_2. As optical microscopy is a fast and uncomplicated method it is natural to utilize it in order to find suitable h-BN flakes as a host material for graphene. An optical image of an h-BN flake is shown in the inset of Figure 9.2.
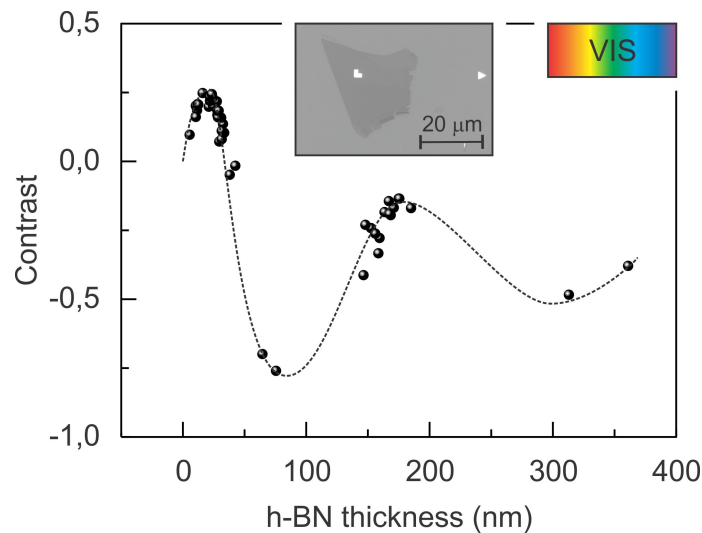
Figure 9.2.: *Optical contrast of h-BN flakes with different thicknesses. The h-BN flakes were prepared with the micro-mechanical cleavage method on top of silicon substrates capped with 300 nm silicon oxide. The inset shows an optical image of one specific flake. The contrast values were extracted from optical microscope images with white light illumination with the help of histograms.*

The main panel of Figure 9.2 shows the optical contrast of several h-BN flakes with

147

various thicknesses prepared with the micro-mechanical cleavage method on silicon substrates capped with 300 nm SiO_2. A histogram was used to extract both axes, the h-BN thickness from AFM measurements as well as the contrast (see Section 8.2) from optical microscopy images with white light illumination. An oscillating behavior was found where both positive and negative contrast values appear. Furthermore, flakes with different thicknesses can have the same contrast value as seen in Figure 9.2 for instance for a thickness of 5 nm and 30 nm. This makes it impossible to determine the thickness of a h-BN flake judging solely from the optical contrast value from white light microscopy.

In order to understand the oscillating behavior we use the theory developed for the visibility of graphene on Si/SiO_2 or any other substrate described in Chapter 8[1]. Figure 9.3 depicts the simulated contrast of an h-BN flake on a silicon substrate covered with 300 nm silicon oxide as a function of flake thickness and illumination wavelength. A recurring pattern with contrast minima and maxima is visible. This explains the observed oscillations in the optical contrast as a function of h-BN thickness as depicted in Figure 9.2.
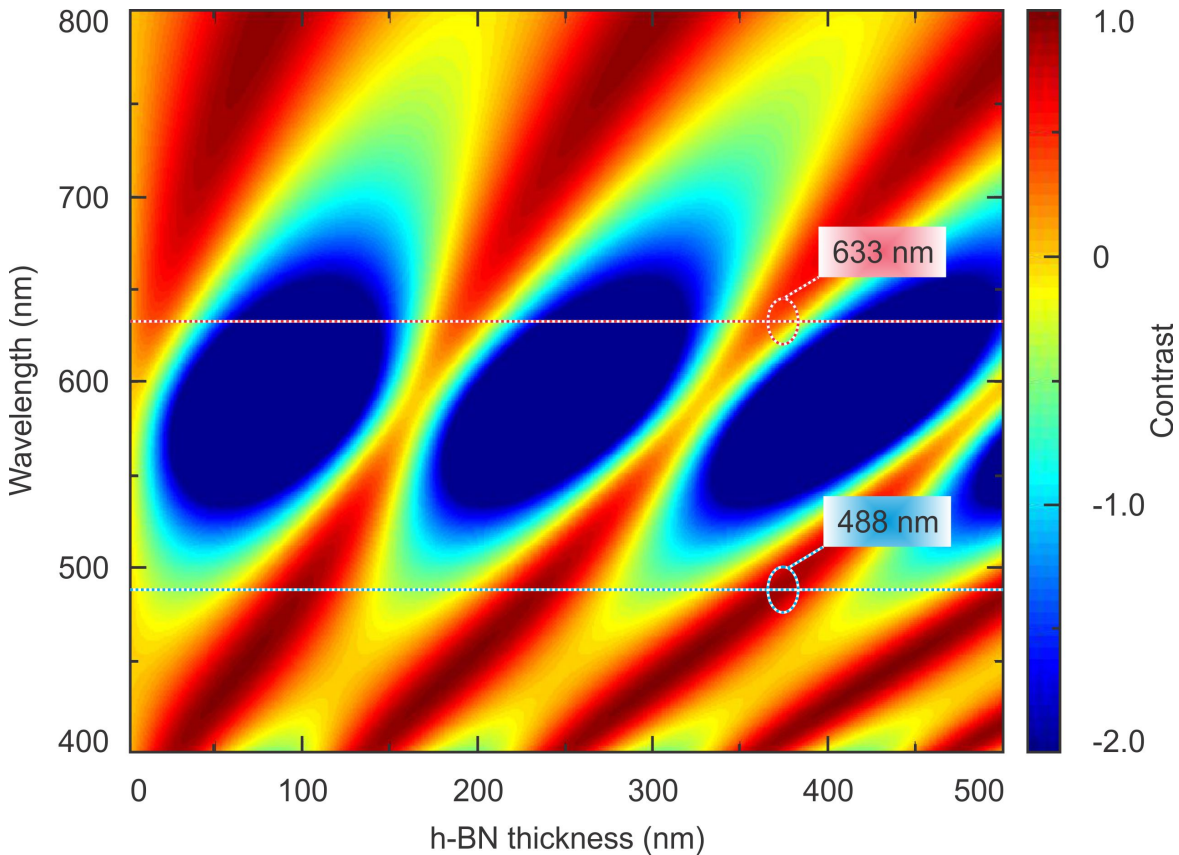
Figure 9.3.: *Optical contrast of h-BN as a function of thickness and illumination wavelength.* *The cuts indicated in this figure along wavelengths of 488 nm and 633 nm are shown in Figure 9.5.*

In order to verify the theory we investigated the contrast of h-BN flakes with varying thickness for two different lasers with wavelengths of 488 nm and 633 nm as illumination

---

[1]We used a refractive index of $n_{h-BN} = 2.2$ for the h-BN.

source. As an example, we show the measurements for one specific h-BN flake with a height of 156 nm. A confocal laser scanning microscope (CLSM) image of this flake obtained by using an excitation wavelength of 488 nm is shown in Figure 9.4 (a). The
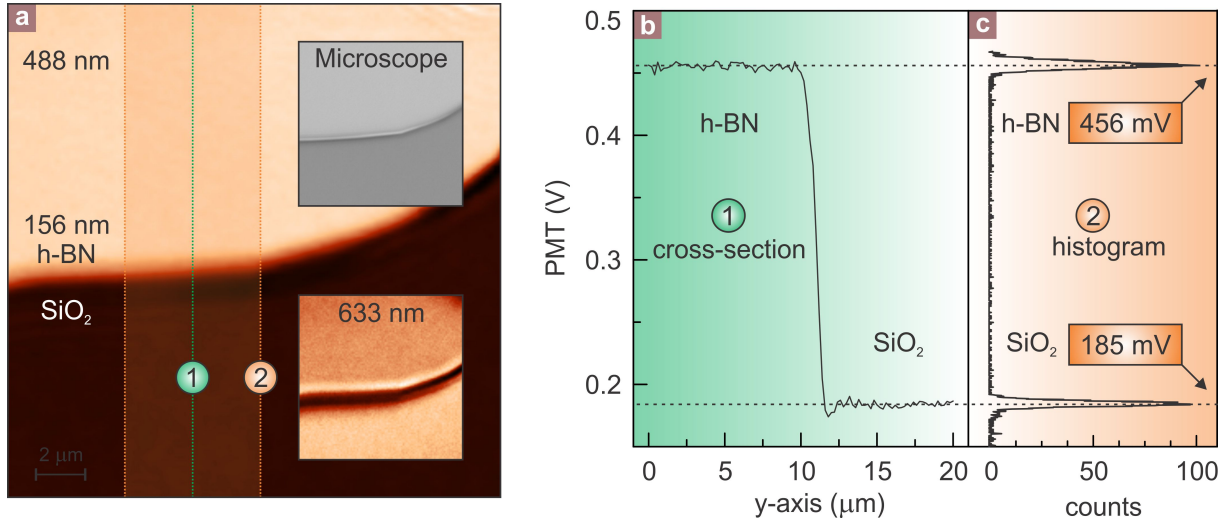

Figure 9.4.: ***Confocal laser scanning measurements of h-BN.*** *(a) Changing the excitation wavelength results in a different contrast in the SCLM images. (b) A cut crossing the edge allows to determine the PMT voltage value for h-BN and substrate. (c) A histogram of the region (2) denoted in (a) increases the accuracy and provides a convenient tool to extract precise values.*

Rayleigh scattered light is detected by a PMT and measured in Volt. The h-BN flake in this case appears brighter than the underlying SiO_2 substrate. This agrees with the optical microscope image included in the upper inset of Figure 9.4 (a). The lower inset shows for comparison a CLSM image acquired with a 633 nm laser source. Contrary to the experiment at 488 nm, the contrast of h-BN and the substrate is reverted and nearly identical. As we will show below this is indeed what the theory predicts. A cross-section along the green line indicated in Figure 9.4 (a) is depicted in Figure 9.4 (b). It shows the PMT voltage measured on the h-BN as well as on the SiO_2 substrate. The accuracy of this measurement can be enhanced by taking a histogram at the orange region (2) in Figure 9.4. This is shown in Figure 9.4 (c) and allows to conveniently determine an averaged value of the PMT voltage for h-BN and SiO_2. The outcome of this analysis for several h-BN flakes is summarized in Figure 9.5. The contrast as a function of the thickness of the h-BN flake is given in Figure 9.5 for an exciting laser wavelength of (a) 633 nm and (b) 488 nm. The theoretical prediction for each wavelength as calculated above and shown in Figure 9.3 is included as a dashed line. It captures the oscillatory behavior. However, the absolute values do not exactly match the predictions from theory. Reasons for this include uncertainties in the refractive index for the materials as well as contaminations during the fabrication process. Hence, optical as well as SCLM are not the most suited methods to find a h-BN flake with a certain thickness. AFM measurements are necessary to choose a suitable flake as discussed in the next section. Furthermore, AFM images allow to assess the surface quality of the h-BN flakes.
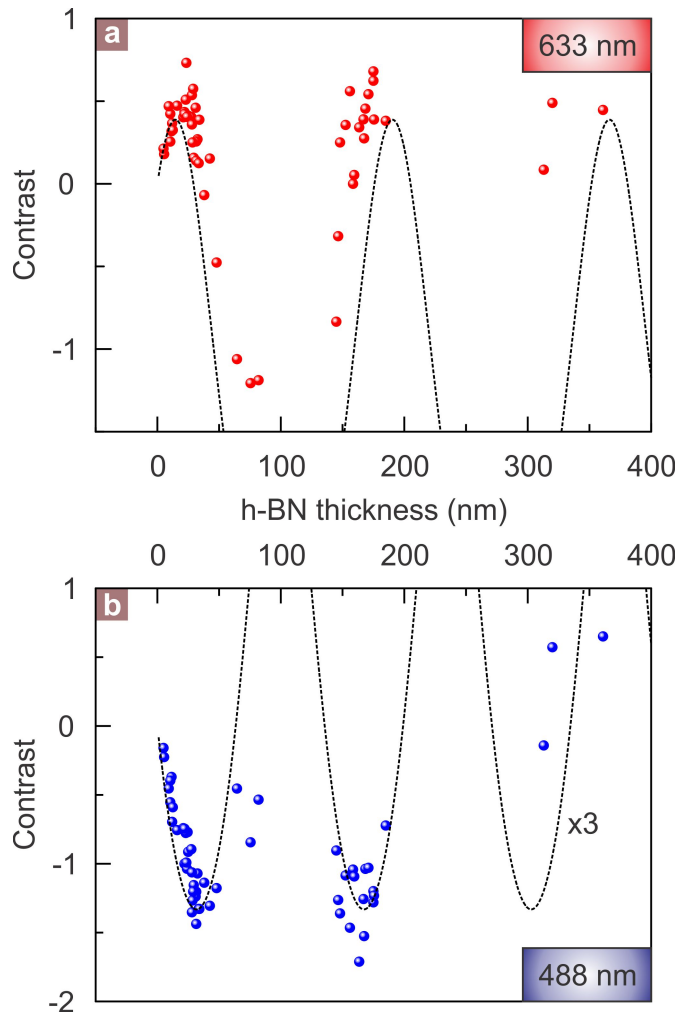
Figure 9.5.: *Contrast determined from confocal laser scanning analysis as a function of h-BN thickness.* The source is a laser with (a) 633 nm and (b) 488 nm wavelength. The dots represent experimental data points whereas the dashed line results from theory.

9.3. Atomic force microscopy of h-BN

One motivation to use h-BN as a substrate for graphene is its lower surface roughness compared to SiO_2 as local curvature may lead to unsolicited electronic effects like doping [206] and random effective magnetic fields [207].

Figure 9.6 (a) shows an AFM topography image of a 500 nm thick h-BN flake on top of 300 nm SiO_2. The 2.5 x 2.5 μm^2 insets are scaled to have the same z-height and already indicate that the h-BN has a much lower surface roughness. A cross-section of the insets obtained from the dashed red and blue line is depicted in Figure 9.6 (b). Two types of fluctuations are discernible on SiO_2: (i) strong fluctuations with a high magnitude up to 1 nm and high spatial extent, as well as (ii) small distance fluctuations from one data point to the adjacent one. Both fluctuations are considerably smaller for the h-BN flake and demonstrate the superior flatness of h-BN. A more quantitative way to study the
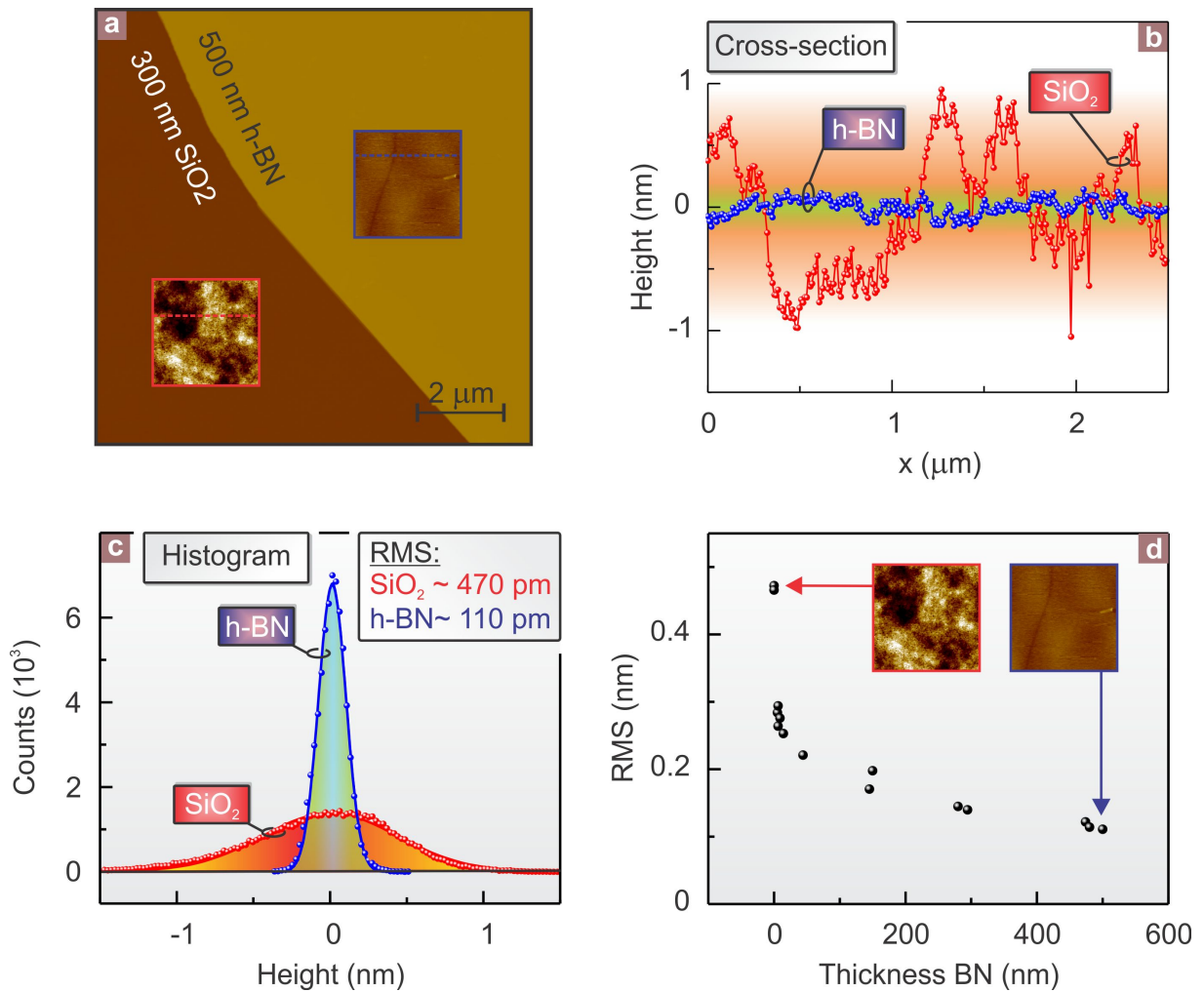
Figure 9.6.: **Atomic force microscopy of h-BN.** (a) AFM topography of a 500 nm thick h-BN flake on top of the SiO₂ substrate. The insets are scaled to have the same color coded height and reveal the lower surface roughness of the h-BN flake. The cross-sections as marked by the dashed lines in the inset are shown in (b). (c) Histogram of the height distribution for SiO₂ (red) and h-BN (blue) along with Lorentzian curves fitted to the experimental data and the corresponding RMS values. The RMS for h-BN is lower by more than a factor of four. (d) Thickness dependence of the RMS for several h-BN flakes. The thicker the h-BN the lower the RMS.

surface roughness is to analyze the fluctuations around the mean value in a histogram. Figure 9.6 (c) shows such a histogram for the two 2.5 x 2.5 μm^2 areas marked in Figure 9.6 (a) and the corresponding root mean square (RMS) value which constitutes a convenient measure for the surface roughness. In the case of 500 nm thick h-BN the RMS is more than four times smaller than for the bare SiO₂ surface. Extending the measurement to several h-BN flakes reveals that the RMS strongly depends on the h-BN thickness as depicted in Figure 9.6 (d). The RMS of the bare SiO₂ substrate is included on the left as a reference. Already for h-BN flakes with a thickness of around 10 nm the RMS value is reduced by a factor of two and keeps decreasing with increasing h-BN thickness. The data

points were extracted from histograms with 2.5 x 2.5 μm^2 areas as this is a meaningful size when it comes to device fabrication. The areas were chosen to be free of wrinkles and dirt and hence present a lower limit for the RMS. We note that choosing a smaller area for evaluating the histogram will yield lower RMS values.

From the surface roughness point of view a thicker h-BN is preferable as a substrate. For magneto-transport data, however, a back-gate is used to tune the carrier concentration. For a thicker h-BN flake underneath the graphene a higher back-gate voltage has to be applied to reach the same density. This decreases the maximal achievable carrier density before the back-gate starts to leak or break through. Consequently a tradeoff between low surface roughness and high carrier density has to be used.

10. Unconventional Sequence of Fractional Quantum Hall States in Suspended Graphene
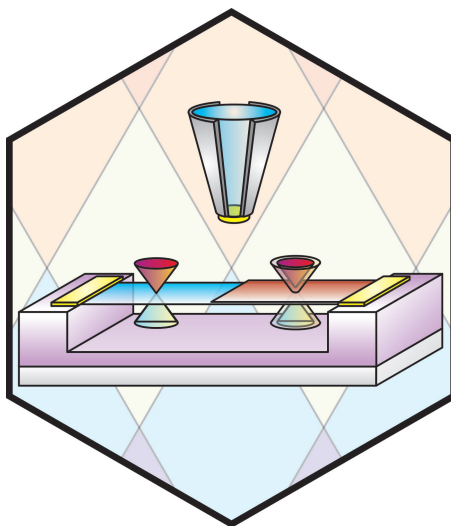
Interactions among electrons can significantly alter the properties of two-dimensional systems. They give rise to striking collective phenomena such as the fractional quantum Hall effect. At certain magnetic fields and carrier densities the electrons condense with a specific number of flux quanta into new quasiparticles, called composite fermions.

In this part of the thesis we use a single-electron transistor (SET) [208,209] mounted on a scanning microscope as a probe to image the local inverse electronic compressibility of a graphene monolayer. The current-voltage characteristic of the SET as a nanometer-sized tunneling device is governed by the Coulomb blockade effect and acts as a very sensitive electrometer. Whereas for a free non-interacting electron gas the compressibility equals the single particle density of states, the exchange energy and electron correlations may also contribute to the compressibility if interactions are included.

10.1. Introduction

Application of a strong perpendicular magnetic field B to a two-dimensional electron gas effectively quenches the kinetic energy of electrons and gives rise to flat energy bands called Landau levels (LLs) which contain a total of eB/h states, where e is the electron charge and h is Planck's constant. In graphene, each of these states has an additional fourfold degeneracy due to the spin and valley degrees of freedom, and the LLs possess an approximate SU(4) symmetry [210]. Incompressible quantum Hall states are formed when the Fermi energy lies between LLs. This occurs in graphene at filling factors $\nu = neB/h = 4(N + 1/2)$ in the absence of interelectron interactions [6, 7, 211] where n is the charge carrier density and N is the orbital index. Hence, the quantum Hall sequence is shifted by a half-integer, a distinctive signature that reflects the sublattice pseudospin of graphene.

When disorder is low and at high magnetic field, Coulomb forces between electrons become important and many-body effects emerge. One example is the fractional quantum Hall effect (FQHE) [212–215], in which correlations between electrons generate excitations with fractional charge at certain rational filling fractions. Recently, the FQHE of Dirac fermions has attracted considerable attention [216–229]. In graphene, the low dielectric constant and unique band structure lead to fractional quantum Hall states with energy gaps that are larger than in GaAs at the same field, particularly in the $N = 1$ LL [217, 223, 224]. Since graphene is accessible at the surface one may even envision a way to continuously tune the interactions in graphene by controlling the dielectric environment. Moreover, the SU(4) symmetry of charge carriers in graphene could yield fractional quantum Hall states without analogues in GaAs [218–220]. The FQHE was recently observed [230–232] in suspended graphene samples at $\nu = 1/3$ and 2/3, with an activation gap at $\nu = 1/3$ of approximately 2 meV at B = 14 T. Measurements of graphene on hexagonal boron nitride substrates [204] revealed further fractional quantum Hall states at all multiples of $\nu = 1/3$ up to 13/3, except at $\nu = 5/3$, but no conductance plateaus were observed at filling factors with higher denominators. It was suggested that the absence of a fractional quantum Hall state at $\nu = 5/3$ might result from low-lying excitations associated with SU(2) or SU(4) symmetry, but alternate scenarios associated with disorder could not be ruled out [204].

10.2. Experiment

The measurements described in this chapter were obtained at the Harvard University in collaboration with Ben Feldman and Amir Yacoby. Figure 10.1 shows a schematic of the measurement setup. By modulating the carrier density and monitoring the resulting change in SET current, we measure both the local chemical potential μ and the local inverse electronic compressibility $\chi^{-1} = n^2 \cdot \mathrm{d}\mu/\mathrm{d}n$ of the graphene flake (see Section 4.1). However, for convenience we hereafter drop the prefactor and use inverse compressibility to mean $\mathrm{d}\mu/\mathrm{d}n$. Our technique provides a direct thermodynamic measurement of bulk sample properties. Moreover, we obtain local measurements, and are therefore sensitive to weak effects which may be obscured by disorder in global transport studies.
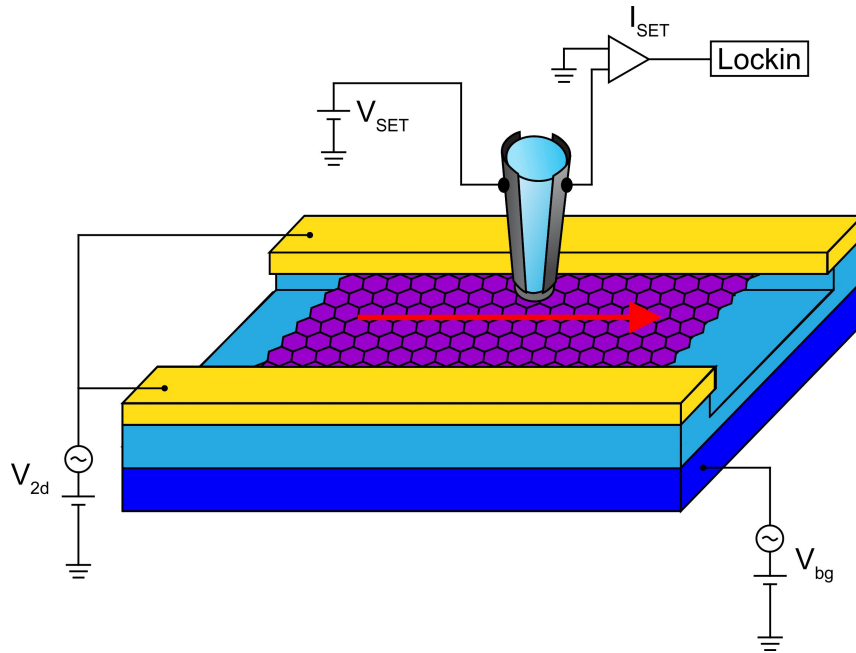
Figure 10.1.: **_Schematic of the measurement setup._** _The single-electron transistor is approximately 100 nm in size and is held 50-150 nm above the graphene flake. The red arrow indicates the path of the spatial scans in Figures 10.10, 10.12 and 10.17._

The measured inverse electronic compressibility as a function of carrier density and magnetic field is shown in Figure 10.2. At zero magnetic field and low density, we observe an incompressible peak that arises from the vanishing density of states at the charge neutrality point in graphene. For $B > 0$, strong incompressible behavior occurs at $\nu = 4(N + 1/2)$, confirming the monolayer nature of our sample. In addition to the single-particle quantum Hall features, we observe incompressible states at intermediate integer filling factors $\nu = 0, 1, 3, 4, 5, 7, 8$ and 9. These integer broken-symmetry states arise from interactions among electrons [204, 232–234] and are visible at fields well below 1 T, indicating the high quality of our sample. Figure 10.3 explains the observed integer sequence of incompressible states. The LL structure in graphene without interactions are shown in Figure 10.3 (a). The enlargement of what happens to the zero mode is illustrated in Figure 10.3 (b). The four fold degeneracy resulting from the valley and spin degrees of freedom, is lifted. If we assume that the spin degeneracy is lifted first yields the situation depicted in Figure 10.3 (c). If also the valley degeneracy is lifted incompressible states are observed at all integer filling factors $\nu = 0, \pm1, \pm 2$ etc. as shown in Figure 10.3 (d) and measured in Figure 10.2.

Most intriguing, however, is the appearance of incompressible peaks at fractional filling factors, the strongest are visible at fields as low as 1 T. We note that it is straightforward to distinguish fractional quantum Hall states from oscillations in compressibility caused by localized states. Localized states occur at a constant density offset from their parent quantum Hall state and are therefore parallel to lines of constant filling factor in the $n-B$ plane [211]. When plotted against filling factor (Figure 10.4), localized states curve as the magnetic field is changed, whereas any incompressible behavior caused by an integer or fractional quantum Hall state appears as a vertical feature.
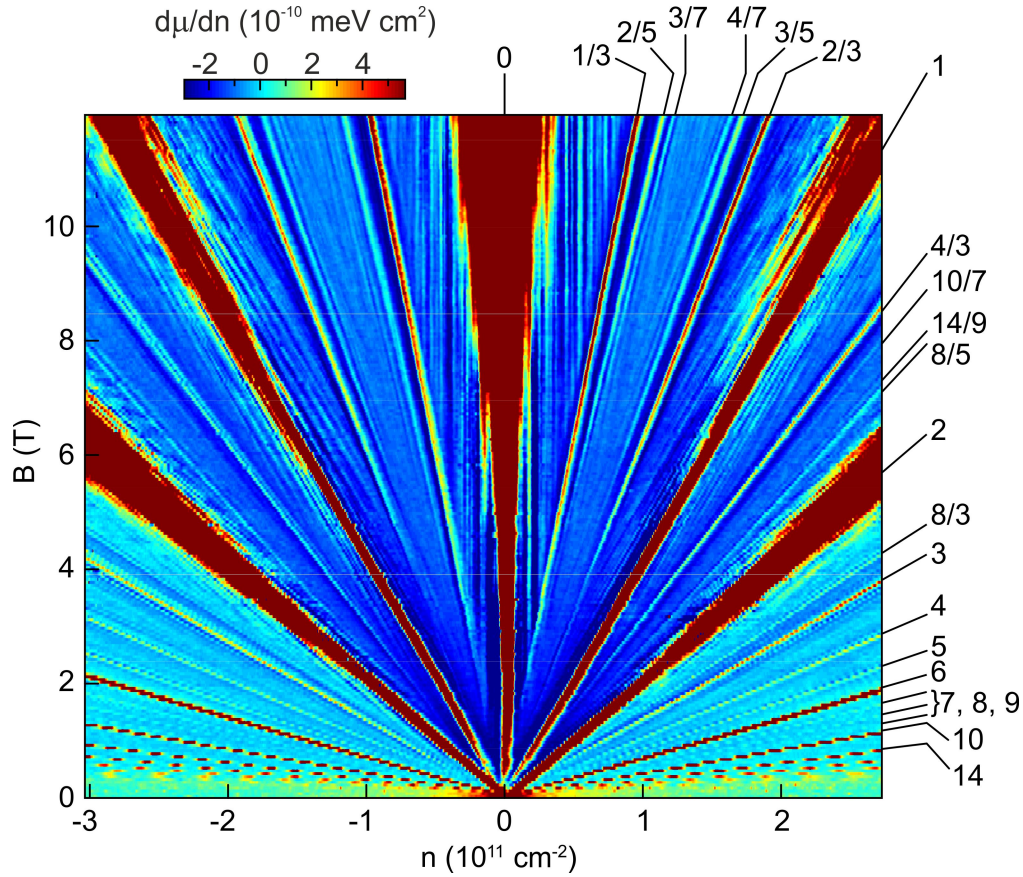
Figure 10.2.: *Inverse compressibility as a function of carrier density n and magnetic field B. Broken-symmetry quantum Hall states occur at all integers in the lowest Landau levels and fractional quantum Hall states emerge above $B \approx 1$ T. Oscillations in compressibility that run parallel to quantum Hall states in the $n - B$ plane are caused by localized states. Principle integer and fractional quantum Hall states are labeled.*

10.3. Sequence of fractional quantum Hall states

Figure 10.5 (a) shows a finer measurement of the inverse compressibility as a function of filling factor and magnetic field for $\nu < 1$. Incompressible peaks occur at $\nu = 1/3$, 2/3, 2/5, 3/5, 3/7, 4/7 and 4/9, reproducing the standard composite fermion sequence observed in GaAs. We resolve the strongest incompressible states, $\nu = 1/3$ and 2/3, down to B ≈ 1 T, although $\nu = 2/3$ weakens considerably below 4 T. As filling factor denominator increases, the field at which the corresponding state emerges also increases, with $\nu = 4/9$ only apparent above B ≈ 9 T. Between $\nu = 1$ and 2, we observe a different pattern of incompressible behavior (Figure 10.5 (b)). Surprisingly, no fractional quantum Hall states with odd numerators occur in this regime. Instead, the system condenses into incompressible states only at $\nu = 4/3$, 8/5, 10/7 and 14/9. The incompressible peaks at ν = 4/3 and 8/5 are most robust, persisting down to 1 and 1.5 T, respectively. In graphene, $\nu = 2$ corresponds to a filled LL; defining filling fraction $\nu^* = 2 - \nu$ reveals a clear pattern of incompressible peaks at $\nu^* = 2p/(4p \pm 1)$ for $p \leq 2$. This sequence is similar to that displayed by composite fermions, except that only filling fractions with even numerators
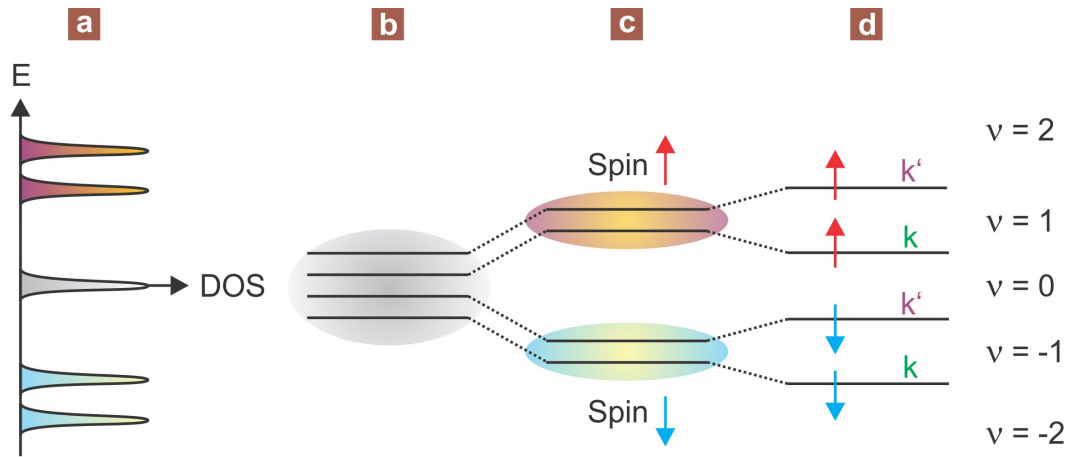
Figure 10.3.: **Landau level in graphene without and with interactions among electrons.** *(a) Without interactions, the zero energy LL has a four fold degeneracy (b). If the spin (c) and valley (d) degeneracies are lifted all integer filling factors are observable.*
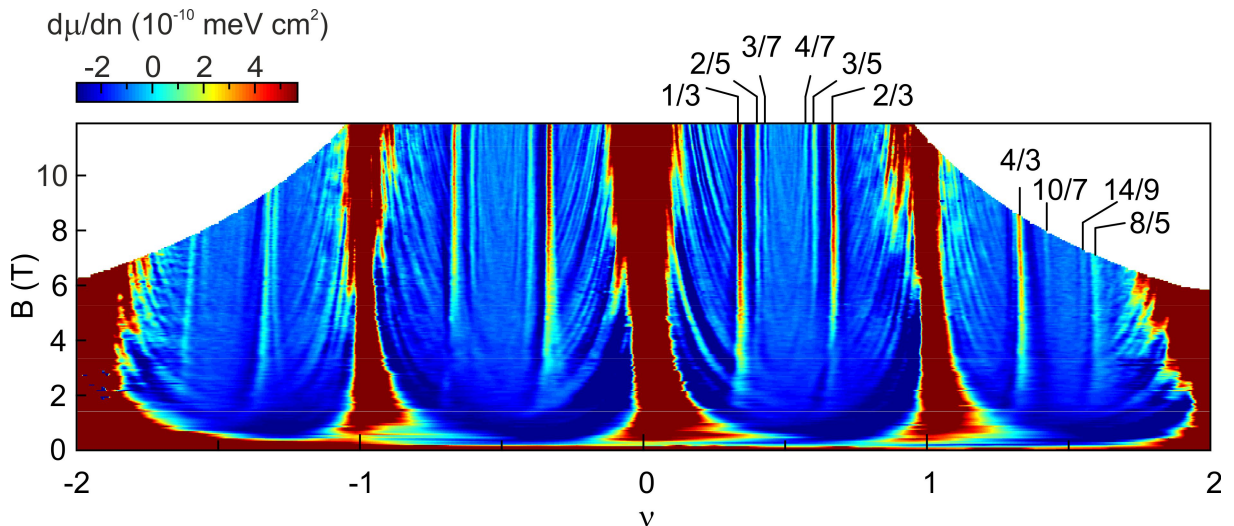

Figure 10.4.: **Inverse compressibility as a function of filling factor ν and magnetic field B.** *Same data as in Figure 10.2. Vertical features correspond to quantum Hall states, whereas localized states curve as magnetic field is changed. Principle fractional quantum Hall states are labeled.*

lead to incompressible states. The absence of odd-numerator fractions suggests that either a robust underlying symmetry prevents the formation of incompressible states or that low-lying excitations are available. One possible explanation is that the Zeeman effect lifts spin degeneracy, but valley symmetry remains intact, allowing large valley skyrmions to form with a minimal energy penalty at odd-numerator filling factors. The behavior we observe between $\nu = 1$ and 2 is reminiscent of results from strained Si and AlAs two-dimensional electron systems, which also have a valley degree of freedom and exhibit weakened odd-numerator states [235–238]. However, the analogy is not perfect. The large effective mass and g-factor in these semiconducting materials lead to fully spin-polarized
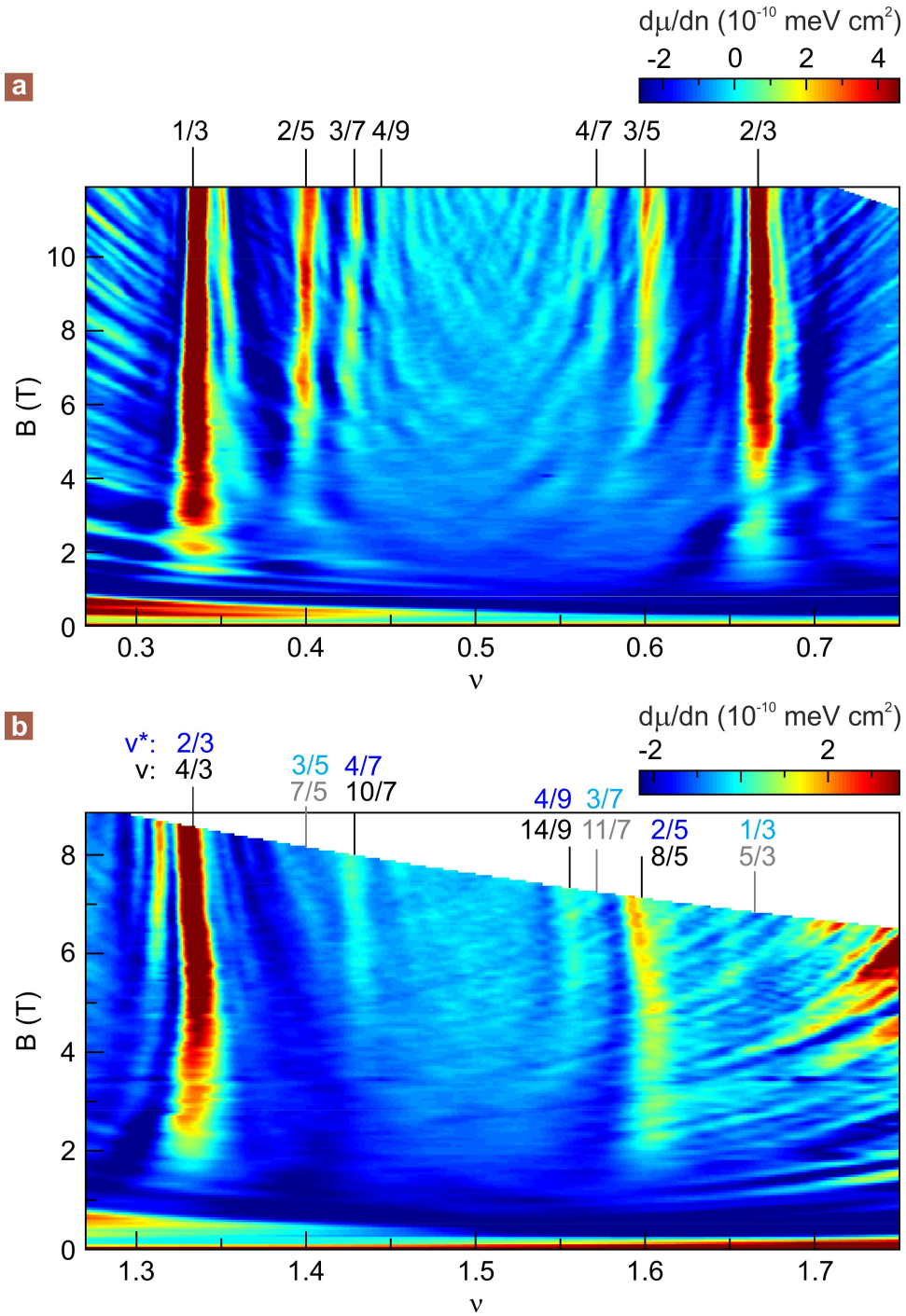
Figure 10.5.: *Incompressible fractional quantum Hall states in the lowest Landau level.* (a) Finer measurement of dµ/dn as a function of filling factor and magnetic field. Incompressible states follow the standard composite fermion sequence between ν = 0 and 1. (b) Finer measurement of dµ/dn between ν = 1 and 2. Incompressible states occur only at filling fractions with even numerators.

LLs due to single-particle effects; in contrast, the Zeeman energy is significantly smaller than LL separation in graphene. In valley-symmetric AlAs, the energy gap at $\nu = 1/3$ is large compared to that at $\nu = 5/3$ [237], opposite from the behavior that we observe at $\nu^* = 1/3$ and 5/3 when we account for the half-integer shift of LLs in graphene. This suggests that total electron density, and not just filling fraction, may play an important role in electronic interactions in the lowest LL, a topic which has only recently started to be explored [239]. Moreover, while the incompressible behavior we observe between $\nu = 1$ and 2 is consistent with SU(2) symmetry, it is evident that this symmetry does not persist between $\nu = 0$ and 1, where the full composite fermion sequence is present. We are not aware of an explanation in the literature for the differing behavior above and below $\nu = 1$, but it suggests an interplay between the inherent symmetries of graphene and electronic correlations in the lowest LL. While further study is necessary to determine the nature of the ground state and excitations of each fractional quantum Hall state, our results conclusively establish that the FQHE in graphene is qualitatively different from that observed in conventional semiconductors.

The magnitudes of the incompressible peaks in Figure 10.5 do not decrease smoothly as a function of magnetic field. This is particularly evident for fractions with high denominators and at low magnetic field. The phenomenon is sometimes so strong that an incompressible peak vanishes, only to reappear again at lower field. Modulations in the inverse compressibility may be caused by crossing localized states associated with other quantum Hall states. Alternatively, the disappearance and re-emergence of particular fractions, such as $\nu = 2/3$ around 3.5 T, may indicate a phase transition where the spin and/or valley polarization of the fractional quantum Hall state changes, as observed in GaAs [240].

Averaging over magnetic field helps to reduce fluctuations from localized states because they do not occur at constant filling factor as magnetic field is varied. Figure 10.6 shows the inverse compressibility between $\nu = 0$ and 1, averaged over 9-11.9 T (blue), and between $\nu = 1$ and 2, averaged over 4.9-6.4 T (red). These curves reveal clear incompressible peaks centered at the filling fractions discussed above, as well as negative contributions to the inverse compressibility immediately surrounding each fractional quantum Hall state, which can be ascribed to interactions among the quasiparticles and quasiholes involved in the FQHE [241]. It is worthwhile to note that a slight incompressible peak occurs at $\nu = 1.65$ in Figure 10.6. While this may indicate the emergence of a fractional quantum Hall state at $\nu = 5/3$, it is much weaker than all other multiples of $\nu = 1/3$ and is therefore consistent with the conclusion that all odd-numerator fractional quantum Hall states are suppressed.

10.4. Gap size of fractional quantum Hall states

Integrating the inverse compressibility with respect to carrier density allows us to extract the step in chemical potential $\Delta\mu_\nu$ associated with each fractional quantum Hall state and thereby determine the corresponding energy gap Δ_ν. Figure 10.7 (a) displays the chemical potential as a function of carrier density at B = 11.9 T. We define $\Delta\mu_\nu$ as the difference
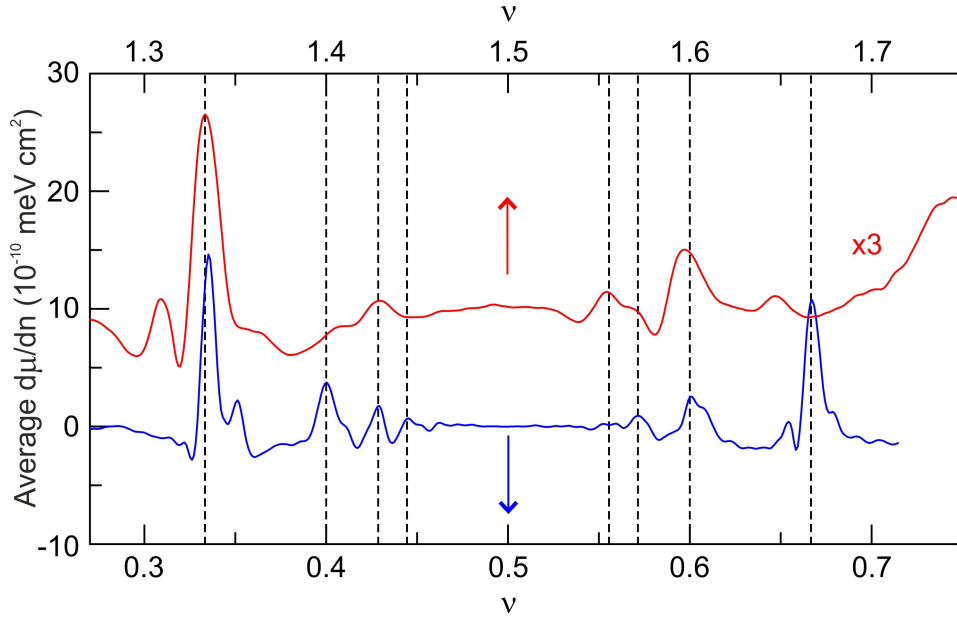
Figure 10.6.: ***Averaged incompressible FQH states in the lowest Landau level.*** *$d\mu/dn$ between $\nu = 0$ and 1, averaged over 9-11.9 T (blue) and between $\nu = 1$ and 2, averaged over 4.9-6.4 T (red). Curves are offset for clarity. Averaging over magnetic field reduces the influence of localized states and shows clear incompressible peaks centered at $\nu = 1/3, 2/3, 4/3, 2/5, 3/5, 8/5, 3/7, 4/7, 10/7, 4/9$ and $14/9$.*

between the local maximum and minimum in the chemical potential. Due to the finite size of the sample, some fringing fields from the back gate directly affect the SET, giving rise to a constant positive offset in the measured inverse compressibility. To accurately extract $\Delta\mu_\nu$ of each fractional quantum Hall state, this parasitic capacitance must be taken into account. Determining the zero of $d\mu/dn$ is complicated because interactions among charge carriers produce a negative contribution to the inverse compressibility that depends on magnetic field [241]. Figure 10.8 shows the average inverse compressibility as a function of magnetic field for the filling factor ranges $0.45 \leq \nu \leq 0.55$ and $1.45 \leq \nu \leq 1.55$. The inverse compressibility in both ranges is similar, and is fit well by a $d\mu/dn \propto -B^{-1/2}$ dependence, as expected for interacting particles with a density $n \propto B$. The fit to these curves is used to define $d\mu/dn = 0$ at each field for the extraction of $\Delta\mu_\nu$. Figures showing linecuts of $d\mu/dn$ as a function of density also follow the convention that $d\mu/dn = 0$ at $\nu = 1/2$. However, the inverse compressibility in color plots is typically defined so that $d\mu/dn = 0$ in the compressible regions associated with Landau levels at filling factors $\nu > 2$ (e.g. at $\nu = 3.5$).

It is also important to note that the chemical potential is defined with respect to electrons. Therefore, the step in chemical potential must be multiplied by the ratio of the quasiparticle charge to the electron charge in order to obtain the energy gap of fractionally charged quasiparticles.

The values for $\Delta\mu_\nu$ for each fractional quantum Hall state as a function of magnetic field are plotted in Figures 10.7 (b) and (c). The steps in chemical potential at each multiple of $\nu = 1/3$ have a similar magnitude (Figure 10.7 (b)). It reaches a maximum of about 3.5 meV at $B = 11.9$ T. Both $\Delta\mu_{1/3}$ and $\Delta\mu_{2/3}$ also have a similar dependence on magnetic
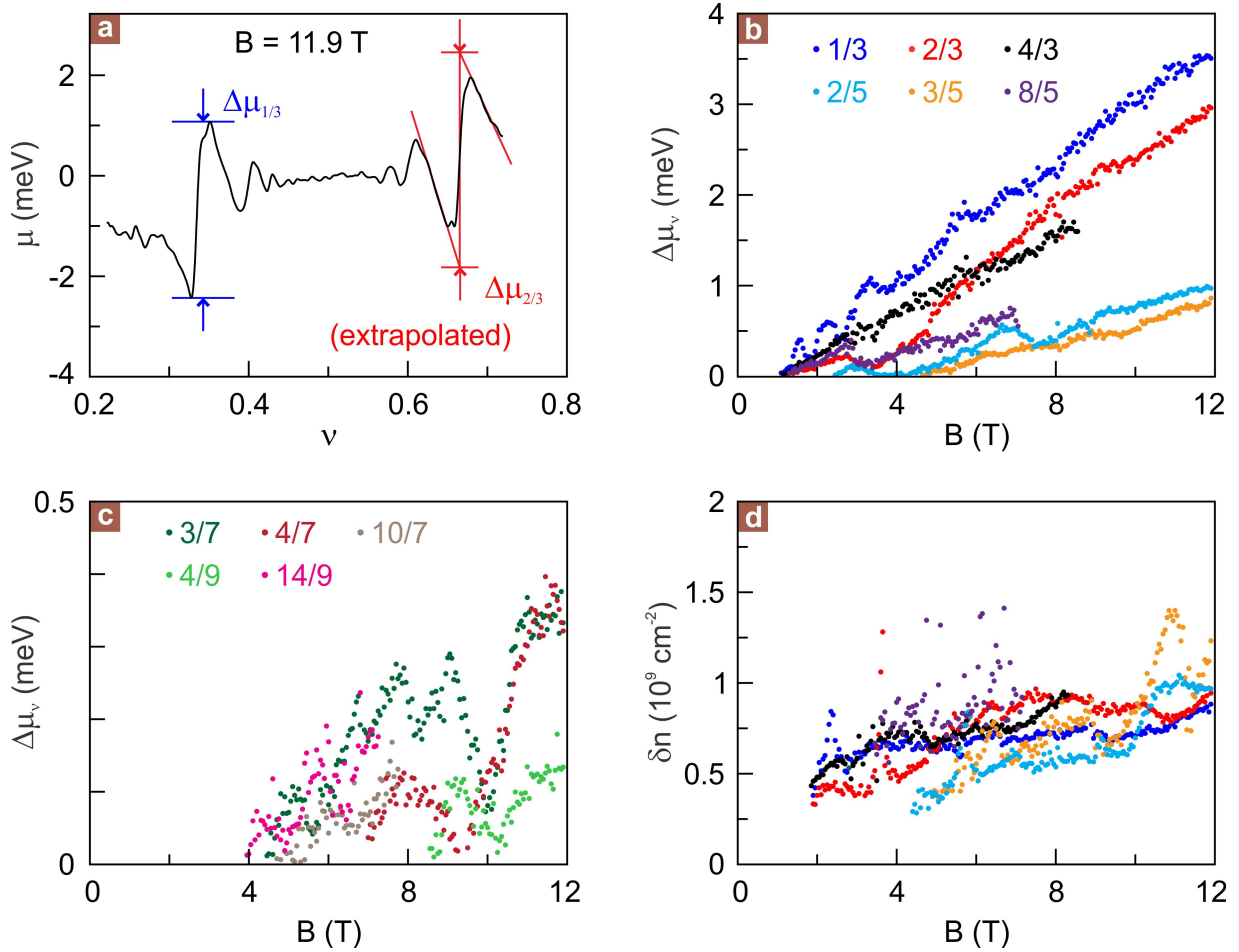
Figure 10.7.: *Steps in chemical potential and incompressible peaks widths.*
(a) Chemical potential relative to its value at ν = 1/2 as a function of carrier density
at 11.9 T. The step in chemical potential of each incompressible state is given by the
difference in chemical potential between the local maximum and minimum (blue). Data
presented in panels (b) and (c) were extracted using this method. Disorder smears out the
cusps of each incompressible peak, but an estimate of the intrinsic behavior can be made
by extrapolation from the linear sloped regions surrounding each fractional quantum Hall
state (red; see Figure 10.9 and Table 10.1). (b) Steps in chemical potential associated with
fractional quantum Hall states at measured multiples of ν = 1/3 and 1/5 as a function
of magnetic field. (c) Steps in chemical potential of fractional quantum Hall states at
measured multiples of ν = 1/7 and 1/9 as a function of magnetic field. Localized states
give rise to especially large fluctuations in the apparent strength of these states. (d)
Incompressible peak width of the fractional quantum Hall states as a function of magnetic
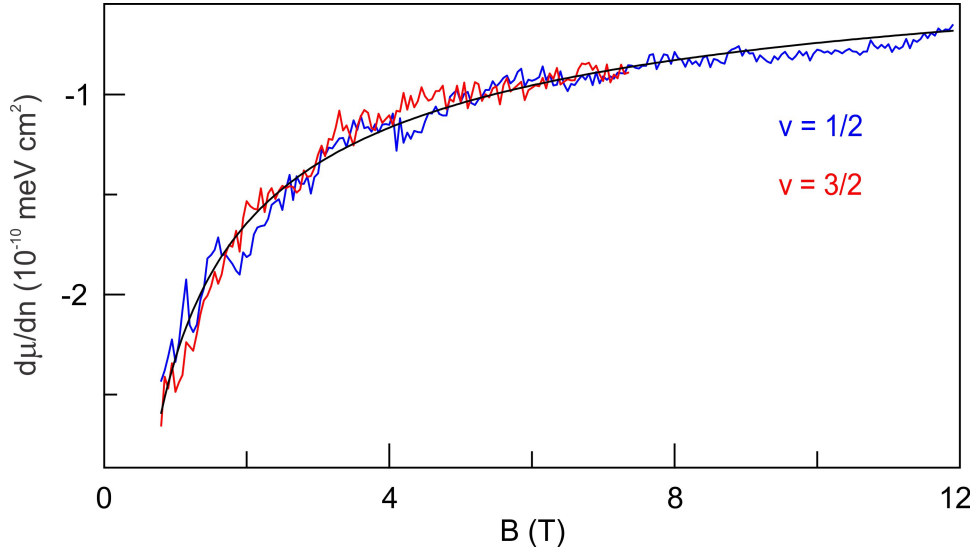*field.*

Figure 10.8.: ***Determining the zero of inverse compressibility.*** *Average inverse compressibility as a function of magnetic field for the filling factor ranges $\nu = 0.45$ - 0.55 (blue) and $\nu = 1.45$ - 1.55 (red). The data are well fit by a $-B^{-1/2}$ dependence, as shown by the black fit. The black fit is used to determine $d\mu/dn = 0$ for the purpose of fractional quantum Hall gap size extraction at each field.*

field; they scale approximately linearly with field and exhibit a steeper slope than that of $\Delta\mu_{4/3}$. We note that the energy gap at $\nu = 2/3$ nearly closes around $B = 3.5$ T before reviving again. This is potential evidence for a change in the spin and/or valley polarization of the $\nu = 2/3$ state. The steps in chemical potential at $\nu = 2/5$, 3/5 and 8/5 can all be described by a linear dependence on magnetic field with a similar slope, but their intercepts are different. At $B = 12$ T, $\Delta\mu_{2/5}$ and $\Delta\mu_{3/5}$ are approximately 1 and 0.9 meV, respectively, and $\Delta\mu_{8/5}$ reaches a maximum of about 0.7 meV at 7 T. Although $\Delta\mu_{\nu}$ for the states discussed above can be described by a linear dependence on field, we cannot rule out a $B^{1/2}$ scaling, particularly at high magnetic field. The steps in chemical potential at $\nu = 3/7$, 4/7, 10/7, 4/9 and 14/9 are smaller (Figure 10.7 (c)), and their extracted magnitudes fluctuate substantially as a function of magnetic field, presumably due to the influence of localized states at the measurement point. Although the energy gaps associated with fractional quantum Hall states closer to $\nu = 0$ are larger and persist to lower fields than do their counterparts near $\nu = 1$ with the same denominator, this behavior is not robust; before current annealing our sample, we observed the opposite trend (see Section 10.6).

The energy gaps that we extract are smaller than theoretical predictions [216, 217, 220, 223, 224, 227] but are comparable to results from activation studies [204, 230], which yielded $\Delta_{1/3} \approx 1.4$ - 1.8 meV at 12 T and $\Delta_{4/3} \approx 1.6$ meV at 35 T. Although comparison to $\Delta_{4/3}$ at 35 T is difficult due to the discrepancy in field strength, extrapolating the linear slope we measure in $\Delta_{4/3}$ yields a value of about 2.8 meV at 35 T. Our measured energy gaps are only slightly smaller than theoretical predictions at $\nu = 1/3$, but are 3 - 10 times smaller than those theoretically predicted at $\nu = 2/3$, 4/3, 2/5 and 8/5 (see Table 10.1). The comparatively small experimental energy gaps are likely a result of sample disorder, which smears out the cusps in $\mu(n)$ and therefore decreases the apparent step in chemical

potential. This can be partially mitigated by linear extrapolation of the negative slope in $\mu(n)$ surrounding each fractional quantum Hall state [242] (Figure 10.7 (a) shown in red). The steps in the chemical potential are then larger (see Table 10.1 and Figure 10.9). We estimate an energy gap of $\Delta_{1/3} \approx 1.5$ meV, which is within the range spanned by theoretical predictions. In contrast, even the extrapolated $\Delta_{2/3} \approx 1.5$ meV is still 2-3 times smaller than theoretically predicted. Similarly, the estimated value of $\Delta_{2/5}$ from the extrapolation in Figure 10.9 is only about 0.4 meV at $B = 12$ T, approximately 4-5 times smaller than theoretically predicted. Although the extrapolated steps in chemical potential at $\nu = 4/3$ are not shown in Figure 10.9, $\Delta_{4/3} \approx 0.75$ meV at 8 T, about 4-5 times smaller than the theoretical prediction. Finally, we note that linear extrapolation was not possible at $\nu = 8/5$ or $14/9$, but the energy gaps at these filling factors are also significantly smaller than expected.

ν	Theoretically predicted Δ_ν	Predicted Δ_ν at largest B (meV)	Experimental Δ_ν at largest B (meV)	Extrapolated Δ_ν at largest B (meV)
1/3	$(0.03\text{-}0.1)e^2/\epsilon l_B$	1.3 - 4.3 (at 12 T)	1.2	1.5
2/3	$(0.08\text{-}0.11)e^2/\epsilon l_B$	3.5 - 4.8 (at 12 T)	1	1.5
4/3	$(0.08\text{-}0.11)e^2/\epsilon l_B$	2.8-3.9 (at 8 T)	0.5	0.75
2/5	$(0.04\text{-}0.051)e^2/\epsilon l_B$	1.7 - 2.2 (at 12 T)	0.2	0.4
8/5	$(0.02\text{-}0.051)e^2/\epsilon l_B$	0.7 - 1.7 (at 7 T)	0.15	-
14/9	$0.019e^2/\epsilon l_B$	0.6 (at 7 T)	0.02	-

Table 10.1.: **Summary of fractional quantum Hall gap strengths.** *Theoretical predictions for gap size at the highest experimentally accessible magnetic field are compared with the corresponding measured and extrapolated values. Experimental and extrapolated values assume that the charge of the quasiparticles involved is given by the electron charge divided by the denominator of the filling factor. We assume a dielectric constant of 4.5 in suspended graphene [176]. Linear extrapolation was not possible at $\nu = 8/5$ and $14/9$.*

The width δn are shown for the most robust fractional quantum Hall states in Figure 10.7 (d). Widths were determined by fitting a Gaussian to the incompressible peak at each filling factor. All fractional quantum Hall states have similar δn of about 4 - 10 · 10^8 cm^{-2}, which does not depend strongly on magnetic field. This field-independence can be understood to arise from nonlinear screening [211], suggesting that δn reflects the amount of local disorder in our device. The exceptionally small peak widths provide another indication that the sample is especially clean.
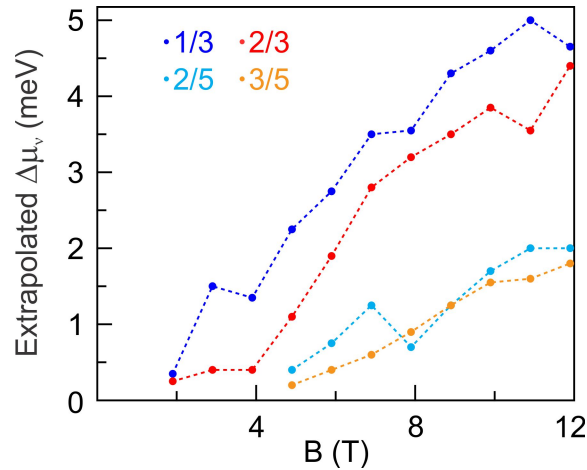
Figure 10.9.: ***Extrapolated gap sizes.*** *Steps in chemical potential at $\nu = 1/3$ (blue), 2/3 (red), 2/5 (cyan) and 3/5 (orange) obtained by linearly extrapolating the negative compressibility surrounding each fractional quantum Hall state, as illustrated in Figure 10.7 (a). Lines between data points are guides to the eye.*

10.5. Spatial dependence of fractional quantum Hall states

All the measurements described so far were taken at single positions. We now discuss the spatial dependence of each fractional quantum Hall state. Line scans of the inverse compressibility as a function of filling factor and position at $B = 6$ and 12 T are shown in Figures 10.10 (a) and (b), respectively. The density at which incompressible peaks occur varies with position, which can be explained by local density fluctuations. The magnitude of these fluctuations is similar to the width of the fractional quantum Hall states, and may explain why the FQHE has been so difficult to observe in transport studies: different regions of the sample form a given fractional quantum Hall state at different back gate voltages. The transport measurement in Figure 10.11 shows the resistance of the device as a function of carrier density n and magnetic field B. The device is a hybrid consisting of monolayer and bilayer graphene in parallel. We observe several quantum Hall features, with resistance maxima occurring at $\nu = 0, 1, 2, 3, 4$ and 6. This sequence includes the strongest monolayer and bilayer states, consistent with previous measurements [243]. Conductance plateaus at approximately the expected quantized value occur at filling factors $\nu = 1$ and 2 suggesting that both the monolayer and bilayer sides are simultaneously in a fully developed quantum Hall state. Conductance is also suppressed strongly at the charge neutrality point, with resistance reaching approximately 1 MΩ. However, no oscillations in resistance occur at fractional filling factors. This likely reflects the charge inhomogeneity in the sample, as discussed above. It is worthwhile to note that in transport, the resistive region at $\nu = 0$ is so wide that it envelops $\nu = 1/3$, even though $\nu = 1/3$ is visible at virtually all positions along the monolayer in local compressibility measurements.

Figure 10.10 also shows that incompressible peak magnitude fluctuates substantially as a function of position. Although some incompressible states, such as those at $\nu = 1/3$
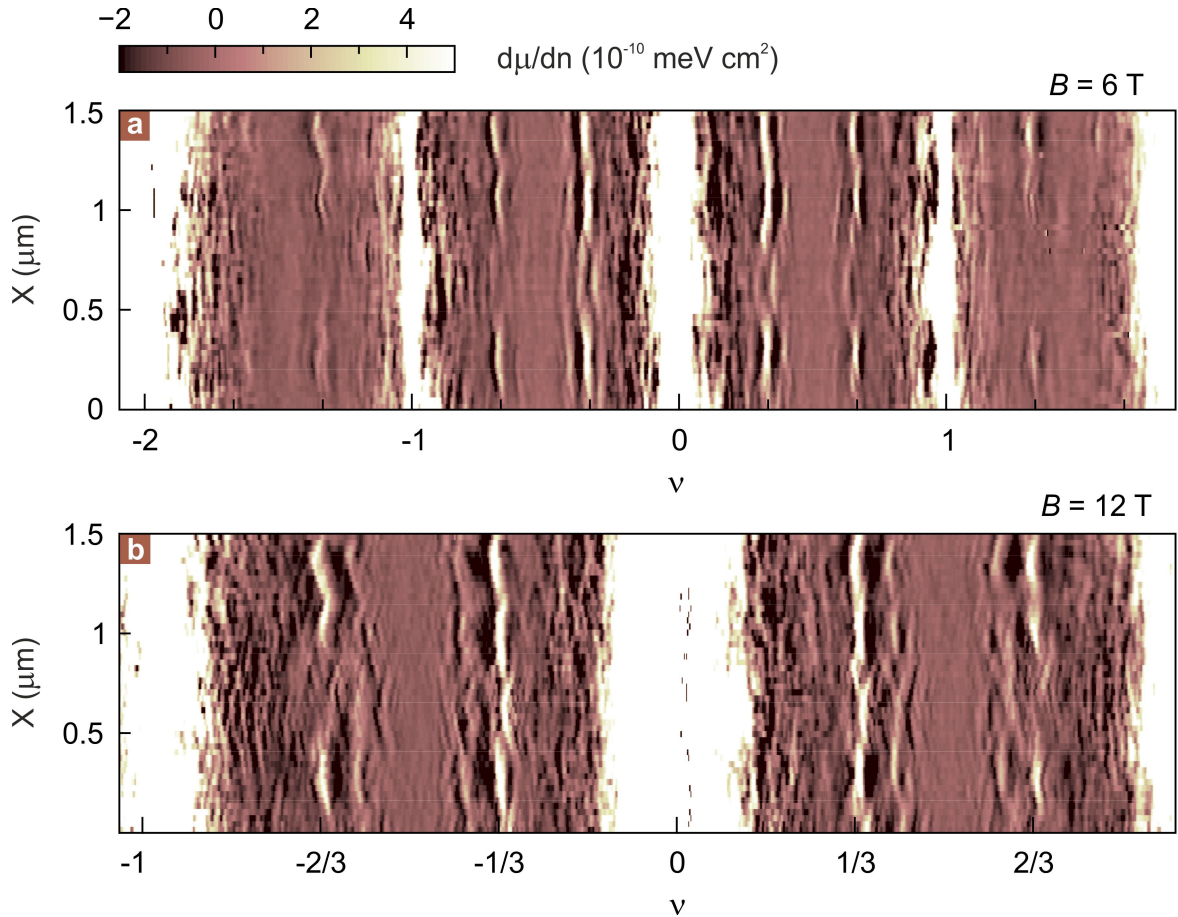
Figure 10.10.: **_Spatial dependence of fractional quantum Hall states._** _(a) dμ/dn as a function of filling factor and position X along the flake (red arrow in Figure 10.1 (a)) at B = 6 T. (b) dμ/dn as a function of carrier density and position at B = 12 T. At both fields, we observe density fluctuations and variations in the strength of the fractional quantum Hall states as a function of position. States at ν = 2/3 and 4/3 appear more susceptible to disorder than the state at ν = 1/3._

persist at virtually all positions, others are more susceptible to disorder. Both $\nu = 2/3$ and 4/3 fully disappear in some locations, which seem to be correlated with the areas where the integer quantum Hall states are wider, a sign that local disorder is comparatively large. We note that before aggressive current annealing, the flake was much more homogeneous, but the overall level of disorder was larger. All the data presented so far were taken after two rounds of current annealing. The sample changed substantially as a result of each current annealing step. Next, we discuss the progression of the flake associated with these cleaning procedures.

10.6. Role of disorder

Figures 10.12, 10.13 10.14 and 10.15 show data prior to current annealing, and Figures 10.16 and 10.17 display data taken after gentle current annealing. Even before current an-
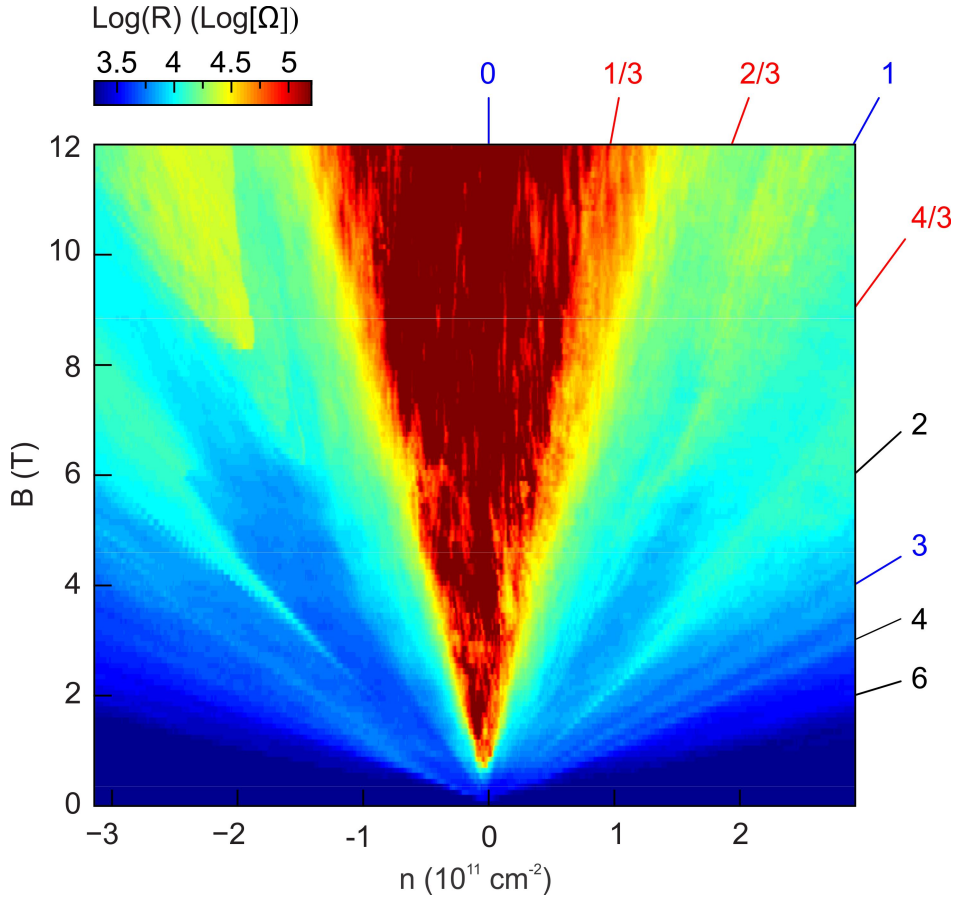
Figure 10.11.: *Magnetotransport measurement.* *Sample resistance R as a function of carrier density n and magnetic field B. Numbers and solid slanted lines at the edge of the plot indicate selected filling factors ν. No signs of fractional filling factors are visible in this global experiment, although locally fractions are observed (see for instance Figure 10.5).*

nealing the device, incompressible fractional quantum Hall states were visible. Fractional quantum Hall states are clearly distinguishable in Figure 10.12 above 5-6 T, although the incompressible peaks are not nearly as pronounced, and localized states significantly modulate their apparent strength. The increased disorder is particularly evident in the breadth of localized states surrounding $\nu = 2$, which obscure all fractional quantum Hall states above $\nu = 4/3$. Figures 10.13 (a) and 10.13 (b) show spatial maps at $B = 8$ and 12 T, respectively, and the average compressibility over these spatial regions is plotted in Figure 10.13 (c). Incompressible behavior is only evident at multiples of $\nu = 1/3$, but the data reveal relatively homogeneous strength of each fractional quantum Hall state as a function of position, particularly compared to that presented in Figure 10.10.

Finer measurements which reveal fractional quantum Hall states at $\nu = 1/3$, 2/3, 4/3, 2/5, 3/5 and 4/7 are shown in Figures 10.14 (a) and (b). A three-dimensional rendering of the high-field data is plotted as a function of filling factor in Figure 10.14 (c), and the average of inverse compressibility over this field range can be seen Figure 10.14 (d). Interestingly, the incompressible behavior at $\nu = 2/3$ persists to lower fields than $\nu = 1/3$, and the same is true for $\nu = 3/5$ with respect to $\nu = 2/5$. This is the opposite
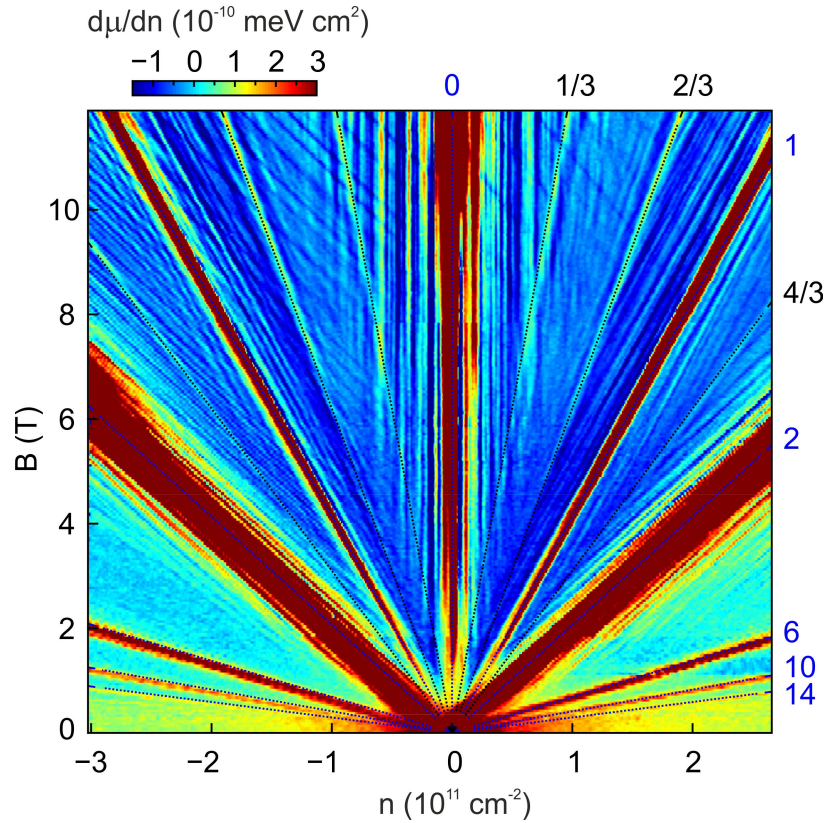
Figure 10.12.: ***Inverse compressibility of the pristine graphene device.*** *Inverse compressibility dμ/dn as a function of density n and magnetic field B. Incompressible fractional quantum Hall states emerge around 5-6 T. Localized states associated with ν = -2 are especially broad.*

behavior from that observed after current annealing. The data presented in Figure 10.14 are actually an average over measurements performed at six different locations, each separated by about 200 nm. Spatial averaging mitigates the fluctuations in compressibility caused by localized states to some degree. Nonetheless, the incompressible peaks at $\nu = 1/3$ and $2/5$ are still strongly modulated by localized states, which may explain why they disappear at higher fields than their counterparts near $\nu = 1$ with the same denominator.

The steps in chemical potential $\Delta\mu_\nu$ and incompressible peak widths δn associated with each fractional quantum Hall state prior to current annealing are shown in Figure 10.15. The extracted values of $\Delta\mu_\nu$ were smaller before annealing for all states, with $\Delta\mu_{1/3}$ and $\Delta\mu_{2/3}$ reaching only 1 meV at 12 T. Moreover, the steps in chemical potential depended primarily on filling factor denominator, with no differences evident over the fluctuations caused by localized states. All incompressible fractional quantum Hall peaks had similar widths, but they were slightly wider than after current annealing, indicating increased charge inhomogeneity.

Next, we current annealed the sample gently, applying only 1 V between contacts. This had no effect on electronic transport, but dramatically improved sample quality. The data reveal additional incompressible fractional quantum Hall states at $\nu = 8/5$, $3/7$ and $10/7$, and a large increase in the magnitude of the incompressible peaks associated with other
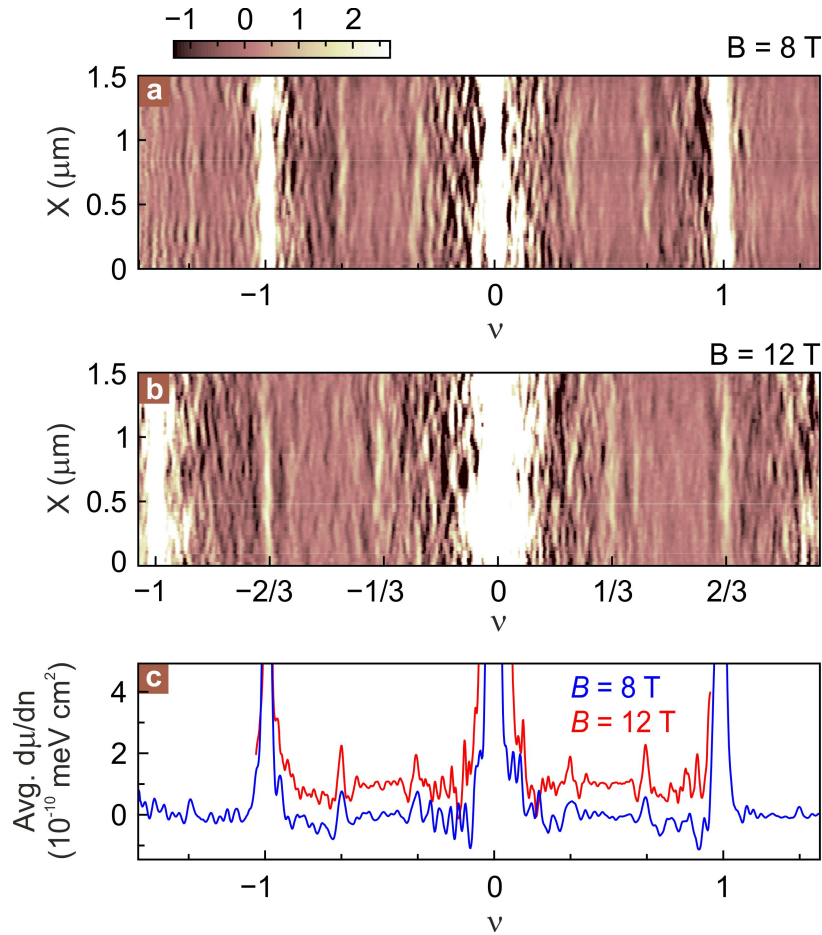
Figure 10.13.: ***Spatial dependence of the inverse compressibility of the pristine graphene device.*** *(a) dμ/dn as a function of filling factor and position X along the flake at B = 8 T. (b) dμ/dn as a function of carrier density and position along the flake at B = 12 T. (c) Spatial average of dμ/dn at 8 T (blue) and 12 T (red). Curves are offset for clarity.*

fractional quantum Hall states (Figure 10.16). Each incompressible state persists to lower field as well, with $\nu = 1/3$, $4/3$ and $8/5$ all visible at 2 T. It is worthwhile to note that $\nu = 2/3$ is less robust, disappearing around 4 T, consistent with the diminished gap observed around 3.5 T after the second round of current annealing (see Figure 10.5 (a)). The step in chemical potential associated with each fractional quantum Hall state increased as a result of current annealing as well, with $\Delta\mu_{1/3}$ reaching 2.5 meV and $\Delta\mu_{3/5}$ reaching 0.7 meV at 12 T (Figure 10.17 (a)). Moreover, the incompressible peak magnitude remained approximately independent of position, as illustrated in Figure 10.17 (b).
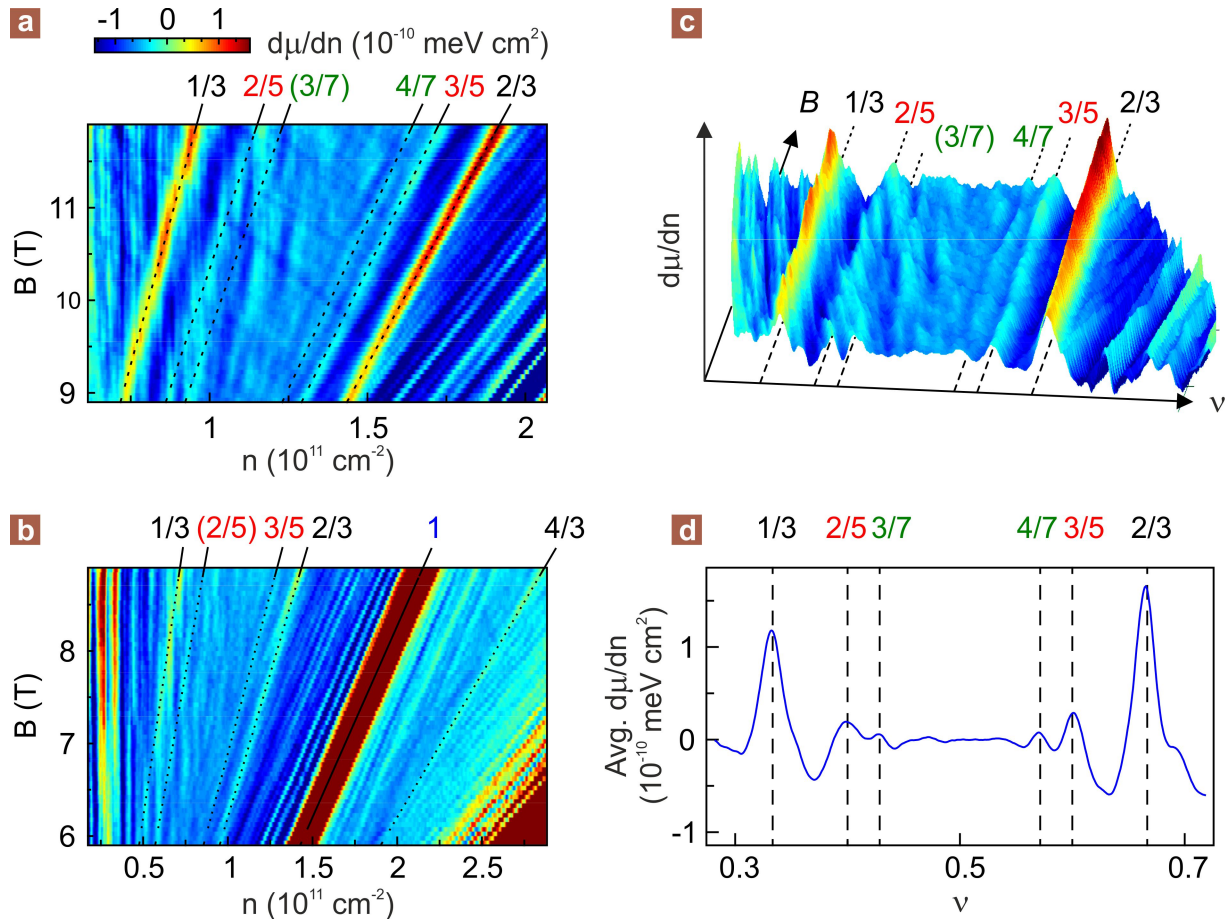
Figure 10.14.: **Fractional quantum Hall states measured on the pristine graphene device.** (a) and (b) Spatial average of dμ/dn as a function of carrier density and magnetic field taken at six different locations. Incompressible states occur at ν = 1/3, 2/3, 2/5, 3/5 and 4/7 which are marked by dashed lines. Despite the averaging, localized states parallel to ν = 0 and 1 are still visible and modulate the apparent amplitude of the fractional states. (c) Three-dimensional rendering of the data in (a) plotted as a function of filling factor. In this rendering, localized states appear as curved compressibility oscillations rather than straight lines. (d) dμ/dn as a function of filling factor, averaged over the field range shown in (a).
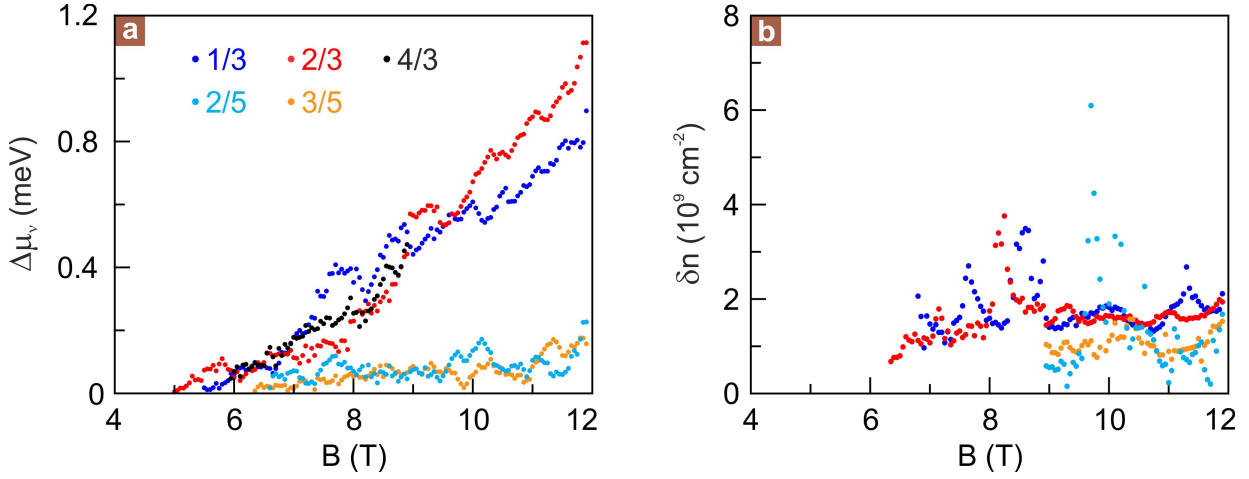
Figure 10.15.: *Steps in chemical potential and peak widths of the pristine graphene device. (a) Energy gaps of each fractional quantum Hall state as a function of magnetic field. The gap size depends primarily on the denominator of the filling factor. (b) Incompressible peak widths of each fractional quantum Hall state, which are not strongly dependent on magnetic field.*
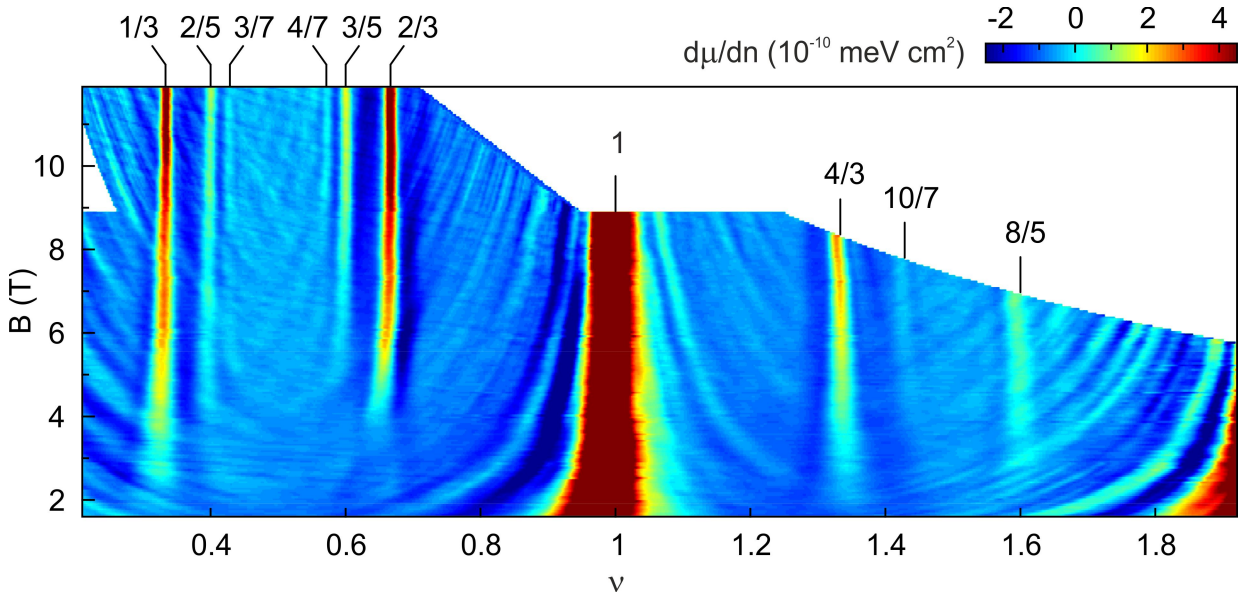
Figure 10.16.: *Inverse compressibility after gentle current annealing. Inverse compressibility as a function of filling factor and magnetic field. Clear incompressible peaks occur at $\nu = 1/3, 2/3, 2/5, 3/5, 3/7, 4/7, 4/3, 8/5$ and $10/7$. Few localized states are visible due to the decreased sample disorder and the relatively large excitation in density: approximately $1.5 \cdot 10^9$ cm^{-2}, which is identical to that used to take the data in Figures 10.12 and 10.14, but 2.5 times larger than used in the measurements presented in Figures 10.2 - 10.5.*

Figure 10.17.: ***Steps in chemical potential after gentle current annealing.*** *(a) Steps in chemical potential of each fractional quantum Hall state a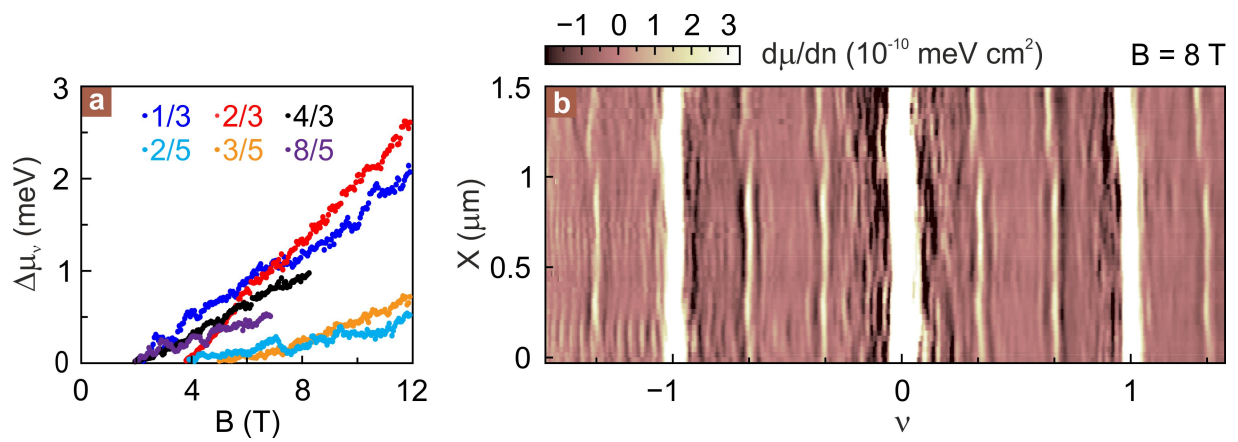s a function of magnetic field. (b) $d\mu/dn$ as a function of filling factor and position X along the flake at $B = 8$ T. Incompressible peaks are visible at $\nu = 1/3, 2/5, 3/5, 2/3$ and $4/3$, and sample behavior varies only moderately with position.*

10.7. Summary and outlook

Despite the existence of disordered regions, the ability to perform local measurements reveals a multitude of fractional quantum Hall states in the cleanest areas. The observation of incompressible behavior at multiples of $\nu = 1/9$ indicate that graphene is quickly approaching the sample quality obtained in GaAs. Graphene may soon provide a platform in which to investigate some of the more exotic electronic states observed in conventional two-dimensional electron systems. We eagerly expect results and new physics after additional current annealing steps performed on this device.

Whereas the measurements described above mainly focus on the novel fractional quantum Hall findings on the monolayer part, a cornucopia of effects is expected at the interface between the mono- and bilayer part like edge modes and charge redistribution. An example of a spatial map of the inverse compressibility is shown in Figure 10.18 with zero backgate voltage applied. The increased compressibility at the interface might be an indication for the presence of edge modes. In these 2D scans, localized states appear as circles and might allow to measure the charge of fractionally charged quasi-particles.
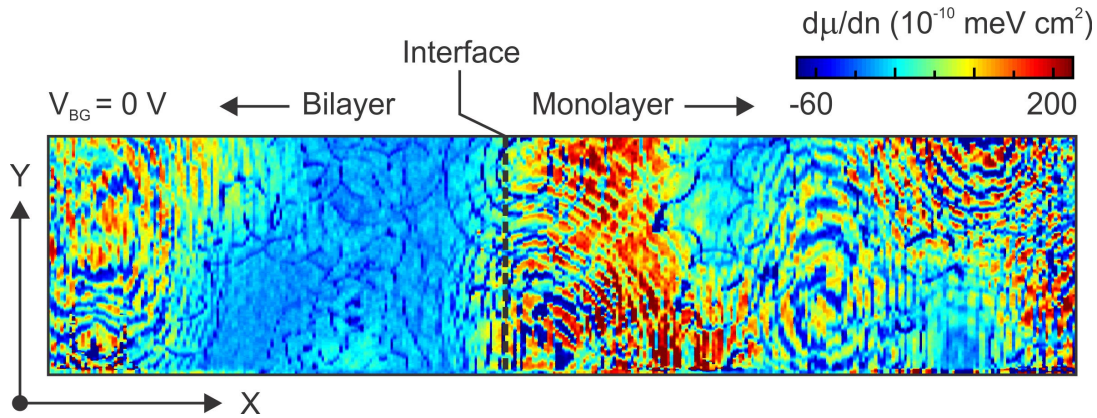

Figure 10.18.: *Spatial map of inverse compressibility. Localized states appear as circles. A region of increased compressibility is measured at the interface between mono- and bilayer parts. Zero backgate bias applied.*

11. Summary

The aim of the present thesis is to shed some light on different properties of graphene, a single atomic layer of carbon atoms. Since the discovery of an easy way to fabricate graphene from graphite by exfoliation in 2004, a huge increase in graphene related research occurred and led to the new research field of ultra-relativistic condensed matter physics. The impact of graphene in fundamental research as well as applications in nanoelectronics steadily increases.

In the framework of this thesis we focus on scanning probe spectroscopy methods to study this truly two-dimensional material. Hereby we take advantage of the fact, that graphene and its two-dimensional electron gas is readily accessible at the surface and not buried in a bulk material. The two main methods, scanning confocal Raman spectroscopy and scanning single-electron transistor microscopy, allow to determine such different information like the interaction strength between phonons and charge carriers, the chirality of the graphene edge or the consequences of interactions between electrons. The cornucopia of extractable information from Raman spectroscopy results mainly from the resonance mechanism, linking electronic with phononic properties. The interest in single-electron transistors as a local probe is based on its extraordinary high sensitivity to electrostatic potentials.

CHAPTER 2 - 4 · · · PP. 13-80
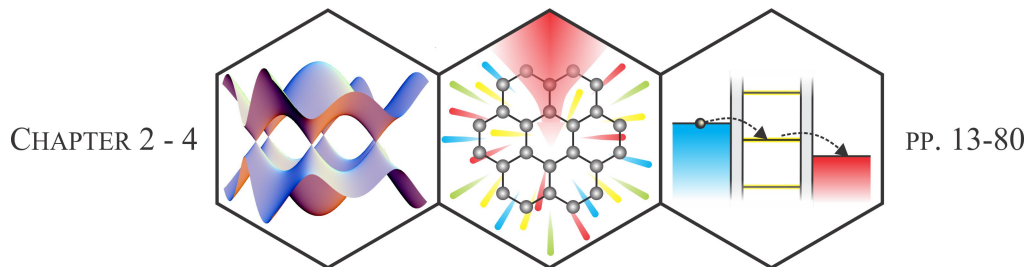
In the first part of this work we discussed the fundamentals of graphene as well as the scanning probe methods and experimental setups. In the following we will briefly summarize the main findings of the experiments described in the second part.
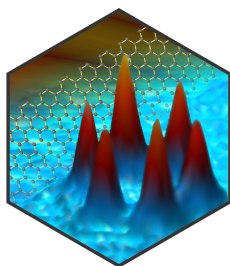
CHAPTER 5   PP. 83-106

In the first experimental chapter we demonstrate that Raman spectroscopy of graphene is invasive, in contrast to common believe. We show that laser light is not necessarily benign and modifies graphene even at moderate light power of 1 mW. For our studies we combine time and spatially resolved Raman and atomic force measurements and corroborate our findings with electrical and transmission electron microscopy studies. It turns out that laser irradiation locally disassembles a single crystalline layer of graphene into a network of interconnected nanocrystallites. An important consequence of this is that for conventional Raman spectroscopy measurements the irradiation has to be dosed carefully in order to prevent these modifications. On the other hand these modifications can be exploited on purpose. The additional boundaries provide docking sites for molecular adsorbates and hence enhance the reactivity locally.
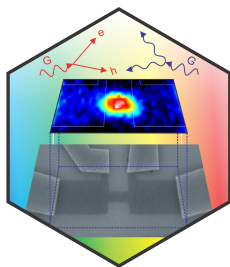
CHAPTER 6   PP. 107-122

In this chapter we study the interactions between phonons and charge carriers, which have an impact on the device performance. We show that a high current flow through a graphene device can significantly overpopulate phonon modes, which impede transport. To gain a deeper understanding, we use an electrically biased graphene constriction to locally increase the phonon occupation number. This allows us to disentangle carrier-phonon and phonon-phonon contributions. With Raman spectroscopy we are able to simultaneously measure the two most important parameters in this context: the temperature and the interaction strength of phonons with quasi-particles. Different to other materials, graphene is gapless and the Fermi temperature is tunable. This offers us the unique opportunity to control decay channels. We are able to prepare graphene in such a state that the temperature dependence of the phonon line width, which mirrors interactions, is nonmonotonic and even decreases with increasing temperature for a certain range.
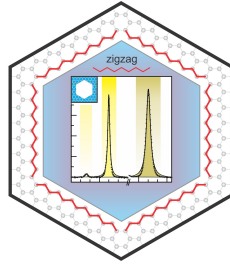
CHAPTER 7   PP. 123-134

The importance of the graphene edge and the associated electronic states has been the focus of intense research. Theory has predicted rich and very distinct physics for graphene devices if their boundaries are formed by carbon atoms arranged in the zigzag or armchair configuration. Whereas zigzag edges are composed of atoms that all belong to one and the same sublattice, the armchair edge contains carbon atoms from either sublattice. This distinction has profound consequences and a plethora of different effects is predicted. In order to unlock this physics, one has to be able to produce graphene devices that possess boundaries with a pure edge chirality and to identify this high chiral purity. We introduce an anisotropic etching procedure that creates well defined zigzag edges and demonstrate the all optical detection of the edge chirality using Raman spectroscopy. Here, the so-called Raman D peak serves as the litmus test. We explain the corresponding theory. With this method we add a powerful capability to the graphene toolbox. Combining the anisotropic etching procedure with the identification of the edge chirality is a straightforward technique to identify the crystallographic orientation of graphene flakes. Finally we show how to use the etching procedure in order to fabricate graphene constrictions, one-dimensional channels and quantum dots which are bounded exclusively by zigzag edges.
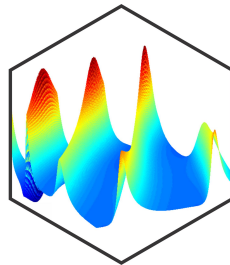
CHAPTER 8   PP. 135-144

Single layers of graphene are visible on silicon substrates covered with 300 nm silicon oxide, despite the fact that graphene layers are only one atom thick. Hence, optical microscopy provides a fast and easy way to find and identify the number of layers of small graphene flakes obtained by the micro-mechanical cleavage method. We use a model based on Fresnel laws that allows to calculate the contrast of mono and few layer graphene on the standard Si/SiO_2 substrates but also on arbitrary material arrangements. Using the example of indium tin oxide as a transparent yet conductive layer, for instance suited for STM studies of the graphene edge, we demonstrate the validity of this model. We show how to choose the best suited thickness of the material in order to maximize the contrast.
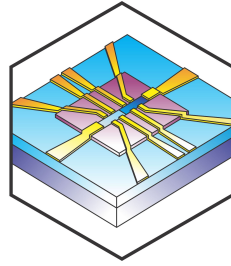
CHAPTER 9   PP. 145-152

The mobility of a material is important for the device performance. Although graphene typically has a rather high mobility even at room temperature, the measured characteristics are up to now inferior to the theoretically expected values. Some problems come from the substrate that supports the graphene monolayer. Disturbing are for instance the surface roughness, surface optical phonons and scattering from charged impurities located inside the substrate or in between the graphene and the substrate. And indeed, if the substrate underneath the graphene is removed, the mobility of suspended devices is much higher and disorder lower (as we show in the last experimental chapter). On the down side, suspended devices are fragile and break easily. Especially if a back-gate voltage is applied in order to change the carrier density, electrostatic forces tend to destroy the flake. The achievable density is one order of magnitude lower than for supported devices. Another route for high quality devices that maintains the high carrier density range of supported graphene is replacing the SiO_2 interface by a material which is flatter and less prone to attracting adsorbates. An example is hexagonal boron nitride (h-BN). It is atomically flat and free of dangling bonds and surface charge traps. Because h-BN itself is typically only a small flake on the order of several micrometer we explain one possible way to accomplish the task of placing graphene on top of h-BN. We investigate the optical visibility of h-BN depending on its thickness and compare experimental results with the theory developed in the previous chapter. Finally we focus on the surface roughness of h-BN as a function of its thickness.
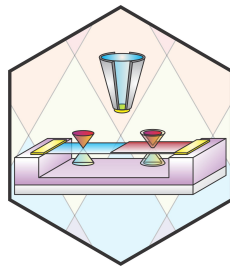
CHAPTER 10   PP. 153-172

Graphene provides a platform to study novel many-body effects due to its massless chiral charge carriers and the fourfold degeneracy that arises from their spin and valley degrees of freedom. In this chapter we report local electronic compressibility measurements of a suspended high quality graphene flake. These measurements are performed with the help of a single-electron transistor mounted on a scanning microscope. We observe a whole series of incompressible fractional quantum Hall states that follow the standard composite fermion sequence between filling factors $\nu = 0$ and 1. Between $\nu = 1$ and 2 only even-numerator fractions occur. We further investigate this unusual hierarchy by extracting the corresponding energy gaps as a function of magnetic field. The sequence and relative

strengths of the fractional quantum Hall states are markedly different from those in two-dimensional electron systems with only one degree of freedom, and they provide insight into the interplay between electronic correlations and the inherent symmetries of graphene. By measuring the spatial dependence of the fractional quantum Hall states we are able to explain why these fragile fractional quantum Hall states are observable locally with an SET but not in standard transport experiments. The fact that we see incompressible behavior at multiples of 1/3, 1/5, 1/7 and even 1/9 indicates that graphene is quickly approaching the sample quality obtained in GaAs. During the process of writing this thesis, we observed even higher denominator fractions up to 1/15. Graphene may soon allow to investigate some of the more exotic electronic states observed in conventional two-dimensional systems. We are curious to find out what surprises the SU(4) symmetry and the Dirac nature of the charge carriers will bring.

12. Zusammenfassung

Graphen ist eine ein-atomare Lage aus Kohlenstoffatomen, welche in einer Bienenwaben-struktur angeordnet sind. Seitdem im Jahr 2004 eine einfache Methode entwickelt wurde, um Graphen aus Graphit herzustellen, hat das Interesse an der Graphenforschung stark zugenommen. Dies führte zu einem neuen Forschungsgebiet, der ultra-relativistischen Festkörperphysik. Die Bedeutung von Graphen für die Grundlagenforschung, sowie für Anwendungen z.B. in der Nanoelektronik wächst weiterhin unbegrenzt. Das Ziel der vorliegenden Doktorarbeit ist es, Licht auf einige der ungewöhnlichen Eigenschaften dieses besonderen Materials zu werfen.

Im Rahmen dieser Arbeit liegt unser Schwerpunkt bei der Untersuchung dieser wirklich zwei-dimensionalen Modifikation auf den Raster-Sonden-Methoden. Dabei haben wir den großen Vorteil, dass Graphen und sein zwei-dimensionales Elektronengas frei zugänglich sind und nicht, wie sonst häufig, verborgen in einer Materialkombination. Mit Hilfe der zwei verwendeten Hauptuntersuchungsmethoden, der ortsaufgelösten konfokalen Raman Spektroskopie und der Einzel-Elektronen-Transistor Mikroskopie, können wir so unterschiedliche Informationen wie z.B. die Wechselwirkung von Phononen mit Ladungsträgern oder die Chiralität von Graphenrändern und sogar die Auswirkung der Wechselwirkung von Elektronen untereinander bestimmen. Die Vielfalt der Informationen, die mit Hilfe der Raman Spektroskopie gewonnen werden können, haben ihren Ursprung in Resonanzmechanismen, welche phononische Eigenschaften mit elektronischen verknüpfen. Auf der anderen Seite verfügen Einzel-Elektronen Transistoren über eine außergewöhnlich hohe Empfindlichkeit, wenn es um die Messung von elektrostatischen Potentialen geht. Dies nutzen wir in unseren Raster-Sonden-Spektroskopie-Untersuchungen aus.

CHAPTER 2 - 4   PP. 13-80
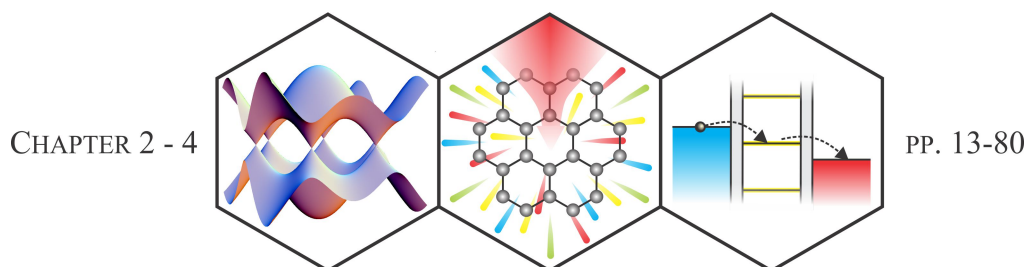
Während wir im ersten Teil die notwendigen Grundlagen dieser Untersuchungsmethoden und den experimentellen Aufbau erläutern, fassen wir nun noch einmal die wichtigsten Resultate der Experimente des zweiten Teils zusammen.
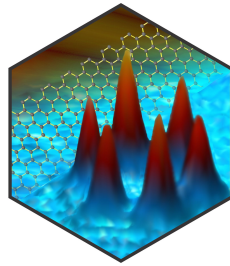
CHAPTER 5   pp. 83-106

Das erste Kapitel startet mit einer Überraschung: Wir zeigen, dass die Raman Spektroskopie, entgegen allgemeiner Meinung und wie ursprünglich angenommen, nicht harmlos ist. Ganz im Gegenteil, denn das verwendete Laserlicht verändert Graphen selbst bei normaler Leistung von 1 mW. Für unsere Untersuchungen wenden wir eine Kombination aus orts- und zeitaufgelösten Raman und Rasterkraft-Messungen an. Die gewonnenen Ergebnisse untermauern wir mit elektrischen Untersuchungen und der Transmissions-Elektronen-Mikroskopie. Wir finden heraus, dass das Beleuchten von Graphen mit Laserlicht die ursprünglich einkristalline Lage in ein Netzwerk aus verknüpften Nanokristalliten verwandelt. Um normale Raman Spektroskopie an Graphen durchzuführen, muss man folglich das Licht vorsichtig dosieren, damit die oben genannte Modifikation nicht eintritt. Andererseits können die Veränderungen aber auch gezielt eingesetzt werden, unter anderem da die erzeugten zusätzlichen Ränder Andockstationen für molekulare Adsorbate darstellen. Hierdurch lässt sich die Reaktivität von Graphen in Bezug auf gewisse Gase stark erhöhen und das sogar ortsaufgelöst. Für Gas-Sensoren stellt dies zum Beispiel einen sehr interessanten Gesichtspunkt dar.
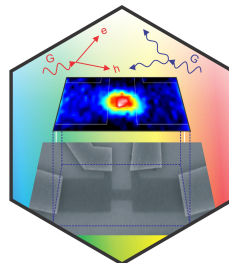
CHAPTER 6   pp. 107-122

In diesem Kapitel untersuchen wir die Wechselwirkung von Phononen mit anderen Quasiteilchen. Speziell die Wechselwirkung mit Ladungsträgern interessiert uns, da dies einen starken Einfluss auf die Performance von Bauelementen hat. Wir zeigen, dass ein hoher Stromfluss durch Graphen die Anzahl der Phononen einer Mode überhöhen kann und dadurch den Transport behindert. Um dies besser zu verstehen, verwenden wir eine elektrisch kontaktierte Graphenprobe mit einer Verengung in der Mitte, wodurch wir gezielt die Phononenbesetzungszahl erhöhen können. Hierdurch lassen sich die Beiträge der Wechselwirkung zwischen Phononen und Ladungsträgern sowie zwischen Phononen selbst trennen. Die zwei in diesem Zusammenhang wichtigsten Größen sind die Temperatur und die Wechselwirkungsstärke der Phononen mit Quasi-Teilchen. Beide Größen lassen sich gleichzeitig mit Hilfe der Raman Spektroskopie bestimmen. Dank der Tatsache, dass Graphen, anders als sonstige Materialien keine Bandlücke hat und wir gleichzeitig die Fermi Temperatur experimentell einstellen können, haben wir die einzigartige Möglichkeit, Zerfallskanäle zu kontrollieren. Hierdurch können wir Graphen in

solch einen Zustand bringen, dass die Temperaturabhängigkeit der Phononen-Peakbreite, welche die Wechselwirkungsstärke wiederspiegelt, nicht monoton ist und für einen gewissen Bereich sogar mit steigender Temperatur abnimmt. Dies wurde, soweit wir wissen, in keinem anderen Material jemals vorher beobachtet.
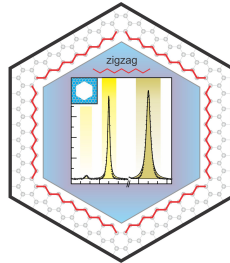
CHAPTER 7   PP. 123-134

Die Bedeutung des Graphenrandes und die damit verbundenen elektronischen Zustände sind schon lange im Fokus intensiver Forschung. So sagen theoretische Untersuchungen vielfältige und sehr unterschiedliche physikalische Effekte für die Fälle voraus, dass die Kohlenstoffatome am Rand entweder in der "Zickzack" oder der "Armchair" Konfiguration vorliegen. Zickzack Ränder setzen sich aus Atomen zusammen, die alle zum selben Untergitter gehören, wohingegen die Armchair Konfiguration aus Atomen aus beiden Untergittern gebildet wird. Dieser Unterschied hat tiefgreifende Konsequenzen und eine Vielzahl erstaunlicher Effekte wird erwartet. Um dieses physikalische Nirwana zu erschließen, muss man allerdings erst einmal in der Lage sein, Graphenproben mit einem wohldefinierten Rand herzustellen. Weiterhin muss auch nachgewiesen werden können, dass dieser Rand eine genau bekannte Chiralität besitzt. Wir stellen in diesem Kapitel eine Methode vor, welche durch anisotropes Ätzen saubere Zickzack Ränder herstellt. Weiterhin demonstrieren wir, dass es mit Hilfe der Raman Spektroskopie als rein optische Untersuchungsmethode möglich ist, die Chiralität der Ränder experimentell zu bestimmen. Als Indikator verwenden wir hierfür den Raman D Peak von Graphen und erklären auch die dazugehörige Theorie. Diese Methode zur Klassifizierung von Graphenrändern stellt eine sehr mächtige Fähigkeit dar. So kann man zum Beispiel durch die Kombination des anisotropen Ätzens und der Raman Spektroskopie relativ einfach die kristallografische Ausrichtung von Graphenflocken bestimmen. Zum Schluss zeigen wir noch auf, wie man die Ätzprozedur verwenden kann, um Verengungen im Graphen, ein-dimensionale Kanäle und sogar Quantenpunkte herzustellen, deren Ränder einzig und allein aus der Zickzack Konfiguration bestehen.
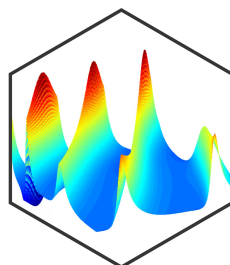

CHAPTER 8   PP. 135-144

Obwohl Monolagen Graphen nur ein Atom dick sind, sind sie auf einem Silizium Substrat, welches mit 300 nm Siliziumoxid bedeckt ist, sichtbar. Somit kann die optische

Mikroskopie als einfache und schnelle optische Untersuchungsmethode verwendet werden, um Graphen Mono- und Mehrfachlagen zu finden und zu identifizieren. Mit einem eleganten Modell, basierend auf den Fresnelschen Formeln, können wir die Sichtbarkeit, d.h. den Kontrast, berechnen. Und das für Graphen auf Si/SiO$_2$ und ganz allgemein auf Substraten mit beliebigen Lagen und Anordnungen dieser Lagen. Als Beispiel verwenden wir Indium-Zinn-Oxid (ITO) auf Si/SiO$_2$. Da ITO transparent und dennoch elektrisch leitend ist, eignet es sich bestens für STM Messungen der Graphenränder. Wir zeigen auf, wie man mit Hilfe des oben beschriebenen Modells die am besten geeignete ITO Dicke für eine maximale Sichtbarkeit berechnet und präparieren Graphen auf ITO. Somit können wir Modell und Experiment direkt miteinander vergleichen und bestätigen.

CHAPTER 9 PP. 145-152
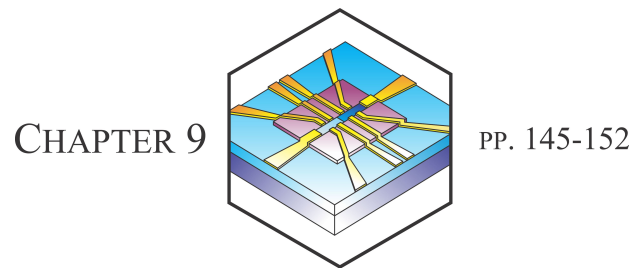
Eine wichtige Messgröße bei elektronischen Bauteilen ist die Beweglichkeit, welche den Zusammenhang zwischen der Driftgeschwindigkeit von Ladungsträgern und dem angelegten elektrischen Feld beschreibt. Graphen hat selbst bei Raumtemperatur schon eine sehr hohe Beweglichkeit, jedoch liegt sie weit unterhalb von theoretischen Erwartungen. Gründe hierfür gibt es genügend. So ist zum Beispiel das unter dem Graphen liegende Substrat nicht perfekt, seine Oberflächenrauhigkeit und optische Oberflächenphononen wirken sich negativ auf die Beweglichkeit aus, ebenso wie geladene Störstellen im Substrat und an der Grenzfläche zwischen Substrat und Graphen. Tatsächlich ist die Beweglichkeit deutlich höher und die Unordnung niedriger, wenn man das Substrat entfernt und das Graphen somit freischwebend zwischen den Kontakten gespannt ist. Dies nutzen wir im nächsten Kapitel aus. Die Kehrseite der Medaille ist jedoch, dass freitragendes Graphen sehr empfindlich ist und leicht zerstört wird. Speziell wenn man eine Backgate-Spannung anlegt, um die Ladungsträgerdichte durchzufahren, wird die Probe schnell durch elektrostatische Kräfte zerstört. Somit kann man keine hohen Spannungen anlegen und die erreichbaren Ladungsträgerdichten sind viel geringer als bei Graphenproben mit Substrat. Eine andere Möglichkeit für Bauteile, welche die Vorteile hoher Beweglichkeiten, hoher Stabilität und hoher Ladungsträgerdichte kombiniert, ist der Ersatz der Grenzfläche zum SiO$_2$ durch ein anderes Material, z.B. durch hexagonales Bornitrid (h-BN). Dieses ist atomar flach und frei von ungesättigten Bindungen oder geladenen Störstellen an der Oberfläche und somit perfekt für dieses Vorhaben. Allerdings ist h-BN meist auch nur in Form kleiner Flocken im Mikrometerbereich verfügbar. Wir erklären eine Möglichkeit, wie man Graphen auf h-BN herstellen kann. Daraufhin untersuchen wir die Sichtbarkeit von h-BN in Abhängigkeit seiner Dicke und vergleichen die experimentell gewonnenen Daten mit der Theorie aus dem vorherigen Kapitel. Schließlich beschäftigen wir uns noch mit der Oberflächenrauhigkeit von h-BN und den daraus resultierenden Konsequenzen.
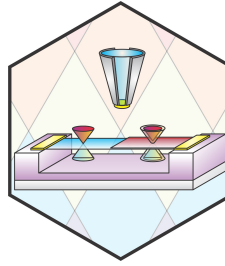
Die Ladungsträger im Graphen verhalten sich wie masselose chirale Fermionen mit einer vierfachen Entartung, welche von den Spin- und Valley-Freiheitsgraden herrührt. Hierdurch lassen sich noch nie dagewesene Vielteilchen-Effekte untersuchen. In diesem letzten experimentellen Kapitel beschreiben wir Raster-Sonden Experimente, die wir mit einem Einzel-Elektronen Transistor (SET) an einer freitragenden Graphen Monolage durchführen. Die hohe Qualität der Probe kann man schon am Auftreten der symmetriegebrochenen Zustände erahnen. Weiterhin beobachten wir ein interessantes Muster inkompressibler gebrochenzahliger Quanten-Hall-Zustände. Zwischen den Füllfaktoren $\nu = 0$ und 1 folgen diese Zustände dem Schema der normalen "composite fermions". Zwischen $\nu = 1$ und 2 treten sie jedoch nur noch mit geradem Zähler auf. Um diese ungewöhnliche Hierarchie der Zustände besser zu verstehen, messen wir die zugehörigen Energielücken in Abhängigkeit des Magnetfelds. Aus ortsaufgelösten Messungen der gebrochenzahligen Quanten-Hall-Zustände können wir erklären, warum diese empfindlichen Zustände zwar lokal mit Hilfe eines SETs beobachtet werden können, jedoch nicht global mit normalen Transportmessungen. Die Tatsache, dass wir inkompressible Zustände bei vielfachem von 1/3, 1/5, 1/7 und sogar 1/9 beobachten, lässt erwarten, dass Graphen schon sehr bald die hohe Qualität von Systemen wie GaAs erreichen wird. So konnten wir, während der Zeit in der diese Doktorarbeit verfasst wurde, die Probenqualität so weit verbessern, dass wir nun sogar schon Zustände bis 1/15 sehen. Schon bald wird man in Graphen voraussichtlich einige der exotischen elektronischen Zustände messen können, wie sie auch in GaAs auftreten. Wir sind gespannt, welche Überraschungen die Dirac-Natur der Ladungsträgerdichte und ihre SU(4)-Symmetrie bereithalten.

Bibliography

[1] H. Beyer, *Lehrbuch der organischen Chemie.* S. Hirzel Verlag Leipzig, 1968.

[2] S. Iijima, "Helical microtubules of graphitic carbon," *Nature*, vol. **354**, p. 56, 1991.

[3] H. W. Kroto, J. R. Heath, S. C. O'Brien, R. F. Curl, and R. E. Smalley, "C60: Buckminsterfullerene," *Nature*, vol. **318**, p. 162, 1985.

[4] N. D. Mermin, "Crystalline order in two dimensions," *Phys. Rev.*, vol. **176**, pp. 250–254, 1968.

[5] K. S. Novoselov et al., "Electric field effect in atomically thin carbon films," *Science*, vol. **306**, pp. 666–669, 2004.

[6] K. S. Novoselov et al., "Two-dimensional gas of massless Dirac fermions in graphene," *Nature*, vol. **438**, pp. 197–200, 2005.

[7] Y. Zhang, Y. W. Tan, H. L. Stormer, and P. Kim, "Experimental observation of the quantum Hall effect and Berry's phase in graphene," *Nature*, vol. **438**, pp. 201–204, 2005.

[8] K. v. Klitzing, G. Dorda, and M. Pepper, "New method for high-accuracy determination of the fine-structure constant based on quantized Hall resistance," *Phys. Rev. Lett.*, vol. **45**, pp. 494–497, Aug 1980.

[9] K. S. Novoselov et al., "Room-temperature quantum Hall effect in graphene," *Science*, vol. **315**, p. 1379, 2007.

[10] S. Bae et al., "Roll-to-roll production of 30-inch graphene films for transparent electrodes," *Nat. Nanotechnol.*, vol. **5**, pp. 574–578, 2010.

[11] H. Wang, T. Taychatanapat, A. Hsu, K. Watanabe, T. Taniguchi, P. Jarillo-Herrero, and T. Palacios, "BN/graphene/BN transistors for RF applications," *Electron Device Letters, IEEE*, vol. **32**, pp. 1209 –1211, 2011.

[12] Y. M. Lin et al., "Operation of graphene transistors at gigahertz frequencies," *Nano Lett.*, vol. **9**, pp. 422–426, 2009.

[13] R. Saito, M. S. Dresselhaus, and G. Dresselhaus, *Physical Properties of Carbon Nanotubes.* Imperial College Press, London, 1998.

[14] O. Madelung, *Introduction to Solid-State Theory.* Springer, Berlin, 1996.

[15] J. C. Charlier, P. C. Eklund, J. Zhu, and A. C. Ferrari, "Electron and phonon properties of graphene: Their relationship with carbon nanotubes," *Top. Appl. Phys.*, vol. **111**, p. 673, 2008.

[16] J. Weis, "Semiconductor physics," Stuttgart, July 2005. Lecture Term 2004/2005.

[17] P. R. Wallace, "The band theory of graphite," *Phys. Rev.*, vol. **71**, pp. 622–634, 1947.

[18] B. Partoens and F. M. Peeters, "From graphene to graphite: Electronic structure around the K point," *Phys. Rev. B*, vol. **74**, p. 075404, 2006.

[19] F. Schwabl, *Quantenmechanik für Fortgeschrittene.* Springer, 2005.

[20] M. I. Katsnelson, "Graphene: Carbon in two dimesions," *Mat. Today*, vol. **10**, pp. 20–27, 2007.

[21] D. Allor, T. D. Cohen, and D. A. McGady, "Schwinger mechanism and graphene," *Phys. Rev. D*, vol. **78**, p. 096009, 2008.

[22] C. W. J. Beenakker, "Andreev reflection and Klein tunneling in graphene," *Rev. Mod. Phys.*, vol. **80**, pp. 1337–1354, 2008.

[23] J. M. B. Lopes dos Santos, N. M. R. Peres, and A. H. Castro Neto, "Graphene bilayer with a twist: Electronic structure," *Phys. Rev. Lett.*, vol. **99**, p. 256802, 2007.

[24] M. Kuwabara, D. R. Clarke, and D. A. Smith, "Anomalous superperiodicity in scanning tunneling microscope images of graphite," *Appl. Phys. Lett.*, vol. **56**, p. 2396, 1990.

[25] Z. Y. Rong and P. Kuiper, "Electronic effects in scanning tunneling microscopy: Moiré pattern on a graphite surface," *Phys. Rev. B*, vol. **48**, pp. 17427–17431, Dec 1993.

[26] A. Luican et al., "Single-layer behavior and its breakdown in twisted graphene layers," *Phys. Rev. Lett.*, vol. **106**, p. 126802, Mar 2011.

[27] K. Kim et al., "Raman spectroscopy study of rotated double-layer graphene: Misorientation angle dependence of electronic structure." http://arxiv.org/abs/1201.4221.

[28] M. Sprinkle et al., "First direct observation of a nearly ideal graphene band structure," *Phys. Rev. Lett.*, vol. **103**, p. 226803, Nov 2009.

[29] G. Trambly de Laissardière, D. Mayou, and L. Magaud, "Localization of Dirac electrons in rotated graphene bilayers," *Nano Lett.*, vol. **10**, pp. 804–808, 2010.

[30] M. Janßen, O. Viehweger, U. Fastenrath, and J. Hajdu, *Introduction to the Theory of the Integer Quantum Hall Effect.* VCH, Weinheim, 1994.

[31] V. P. Gusynin and S. G. Sharapov, "Unconventional integer quantum Hall effect in graphene," *Phys. Rev. Lett.*, vol. **95**, p. 146801, Sep 2005.

[32] J. Martin et al., "Observation of electron-hole puddles in graphene using a single-electron transistor," *Nature Phys.*, vol. **4**, pp. 144–148, 2008.

[33] H. O. Pierson, *Handbook of Carbon, Graphite, Diamond and Fullerenes.* Noyes Publication, 1993.

[34] U. Starke, J. Bernhardt, J. Schardt, and K. Heinz, "SiC surface reconstruction: Relevancy of atomic structure for growth technology," *Surf. Rev. Lett.*, vol. **6**, p. 1129, 1999.

[35] C. Berger et al., "Ultrathin epitaxial graphite: 2D electron gas properties and a route toward graphene-based nanoelectronics," *J. Phys. Chem. B*, vol. **108**, pp. 19912–19916, 2004.

[36] K. V. Emtsev et al., "Towards wafer-size graphene layers by atmospheric pressure graphitization of silicon carbide," *Nat. Mater.*, vol. **8**, p. 203, 2009.

[37] C. Riedl, C. Coletti, T. Iwasaki, A. A. Zakharov, and U. Starke, "Quasi-free standing epitaxial graphene on SiC obtained by hydrogen intercalation," *Phys. Rev. Lett.*, vol. **103**, p. 246804, 2009.

[38] C. Riedl, *Epitaxial Graphene on Silicon Carbide Surfaces: Growth, Characerization, Doping and Hydrogen Intercalation.* PhD thesis, Max Planck Institute for Solid State Research, 2010.

[39] D. S. Lee, C. Riedl, B. Krauss, K. von Klitzing, U. Starke, and J. H. Smet, "Raman spectra of epitaxial graphene on SiC and of epitaxial graphene transferred to SiO_2," *Nano Lett.*, vol. **8**, p. 44320, 2008.

[40] C. Coletti, C. Riedl, D. S. Lee, B. Krauss, L. Patthey, K. von Klitzing, J. H. Smet, and U. Starke, "Charge neutrality and band-gap tuning of epitaxial graphene on SiC by molecular doping," *Phys. Rev. B*, vol. **81**, p. 235401, 2010.

[41] A. Srivastava et al., "Novel liquid precursor-based facile synthesis of large-area continuous, single, and few-layer graphene films," *Chem. of Mater.*, vol. **22**, pp. 3457–3461, 2010.

[42] X. Li et al., "Large-area synthesis of high-quality and uniform graphene films on copper foils," *Science*, vol. **324**, p. 1312, 2009.

[43] R. Rosei et al., "Structure of graphitic carbon on Ni(111): A surface extended-energy-loss fine-structure study," *Phys. Rev. B*, vol. **28**, p. 1161, 1983.

[44] A. M. Shikin, G. V. Prudinkova, V. K. Adamchuk, F. Moresco, and K. H. Rieder, "Surface intercalation of gold underneath a graphite monolayer on Ni(111) studied by angle-resolved photoemission and high-resolution electron-energy-loss spectroscopy," *Phys. Rev. B*, vol. **62**, pp. 13202–13208, 2000.

[45] A. Varykhalov et al., "Electronic and magnetic properties of quasifreestanding graphene on Ni," *Phys. Rev. Lett.*, vol. **101**, p. 157601, 2008.

[46] H. Zi-Pu, O. D.F., V. H. M.A., and S. G.A., "Leed theory for incommensurate overlayers: Application to graphite on Pt(111)," *Surface Science*, vol. **180**, no. 2-3, pp. 433 – 459, 1987.

[47] N. Kholin, R. E.V., and T. A.Y., "The nature of the adsorption bond between graphite islands and iridium surface," *Surface Science*, vol. **139**, pp. 155 – 172, 1984.

[48] I. Pletikosić et al., "Dirac cones and minigaps for graphene on Ir(111)," *Phys. Rev. Lett.*, vol. **102**, p. 056808, Feb 2009.

[49] A. B. Preobrajenski, M. L. Ng, A. S. Vinogradov, and N. Mårtensson, "Controlling graphene corrugation on lattice-mismatched substrates," *Phys. Rev. B*, vol. **78**, p. 073401, Aug 2008.

[50] P. W. Sutter, J. I. Flege, and E. A. Sutter, "Epitaxial graphene on ruthenium," *Nature Mater.*, vol. **7**, pp. 406–411, 2008.

[51] D. Eom et al., "Structure and electronic properties of graphene nanoislands on Co(0001)," *Nano Letters*, vol. **9**, no. 8, pp. 2844–2848, 2009. PMID: 19630380.

[52] A. Reina et al., "Large area, few-layer graphene films on arbitrary substrates by chemical vapor deposition," *Nano Lett.*, vol. **9**, pp. 30–35, 2009.

[53] N. Zhan, M. Olmedo, G. Wang, and J. Liu, "Layer-by-layer synthesis of large-area graphene films by thermal cracker enhanced gas source molecular beam epitaxy,"

Carbon, vol. **49**, no. 6, pp. 2046 – 2052, 2011.

[54] N. Zhan, G. Wang, and J. Liu, "Cobalt-assisted large-area epitaxial graphene growth in thermal cracker enhanced gas source molecular beam epitaxy," *Appl. Phys. A: Mater. Sci. Process.*, vol. **105**, pp. 341–345, 2011.

[55] D. V. Kosynkin et al., "Longitudinal unzipping of carbon nanotubes to form graphene nanoribbons," *Nature*, vol. **458**, pp. 872–876, 2009.

[56] S. Stankovich et al., "Synthesis of graphene-based nanosheets via chemical reduction of exfoliated graphite oxide," *Carbon*, vol. **45**, pp. 1558–1565, 2007.

[57] H. Duan, E. Xie, L. Han, and Z. Xu, "Turning PMMA nanofibers into graphene nanoribbons by in situ electron beam irradiation," *Advanced Materials*, vol. **20**, no. 17, pp. 3284–3288, 2008.

[58] K. S. Subrahmanyam, L. S. Panchakarla, A. Govindaraj, and C. N. R. Rao, "Simple method of preparing graphene flakes by an arc-discharge method," *The Journal of Physical Chemistry C*, vol. **113**, no. 11, pp. 4257–4259, 2009.

[59] T. Lohmann, K. von Klitzing, and J. H. Smet, "Four-terminal magneto-transport in graphene p-n junctions created by spatially selective doping," *Nano Lett.*, vol. **9**, pp. 1973–1979, 2009.

[60] T. Lohmann, *Elektronischer Transport in Graphen*. PhD thesis, Max-Planck-Insitut für Festkörperforschung, 2010.

[61] J. Ye et al., "Accessing the transport properties of graphene and its multilayers at high carrier density," *PNAS*, vol. **108**, p. 32, 2011.

[62] D. K. Efetov and P. Kim, "Controlling electron-phonon interactions in graphene at ultrahigh carrier densities," *Phys. Rev. Lett.*, vol. **105**, p. 256805, 2010.

[63] C. V. Raman and K. S. Krishnan, "A new type of secondary radiation," *Nature*, vol. **121**, p. 501, 1928.

[64] J. I. Steinfeld and J. Wormhoudt, "Explosives detection: a challenge for physical chemistry," *Annu. Rev. Phys. Chem.*, vol. **49**, pp. 202–232, 1998.

[65] M. T. Bremer, P. J. Wrzesinski, N. Butcher, V. V. Lozovoy, and M. Dantus, "Highly selective standoff detection and imaging of trace chemicals in a complex background using single-beam coherent anti-Stokes Raman scattering," *Appl. Phys. Lett.*, vol. **99**, p. 101109, 2011.

[66] D. I. Ellis and R. Goodacre, "Metabolic fingerprinting in disease diagnosis: Biomed-

ical applications of infrared and Raman spectroscopy," *Analyst*, vol. **131**, pp. 875–885, 2006.

[67] P. C. Painter, L. E. Mosher, and C. Rhoads, "Low-frequency modes in the Raman spectra of proteins," *Biopolymers*, vol. **21**, pp. 1469–1472, 1982.

[68] P. C. Painter, L. E. Mosher, and C. Rhoads, "Low-frequency modes in the Raman spectrum of DNA," *Biopolymers*, vol. **20**, pp. 2477–2481, 1981.

[69] H. Ibach and H. Lüth, *Solid-State Physics*. Springer, Berlin, 1996.

[70] J. D. Jackson, *Klassische Elektrodynamik*. Walter de Gryter, Berlin, 4th ed., 2006.

[71] B. Krauss, "Scanning probe spectroscopy of graphene nanostructures," Master's thesis, Max-Planck-Institute for Solid State Research and University of Stuttgart, 2007.

[72] P. Y. Yu and M. Cardona, *Fundamentals of Semiconductors*. Springer, Berlin, 2005.

[73] M. A. Pimenta, G. Dresselhaus, M. S. Dresselhaus, L. G. Cancado, A. Jorio, and R. Saito, "Studying disorder in graphite-based systems by Raman spectroscopy," *Phys. Chem. Chem. Phys.*, vol. **9**, pp. 1276–1291, 2007.

[74] S. Reich and C. Thomsen, "Raman spectroscopy of graphite," *Phil. Trans. R. Soc. Lond. A*, vol. **362**, pp. 2271–2288, 2004.

[75] H. Haken and H. C. Wolf, *Molekülphysik und Quantenchemie*. Springer, Berlin, 2006.

[76] R. Al-Jishi and G. Dresselhaus, "Lattice-dynamical model for graphite," *Phys. Rev. B*, vol. **26**, pp. 4514–4522, 1982.

[77] Y. Kawashima and G. Katagiri, "Observation of the out-of- plane mode in the Raman scattering from the graphite edge plane," *Phys. Rev. B*, vol. **59**, pp. 62–64, 1999.

[78] T. M. G. Mohiuddin et al., "Uniaxial strain in graphene by Raman spectroscopy: G peak splitting, Grüneisen parameters, and sample orientation," *Phys. Rev. B*, vol. **79**, p. 205433, May 2009.

[79] K. Sasaki, R. Saito, K. Wakabayashi, and T. Enoki, "Identifying the orientation of edge of graphene using G band Raman spectra," *J. Phys. Soc. Jpn.*, vol. **79**, p. 044603, 2010.

[80] C. Cong, T. Yu, and H. Wang, "Raman study on the G mode of graphene for determination of edge orientation," *ACS Nano*, vol. **4**, pp. 3175–3180, 2010.

[81] I. Calizo, I. Bejenari, M. Rahman, G. Liu, and A. A. Balandin, "Ultraviolet Raman microscopy of single and multilayer graphene," *Journal of Appl. Phys.*, vol. **106**, p. 043509, 2009.

[82] R. P. Vidano, D. B. Fischbach, L. J. Willis, and T. M. Loehr, "Observation of Raman band shifting with excitation wavelength for carbons and graphites," *Sol. State Comm.*, vol. **39**, pp. 341–344, 1981.

[83] C. Thomsen and S. Reich, "Double resonant Raman scattering in graphite," *Phys. Rev. Lett.*, vol. **85**, pp. 5214–5217, 2000.

[84] R. M. Martin and L. M. Falicov, *Light Scattering in Solids I*, vol. **8**. Springer, Berlin, 1983.

[85] A. C. Ferrari et al., "Raman spectrum of graphene and graphene layers," *Phys. Rev. Lett.*, vol. **97**, p. 187401, 2006.

[86] Z. Ni, Y. Wang, T. Yu, Y. You, and Z. Shen, "Reduction of the Fermi velocity in folded graphene observed by resonance Raman spectroscopy," *Phys. Rev. B*, vol. **77**, p. 235403, 2008.

[87] F. Tuinstra and J. L. Koenig, "Raman spectrum of graphite," *J. Chem. Phys.*, vol. **53**, p. 1126, 1970.

[88] Y. Wang, D. C. Alsmeyer, and R. L. McCreery, "Raman spectroscopy of carbon materials: Structural basis of observed spectra," *Chem. Mater.*, vol. **2**, pp. 557–563, 1990.

[89] J. Maultzsch, S. Reich, and C. Thomsen, "Double-resonant Raman scattering in graphite: Interference effects, selection rules, and phonon dispersion," *Phys. Rev. B*, vol. **70**, p. 155403, 2004.

[90] D. M. Basko, "Theory of resonant multiphonon Raman scattering in graphene," *Phys. Rev. B*, vol. **78**, p. 125418, 2008.

[91] C. Kittel, *Einführung in die Festkörperphysik*. R. Oldenburg, München, 1983.

[92] L. A. Falkovsky, "Phonon dispersion in graphene," *J. Exp. and Theo. Phys.*, vol. **105**, pp. 397–403, 207.

[93] M. S. Dresselhaus and P. C. Eklund, "Phonons in carbon nanotubes," *Advances in Physics*, vol. **49**, pp. 705–814, 2000.

[94] L. Wirtz and A. Rubio, "The phonon dispersion of graphite revisited," *Solid State Commun.*, vol. **131**, pp. 141–152, 2004.

[95] E. Hecht, *Optics*. Addison Wesley, 2002.

[96] J. Martin, *The ultimate guide to the SPM*. 2010.

[97] Y. Y. Wang, Z. H. Ni, Z. X. Shen, H. M. Wang, and Y. H. Wu, "Interference enhancement of Raman signal of graphene," *Appl. Phys. Lett.*, vol. **92**, p. 043121, 2008.

[98] C. Cong, T. Yu, R. Saito, G. F. Dresselhaus, and M. S. Dresselhaus, "Second-order overtone and combination Raman modes of graphene layers in the range of 1690 - 2150 cm^{-1}," *ACS Nano*, vol. **5**, pp. 1600–1605, 2011.

[99] R. Rao et al., "Effects of layer stacking on the combination Raman modes in graphene," *ACS Nano*, vol. **5**, pp. 1594–1599, 2011.

[100] A. C. Ferrari, "Raman spectroscopy of graphene and graphite: Disorder, electron-phonon coupling, doping and nonadiabatic effects," *Solid State Communications*, vol. **143**, no. 1-2, pp. 47–57, 2007. Exploring graphene - Recent research advances.

[101] S. A. Solin and A. K. Ramdas, "Raman spectrum of diamond," *Phys. Rev. B*, vol. **1**, p. 1687, 1970.

[102] K. N. Kudin et al., "Raman spectra of graphite oxide and functionalized graphene sheets," *Nano Lett.*, vol. **8**, p. 36, 2008.

[103] M. Hulman, M. Haluska, G. Scalia, D. Obergfell, and S. Roth, "Effects of charge impurities and laser energy on raman spectra of graphene," *Nano Lett.*, vol. **8**, p. 3594, 2008.

[104] S. Pisana et al., "Breakdown of the adiabatic Born - Oppenheimer approximation in graphene," *Nature Mater.*, vol. **6**, p. 198, 2007.

[105] J. Yan, Y. Zhang, P. Kim, and A. Pinczuk, "Electric field effect tuning of electron-phonon coupling in graphene," *Phys. Rev. Lett.*, vol. **98**, p. 166802, 2007.

[106] A. Das et al., "Monitoring dopants by Raman scattering in an electrochemically top-gated graphene transistor," *Nat. Nanotechnol.*, vol. **3**, p. 210, 2008.

[107] C. Casiraghi, S. Pisana, K. S. Novoselov, A. K. Geim, and A. C. Ferrari, "Raman fingerprint of charged impurities in graphene," *Appl. Phys. Lett.*, vol. **91**, p. 233108, 2007.

[108] Z. H. Ni et al., "Probing charged impurities in suspended graphene using Raman spectroscopy," *ACS Nano*, vol. **3**, p. 569, 2009.

[109] S. Berciaud, S. Ryu, L. E. Brus, and T. F. Heinz, "Probing the intrinsic properties

of exfoliated graphene: Raman spectroscopy of free-standing monolayers," *Nano Lett.*, vol. **9**, p. 346, 2009.

[110] C. Stampfer et al., "Raman imaging of doping domains in graphene on SiO_2," *Appl. Phys. Lett.*, vol. **91**, p. 241907, 2007.

[111] A. C. Ferrari and J. Robertson, "Resonant Raman spectroscopy of disordered, amorphous, and diamandlike carbon," *Phys. Rev. B*, vol. **64**, p. 075414, 2001.

[112] A. Singha and A. Roy, "Phonon confinement and surface phonon modes in CdSe-CdS core-shell nanocrystals," *Rev. Adv. Mater. Sci.*, vol. **10**, p. 462, 2005.

[113] J. Maultzsch, S. Reich, C. Thomsen, H. Requardt, and P. Ordejón, "Phonon dispersion in graphite," *Phys. Rev. Lett.*, vol. **92**, p. 075501, 2004.

[114] M. Lafkioti, B. Krauss, T. Lohmann, U. Zschieschang, H. Klauk, K. v. Klitzing, and J. H. Smet, "Graphene on a hydrophobic substrate: Doping reduction and hysteresis suppression under ambient conditions," *Nano Lett.*, vol. **10**, pp. 1149–1153, APR 2010.

[115] M. Ishigami, J. Chen, W. Cullen, M. Fuhrer, and E. Williams, "Atomic structure of graphene on SiO_2," *Nano Lett.*, vol. **7**, pp. 1643–1648, 2007.

[116] M. Luna, J. Colchero, and A. M. Baró, "Study of water droplets and films on graphite by noncontact scanning force microscopy," *The Journal of Physical Chemistry B*, vol. **103**, no. 44, pp. 9576–9581, 1999.

[117] F. Schedin et al., "Detection of individual gas molecules adsorbed on graphene," *Nat. Mater.*, vol. **6**, pp. 652–655, 2007.

[118] Z. Yao, C. L. Kane, and C. Dekker, "High-field electrical transport in single-wall carbon nanotubes," *Phys. Rev. Lett.*, vol. **84**, pp. 2941–2944, Mar 2000.

[119] J. Y. Park and et al., "Electron-phonon scattering in metallic single-walled carbon nanotubes," *Nano Letters*, vol. **4**, no. 3, pp. 517–520, 2004.

[120] A. W. Bushmaker, V. V. Deshpande, M. W. Bockrath, and S. B. Cronin, "Direct observation of mode selective electron-phonon coupling in suspended carbon nanotubes," *Nano Letters*, vol. **7**, no. 12, pp. 3618–3622, 2007. PMID: 18020473.

[121] M. Oron-Carl and R. Krupke, "Raman spectroscopic evidence for hot-phonon generation in electrically biased carbon nanotubes," *Phys. Rev. Lett.*, vol. **100**, p. 127401, 2008.

[122] M. Steiner et al., "Phonon populations and electrical power dissipation in carbon

nanotube transistors," *Nat. Nanotechnol.*, vol. **4**, pp. 320–324, 2009.

[123] M. Lazzeri and F. Mauri, "Coupled dynamics of electrons and phonons in metallic nanotubes: Current saturation from hot-phonon generation," *Phys. Rev. B*, vol. **73**, p. 165419, 2006.

[124] E. Pop et al., "Negative differential conductance and hot phonons in suspended nanotube molecular wires," *Phys. Rev. Lett.*, vol. **95**, p. 155505, 2005.

[125] I. Meric et al., "Current saturation in zero-bandgap, top-gated graphene field-effect transistors," *Nat. Nanotechnol.*, vol. **3**, pp. 654–659, 2008.

[126] G. Lang et al., "Anharmonic line shift and linewidth of the Raman mode in covalent semiconductors," *Phys. Rev. B*, vol. **59**, pp. 6182–6188, 1999.

[127] H. Schulz and S. Hüfner, "Anharmonicity in the TO optical phonon of Zn," *Sol. State Comm.*, vol. **20**, pp. 827–830, 1976.

[128] J. Höhne, U. Wenning, H. Schulz, and S. Hüfner, "Temperature dependence of the $k=0$ optical phonons of Bi and Sb," *Z. Phys. B*, vol. **27**, pp. 297–302, 1977.

[129] J. Moser, A. Barreiro, and A. Bachtold, "Current-induced cleaning of graphene," *Appl. Phys. Lett.*, vol. **91**, p. 163513, 2007.

[130] A. A. Balandin et al., "Superior thermal conductivity of single-layer graphene," *Nano Letters*, vol. **8**, pp. 902–907, 2008.

[131] N. Bonini, M. Lazzeri, N. Marzari, and F. Mauri, "Phonon anharmonicities in graphite and graphene," *Phys. Rev. Lett.*, vol. **99**, p. 176802, 2007.

[132] B. Krauss et al., "Laser-induced disassembly of a graphene single crystal into a nanocrystalline network," *Phys. Rev. B*, vol. **79**, p. 165428, 2009.

[133] M. Lazzeri and F. Mauri, "Nonadiabatic Kohn anomaly in a doped graphene monolayer," *Phys. Rev. Lett.*, vol. **97**, p. 266407, 2006.

[134] D. Mann et al., "Electrically driven thermal light emission from individual single-walled carbon nanotubes," *Nat. Nanotechnol.*, vol. **2**, pp. 33–38, 2007.

[135] H. Kuzmany, *Solid-State Spectroscopy*. Springer-Verlag: Berlin, 1998.

[136] N. W. Ashcroft and N. D. Mermin, *Solid State Physics*. Thomson Learning: London, 1976.

[137] Y. W. Son, M. L. Cohen, and S. G. Louie, "Energy gaps in graphene nanoribbons," *Phys. Rev. Lett.*, vol. **97**, p. 216803, 2006.

[138] M. Y. Han, B. Oezyilmaz, Y. Zhang, and P. Kim, "Energy band-gap engineering of graphene nanoribbons," *Phys. Rev. Lett.*, vol. **98**, p. 206805, 2007.

[139] L. Yang, M. L. Cohen, and S. G. Louie, "Excitonic effects in the optical spectra of graphene nanoribbons," *Nano Lett.*, vol. **7**, p. 3112, 2007.

[140] Y. W. Son, M. L. Cohen, and S. G. Louie, "Half-metallic graphene nanoribbons," *Nature*, vol. **444**, p. 347, 2006.

[141] A. G. Moghaddam and M. Zareyan, "Graphene-based superconducting quantum point contacts," *Appl. Phys. A: Mater. Sci. Process.*, vol. **89**, p. 579, 2007.

[142] K. Nakada, M. Fujita, G. Dresselhaus, and M. S. Dresselhaus, "Edge state in graphene ribbons: Nanometer size effect and edge shape dependence," *Phys. Rev. B*, vol. **54**, p. 17954, 1996.

[143] K. Wakabayashi, M. Fujita, H. Ajiki, and M. Sigrist, "Electronic and magnetic properties of nanographite ribbons," *Phys. Rev. B*, vol. **59**, p. 8271, 1999.

[144] Y. Kobayashi, K. Kusakabe, K. Fukui, and T. Enoki, "STM/STS observation of peculiar electronic states at graphite edges," *Phys. E (Amsterdam, Neth.)*, vol. **34**, pp. 678–681, 2006.

[145] D. A. Abanin, P. A. Lee, and L. S. Levitov, "Charge and spin transport at the quantum hall edge of graphene," *Solid State Commun.*, vol. **143**, p. 77, 2007.

[146] K. Sasaki, J. Jiang, R. Saito, S. Onari, and Y. Tanaka, "Theory of superconductivity of carbon nanotubes and graphene," *J. Phys. Soc. Jpn.*, vol. **76**, p. 033702, 2007.

[147] O. V. Yazyev, "Emergence of magnetism in graphene materials and nanostructures," *Rep. Prog. Phys.*, vol. **73**, p. 056501, 2010.

[148] B. Trauzettel, D. V. Bulaev, D. Loss, and G. Burkard, "Spin qubits in graphene quantum dots," *Nat. Phys.*, vol. **3**, pp. 192–196, 2007.

[149] A. Rycerz, J. Tworzydlo, and C. W. J. Beenakker, "Valley filter and valley valve in graphene," *Nat. Phys.*, vol. **3**, pp. 172–175, 2007.

[150] C. O. Girit et al., "Graphene at the edge: Stability and dynamics," *Science*, vol. **323**, p. 1705, 2009.

[151] L. Tapaszto, G. Dobrik, P. Lambin, and L. P. Biro, "Tailoring the atomic structure of graphene nanoribbons by scanning tunnelling microscope lithography," *Nat. Nanotechnol.*, vol. **3**, p. 397, 2008.

[152] L. G. Cancado, M. A. Pimenta, B. R. A. Neves, M. S. S. Dantas, and A. Jorio,

"Influence of the atomic structure on the Raman spectra of graphite edges," *Phys. Rev. Lett.*, vol. **93**, p. 247401, 2004.

[153] D. M. Basko, "Boundary problems for Dirac electrons and edge-assisted Raman scattering in graphene," *Phys. Rev. B*, vol. **79**, p. 205428, 2009.

[154] A. K. Gupta, T. J. Russin, H. R. Gutierrez, and P. C. Eklund, "Probing graphene edges via Raman scattering," *ACS Nano*, vol. **3**, p. 45, 2009.

[155] Y. You, Z. Ni, T. Yu, and Z. Shen, "Edge chirality determination of graphene by Raman spectroscopy," *Appl. Phys. Lett.*, vol. **93**, p. 163112, 2008.

[156] C. Casiraghi et al., "Raman spectroscopy of graphene edges," *Nano Lett.*, vol. **9**, p. 1433, 2009.

[157] L. P. Biro and P. Lambin, "Nanopatterning of graphene with crystallographic orientation control," *Carbon*, vol. **48**, pp. 2677–2689, 2010.

[158] A. Incze, A. Pasturel, and C. Chatillon, "Ab inito study of graphite prismatic surfaces," *Appl. Surface Science*, vol. **177**, pp. 221–225, 2001.

[159] J. Gonzalez, M. d. C. Ruiz, A. Bohe, and D. Pasquevich, "Oxidation of carbons in the presence of chlorine," *Carbon*, vol. **37**, pp. 1979–1988, 1999.

[160] A. Incze, A. Pasturel, and C. Chatillon, "Oxidation of graphite by atomic oxygen: a first-principles approach," *Surface Science*, vol. **537**, pp. 55–63, 2003.

[161] D. Tandon, E. J. Hippo, H. Marsh, and E. Sebok, "Surface topography of oxidized HOPG by scanning tunneling microscopy," *Carbon*, vol. **35**, pp. 35–44, 1997.

[162] J. Lahaye and P. Ehrburger, eds., *Fundamental Issues in Control of Carbon Gasification Reactivity*. Kluwer Academic Publishers, 1991.

[163] X. Y. Zhu, S. M. Lee, Y. H. Lee, and T. Frauenheim, "Adsorption and desorption of an O_2 molecule on carbon nanotubes," *Phys. Rev. Lett.*, vol. **85**, p. 2757, 2000.

[164] S. S. Datta, D. R. Strachan, S. M. Khamis, and A. T. C. Johnson, "Crystallographic etching of few-layer graphene," *Nano Lett.*, vol. **8**, p. 1912, 2008.

[165] L. Ci et al., "Controlled nanocutting of graphene," *Nano Res.*, vol. **1**, p. 116, 2008.

[166] L. C. Campos, V. R. Manfrinato, J. D. Sanchez-Yamagishi, J. Kong, and P. Jarillo-Herrero, "Anisotropic etching and nanoribbon formation in single-layer graphene," *Nano Lett.*, vol. **9**, p. 2600, 2009.

[167] P. Nemes-Incze, G. Magda, K. Kamaras, and L. P. Biro, "Crystallographically se-

lective nanopatterning of graphene on SiO$_2$," *Nano Res.*, vol. **3**, p. 110, 2010.

[168] L. Liu et al., "Graphene oxidation: Thickness-dependent etching and strong chemical doping," *Nano Lett.*, vol. **8**, p. 1965, 2008.

[169] D. C. Elias et al., "Control of graphene's properties by reversible hydrogenation: Evidence for graphane," *Science*, vol. **323**, p. 610, 2009.

[170] J. Zhang et al., "Reduction of graphene oxide via L-ascorbic acid," *Chem. Commun.*, vol. **46**, p. 1112, 2010.

[171] D. Kärcher, "Controlling the edge of graphene," Master's thesis, Universität Stuttgart / MPI FKF, 2011.

[172] M. I. Katsnelson and A. K. Geim, "Electron scattering on microscopic corrugations in graphene," *Phil. Trans. R. Soc. A*, vol. **366**, pp. 195–204, 2007.

[173] S. V. Morozov et al., "Giant intrisic carrier mobilities in graphene and its bilayer," *Phys. Rev. Lett.*, vol. **100**, p. 016602, 2008.

[174] S. Fratini and F. Guinea, "Substrate-limited electron dynamics in graphene," *Phys. Rev. B*, vol. **77**, p. 195415, 2008.

[175] J.-H. Chen, C. Jang, S. Xiao, M. Ishigami, and M. S. Fuhrer, "Intrinsic and extrinsic performance limits of graphene devices on SiO$_2$," *Nature Nanotechnol.*, vol. **3**, pp. 206–209, 2008.

[176] T. Ando, "Screening effect and impurity scattering in monolayer graphene," *J. Phys. Soc. Jpn.*, vol. **75**, p. 074716, 2006.

[177] K. Nomura and A. H. MacDonald, "Quantum transport of massless Dirac fermions," *Phys. Rev. Lett.*, vol. **98**, p. 076602, 2007.

[178] E. H. Hwang, S. Adam, and S. Das Sarma, "Carrier transport in two-dimensional graphene layers," *Phys. Rev. Lett.*, vol. **98**, p. 186806, 2007.

[179] S. Adam, E. H. Hwang, V. Galitski, and S. Das Sarma, "A self-consistent theory for graphene transport," *Proc. Natl. Acad. Sci. USA*, vol. **104**, p. 18392, 2007.

[180] K. S. Novoselov et al., "Unconventional quantum Hall effect and Berry's phase of 2π in bilayer graphene.," *Nature Phys.*, vol. **2**, pp. 177–180, 2006.

[181] T. Taychatanapat, K. Watanabe, T. Taniguchi, and P. Jarillo-Herrero, "Quantum Hall effect and Landau-level crossing of Dirac fermions in trilayer graphene," *Nature Phys.*, vol. **7**, pp. 621–625, 2011.

[182] F. Guinea, A. H. C. Neto, and N. M. R. Peres, "Electronic states and Landau levels in graphene stacks," *Phys. Rev. B*, vol. **73**, p. 245426, 2006.

[183] S. Latil and L. Henrard, "Charge carriers in few-layer graphene films," *Phys. Rev. Lett.*, vol. **97**, p. 036803, 2006.

[184] P. Blake et al., "Making graphene visible," *Appl. Phys. Lett.*, vol. **91**, p. 063124, 2007.

[185] D. S. Abergel, A. Russell, and V. I. Falko, "Visibility of graphene flakes on a dielectric substrate," *Appl. Phys. Lett.*, vol. **91**, p. 063125, 2007.

[186] S. Roddaro, P. Pingue, V. Piazza, V. Pellegrini, and F. Beltram, "The optical visibility of graphene: Interference colors of ultrathin graphite on SiO_2," *Nano Lett.*, vol. **7**, pp. 2707–2710, 2007.

[187] C. Casiraghi et al., "Rayleigh imaging of graphene and graphene layers," *Nano Lett.*, vol. **7**, pp. 2711–2717, 2007.

[188] I. Jung et al., "Simple approach for high-contrast optical imaging and characterization of graphene-based sheets," *Nano Lett.*, vol. **7**, pp. 3569–3575, 2007.

[189] M. Bruna and S. Borini, "Optical constants of graphene layers in the visible range," *Appl. Phys. Lett.*, vol. **94**, p. 031901, 2009.

[190] H. Anders, *Dünne Schichten für die Optik*. Wissenschaftliche Verlagsgesellschaft MBH Stuttgart, 1965.

[191] W. Demtröder, *Experimentalphysik 2: Elektrizität und Optik*. Springer- Verlag Berlin Heidelberg, 2009.

[192] A. Vasicek, "The reflection of light on glass supporting multiple thin films. sur la réflexion de la lumière sur des verres supportant des couches minces multiples," *Le journal de physique et le radium*, vol. **11**, p. 342, 1950.

[193] H. Schröder *Ztschr. f. angew. Phys.*, vol. **3**, p. 53, 1951.

[194] D. L. Caballero, "A theoretical development of exact solution of reflectance of multiple layer optical coatings," *J. Opt. Soc. Am.*, vol. **37**, p. 176, 1947.

[195] W. L. Wilcock, "On a paper by Vasicek concerning reflection from multilayer films," *J. Opt. Soc. Am.*, vol. **39**, p. 889, 1949.

[196] H. D. Polster, "Reflection from a multilayer filter," *J. Opt. Soc. Am.*, vol. **39**, p. 1038, 1949.

[197] A. Vasicek, "The reflection of light from glass with double and multiple films," *J. Opt. Soc. Am.*, vol. **37**, p. 623, 1947.

[198] A. W. Crook, "The reflection and transmission of light by any system of parallel isotropic films," *J. Opt. Soc. Am.*, vol. **38**, p. 954, 1948.

[199] K. Watanabe, T. Taniguchi, and H. Kanda, "Direct-bandgap properties and evidence for ultraviolet lasing of hexagonal boron nitride single crystal," *Nature Mater.*, vol. **3**, pp. 404–409, 2004.

[200] C. R. Dean et al., "Boron nitride substrates for high-quality graphene electronics," *Nat. Nanotechnol.*, vol. **5**, p. 722, 2010.

[201] J. Xue et al., "Scanning tunneling microscopy and spectroscopy of ultra-flat graphene on hexagonal boron nitride," *Nat. Mater.*, vol. **10**, p. 282, 2011.

[202] J. Slawinska, I. Zasada, and Z. Klusek, "Energy gap tuning in graphene on hexagonal boron nitride bilayer system," *Phys. Rev. B*, vol. **81**, p. 155433, 2010.

[203] G. Giovannetti, P. A. Khomyakov, G. Brocks, P. J. Kelly, and J. van den Brink, "Substrate-induced band gap in graphene on hexagonal boron nitride: *Ab initio* density functional calculations," *Phys. Rev. B*, vol. **76**, p. 073103, Aug 2007.

[204] C. R. Dean et al., "Multicomponent fractional quantum Hall effect in graphene," *Nat. Phys.*, vol. **7**, p. 693, 2011.

[205] T. Taniguchi and K. Watanabe, "Synthesis of high-purity boron nitride single crystals under high pressure using Ba-Bn solvent," *J. Cryst. Growth*, vol. **303**, pp. 525–529, 2007.

[206] E. A. Kim and A. H. C. Neto, "Graphene as an electronic membrane," *Europhys. Lett.*, vol. **84**, p. 57007, 2009.

[207] F. Guinea, M. I. Katsnelson, and M. A. H. Vozmediano, "Midgap states and charge inhomogeneities in corrugated graphene," *Phys. Rev. B*, vol. **77**, p. 075422, 2008.

[208] M. J. Yoo et al., "Scanning single-electron transistor microscopy: Imaging individual charges," *Science*, vol. **276**, p. 579, 1997.

[209] A. Yacoby, H. F. Hess, T. A. Fulton, L. N. Pfeiffer, and K. W. West, "Electrical imaging of the quantum Hall state," *Solid State Comm.*, vol. **111**, p. 1, 1999.

[210] K. Nomura and A. H. MacDonald, "Quantum Hall ferromagnetism in graphene," *Phys. Rev. Lett.*, vol. **96**, p. 256602, 2006.

[211] J. Martin et al., "The nature of localization in graphene under quantum Hall con-

ditions," *Nature Phys.*, vol. **5**, p. 669, 2009.

[212] D. C. Tsui, H. L. Stormer, and A. C. Gossard, "Two-dimensional magnetotransport in the extreme quantum limit," *Phys. Rev. Lett.*, vol. **48**, p. 1559, 1982.

[213] R. B. Laughlin, "Anomalous quantum Hall-effect - an incompressible quantum fluid with fractionally charged excitations," *Phys. Rev. Lett.*, vol. **50**, p. 1395, 1983.

[214] J. K. Jain, "Composite-fermion approach for the fractional quantum Hall-effect," *Phys. Rev. Lett.*, vol. **63**, p. 199, 1989.

[215] B. I. Halperin, "Theory of the quantized Hall conductance," *Helvetica Physica Acta*, vol. **56**, p. 75, 1983.

[216] V. M. Apalkov and T. Chakraborty, "Fractional quantum Hall states of Dirac electrons in graphene," *Phys. Rev. Lett.*, vol. **97**, p. 126801, 2006.

[217] C. Toke, P. E. Lammert, V. H. Crespi, and J. K. Jain, "Fractional quantum Hall effect in graphene," *Phys. Rev. B*, vol. **74**, p. 235417, 2006.

[218] S. Modak, S. S. Mandal, and K. Sengupta, "Fermionic Chern-Simons theory of SU(4) fractional quantum Hall effect." http://arxiv.org/abs/1105.2828.

[219] M. O. Goerbig and N. Regnault, "Analysis of a SU(4) generalization of Halperin's wave function as an approach towards a SU(4) fractional quantum Hall effect in graphene sheets," *Phys. Rev. B*, vol. **75**, p. 241405, 2007.

[220] C. Toke and J. K. Jain, "SU(4) composite fermions in graphene: Fractional quantum Hall states without analog in GaAs," *Phys. Rev. B*, vol. **75**, p. 245440, 2007.

[221] K. Yang, S. Das Sarma, and A. H. MacDonald, "Collective modes and skyrmion excitations in graphene su(4) quantum hall ferromagnets," *Phys. Rev. B*, vol. **74**, p. 075423, 2006.

[222] D. V. Khveshchenko, "Composite dirac fermions in graphene," *Phys. Rev. B*, vol. **75**, p. 153405, 2007.

[223] N. Shibata and K. Nomura, "Coupled charge and valley excitations in graphene quantum Hall ferromagnets," *Phys. Rev. B*, vol. **77**, p. 235426, 2008.

[224] N. Shibata and K. Nomura, "Fractional quantum Hall effect in graphene and its bilayer," *Journal of the Phys. Soc. of Japan*, vol. **78**, p. 104708, 2009.

[225] Z. Papic, M. O. Goerbig, and R. N., "Theoretical expectations for a fractional quantum hall effect in graphene," *Solid State Commun.*, vol. **149**, p. 1056, 2009.

[226] Z. Papic, M. O. Goerbig, and R. N., "Atypical fractional quantum hall effect in graphene at filling factor 1/3," *Phys. Rev. Lett.*, vol. **105**, p. 176802, 2010.

[227] C. Toke and J. K. Jain, "Multi-component fractional quantum Hall states in graphene: SU(4) versus SU(2)." http://arxiv.org/abs/1105.5270.

[228] M. O. Goerbig and R. N., "Theoretical aspects of the fractional quantum hall effect in graphene." http://arxiv.org/abs/1106.4939.

[229] Z. Papic, D. A. Abanin, Y. Barlas, and R. N. Bhatt, "Tunable interactions and phase transitions in Dirac materials in a magnetic field." http://arxiv.org/abs/1108.1339.

[230] F. Ghahari, Y. Zhao, P. Cadden-Zimansky, K. Bolotin, and P. Kim, "Measurement of the ν=1/3 fractional quantum Hall energy gap in suspended graphene," *Phys. Rev. Lett.*, vol. **106**, p. 046801, 2011.

[231] K. I. Bolotin, F. Ghahari, M. D. Shulman, H. L. Stormer, and P. Kim, "Observation of the fractional quantum Hall effect in graphene," *Nature*, vol. **462**, p. 196, 2009.

[232] X. Du, I. Skachko, F. Duerr, A. Liuican, and E. Y. Andrei, "Fractional quantum Hall effect and insulating phase of Dirac electrons in graphene," *Nature*, vol. **462**, p. 192, 2009.

[233] Y. Zhang et al., "Landau-level splitting in graphene at high magnetic fields," *Phys. Rev. Lett.*, vol. **96**, p. 136806, 2006.

[234] Z. Jiang, Y. Zhang, H. L. Stormer, and P. Kim, "Quantum Hall states near the charge-neutral Dirac point in graphene," *Phys. Rev. Lett.*, vol. **99**, p. 106802, 2007.

[235] K. Lai et al., "Two-flux composite fermion series of the fractional quantum hall states in strained si," *Phys. Rev. Lett.*, vol. **93**, p. 156805, 2004.

[236] N. C. Bishop et al., "Valley polarization and susceptibility of composite fermions around a filling factor $\nu = 3/2$," *Phys. Rev. Lett.*, vol. **98**, p. 266404, 2007.

[237] M. Padmanabhan, T. Gokmen, and M. Shayegan, "Ferromagnetic fractional quantum hall states in a valley-degenerate two-dimensional electron system," *Phys. Rev. Lett.*, vol. **104**, p. 016805, 2010.

[238] M. Padmanabhan, T. Gokmen, and M. Shayegan, "Density dependence of valley polarization energy for composite fermions," *Phys. Rev. B*, vol. **80**, p. 035423, 2009.

[239] M. Padmanabhan, T. Gokmen, and M. Shayegan, "Composite fermion valley polarization energies: Evidence for particle-hole asymmetry," *Phys. Rev. B*, vol. **81**, p. 113301, 2010.

[240] J. P. Eisenstein, H. L. Stormer, L. N. Pfeiffer, and K. W. West, "Evidence for a spin transistion in the ν=2/3 fractional quantum Hall-effect," *Phys. Rev. B*, vol. **41**, p. 7910, 1990.

[241] J. P. Eisenstein, L. N. Pfeiffer, and K. W. West, "Negative compressibility of the interacting 2-dimensional electron and quasi-particle gases," *Phys. Rev. Lett.*, vol. **68**, p. 674, 1992.

[242] V. S. Khrapai et al., "Filling factor dependence of the fractional quantum Hall effect gap," *Phys. Rev. Lett.*, vol. **100**, p. 196805, 2008.

[243] C. P. Puls, N. E. Staley, and Y. Liu, "Interface states and anomalous quantum oscillations in hybrid graphene structures," *Phys. Rev. B*, vol. **79**, p. 235415, 2009.

Acknowledgments

Last but not least I want to acknowledge the support of all people who helped me directly and indirectly with this thesis. My special thanks goes to:

- Dr. Jurgen H. Smet for bringing together graphene and me. His combination of leadership and scientific freedom allows professional and also personal growth. He is a great supervisor who constantly motivated me to take on new challenges. Also he provided the best imaginable support, both intellectual and material.

- Prof. Dr. Klaus v. Klitzing for offering me the grand opportunity to work in his department. I always enjoyed our stimulating and inspiring discussions. His interest in this work often brought new insights, knowledge and ideas.

- Prof. Dr. Amir Yacoby (Harvard University) for welcoming me in his group for some exciting and most educational months. Working with him and his team was an outstanding experience.

- Prof. Dr. Jörg Wrachtrup and Prof. Dr. Günter Wunner from the University of Stuttgart for the external report and supervising this thesis.

- Ben Feldmann (Harvard University) who taught me everything about the scanning SET, from theory to practice. He was not only a great co-worker but became a close friend. Thanks to him and urbandictionary.com I was able to expand my vocabulary beyond the common gobbbledygook.

- Dr. Johannes Nübler, I learned a lot from you. Although absolutely nothing about graphene. We had many great days windsurfing at Lago di Garda and I hope many more will follow. Thanks for proofreading this manuscript.

- The persons with whom I shared office and knowledge during my time at the MPI. It always was a pleasant and excellent scientific working atmosphere: Dr. Timm Lohmann, Dr. Dong-Hun Chae, Dr. Gerhard Ulbricht, Dr. Myrsini Lafkioti, Dr. Shu Xu, and Yani Zhai. Especially the most recent office constellation turned out to be very vibrant: Thomas Beringer, Federico Paolucci and Daniel Kärcher.

- Dr. DongSu Lee and Prof. Dr. Viera Skakalova for the interesting and stimulating work on many different projects.

- Ruth Jenz for successfully taking care of all the administrative work and her kind and always helpful way.

- Our technical staff for their constant and valuable support: Steffen, Ingo, Manfred and Gunther as well as Ulli, Achim and Thomas in the cleanroom.

- All our HiWis who fabricated graphene and hence enabled me to focus on the experiments and measurements.

- The people in the von Klitzing department and Mannhard department who contributed to the excellent working atmosphere. It was a great, educating and also

Curriculum Vitae

Persönliche Daten:

Name:	Benjamin Krauß
Geburtsdatum:	13.09.1981
Geburtsort:	Böblingen

Ausbildung:

2008-2012	Promotion Max-Planck-Institut für Festkörperforschung, Stuttgart
2010-2011	Bayer Fellowship Program Harvard University, Cambridge, MA, USA
2007	Diplomarbeit Max-Planck-Institut für Festkörperforschung, Stuttgart
2006	Physikstudium National University of Singapore
2002-2006	Physikstudium Universität Stuttgart
2001-2002	Technische Schule der Luftwaffe Kaufbeuren
1992-2001	Andreae-Gymnasium Herrenberg

Engagement:

2010-2011	Lehrbeauftragter für Experimentalphysik Hochschule Esslingen
2009-2010	Tutor für Experimentalphysik Hochschule Esslingen
2007-2009	Betreuung AP, EP und FP Universität Stuttgart
2003-2006	Wissenschaftlicher Hilfsmitarbeiter Universität Stuttgart